Fall 10-1-2021

Nitrogen Cycle Chemistry with Metal-Pincer Complexes Relevant to Electrochemical Nitrogen Fixation

Gannon Patrick Connor
Yale University Graduate School of Arts and Sciences, gannon.connor@gmail.com

Abstract

Nitrogen Cycle Chemistry with Metal-Pincer Complexes Relevant to Electrochemical Nitrogen Fixation

Gannon Patrick Connor

2021

The large-scale industrial fixation of N_2 to NH_3 through the Haber-Bosch process has cemented itself as the primary means to provide N for fertilizer and commodity chemicals globally. However, our dependence on this process is unsustainable in the long term due to its reliance on fossil fuels to generate H_2 and to provide the substantial energy input for the reaction, paired with high infrastructure requirements that necessitate centralized synthesis plants and sophisticated transportation networks. As an alternative, electrochemical fixation of N_2, coupling water oxidation to provide proton (H^+) and electron (e^-) equivalents with the N_2 reduction reaction (NRR) to achieve the $6H^+/6e^-$ reduction of N_2 to 2 NH_3, could operate on a smaller, localized scale while utilizing renewable sources to generate electrical energy to drive the reaction. A key challenge in achieving electrochemical N_2 fixation is the development of catalysts for electrochemical NRR. Existing heterogeneous catalysts for NRR suffer from poor activity, selectivity, and robustness. Insights that aid the development of better NRR catalysts may be found by studying molecular systems that can reduce N_2. This thesis probes potential N_2 functionalization pathways that could be involved in electrochemical NRR by studying molecular model systems in which N_2 binds to, or is cleaved by, reduced metal-pincer complexes.

Chapter 1 describes electrochemical N_2 fixation as an alternative to the Haber-Bosch process. A molecular approach towards understanding electrochemical NRR is

proposed, especially through bimetallic N_2 cleavage to form metal nitrides. Strategies for the subsequent functionalization of the metal nitride are discussed, primarily via proton-coupled electron transfer (PCET) reduction of the nitride into NH_3. Challenges involved in PCET nitride reduction, as well as opportunities inspired by molecular N_2 reduction catalysts and recent discoveries of potent PCET reagents, are identified and applied to a hypothetical system for electrochemical NRR.

Chapter 2 describes the protonation and electrochemical reduction of Ir- and Rh-pincer complexes that can strongly bind N_2. The potential utility of these complexes in an electrochemical NRR system are assessed by complimentary electrochemical and spectroscopic studies exploring their stepwise protonation and electrochemical reduction. Protonation was found to be a prerequisite for electrochemical reduction of the N_2 complexes, with protonation occurring at the metal center to form metal hydrides. Protonation triggers release of the N_2 ligand, preventing reductive N_2 functionalization with these complexes.

Chapter 3 investigates the possibility of oxidative functionalization of an N_2-derived Re nitride in order to form NO_x species. Although no N–O bond formation was achieved at the nitride, a series of Re nitrides was synthesized and characterized in which the metal center is oxidized by $1e^-$ and/or the supporting pincer ligand is oxidized to a nitroxide. The Re-nitride interaction was monitored over the series using NMR and IR spectroscopies, X-ray crystallography, and computational methods. Cooperative oxidation of both the metal center and the supporting ligand results in the weakest Re-nitride interaction, more localization of the LUMO at the nitride ligand, and an *umpolung* in nitride reactivity.

Chapter 4 applies PCET methods to N_2-derived Re nitrides in an attempt to reduce the nitride to NH_3, thus closing the cycle of N_2 to NH_3. Stepwise PCET mechanisms were prohibited by high-energy intermediates in both systems; however, the combination of SmI_2 and H_2O to generate a strong concerted PCET reagent resulted in formation of 74% yield of NH_4^+ in one system, but exclusive production of H_2 in the other. Other PCET methods, such as pairing organic H-atom transfer reagents with SmI_2, are also assessed for PCET nitride reduction.

Chapter 5 studies the conversion of NH_3 to a nitride in a Re system that can also cleave N_2. Re-ammine and Re-amide intermediates were isolated, and the mechanisms of H atom removal from these to form the nitride were identified. Experimental determination of the N–H bond enthalpies in the Re-amide were used to benchmark computational studies elucidating the thermodynamics of N–H bond cleavage (and formation, the microscopic reverse). The putative Re-imide intermediate in the PCET reduction pathway was found to feature a particularly weak N–H bond, representing a thermodynamic bottleneck to PCET nitride reduction in this system.

Nitrogen Cycle Chemistry with Metal-Pincer Complexes Relevant to Electrochemical Nitrogen Fixation

A Dissertation
Presented to the Faculty of the Graduate School
of
Yale University
in Candidacy for the Degree of
Doctor of Philosophy

by
Gannon Patrick Connor

Dissertation Directors: Patrick L. Holland and James M. Mayer

December 2021

Dedicated to my collaborators at UNC, Rutgers, and Yale,
for providing a village to raise me.

Table of Contents

Acknowledgements

Thank you to all of my science teachers that have taught me the scientific method. This is all your fault. Special thanks to Bill McNamara for getting me hooked on research and convincing me to go to Yale. You were completely right about the exceptional quality of the department, the people, and New Haven.

Well, it turns out grad school is hard. I owe everything to my friends and family, who helped me traverse the trials and tribulations of a PhD program. Thank you, Mom, Dad, Hallett, Zoe, and Aidan for continuously telling me how smart and capable I am for the past six years (and for letting me drone on about my chemistry to you). It's been wonderful sharing my excitement getting new results and publications with you—no matter if I was able to clearly communicate them with you or not! You are the perfect family.

I found so much love in New Haven. My favorite part of this whole experience has been the people I've been able to spend time with in grad school. Thank you to my best friends, Tom, Jake, Brian, Danica, Hannah, and Tim. I'm humbled by your unabashed displays of how much you care for me, and I only hope you know how much I deeply care for you. Thank you for the most fun I've ever had, and thank you for your tangible love and support. Thank you, Sean, Scott, Julia, Meg, Janelle, Evan, Majed, Colin, Mike, Andrew, Steve, and the Riperooni soccer crew. We've had so many fantastic experiences! It's impossible for me to imagine meeting a better group of people. Thank you for (literally) everything.

I owe much of my success as a scientist to my collaborators, Alex Miller, Alan Goldman, Brian, Faraj, Santanu, Ben, Nick, Andrea, Noah, and especially Quinton, Jeremy, and Brandon. The monthly meetings and discussions about our project were

critical to keep me thinking about my chemistry, teaching me how to design experiments and communicate results, and keeping me motivated and excited. Whenever working as the sole Yale grad student on this project felt too isolating, y'all have been my scientific "home." Quinton—thank you for the close collaboration. You're an incredible chemist, and I'm excited to see what the future holds for you.

I would not have even come close to finishing this program if it weren't for my advisors, Pat and Jim. I owe the rest of my success as a scientist to you two. Thank you both for the incredible amount of independence you've given me, both in chemistry projects and extracurriculars (especially the outreach). Jim—you encouraged a sense of exploration and creativity in chemistry right from the start that provided me with inspiration throughout grad school. Your perspectives, thoughtful questions, and spicy ideas helped craft the way I think about these projects, and I learned confidence through your encouragement. Thank you for letting me work on a brand-new project, that could have only lasted a year, on my own, doing something that you had never done in your group. Pat—you single-handedly dragged me to the finish line. You are an extraordinary advisor, mentor, teacher, and friend. You truly believed in me throughout grad school as a scientist and a person, even when I didn't believe in myself. I cannot express in words how important your unwavering, unbelievable support has been to me. Please know that the lessons you've taught me through your kindness will continue to live with me long after grad school.

Pat and Jim, thank you so much, I owe you one.

List of Figures

1 A molecular approach to electrochemical nitrogen fixation

This chapter is reproduced in part from Bruch, Q. J.; Connor, G. P.; McMillion, N. D.; Goldman, A. S.; Hasanyn, F.; Holland, P. L.; Miller, A. J. M. Considering Electrocatalytic Ammonia Synthesis via Bimetallic Dinitrogen Cleavage. *ACS Catal.* **2020**, *10*, in press. *The section linking molecular studies to analogous heterogeneous studies is reproduced in part from* Connor, G. P.; Holland, P. L. Coordination chemistry insights into the role of alkali metal promoters in dinitrogen reduction. *Catalysis Today.* **2017**, *286*, 20–40.

1.1 Introduction

1.1.1 Nitrogen fixation and the Haber-Bosch process

Nitrogen fixation, or the conversion of dinitrogen (N_2) in the atmosphere into biologically accessible forms of N such as ammonia (NH_3) and nitrate (NO_3^-), is necessary to support life.[1-3] Nitrogen fixation is difficult because the strong, nonpolar N≡N triple bond of N_2, with a bond dissociation energy of 226 kcal/mol,[4] renders it kinetically and thermodynamically inert. In fact, N_2 is intimately associated with inertness: in amusing contradiction to its biological importance, the word for "nitrogen" in many languages is derived from the Greek word *azote*, meaning "without life."[5] However, since atmospheric N_2 is overwhelmingly the most abundant source of nitrogen on the planet, biology has evolved methods of nitrogen fixation that overcome the challenges of breaking the N–N bond in N_2 in order to exploit its abundance.

Biological nitrogen fixation occurs exclusively through the enzymatic conversion of N_2 to NH_3 by nitrogenase enzymes in various species of archaea and bacteria, the most common of which are found in the root nodules of legumes.[1] Biological formation of NO_3^- mostly occurs through the stepwise oxidation of NH_3 via enzymatic reactions by nitrifying bacteria and archaea,[6-8] although there is also evidence for direct assimilation of NO_3^- from

nitrate-rich bedrock.[9] A comparatively small amount of direct nitrogen fixation to NO_x also occurs in the atmosphere, facilitated by lightning.[10] From a human perspective, nitrogen fixation to NH_3 and NO_3^- is vital for agriculture, human nutrition, and modern society, providing the core ingredients for fertilizer production and the building blocks for incorporating N into commodity chemicals.[3] However, the scale of biological nitrogen fixation is insufficient to support the current and future human population.

The current global population is a direct result of the 1909 invention of industrial, large-scale N_2 fixation to NH_3 through the Haber-Bosch process (HB).[11] The invention of HB marks a turning point in humankind, representing a "detonator to the population explosion" of the 20th century (perhaps an ironic moniker considering the original role of HB in allowing a blockaded World War I Germany to continue manufacturing explosives) by allowing the radical increase in fertilizer production necessary to support an exponentially growing global population.[12] In his essay championing HB as one of humankind's most important inventions, Smil emphasized the importance of HB by suggesting that, without it, 40% of the world's population would not be here due to the inability to grow enough food to support them.[13] Nowadays, nitrogen input into global agriculture is derived roughly evenly from HB and the nitrogen cycle, meaning that approximately 50% of the nitrogen in an average person who lives in a developed country originates from HB.[14, 15]

HB combines a 3:1 ratio of H_2 and N_2 feedstock gases at high temperatures (up to 700 K) and pressures (up to 100 bar) over a fused-Fe catalyst doped with promoters such as alumina and potassium oxide.[16-19] Under these conditions, partial conversion of the feedstock gases to NH_3 occurs, which can be condensed out of the gaseous mixture and

separated from the process loop as a liquid. The high temperature of HB is necessary to overcome the kinetic challenge of N_2 splitting (even catalyzed), while the high pressures overcome the entropic penalty of converting four molecules into two and shift the reaction equilibrium more in favor of NH_3. Efforts to address the inherent challenges associated with NH_3 production via HB have led to significant advancements in the fields of engineering and chemistry, specifically in high-pressure reaction methods,[20] heterogenous catalyst development,[18] and surface characterization.[21] It is also noteworthy that HB today is conceptually the same as over a century ago, with innovations mostly limited to catalyst modification and improvements in process engineering.[22]

In response to the increased demand associated with population growth, the global scale of HB is astonishing: HB results in the production of around 500 billion lbs of anhydrous NH_3 annually, which is over double the production of NH_3 via biological nitrogen fixation.[1, 14, 23] The enormous scale of HB requires a proportionally enormous amount of H_2 gas. H_2 for HB is currently synthesized through the steam reforming of hydrocarbons obtained mostly from non-renewable fossil fuels, releasing CO_2 on a commensurate scale in the process.[24] The overall combination of these processes, representing the net conversion of hydrocarbons, water, and N_2 to form NH_3, is tremendously energy and resource intensive, accounting for *ca.* 2% of global fossil fuel energy consumption and 3–5% of global natural gas consumption annually.[25-27] A shift towards more sustainable, less energy-intensive routes of synthetic nitrogen fixation is vital in order to avoid the environmental strain that results from HB.[23, 27] For example, a global shift away from fossil fuel to renewable energy sources and investing in large-scale, economical processes to electrochemically manufacture H_2 from renewable sources will

help mollify the strain of HB.[28] However, a more viable long-term solution is to develop nitrogen-fixing methods that can utilize electrical energy derived from renewable resources and operate at ambient temperature and pressure, requiring less energy input.[29-31]

Beyond a sustainability perspective, there are additional advantages of moving beyond HB for nitrogen fixation. The high temperature and pressure requirements of HB lead to high capital costs and require a large scale to be economical.[32] Current ammonia production is therefore centralized, which can lead to high transportation costs.[27] In contrast, electrochemical processes could employ solar energy, which is widely distributed, and could operate on a smaller scale, requiring less investment in infrastructure.[33] It could therefore be possible to decentralize N_2 fixation with a method that could utilize solar electricity and mild reaction conditions. This is advantageous because fertilizer could be produced from sun, air, and water at or near the fields where it is needed, reducing transportation costs. Thus, replacing the current HB method with an electrochemical alternative has the potential for widespread benefit to society.

1.1.2 Electrochemical nitrogen fixation as an alternative to HB

The mechanism of electrochemical nitrogen fixation is fundamentally different from nitrogen fixation via HB. While HB uses H_2 as the reductant, reducing equivalents for electrochemical nitrogen fixation must come in the form of proton/electron (H^+/e^-) pairs (**Figure 1.1**). The only feasible H^+/e^- source for large-scale electrochemical nitrogen fixation is water oxidation, which would comprise the half reaction at the anode. The half reaction at the cathode is the electrochemical nitrogen reduction reaction (NRR), in which N_2 is reduced by $6e^-$ and $6H^+$ to form 2 NH_3. Although the standard reduction potential for this process is close to that of H^+ reduction to H_2 (+0.09 V vs. NHE),[34] a suitable catalyst

that can overcome the high barriers associated with N_2 reduction is vital. In aqueous conditions, the standard cell potential for the overall electrochemical process is –1.14 V vs. NHE (ΔG^o = +79 kcal/mol per mol of NH_3), indicating the need for substantial energy input.[35] An ideal NRR system will utilize electrochemical energy from renewable power, water as the source of H^+/e^-, and catalysts that operate at near-ambient reaction conditions. A recent technoeconomical analysis provides support that an electrochemical approach to nitrogen fixation that couples NRR to water oxidation, such as depicted in **Figure 1.1**, can be cost-effective on a large scale.[28] Assuming the cell can operate at 95% efficiency with a cell overpotential of less than 0.6 V, the electrochemical process is more cost-effective than HB. Additionally, this electrochemical approach avoids the high social cost of CO_2 emission associated with HB.

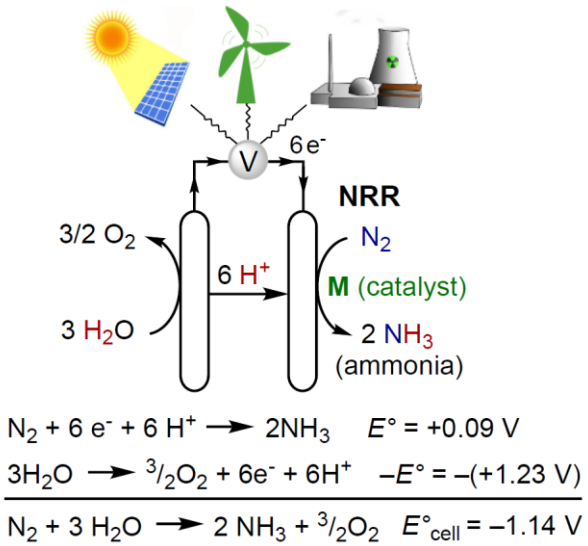

Figure 1.1. Representation of electrocatalytic N_2 fixation that couples water oxidation at the anode to NRR at the cathode. Corresponding potentials for the half- and full-cell reactions are provided at standard state (1 atm N_2 and O_2, 1 M NH_3, pH 0, 298 K).[35] Figure by ASG.

The economic feasibility of electrochemical nitrogen fixation relies on the development of electrocatalysts for NRR that can achieve the necessary metrics for

Faradaic efficiency and cell overpotential. A rapidly growing number of systems that can catalyze N_2 reduction to NH_3 have been reported, almost all of which utilize heterogeneous catalysts.[36] However, reported heterogeneous NRR systems are plagued by poor activity, poor selectivity for N_2 reduction compared to H^+ reduction, the requirement for harsh reaction conditions, and low Faradaic efficiency. In these early stages of developing catalysts for NRR, studying molecular systems that can reduce N_2 to NH_3 can provide key insights to guide and accelerate the development of better NRR catalysts.

1.2 Considering a molecular approach to NRR

Although heterogeneous catalysts are generally better for incorporation into large-scale industrial processes, molecular systems offer some advantages. Molecular systems are more amenable to detailed mechanistic study, which facilitates the identification of key challenges or bottlenecks in the catalytic cycle. With molecular compounds, it is easier to isolate and characterize catalysts, products, and intermediates. Single-crystal X-ray diffraction (XRD) can show structural details of synthetic compounds on an atomic scale, which allows the study of precise atomic interactions. Additionally, it is possible to follow the changes in structures through an entire reaction pathway in solution studies.

From a functional standpoint, molecular NRR catalysts may offer some advantages to heterogeneous catalysts. The ability to study catalytic mechanisms and intermediates along the catalytic cycle leads to a better understanding between catalyst structure and function. This can allow more accurate predictions regarding how modifications to a catalyst will affect its performance. It is also easier to implement precise structural and electronic changes in molecular compounds in order to test these predictions, accelerating

the process of identifying and implementing methods for rational catalyst improvement. The ability to precisely tune steric and electronic features of molecular compounds allows a greater degree of control of the catalytic active site compared to heterogeneous catalysts. This can lead to more easily controlled selectivity for the desired product of catalysis, in this case NH_3 from N_2 reduction over H_2 from H^+ reduction. Finally, the localization of orbitals in molecular complexes result in variations between the strength and lability of catalyst-substrate (*i.e.* metal-ligand) interactions as the reaction proceeds along the cycle, which may be leveraged to overcome specific difficult steps in the catalytic cycle. This is particularly relevant in the context of NRR, in which the substrate (N_2) has different metal-ligand interactions than the product (NH_3) and intermediates (*e.g.* NH_2^- or N^{3-}). In contrast, heterogeneous catalyst-substrate interactions in NRR are proposed to be dominated by scaling free-energy relationships.[37]

Lessons learned from molecular systems can be applicable to analogous heterogeneous systems for the same reaction. For example, atomic-level structural resolution also provides a firm link between the structure of a synthetic compound and its spectroscopic characteristics. This correlation enables one to predict structures based on spectroscopic data, which can be vital when studying complicated interactions between multiple species *in situ*. Comparing the spectroscopy of homogeneous analogs to heterogeneous catalysts allows one to make predictions about interactions on heterogeneous surfaces based on conclusions from solution studies. It is important to note that, despite these comparisons, molecular compounds provide at best a somewhat accurate representation of a heterogeneous surface.[17, 38] Also, the supporting ligands used to solubilize transition metal complexes have strong influences on the reactivity of the

complexes with N_2. Finally, the localized molecular orbitals in molecular complexes do not necessarily translate well to the delocalized band structure of orbitals in extended materials.

1.2.1 Molecular inspirations for NRR

Biological catalytic N_2 reduction by nitrogenase provides the underlying inspiration for developing a molecular catalyst for NRR. Nitrogenases fulfil many of the requirements for an ideal NRR catalyst: they operate at ambient temperature and pressure to catalytically reduce N_2 to NH_3 using H^+ (from water), e^- (delivered at *ca*. –0.4 V, notably close to the standard reduction potential of N_2 to NH_3, adjusted to pH 7, of –0.32 V),[34] and additional energy input from the hydrolysis of 2 ATP per e^-.[1, 38] The active sites of nitrogenases feature multimetallic FeS clusters, implying that synthetic transition metal complexes may be designed that can serve as functional mimics to nitrogenases, or even as NRR catalysts.

Molecular catalysts for N_2 reduction to NH_3 that use strong chemical reductants paired with strong acids have been reported using a variety of transition metals.[39] The most successful catalysts utilize Mo or Fe, with leading examples reported by Schrock,[40, 41] Nishibayashi,[42-47] and Peters[48-51] (**Figure 1.2**). Strikingly, despite the relatively large library of molecular catalysts for N_2 fixation, there is only a single reported example of a molecular electrocatalyst for N_2 reduction to NH_3.[51] This comes from Peters and coworkers, who reported that the electrolysis of a –35 °C solution of a tris(phosphino)borane-supported Fe complex (depicted in **Figure 1.2**) in Et_2O at highly reducing potentials (–2.1 V vs. $Cp_2Fe^{+/0}$) in the presence of strong acid under 1 atm N_2 can generate up to 5.5 equiv of NH_3 per Fe. This represents an exciting bridge between

chemical catalysis and electrocatalysis in molecular N_2 fixation and an initial benchmark for homogeneous NRR catalysts.

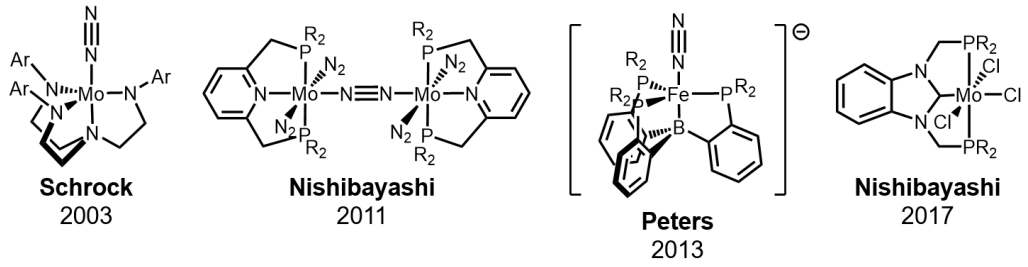

Figure 1.2. Leading examples of molecular catalysts for N_2 reduction to NH_3.

1.2.2 Molecular mechanisms of reductively splitting the N–N bond in N_2

Three mechanistic pathways for N_2 reduction to NH_3 by molecular complexes have been described in the literature, which are depicted in **Figure 1.3**. In the closely-related "alternating" (**Figure 1.3**, purple) and "distal" (**Figure 1.3**, blue) pathways, bound N_2 is reduced by H^+/e^- equivalents until one equivalent of NH_3 is released, breaking the N–N bond. Studies of nitrogenases support an alternating mechanism for N_2 reduction, in which H^+/e^- reducing equivalents form N–H bonds at the distal and proximal N atoms in an alternating fashion.[52-54] However, this mechanistic pathway remains rare in synthetic systems.[55] In the distal pathway, nicknamed the "Chatt cycle" in honor of his pioneering work, N–H bonds are formed at the distal N atom until one equivalent of NH_3 is released.[56-58] Early studies probing the stoichiometric reduction of N_2 bound to simple Mo and W complexes led to the isolation of many intermediates along the distal pathway, most of which were reported by Chatt himself.[59-64] Thirty years later, careful mechanistic evaluation of the first well-defined molecular N_2 reduction catalyst (see **Figure 1.2**, far left) by Schrock confirmed that this pathway is a viable catalytic mechanism for N_2 reduction.[40] Leading examples of Mo and Fe catalysts for N_2 reduction discovered by

Nishibayashi[42, 44] and Peters[48, 50] (see **Figure 1.2**, middle) also show strong evidence for a distal pathway.[39] Currently, this pathway represents the most common mechanism of N_2 reduction by molecular catalysts.

A third mechanism is the bimetallic N_2 cleavage mechanism, in which two metal complexes cooperative cleave the N–N bond to form metal nitrides prior to any N–H bond formation (**Figure 1.3**, red). Since the first demonstration of N_2 cleavage with a molecular complex was reported by Cummins in 1995,[65] numerous examples of cooperative N_2 cleavage to form terminal[46, 47, 66-74] or bridging metal nitrides[75-79] have emerged.[80] This mechanism has a significant advantage over the alternating and distal pathways since it avoids the costly formation of high-energy diazenido and hydrazido intermediates.[81] However, direct cleavage of the N≡N triple bond can be difficult, and examples of this reactivity are still understandably rare. Nevertheless, an N_2 cleavage mechanism has recently been proposed in Mo systems that exhibit the highest reported activity and selectivity for catalytic NH_3 production from N_2 for any molecular catalyst, by far (see **Figure 1.2**, far right).[47, 73, 82]

Scheme 1.1. Mechanistic pathways of molecular N_2 reduction to NH_3. Figure by QJB.

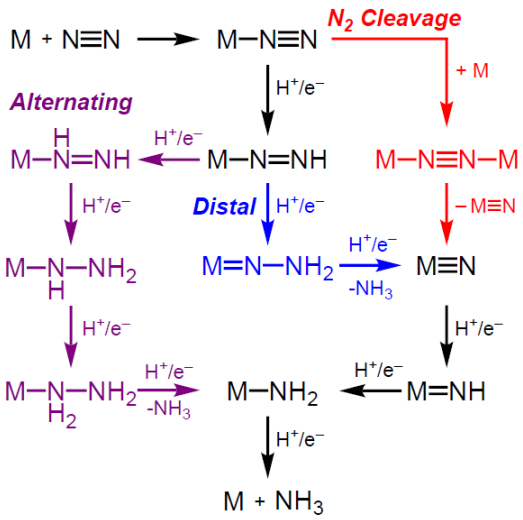

1.3 Bimetallic N–N bond cleavage to form metal nitride complexes

The bimetallic N_2 cleavage mechanism above occurs through the direct splitting of the N–N bond by two metal centers resulting in the formation of terminal metal nitrides. The first reported example of direct N_2 cleavage by a transition metal complex was discovered by Laplaza and Cummins in 1995, who reported that the Mo^{III} complex $[N(^tBu)(Ar)]_3Mo$ (Ar = 3,5-dimethylphenyl) rapidly converts to $[N(^tBu)(Ar)]_3MoN$ under an atmosphere of N_2 at ambient temperatures (**Figure 1.3**).[65] Cummins and coworkers proposed a mechanism that proceeds through initial N_2 binding to form the Mo^{III} terminal N_2 complex, followed by formation of a bridging-N_2 dimer $[\{N(^tBu)(Ar)\}_3Mo]_2(\mu\text{-}N_2)$ that rapidly splits the N–N bond to form two terminal Mo^{VI} nitrides.[83] The rapid rate and near-quantitative yield of the terminal nitride product are notable, and the authors emphasized the implication of direct N_2 bond scission as a potential route for nitrogen fixation.

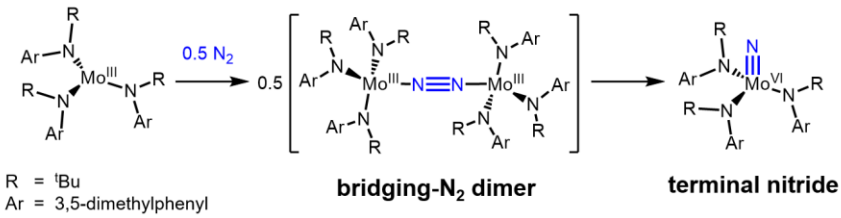

Figure 1.3. First example of bimetallic N_2 cleavage discovered by Laplaza and Cummins.

Despite the excitement regarding this extraordinary reaction, examples of bimetallic N_2 cleavage to terminal nitrides remained rare until the last decade. A recent resurgence in the field has occurred with the discovery that robust, pincer-supported late-row transition metal complexes, especially those of Mo and Re, can also split N_2 to metal nitrides.[46, 47, 66-69, 71, 73, 84, 85] This includes some examples where the N_2-derived nitride can be incorporated into NH_3[46, 47, 73] or organics,[71, 86-89] representing stoichiometric and, more recently, catalytic nitrogen fixation through an N_2 cleavage mechanism. The formation of N–C,[67, 71, 86-90] N–B,[91] and N–Si[85, 92] bonds from N_2-derived terminal nitrides highlights the high potential utility of a bimetallic N_2 cleavage strategy for N_2 fixation: N could be directly incorporated into organics without the need for prerequisite NH_3 formation. The rich reactivity of metal nitrides in general (*i.e.* not limited to N_2-derived nitrides), such as oxidation of nitrides to nitrosyls,[93-97] hints at further unrealized potential.

After Cummins's seminal work, significant contributions to the field by the groups of Schneider,[67, 69, 71, 97, 98] Nishibayashi,[46, 47, 73] Schrock,[66, 99] Mezailles,[85, 91] and the collaborative work of Holland, Mayer, Miller and Hasanayn[84, 98] has led to a strong understanding of what factors facilitate N_2 cleavage at transition metal centers, as well as how this reactivity can be achieved using renewable electro- and photochemical energy.[28, 34, 84, 98, 100] However, significant challenges remain in achieving facile reactivity at the N_2-derived nitride in order to close a hypothetical N_2 fixation cycle. Consequently, bimetallic

N_2-cleaving systems that can either catalytically form N–C bonds from N_2 or achieve NRR have not been discovered yet. These reactions represent the "holy grails" of this field.

1.3.1. Thermolytic and photolytic N–N bond cleavage with chemical reductants

Following the lead of Cummins *et al*., reductive N_2 cleavage to metal nitrides has been demonstrated by close to a dozen other systems. The structural and electronic considerations necessary to achieve this reactivity are generally well understood.[83, 101, 102] A qualitative diagram correlating the molecular orbitals (MOs) relevant to MN and NN bonding involved in a bimetallic N_2 cleavage mechanism, proceeding through a bridging-N_2 "MNNM" dimer, is represented in **Figure 1.4** (adapted from ref. [83]). The diagram assumes $[(L_n)M]_2(\mu\text{-}N_2)$ intermediates of either S_6 symmetry (n = 3, using two idealized D_{3h} metal fragments) or D_{4h} symmetry (n = 4 or 5, using two idealized D_{4h} metal fragments). In the MNNM core, overlap between metal d_{xz},d_{yz} orbitals with N_2 π,π^* MOs form two pairs of e_u and e_g π–MOs. Overlap of metal d_z^2 orbitals with N_2 σ,σ^* MOs form a filled $(1a_g)^2$ σ–MO and a corresponding empty $1a_u$ σ^*–MO. In this discussion, the combined pairs of e_u and e_g π–MOs is referred to as the "π-system."

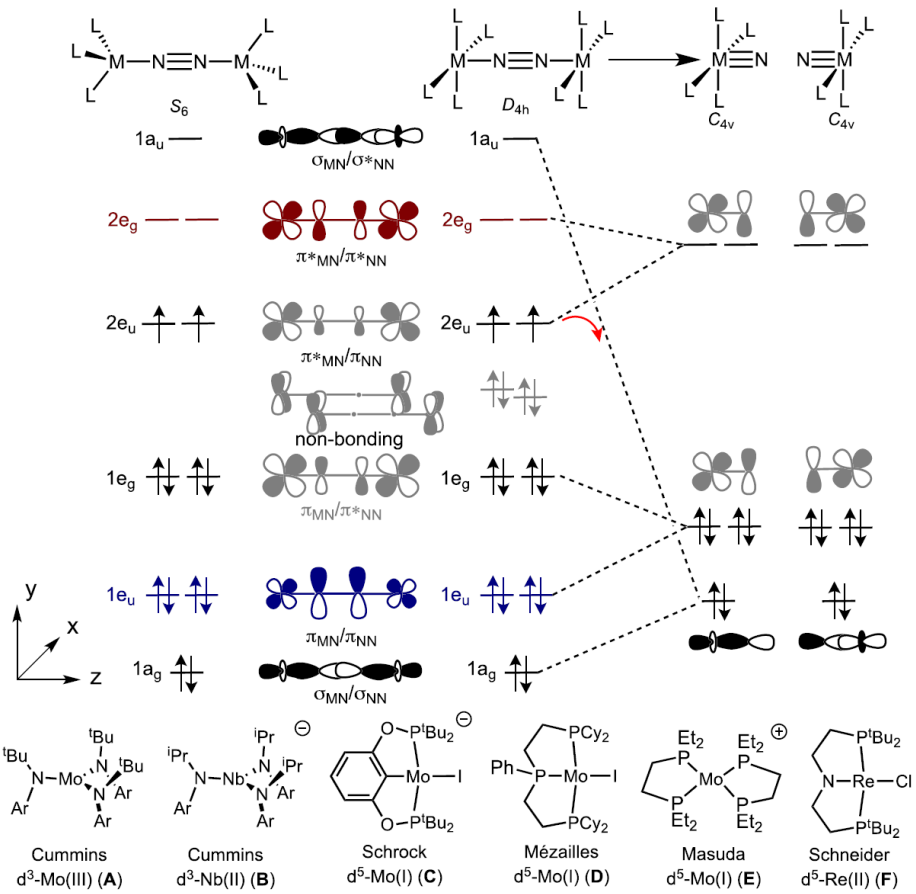

Figure 1.4. Top: Qualitative MO diagram showing the relevant MN and NN orbitals involved with N_2 cleavage from a $[(L_n)M]_2(\mu\text{-}N_2)$ complex to two terminal nitrides, adapted from ref. [83]. **Bottom:** Representative molecular L_3M and L_4M fragments that cleave N_2 to form terminal nitrides, each demonstrating the "10-π" configuration. Figure by P. L. Holland, A. J. M. Miller, and F. Hasanyn.

The valence electron configuration of $[(L_n)M]_2(\mu\text{-}N_2)$ complexes that can cleave N_2 is $(1e_u)^4(1e_g)^4(2e_u)^2(2e_g)^0$, in which each metal center provides three electrons into the π-system in addition to the four electrons in π–MOs of N_2. This results in 10 electrons in the $[(L_n)M]_2(\mu\text{-}N_2)$ π-system overall. Since this valence electron configuration has been observed in each example of bimetallic N_2 cleavage to terminal metal nitrides, it has been referred to as the "10-π" motif. In D_{3h} complexes, two d^3 metals satisfy the 10-π requirement.

In D_{4h} complexes, the orbital picture is essentially analogous, with the exception of the δ-symmetric b_{1u} and b_{2g} MOs from the in-phase and out-of-phase combinations of the d_{xy} orbitals (these are involved in ligand binding in S_6-symmetric cases and thus too high in energy to be relevant). These δ–MOs are orthogonal to the MNNM axis and thus non-bonding with respect to MN, and they are lower in energy than the $2e_u$ π–MOs in the μ-N_2 dimer. This generally requires two d^5 metals to provide the additional four electrons (two per metal) necessary to fill the b_{1u}/b_{2g} δ–MOs before filling the $2e_u$ π–MOs in order to satisfy the 10-π consideration, forming an overall $(1e_u)^4(1e_g)^4(b_{1u}/b_{2g})^4(2e_u)^2(2e_g)^0$ valence structure.[66, 67, 74, 85] However, in recent examples from the Schneider group, N–N bond cleavage has been achieved by D_{4h}-symmetric M^{III}/M^{III} dimers $\{[(^{tBu}P^{H}NP)MCl]_2(\mu\text{-}N_2)\}^{2+}$ (M = Mo or W), which have d^4/d^4 electronic structures.[69, 70] In this case, the neutral dimers $[(^{tBu}PNP)MCl]_2(\mu\text{-}N_2)$, which have a valence structure of $(1e_u)^4(1e_g)^4\text{-}(b_{1u}/b_{2g})^4(2e_u)^0(2e_g)^0$, are stable to N–N bond cleavage. Upon protonation of the central amides in the pincer ligands, the energy gap between the non-bonding δ–MOs and the $2e_u$ π–MOs decreases to the point where a high-spin quintet $(b_{1u}/b_{2g})^2(2e_u)^2$ state is thermally accessible. The quintet state satisfies the 10-π electronic structure, and N–N bond cleavage occurs to give the cationic M^{VI} nitride products, $[(^{tBu}P^{H}NP)M(N)(Cl)]^+$. In the Mo case, DFT calculations indicate that protonation of both pincer-ligand amides also lowers the kinetic barrier to N–N bond cleavage ($\Delta\Delta G^{\ddagger}$ = 16 kcal/mol) and provides more driving force for nitride formation ($\Delta\Delta G$ = –22 kcal/mol).[69]

Cleavage of the N–N bond in the μ-N_2 dimer occurs via a closed shell, singlet transition state (TS) that has a zig-zag geometry.[103] As the geometry of the μ-N_2 complex shifts to a zig-zag conformation, the symmetry decreases so that the $1a_u$ σ*–MO drops in

energy significantly as the $2e_u$ π–MO becomes higher in energy. In crossing, the two unpaired electrons in the $2e_u$ π–MO relocate to the $1a_u$ σ*–MO, breaking a π–NN bond and forming a σ–MN bond. The remaining 8 electrons in the π-system that occupied the $1e_u$ and $1e_g$ π–MOs in the μ-N_2 dimer (which already have MN π-bonding character in the MNNM complex) occupy four filled π–MN bonding orbitals in the products. This transformation thus results in nitride product with the maximum MN bond order of three, which is necessary to thermodynamically drive the cleavage of the strong N≡N triple bond. This driving force is emphatically demonstrated by DFT calculations on a simplified version of Cummins' [{(Ar)(R)N}$_3$Mo]$_2$(μ-N_2) complex, which predict the formation of the two Mo nitride complexes from N_2 to be exergonic by >100 kcal/mol.[103] This startlingly strong driving force is corroborated by experimental studies that estimated the reaction enthalpy of N_2 splitting to form Mo nitrides to be –86 kcal/mol in toluene.[104] Laplaza *et al*. experimentally determined that the kinetic barrier for this N_2 cleavage reaction is relatively small ($\Delta G^{\ddagger}$ = 22 kcal/mol) and thus thermally accessible.[83]

The 10-π electronic configuration appears to be prerequisite to N_2 cleavage from [(L_n)M]$_2$(μ-N_2) complexes. Studies on heterobimetallic S_6-symmetric (L_3)Mo(μ-N_2)Nb(L_3) complexes support this concept. The heterobimetallic complex does not cleave N_2 in the Mo^{III}/Nb^{III} oxidation state, which exhibits a d^3/d^2 (9-π) configuration. However, upon $1e^-$ reduction to the Mo^{III}/Nb^{II} oxidation state (see **Figure 1.4**, complexes **A** and **B**), featuring a d^3/d^3 (10-π) configuration, the N–N bond splits to form the Mo and Nb nitride products.[105] In another study, removal of electrons from [(L_3)Mo]$_2$(μ-N_2) to form 9-π and 8-π configurations prevents any N_2 cleavage reaction: the putative Mo nitrides formed from N–N bond splitting would have reduced MN bond orders and thus do not provide the

necessary driving force. Interestingly, since oxidation of these complexes removes electrons from the $2e_u$ π–MOs (which have π*–NN character), the N–N bond becomes *more* activated in the 9-π and 8-π configurations.[101] Masuda and coworkers reported an interesting case where the D_{4h}-symmetric complex $(dppe)_2Mo(N_2)$ (see **Figure 1.4**, complex **E**), featuring a d^6 configuration, requires $1e^-$ *oxidation* to initiate N_2 cleavage to form the nitride product $[(dppe)_2MoN]^+$. In this case, oxidation serves two purposes: dissociating one N_2 ligand per Mo to allow formation of a μ-N_2 dimer and providing the d^5/d^5 (10-π) configuration to result in a closed shell, nitride product featuring an MN bond order of three.[74]

Satisfying the 10-π electronic configuration is not the only criterion for achieving N_2 cleavage to terminal metal nitrides by $[(L_n)M]_2(\mu\text{-}N_2)$ complexes. Other criteria include having a sufficiently low kinetic barrier to the zig-zag transition state, a thermodynamic driving force to form metal nitride products, and sufficient steric bulk to prevent bridging nitride products. Schrock's $[(N\{CH_2CH_2(R)N\}_3)Mo]_2(\mu\text{-}N_2)$ (R = $SiMe_2{}^tBu$) dimer has the appropriate d^3/d^3 configuration to satisfy the 10-π criterion for S_6-symmetric complexes, but the μ-N_2 dimer is stable to N_2 cleavage.[106] A recent D_{4h}-symmetric example comes from the Schneider group, who isolated a stable d^5/d^5 (10-π) $[(^{iPr}P^HNP)ReCl_2]_2(\mu\text{-}N_2)$.[71] In this case, the kinetic barrier to form the zig-zag TS is predicted by DFT calculations to be quite high ($\Delta G^‡$ = 42 kcal/mol), and the overall driving force for N_2 cleavage to two Re nitrides is predicted to be endergonic by 2 kcal/mol. The unfavorable driving force may be linked to the presence of a Cl^- *trans* to the nitride in the product, which destabilizes the MN interaction.[84] Although the kinetic barrier to N_2 cleavage is too high to access thermally, UV irradiation of this complex results in cleavage of the N–N bond to form the

closed-shell Re nitrides. A few other examples of photochemical N_2 cleavage have also been reported, all of which exhibit a 10-π electronic configuration.[68, 84, 101, 107] While the mechanisms and orbital considerations involved in photochemical bimetallic N_2 cleavage are not currently well understood, one exciting implication of these reactions is the possibility of utilizing photon energy to overcome endergonic reaction thermodynamics, as demonstrated by $[(^{iPr}P^{H}NP)ReCl_2]_2(\mu\text{-}N_2)$.[71]

1.3.2. Electrochemical N–N bond cleavage

Recent studies by the Miller and Schneider groups have demonstrated that N_2 cleavage by Re-pincer complexes can be achieved electrochemically, forming Re nitrides.[98, 100] For example, the electrolysis of Re^{III} complex $(^{tBu}PNP)ReCl_2$ (^{tBu}PNP = $[N(CH_2CH_2P^tBu_2)_2]^-$) at an applied potential of –1.90 V vs. $Cp_2Fe^{+/0}$ forms nitride complex $(^{tBu}PNP)Re(N)(Cl)$ in 58% yield (**Figure 1.5**, top).[98] This reactivity is analogous to chemical $1e^-$ reduction of $(^{tBu}PNP)ReCl_2$ with Na/Hg, which results in formation of a $\mu\text{-}N_2$ dimer intermediate $[(^{tBu}PNP)ReCl]_2(\mu\text{-}N_2)$ at –30 °C in ~75% yield. At ambient temperature, the $\mu\text{-}N_2$ dimer thermally cleaves the N–N bond to give the Re nitride product. DFT calculations on the system support a zig-zag transition state during thermal N–N bond cleavage, in accordance with the mechanism discussed above.

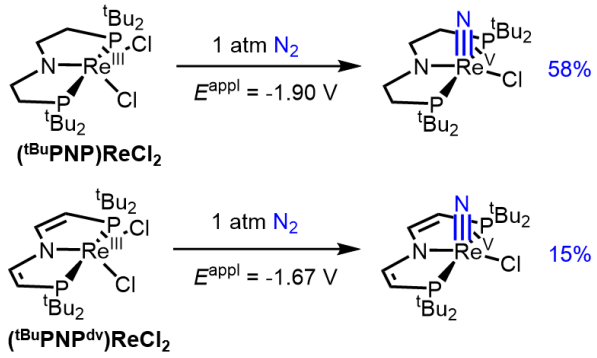

Figure 1.5. Electrochemical N_2 cleavage by (^{tBu}PNP)Re complexes to form terminal nitrides, with applied potentials given vs. $Cp_2Fe^{+/0}$.

Detailed mechanistic studies on the electrochemical cleavage of N_2 with (^{tBu}PNP)$ReCl_2$ using cyclic voltammetry (CV) have elucidated the elementary steps involved in forming (^{tBu}PNP)Re(N)(Cl).[98] The mechanism proceeds through initial $1e^-$ reduction of the Re dichloride followed by rapid N_2 binding and subsequent Cl^- dissociation. The resulting Re^{II}-N_2 complex (^{tBu}PNP)Re(N_2)(Cl) is rapidly reduced again at the electrode to form a Re^{I} intermediate, which comproportionates with (^{tBu}PNP)$ReCl_2$ starting material from the bulk solution to form [(^{tBu}PNP)ReCl]$_2$(μ-N_2). The μ-N_2 dimer then thermally cleaves to form the Re^{V}-nitride product. Spectroelectrochemical experiments monitoring UV-Vis absorbance during electrolysis confirms the formation of [(^{tBu}PNP)ReCl]$_2$(μ-N_2), then (^{tBu}PNP)Re(N)(Cl); additionally, experimentally determined rate constants indicate that these processes occur on a CV timescale, with formation of the μ-N_2 dimer estimated to be between $k^{298\ K} \sim 4 \times 10^3$ and 1×10^4 M^{-1} s^{-1}, and its subsequent cleavage to the nitride measured to be $k^{298\ K} = 1.8 \times 10^{-2}$ s^{-1}.

In a related system that uses the unsaturated analog of the ^{tBu}PNP ligand, (^{tBu}PNP^{dv})$ReCl_2$ (dv = divinyl) also binds N_2 upon electroreduction by $1e^-$, which occurs at a potential 230 mV less cathodic than (^{tBu}PNP)$ReCl_2$.[100] Although N_2 binding is possible

at a less reducing potential for (^{tBu}PNP^{dv})ReCl$_2$, the rate constant for subsequent Cl^- dissociation is 10 times smaller. Both of these observations are attributed to weaker π-donation from the PNP amide, which results in a less electron-rich Re metal center. In the case of (^{tBu}PNP^{dv})Re, multiple deleterious decomposition pathways compete with formation of the μ-N_2 dimer and subsequent N–N bond cleavage, resulting in a 15% yield of nitride product from electrolysis of (^{tBu}PNP^{dv})ReCl$_2$ (**Figure 1.5**, bottom).

The demonstration of rapid electrochemical N_2 cleavage to form metal nitrides is very encouraging for the prospect of utilizing an N_2 splitting mechanism in NRR. Two key observations are particularly encouraging: that formation of the reduced 10-π, μ-N_2 dimer and the subsequent formation of metal nitrides are fast enough for observation on a CV timescale, and that analysis of CV data with varied concentrations of Re, Cl^-, and N_2 provides detailed mechanistic information that elucidate the elementary steps involved in electrochemical N_2 cleavage. The juxtaposition of (^{tBu}PNP)Re and (^{tBu}PNP^{dv})Re shows that slight modifications to the supporting ligand affect the reduction potential that triggers N_2 association, Cl^- dissociation rates, and the relative rates of deleterious pathways, ultimately affecting the overall selectivity for nitride products from electrolysis. These comparisons identify a key trade-off when modulating the electron-richness of the metal center: a less electron-rich complex requires less-reducing potentials to initiate reductive N_2 association, but it consequently increases the reduced complex's affinity for Cl^-. Despite the ability of these systems to electrochemically cleave N_2, neither Re nitride is capable of forming NH_3 to complete the NRR.

1.3.3. Imagining a bimetallic N_2 cleavage approach to electrocatalytic N_2 fixation

The demonstration of electrochemical N–N bond cleavage with Re-pincer complexes is an important proof of concept for a molecular NRR catalyst that operates through an N_2 splitting mechanism. However, this reaction is only one segment of the overall NRR (**Figure 1.6**). The other part of this reaction is the subsequent $3H^+/3e^-$ reduction of the terminal nitride to NH_3 (**Figure 1.6**, red), followed by dissociation of NH_3 and binding of another molecule of N_2 to continue the catalytic cycle. Considering that the overall process for the $6H^+/6e^-$ reduction of N_2 to 2 NH_3 is roughly ergoneutral, the thermodynamics of the N_2 cleavage step must generally offset the thermodynamics of the nitride reduction step. For example, if N–N bond cleavage to form the metal nitrides is exergonic, then the subsequent reduction of the nitride to an ammine is predicted to be endergonic, likely requiring a combination of strongly reducing potentials and strong acids. It is thus very important to consider the reactivity of the N_2-derived terminal nitride in addition to the system's ability to electrochemically split N_2.

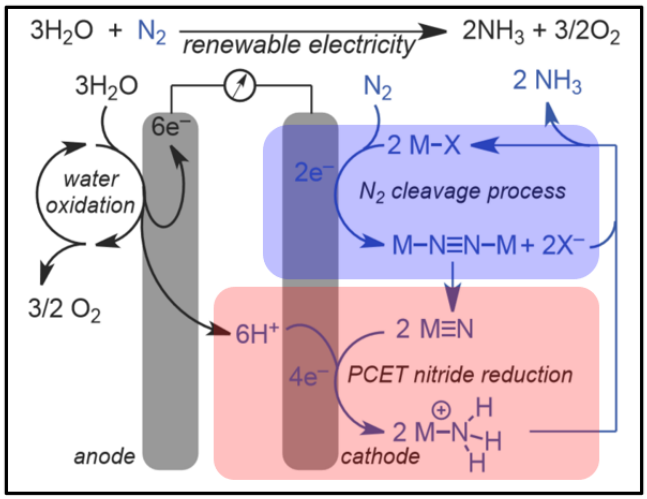

Figure 1.6. Idealized electrocatalytic N_2 fixation cell showing a simplified representation of NRR broken into the N_2 cleavage process (blue) and nitride reduction to NH_3 process (red). Figure adapted from A. J. M. Miller.

The versatility of reactivity that terminal metal-nitride complexes exhibit implies that there are other opportunities for electrochemical N_2 fixation via an N_2 cleavage mechanism. For example, in absence of acid, the cycle will not proceed past the metal nitride intermediate. Rather than continue with NRR via electrochemical $3H^+/3e^-$ reduction to the ammine, the nitride could instead be used as a synthon for N–C or N–O bond formation, ideally resulting in direct N_2 incorporation into amines/nitriles or NO_x species, respectively. While intriguing, this strategy is likely not conducive towards one-pot catalysis because the reducing conditions to generate metal nitrides are typically incompatible with carbon electrophiles for N–C bond formation or oxidants for N–O bond formation. However, it is plausible that turnover may be achieved using a system that can separate the electrochemical and chemical steps, such as a multi-compartment flow cell or a chemically regenerated redox cathode.[108]

The concept of incorporating N_2 into NO_x[109, 110] via N_2 cleavage to a metal nitride, then subsequent chemical oxidation of the nitride is particularly interesting. Both biological NO_3^- formation through nitrification[8] and industrial HNO_3 formation through the Ostwald process[111] require NH_3 as the starting material, since the overall aqueous conversion of N_2 and O_2 to HNO_3 is endergonic (**Figure 1.7**, left).[31] Utilizing an alternative pathway that proceeds through electrochemical N_2 cleavage to metal nitrides would eliminate the need for H_2 as a reductant to form NH_3, potentially offering a less energy-intensive route to NO_x (**Figure 1.7**, right). This represents an unexplored N_2 fixation route to NO_3^-.

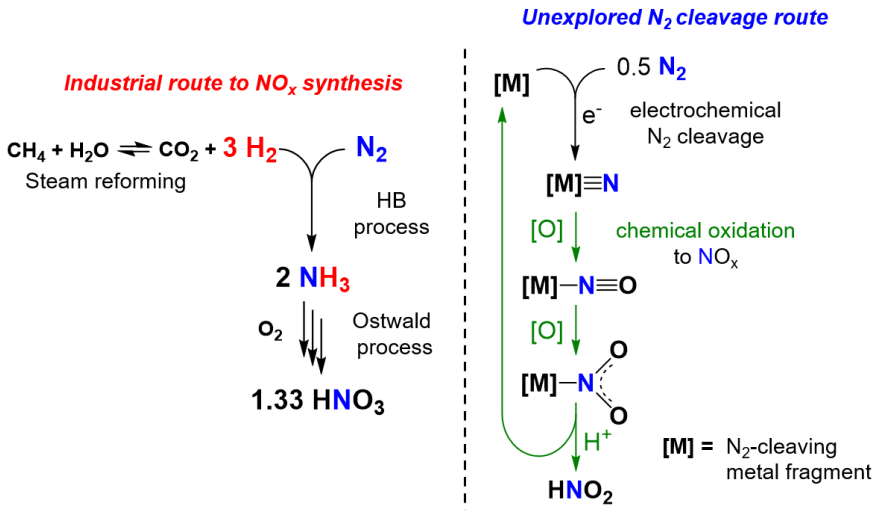

Figure 1.7. Left: Industrial route to NO_3^- from CH_4, H_2O, N_2, and O_2 via steam reforming of methane, HB, and Ostwald process. **Right:** Simplified scheme showing potential unexplored route to NO_x using N_2, oxidant (ideally O_2), and H^+/e^- (from H_2O). Chemical steps are drawn with green arrows, electrochemical steps are drawn with black arrows.

1.4 Reactivity of N_2-derived metal nitrides

The N_2-derived Mo nitride discovered in his group has been described by Cummins as a "reluctant nucleophile".[87] This description has proven to be appropriate for many nitride complexes derived from N_2, which often require forcing reaction conditions for functionalization. The difficulty in coaxing N_2-derived nitride complexes into productive reactions can be traced to the thermodynamic stability of the M≡N bond in these complexes. The N≡N triple bond in N_2 is one of the strongest chemical bonds, with a bond dissociation enthalpy of 226 kcal/mol.[4] Considering the strong bond of N_2, thermodynamically favorable formation of two metal nitrides from N_2 requires that the products have very strong M≡N bonds, likely >113 kcal/mol. To achieve M≡N triple bonds in terminal nitride complexes strong enough to thermodynamically drive the breaking of the N≡N triple bond requires that both σ and π bonding be strong. The Mo–N bond

dissociation enthalpy of the Mo^{VI} nitride $Mo(N)(NRAr)_3$ was experimentally determined to be ΔH^o = 155 kcal/mol.[104] Overall N_2 splitting reactions are also entropically unfavorable, as three molecules are converted to two.

Despite the thermodynamic stability of N_2-derived metal nitrides, N_2 splitting has been used to incorporate N_2 in the direct synthesis of NH_3,[46, 47, 73] silylamines,[85, 92] borylamines,[91] isocyanates,[112] and nitriles.[71, 86-89] Additionally, N–alkyl[67, 88-90] bond formation from N_2-derived nitrides has been demonstrated. These reactions show the utility of N_2 fixation via a N_2 cleavage mechanism, provided that the metal nitride can be coaxed into productive reactivity. Approaches to destabilize metal-nitride interactions to this end include changing the oxidation state of the metal in order to increase nucleophilicity or encourage radical character on the nitride,[113, 114] modifying or replacing the supporting ligands,[71, 89] installing a ligand *trans* to the nitride,[71] and utilizing exogenous Lewis acids or electrophiles to activate the nitride.[87]

1.4.1. Classifying nitride reactivity

Terminal nitride ligands are commonly characterized as either "nucleophilic" or "electrophilic,"[115-118] and several factors can influence their observed reactivity trends. The relative energy of metal *d*-orbitals and nitride *p*-orbitals, for example, affects the localization of antibonding molecular orbitals in a metal nitride complex (**Figure 1.8**).[119] The MN-π* orbitals gain more N character as the energy of metal *d*-orbitals is lowered, such that late transition metal complexes produce better orbital overlap with incoming nucleophiles (electrophilic reactivity); conversely, the MN σ- and π-symmetry orbitals gain more N character as the energy of metal *d*-orbitals is raised, such that earlier transition metal nitride complexes are more nucleophilic.

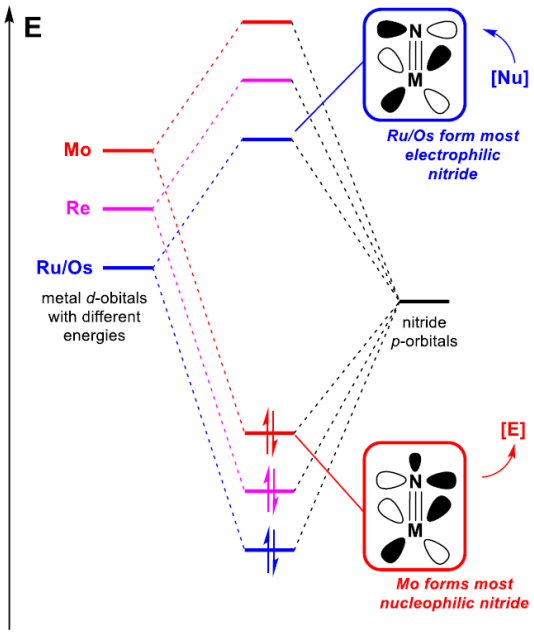

Figure 1.8. Qualitative MO diagram for metal nitrides with different *d*-orbital energies, showing the changes when one assumes identical oxidation states and coordination spheres on the metal.

Additional effects such as coordination geometry, orbital mixing from supporting ligands, and non-innocence of the nitride ligand also affect nitride reactivity.[116] Since the overall behavior of the nitride is linked to all of these factors, nitride reactivity can be difficult to predict from structure alone. Additionally, some metal nitrides exhibit "ambiphilic" nitride ligands that react with both nucleophiles and electrophiles.[120, 121]

1.4.2. Case study for metal effects on nitride reactivity

Schneider and coworkers have studied a series of metal-nitrides supported by a ^{tBu}PNP-pincer ligand (**Figure 1.9**).[67, 69, 70, 88, 121-123] The reactivity of the nitride ligand in these complexes varies, emphasizing the role that the identity and oxidation state of the metal plays on influencing nitride behavior. As one might predict from **Figure 1.8** above, the group 6–7 nitrides are strongly nucleophilic. In contrast, group 8 nitrides (synthesized from azides) are ambiphilic, and hydrogenolysis of the nitride can generate NH_3 and metal

hydrides. Only the Mo, W, and Re nitrides in this series can be generated from N_2 splitting, and functionalization of N_2 has only been reported from the Re nitride.

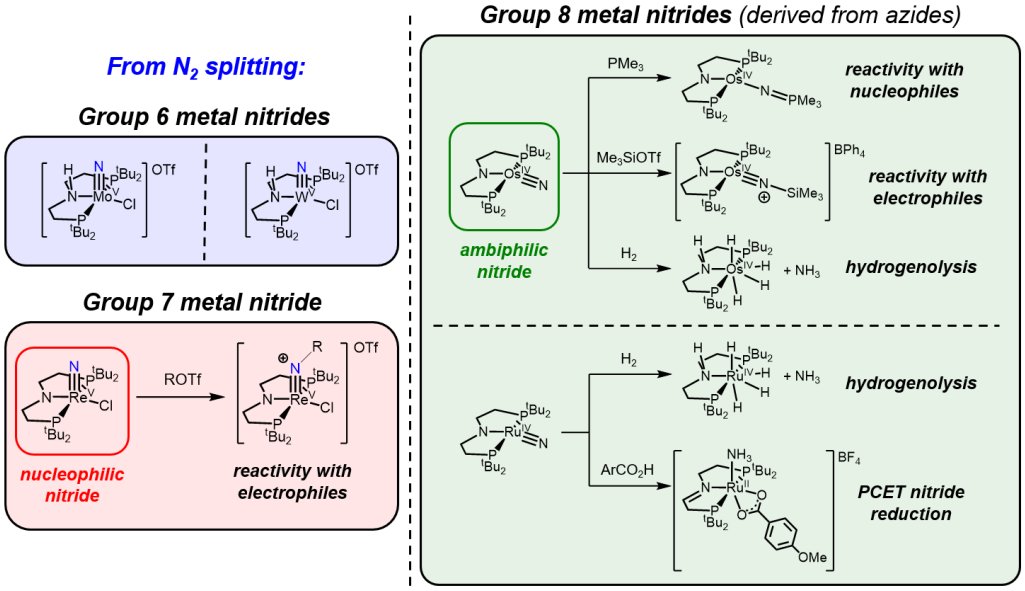

Figure 1.9. Reactivity of group 6-8 metal nitride complexes bearing ^{tBu}PNP ligands.

1.4.3. Case study for ligand effects on nitride reactivity

Schneider's pincer-supported Re nitrides, which are derived from thermolysis or photolysis of N_2, provide an excellent example of how modifying the supporting ligand can greatly facilitate the synthesis of compounds directly from N_2. The N_2-derived Re^V nitride complexes (^{tBu}PNP)Re(N)(Cl) (**G** in **Figure 1.10**)[67, 89] and ($^{iPr}P^{H}$NP)Re(N)(Cl)$_2$ (**H** in **Figure 1.10**)[71] each feature nucleophilic nitrides that can be directly incorporated into the synthesis of benzonitrile. However, in contrast to the five-coordinate complex **G**, the use of a less sterically-bulky PNP-pincer ligand in **H** allows for the coordination of an additional Cl^- ligand *trans* to the nitride. The resulting weakening of the metal-nitride interaction in **H** (exhibiting a 0.03 Å longer Re-nitride bond than **G** by XRD) allows the use of benzoyl chloride rather than benzyl triflate as the electrophile for N–C bond

formation at the nitride. Additionally, the PNP-pincer ligand in **H** exhibits $2H^+/2e^-$ non-innocence that facilitates the direct release of benzamide, whereas **G** requires stoichiometric base and oxidant in order to release benzonitrile. Thus, utilizing the less sterically-bulky, redox-non-innocent ^{iPr}PNP-pincer ligand enables milder reaction conditions for the incorporation of N_2 into organic synthesis.

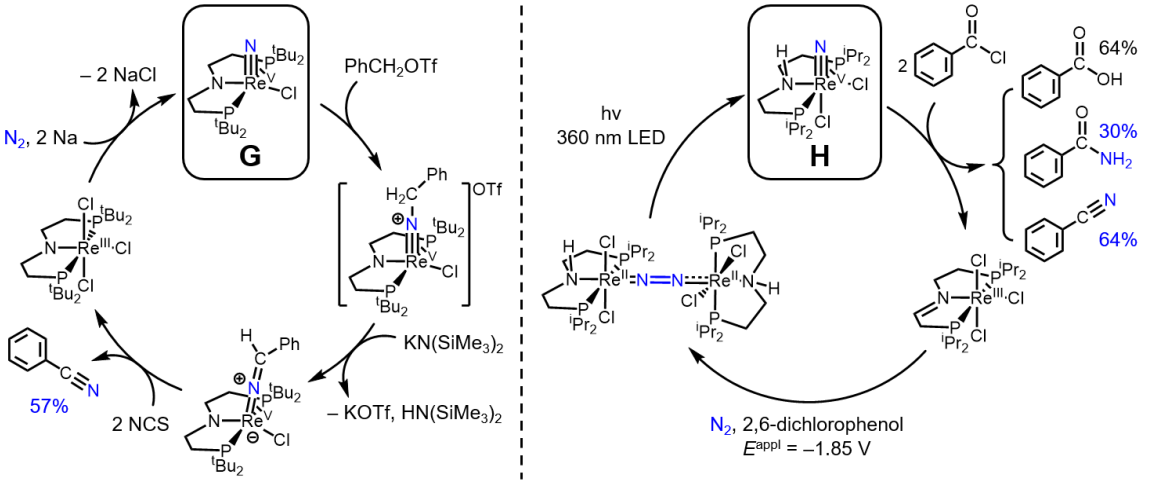

Figure 1.10. Comparison of benzonitrile synthesis from N_2 utilizing (^{R}PNP)Re complexes. **Left:** Synthesis of benzonitrile using complex **G**. **Right:** Synthesis of benzonitrile with complex **H** using milder reaction conditions.

1.4.4. Coaxing reactivity from unreactive nitrides

Existing synthetic routes utilizing N_2 typically require strong reductants to generate the nitrides, but strong electrophiles for nitride functionalization—the reagents for these steps are incompatible. To achieve catalysis, the energetics of N_2 cleavage and nitride functionalization must be balanced. For example, addition of exogenous ligands that can reversibly bind *trans* to the nitride may destabilize the metal-nitride interaction to promote reactivity. Alternatively, a Lewis acid can be added to promote polarization of the metal-nitride bond or change the properties of the ancillary ligand. One can even envision using additives that promote both N_2 splitting and nitride functionalization: in systems where

protonation is required for thermal N_2 splitting,[69, 70] an appropriate conjugate base could subsequently bind *trans* to the nitride.

While N_2-derived nitrides show promise as "reluctant nucleophiles" in reactions with organic electrophiles, these nitrides rarely react productively with proton sources. Protonation of N_2-derived metal nitrides often occurs at the supporting ligand or metal center rather than the nitride ligand (**Figure 1.11**, left).[65-67, 100] Considering the leading role of Mo in molecular catalysis for ammonia synthesis, it is unsurprising that productive protonation of group 6 nitride complexes has been reported (**Figure 1.11**, right), sometimes accompanied by coordination of the conjugate base or counterion.[44, 68] The rarity of direct nitride protonation highlights the need for approaches to N_2 electroreduction to NH_3 that do not rely on nitride protonation. An alternative approach to imide formation from N_2-derived metal nitrides has been to utilize a proton-coupled electron transfer (PCET) strategy, which is outlined in the following section.

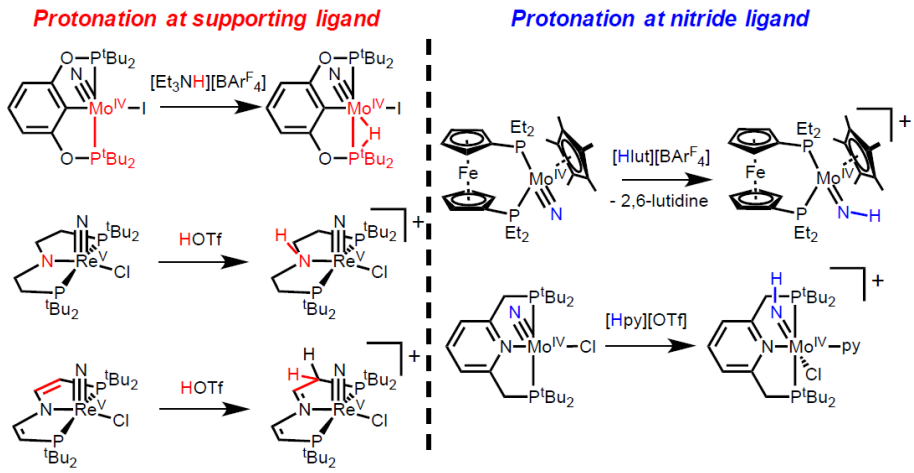

Figure 1.11. Left: Unproductive protonation sites (red) at the supporting ligands of N_2-derived metal nitrides. **Right:** Productive protonation of N_2-derived nitrides to form imide complexes.

1.5 PCET reduction of metal nitrides to form ammonia

As described above in **Figure 1.6**, the electrosynthesis of NH_3 via an N_2 cleavage step can be broken into two halves: the N_2 cleavage process to form a metal nitride complex and the subsequent nitride conversion to NH_3. The latter process requires a $3H^+/3e^-$ reduction of the N_2-derived nitride complex, making it a PCET challenge. Thermodynamically, the two halves of a catalytic N_2-to-NH_3 cycle must offset each other, because the overall process is approximately ergoneutral. Since the typical N_2 cleavage processes that form the metal nitrides are highly exergonic, the PCET nitride reductions to NH_3 must be highly endergonic. Strong reductants and Brønsted acids are thus required to achieve the N–H bond formations needed to make NH_3.

1.5.1. Reduction of nitrides to ammonia via PCET

By nature, a PCET reduction involves the transfer of H^+ and e^-. This process can occur via stepwise proton transfer (PT) followed by electron transfer (ET) or vice versa, in which the thermodynamics of the first step is determined by the nitride Brønsted basicity (pK_a) or metal-nitride reduction potential ($E°$), respectively. Considering the example of the reduction of a neutral metal nitride, stepwise PCET would initially generate a cationic imide from PT (**Figure 1.12**, blue) or an anionic nitride from ET (**Figure 1.12,** red). These charged intermediates can be high in energy, depending on the nitride pK_a and $E°$, providing high thermodynamic barriers to stepwise PCET reduction.[124, 125]

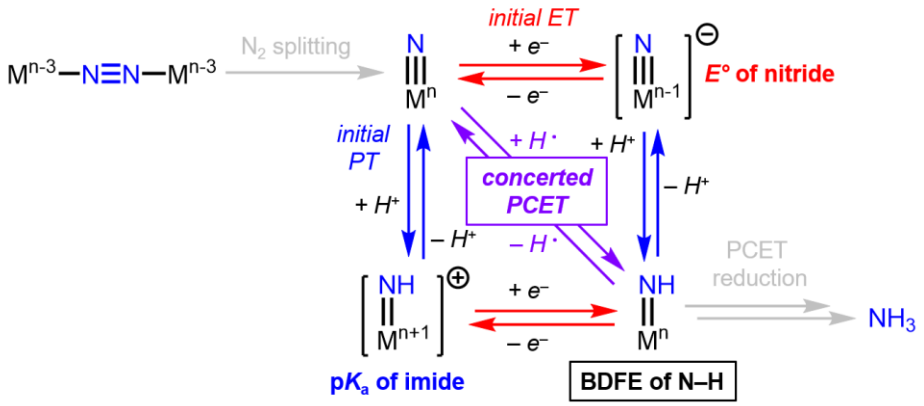

Figure 1.12. Square scheme for the initial PCET reduction of an N_2-derived metal nitride to form the neutral imide complex.

As an alternative to stepwise mechanisms for N–H bond formation, a concerted PCET mechanism (**Figure 1.12,** purple) can couple H^+ and e^- transfer into one elementary step, frequently referred to as H atom transfer (HAT).[124] Assuming a small kinetic barrier to HAT, this can avoid the large thermodynamic barriers associated with stepwise transfer and charged intermediates, allowing PCET to occur more easily. From a HAT standpoint, the overall thermodynamics of PCET reduction can be simplified to comparing the bond dissociation free energy (BDFE) of the X–H bond formed to that of the X–H bond broken, ignoring the charged intermediates in **Figure 1.12**. The Bordwell equation (**eq 1**) can be used to calculate these BDFEs from the individual PT and ET transfer steps along a pathway, using the solvent-dependent constant C_G to account for the free energies of formation and solvation of the H atom in order to satisfy Hess's Law.

$$\mathrm{BDFE_{X-H}} = 1.37(\mathrm{p}K_a) + 23.06(E°) + C_G \qquad \textbf{(1)}$$

1.5.2. Stepwise PCET reduction of nitrides

For metal nitrides derived from N_2 splitting, stepwise mechanisms to N–H bond formation are difficult. Protonation of N_2-derived metal nitrides often occurs at the

supporting ligand or metal center rather than the nitride ligand (see **Figure 1.10**, left), which renders PT-first pathways inaccessible in these systems.[65-67, 100]

A few examples of stepwise N–H bond formation from N_2-derived nitrides via initial PT have been reported (see **Figure 1.10**, right). For example, addition of [Hlut][BAr^F_4] (lut = 2,6-lutidinium, Ar^F = 3,5-trifluoromethyl-phenyl) to (defp)(Cp*)Mo(N) gives 39% of the Mo-imide complex [(defp)(Cp*)Mo(NH)][BAr^F_4] among other byproducts, including H_2.[68] In other instances, protonation of a nitride is accompanied by coordination of the conjugate base or counterion. Pincer-complex (PNP)Mo(N)(Cl) can be protonated by [Hpy][OTf] (py = pyridine) to give the corresponding imide complex [(PNP)Mo(N)(Cl)(py)][OTf] in 53% yield.[44] These systems each involve protonation of a Mo^{IV}-nitride with a strong acid (pK_a = 5.5 for pyridinium in THF).[126] In both cases, subsequent PCET to the imide using excess strong acid and reductant results in formation of substoichiometric NH_3.

Considering an ET-first mechanism, electrochemical studies of N_2-derived metal nitrides show that reduction occurs at highly reducing potentials, if it occurs at all within the solvent window (**Table 1**). At such cathodic potentials, the propensity to favor H_2 formation at the electrode is a significant limitation on ET-first mechanisms in electrocatalytic systems.[34, 127]

Table 1.1. Reported reduction potentials of N_2-derived metal nitrides.

Complex	Peak Reduction Potential (V vs. $Cp_2Fe^{+/0}$)	Solvent	Reference
(PNP)Mo^{IV}(N)(I)	–1.81	THF	[46]
(PONOP)Re^{V}(N)$(Cl)_2$	–2.38	THF	[84]
[(depe)Mo^{IV}(N)]$^+$	–2.83	THF	[74]
(PNP)Re^{V}(N)(Cl)	–3.34	THF	[67]

Despite these challenges, several systems that can catalytically generate NH_3 from N_2 using acid and reductant pairs are believed to proceed through a metal nitride intermediate,[40, 45, 48-50] including some that feature an N_2 splitting step.[46, 47] This necessitates successful PCET reduction of nitride intermediates to form NH_3. These systems rely on strong reductants (metallocenes or alkali metals) and strong acids (lutidinium, $[H_2NPh_2][OTf]$, or $HBAr^F_4$) in order to overcome the high thermodynamic barriers associated with stepwise PCET reduction. Utilizing such strong reagents results in inefficiency via a large excess thermodynamic driving force for NH_3 production when compared to NH_3 synthesis from H_2.[125] Even with attempts to kinetically control for the formation of NH_3 via using low temperatures or employing either an insoluble acid or reductant, H_2 is a significant byproduct in all of these reactions.

1.5.3. Concerted PCET reduction of nitrides

Utilizing a concerted PCET mechanism can avoid the difficulties of stepwise PT or ET to a metal nitride. Rather than being limited by the Brønsted basicity or reduction potential of the nitride, the thermodynamics of concerted PCET reduction of the nitride is tied to the N–H BDFE of the imide product. Therefore, the N–H BDFE of the imide can be used to predict reactivity with various PCET reagents; however, experimental data for these M=NH complexes is lacking.[128] Computational studies have identified two preliminary trends in N–H bond formation on the path to NH_3: the first N–H bond can be particularly weak (**Figure 1.13**, red), and the strength of subsequent N–H bonds generally increases with formation of the amide and ammine ligand (**Figure 1.13**, blue).[125, 129, 130] **Figure 1.14** compares the theoretically estimated N–H BDFE values of a representative series of imide/amide/ammine complexes with BDFE (or $BDFE_{eff}$) values of a range of

PCET reagents. Many commonly utilized PCET reagents contain X–H bonds (BDFE ~ 60–80 kcal/mol) that are likely too strong to render imide N–H bond formation (highlighted in red in **Figures 1.13–14**) exergonic. Reagents that are generated *in situ* upon the pairing of a reductant and acid are more promising (labelled in blue in **Figure 1.14**), with $BDFE_{eff}$ ~ 25–55 kcal/mol.

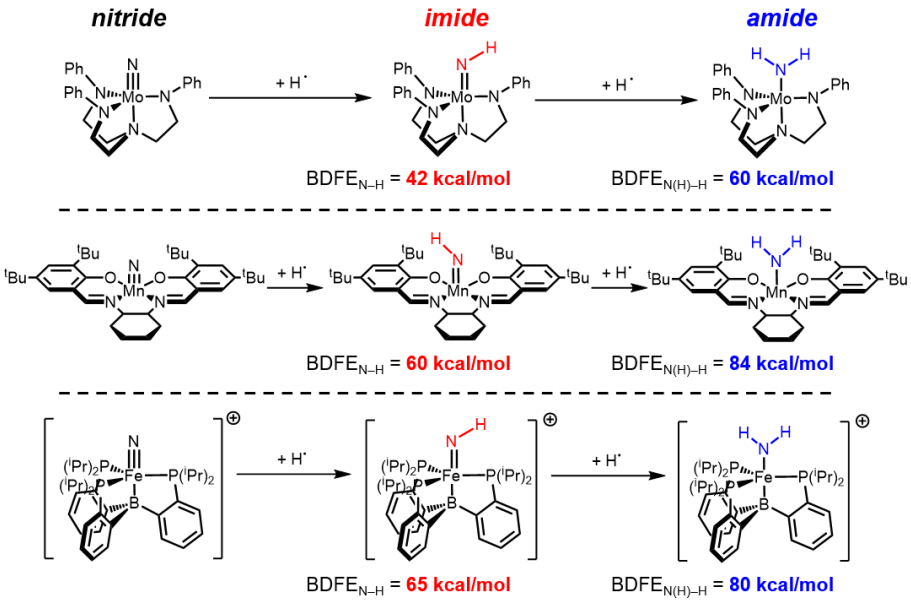

Figure 1.13. DFT calculated $BDFE_{N–H}$ values during the sequential PCET reduction of metal nitrides to imides (red) and amides (blue).

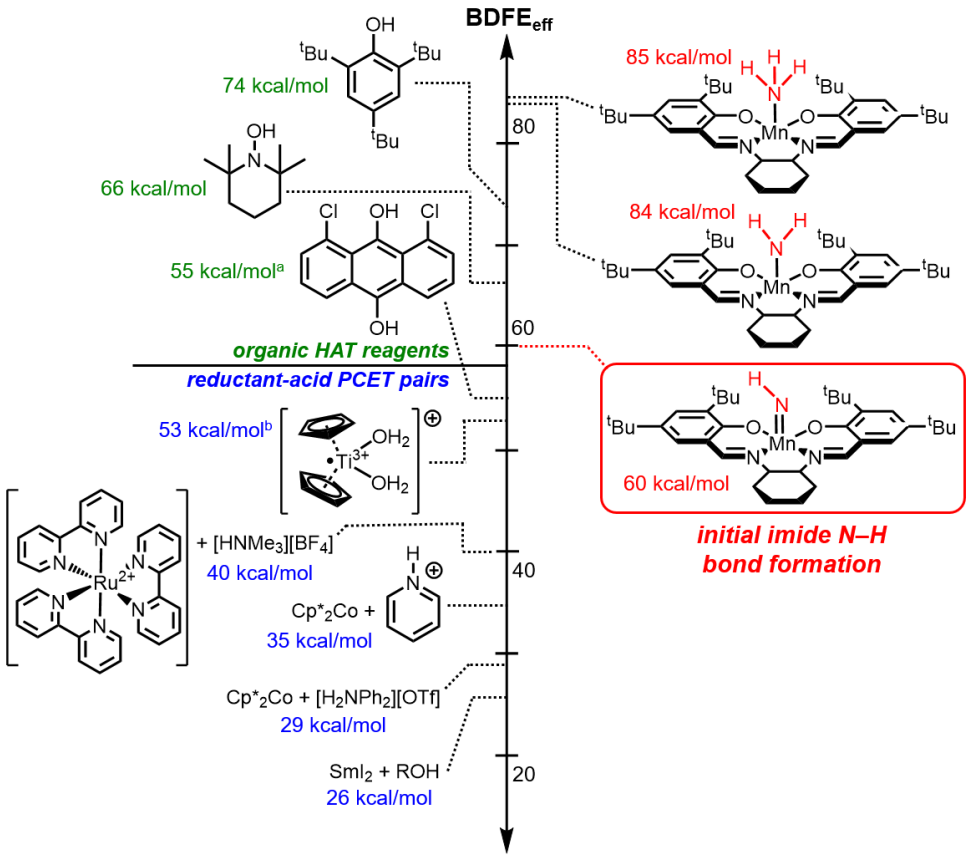

Figure 1.14. Comparison of effective bond-dissociation free energy ($BDFE_{eff}$) values in THF for various PCET reagents and imide, amide, and ammine N–H bonds. **Left:** Experimental values for unimolecular reagents (green) and reductant-acid pairs (blue). [a]Average O–H BDFE.[131] [b]Bond dissociation energy (BDE) reported.[132] **Right:** DFT calculated N–H BDFEs in THF.[129]

1.5.4. Stoichiometric reduction of metal nitrides to NH_3 using concerted PCET

Although HAT from TEMPOH has been used to reduce nitride ligands to amides[133] and NH_3 (**Figure 1.15**, complex **I**),[134] there are currently no examples of PCET reduction of N_2-derived nitrides using unimolecular organic HAT reagents, likely because they do not provide a strong enough driving force for N–H bond formation at N_2-derived nitrides.

It is noteworthy that the catalytic conditions employed in many N_2 to NH_3 systems can generate strong HAT reagents *in situ*. For example, 1e^- reduction of pyridinium acids, such as 2,6-lutidinium and 2,4,6-collidinium, may generate the corresponding pyridinyl radical ($BDFE_{eff}$ ~ 35 kcal/mol), although this proposal lacks much experimental

support.[125, 135] The pairing of strong reductants with pyridinium acids is one of the most commonly employed strategies in homogeneous N_2 reduction chemistry. Its potential utility as a reductant-acid pair for concerted PCET may be evident from reduction of the cationic nitride complex $[(depe)_2Mo^{IV}(N)]^+$ with $[Hlut][BAr^F{}_4]$ and $Cp^*{}_2Co$ (**Figure 1.15**, complex **J**): the cationic complex is unlikely to proceed through an initial-PT pathway, and the metallocene reductant ($E_{1/2}$ = –1.9 V vs. $Cp_2Fe^{+/0}$)[136] employed is not reducing enough to form the neutral Mo^{III}-nitride complex (E_{pc} = –2.8 V vs. $Cp_2Fe^{+/0}$) in an initial-ET pathway.[74] Another example of *in situ* formation of a strong HAT reagent from reductant-acid pairing is protonation of $Cp^*{}_2Co$ with sufficiently acidic aniliniums to form $[(Cp^*)(exo\text{-}\eta^4\text{-}C_5Me_5H)Co]^+$ at low temperatures.[51, 137-139] The utility of $[(Cp^*)(exo\text{-}\eta^4\text{-}C_5Me_5H)Co]^+$ as a potent HAT reagent ($BDFE_{eff}$ ~ 29 kcal/mol)[138] during catalytic N_2 reduction to NH_3 is discussed below.

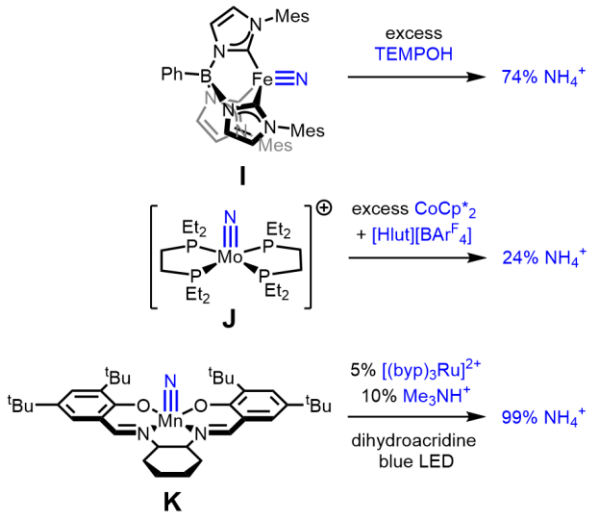

Figure 1.15. Stoichiometric reduction of metal nitrides to form NH_3 using concerted PCET.

Reductant-acid PCET pairs that do not include strong acids may avoid undesirable protonation at the supporting ligand or metal center. Recently, nitride conversion to NH_3

was demonstrated using weak acids, such as trimethylammonium ($HNMe_3^+$), in conjunction with dihydroacridine and $[(bpy)_3Ru^{II}]^{2+}$ as a photoreductant.[129] In this system, HAT to a (salen)Mn^V(N) complex occurs from photogenerated $[(bpy)_3Ru^I]^+$ and a weak acid, representing an example of multi-site, concerted PCET to a nitride (**Figure 1.15**, complex **K**). Importantly, the reductant-acid pair must reach a threshold $BDFE_{eff}$ (less than 49 kcal/mol) in order to generate NH_3 from the nitride in high yields. The authors hypothesize that this threshold represents the minimum sufficient thermodynamic driving force that the reductant-acid PCET pair must provide to form the initial N–H bond ($BDFE_{N–H}$ = 60 kcal/mol). After generating the imide complex (salen)Mn^{IV}(NH), subsequent formation of the amide and ammine intermediates is computed to be much more exergonic ($BDFE_{N–H}$ = 84 and 85 kcal/mol, respectively). Interestingly, utilizing a stronger photoreductant allows for the stepwise ET/PT reduction of (salen)Mn^{IV}(N) to (salen)Mn^{IV}(NH) when paired with a sufficiently strong acid.[140]

The combination of SmI_2 and H_2O (or alcohols) as a reductant-acid PCET pair has been extensively studied. Beyond its ability to efficiently reduce a variety of organic substrates,[141-143] SmI_2/H_2O boasts the weakest $BDFE_{eff}$ reported to date (26 kcal/mol),[143] is kinetically stable from decomposition to form H_2, and can operate through stepwise or concerted PCET mechanisms.[144] Nishibayashi and coworkers recently demonstrated that the combination of SmI_2 and H_2O can be used as the reductant-acid pair for catalytic N_2 reduction to NH_3 using Mo pincer complexes. Utilizing this system, which proceeds through N_2 splitting to form a Mo^{IV}-nitride intermediate,[47] they report the highest turnover of NH_3 per homogeneous catalyst reported to date by an order of magnitude with excellent selectivity for NH_3.[73, 82]

Another mechanism for PCET nitride reduction enlists "non-innocent" supporting ligands to donate H^+ and/or e^- equivalents. For example, Lindley *et al.* recently showed that nitride complex $[(^{tBu}P^{H}NP)Ru^{IV}(N)]^+$ reacts with one equivalent of 4-methoxy-benzoic acid (4-MeO-BzOH) to give ammine complex $[(^{tBu}PN{=}CP)Ru^{II}(NH_3)(OBz\text{-}4\text{-}OMe)]^+$, in which the pincer backbone has been oxidized by $2H^+/2e^-$ to give an imine (**Figure 1.16**, complex **L**).[123] This represents a cooperative $3H^+/2e^-$ reduction of the Ru-nitride directly to NH_3, in which the coordinating acid facilitates intramolecular hydrogen-bonding interactions to shuttle protons to the imide and amide intermediates. Similar ligand non-innocence occurs in a bis(imino)-pyridine-supported Mo^{III}-bis(amide) complex, in which protonation of the bis-amide complex with a single equivalent of [Hlut][OTf] results in formation of the Mo^{III}-bis(ammine) complex (**Figure 1.16**, complex **M**).[145] This involves an intramolecular PT from the bis(imino)-pyridine ligand to one of the amide ligands. A related bis(anilido)-pyridine ligand is used to support the catalytic reduction of a Mo^{VI} nitride to form NH_3 (**Figure 1.16**, complex **N**).[139] Although the mechanism of this reduction is unclear, redox non-innocent behavior at the supporting ligand is a possibility.

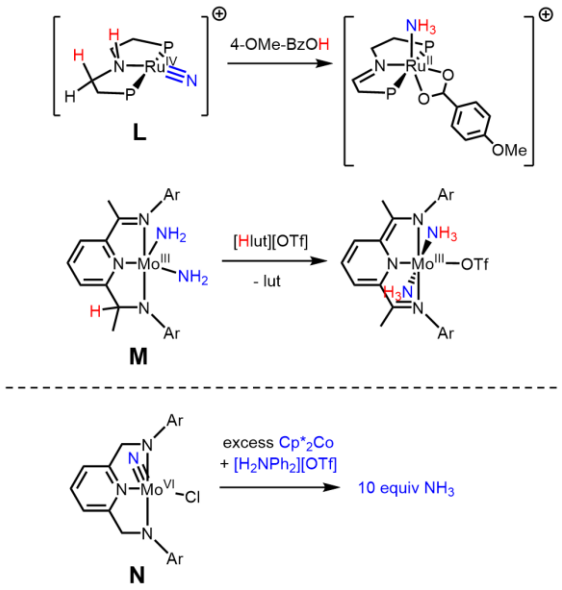

Figure 1.16. Top: Supporting ligand non-innocence to generate NH_3 from a Ru nitride (**L**) and a Mo-amide (**M**) upon protonation. **Bottom:** Catalytic reduction of N_2 to NH_3 using a redox-non-innocent ligand.

1.5.5. Catalytic reduction of N_2 to NH_3 using concerted PCET reagents

Beyond stoichiometrically generating N–H bonds, reductant-acid PCET pairs are also used in the *catalytic* reduction of N_2 to NH_3. Many of the reported homogeneous catalytic systems for N_2 reduction to NH_3 are hypothesized to proceed through a nitride intermediate (**Figure 1.17**). In most cases, the nitride is thought to be formed following release of NH_3 to break the N–N bond;[40, 45, 50, 51, 139] however, some systems utilizing Mo-pincer complexes proceed through direct N_2 splitting to form metal nitrides.[46, 47, 73] Regardless of the mechanism, each of these systems requires PCET reduction of a metal nitride to form NH_3.

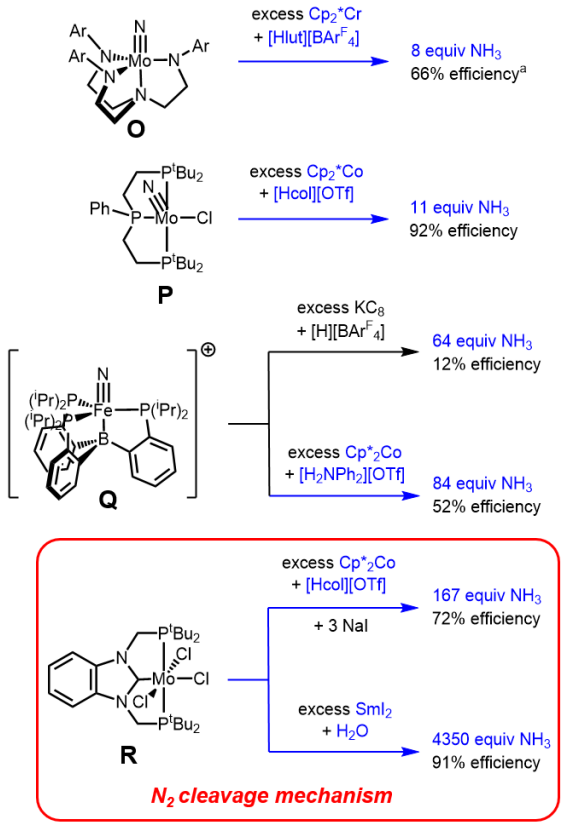

Figure 1.17. Catalytic N_2 to NH_3 systems that proceed through a nitride intermediate. Reactions with reductant-acid PCET pairs that can generate strong HAT reagents are shown in blue. [a]Efficiency defined as yield NH_3 based on amount of reductant added.

Most of the catalytic systems for N_2 reduction to NH_3 that pairs a strong acid and reductant rely on a combination that can hypothetically generate strong HAT reagents *in situ*. The exception to this is the combination of KC_8 and $[H][BAr^F{}_4]$,[139] for example in catalytic NH_3 formation from $(P_3{}^E)Fe$ (E = B, C, Si) (**Figure 1.17**, complex **Q**), in which the reductant-acid pair most likely operate in a stepwise mechanism (although protonation of graphite to generate a HAT reagent cannot be ruled out).[48-50] It is notable that these systems have the lowest efficiency of NH_3 formation compared to the hypothetical yield of NH_3 (12% with catalytic $(P_3{}^B)Fe$ based on reductant).[50] When the reductant-acid pair is replaced with less reducing Cp_2*Co and less acidic $[H_2NPh_2][OTf]$, the efficiency of NH_3

production quadruples to 52% despite the lower driving force for PCET reduction. The authors attribute this to formation of $[(Cp^*)(exo\text{-}\eta^4\text{-}C_5Me_5H)Co]^+$ *in situ*, providing opportunities for concerted PCET reduction along the catalytic cycle to avoid key high-energy intermediates.[51, 138] The HAT reagent $[(Cp^*)(exo\text{-}\eta^4\text{-}C_5Me_5H)Co]^+$ is more kinetically stable at low temperatures;[138] accordingly, performing the same reaction at higher temperatures results in lower turnover and selectivity for NH_3 in both Fe and Mo systems.[51, 139] In catalytic reactions employing pyridinium acids (**Figure 1.17**, complexes **O** and **P**), a similar concerted PCET mechanism may occur involving the pyridinyl radical, all though this possibility has not been assessed experimentally.[125, 135]

The highest turnovers of NH_3 from N_2 reduction using a molecular catalyst have been achieved via combining an N_2 splitting mechanism with reductant-acid PCET pairs that can generate strong HAT reagents. These systems utilize (^{tBu}PNP)Mo or (^{tBu}PCP)Mo (^{tBu}PCP = 1,3-bis((di-*t*Bu-phosphino)methyl)benzimidazol-2-ylidene) in combination with either Cp_2^*Co/[Hcol][OTf][46, 47] or SmI_2/H_2O (**Figure 1.17**, complex **R**).[73, 82] Using SmI_2/H_2O, which provides a stronger thermodynamic driving force, results in a significant increase in efficiency of NH_3 generation by (^{tBu}PCP)$MoCl_3$. The high selectivity towards NH_3 production over H_2 may be a consequence of the kinetic stability of SmI_2/H_2O as a reductant-acid PCET pair, considering that the catalyst is identical in both reactions.

Varying the reductant-acid PCET pair in SmI_2 systems by using alcohols instead of H_2O results in lower selectivity for NH_3 generation in (^{tBu}PCP)Mo-catalyzed N_2 reduction.[47] This may be due to changes in thermodynamic driving force from different SmI_2/alcohol pairs resulting in slower kinetics of N–H bond formation.[146] Linear free-energy relationships have been established between rate and driving force of HAT

reactions,[147] suggesting that more kinetically facile N–H bond formation is related to a higher thermodynamic driving force. Higher driving forces for PCET nitride reduction in Mo systems result in higher selectivity for NH_3 formation, although the reason for this is unclear considering the proportional increase in driving force for H_2 production.[40, 45-47, 73]

1.6 Electrochemical PCET nitride reduction in NRR

The success of acid/reductant pairs seems promising for the development of electrochemical systems, where the potential at the electrode and pK_a of the acid employed can be independently tuned to control the effective BDFE for PCET.[34, 137] **Figure 1.18** shows how different combinations of reductants and acids can achieve the same effective BDFE values. With knowledge of the N–H BDFE of interest, or the MN_xH_y reduction potential, appropriate acids or acid/reductant pairs can be chosen for the desired reaction.

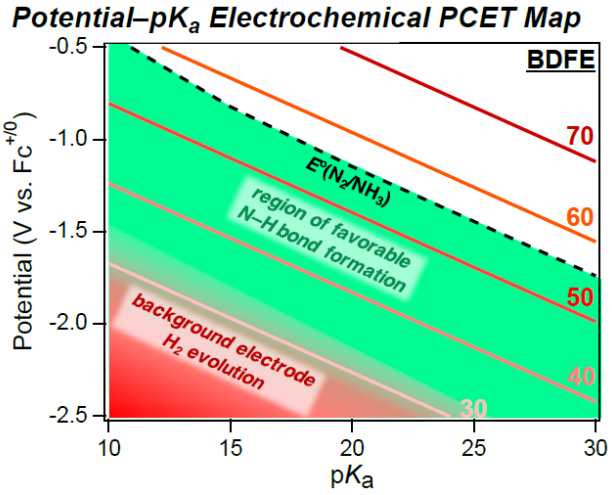

Figure 1.18. Potential-pK_a map in MeCN of favorable N–H bond forming regions (green). Figure by AJMM.

(TPB)Fe represents the only reported molecular system that can achieve electrocatalytic N_2 reduction to NH_3 (**Figure 1.19**). Under N_2 at –35 °C, the electrolysis of

(TPB)Fe (–2.1 V vs. $Cp_2Fe^{+/0}$) can generate up to 5.5 equiv NH_3 per Fe in the presence of 50 equiv of $[H_2NPh_2][OTf]$ and at least 1 equiv of Cp^*_2Co, operating with a Faradaic efficiency of ~20% (**Figure 1.19**).[137] Electrochemical turnover is enhanced by addition of at least 1 equiv of Cp^*_2Co, implicating a key role of $[(Cp^*)(exo\text{-}\eta^4\text{-}C_5Me_5H)Co]^+$ as a PCET mediator. It is likely that this involves PCET to a nitride, since chemical catalysis of N_2 reduction to NH_3 proceeds through a nitride intermediate $[(TPB)Fe(N)]^+$, although this is expected to come from a distal mechanism rather than an N_2 splitting mechanism.[50, 51, 148, 149]

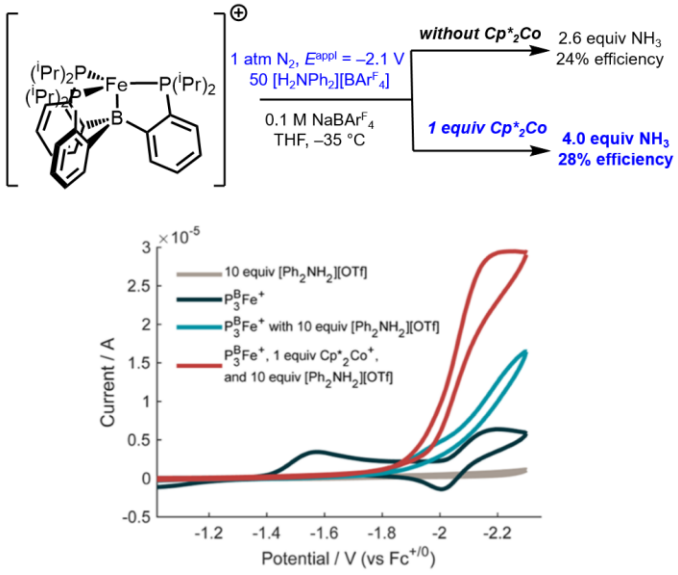

Figure 1.19. Top: N_2 electroreduction to NH_3 catalyzed by a molecular (TPB)Fe system. The system shows an enhancement in NH_3 yield and Faradaic efficiency upon addition of Cp^*_2Co as a HAT mediator, which corresponds to an enhancement in cathodic current passed during cyclic voltammetry experiments (**bottom**, red trace). Potentials are reported vs. $Cp_2Fe^{+/0}$. Reproduced from ref. [137].

1.6.1. Potential challenges involved with electrochemical PCET nitride reduction

PCET at electrode surfaces often follows different mechanisms than molecular reactions in solution, with pre-organization of substrates prior to PCET, such as through hydrogen bonding, playing an important role.[150, 151] Furthermore, kinetics of

electrochemical reduction are different than solution-phase kinetics, involving an interface between the solid electrode and substrate in solution. Consequently, the ability to achieve molecular catalysis of N_2 reduction to NH_3 with a system does not guarantee its ability to do so electrocatalytically.[152]

Considering the difficulty of PT- and ET-first mechanisms for N_2-derived nitrides, stepwise PCET reduction of N_2-derived metal nitrides may be energetically costly. N_2 cleavage to form metal nitrides is more favorable with electron-rich complexes, therefore generating electron-rich nitrides that are difficult to reduce. The reduction potential of some N_2-derived nitride complexes is not reported, presumably because they are not reduced at potentials within the solvent window (up to –3.4 V vs. $Cp_2Fe^{+/0}$ for THF).[71, 100] The complexes that can be electrochemically reduced have very cathodic reduction potentials (E_{pc} more cathodic than –1.8 V vs. $Cp_2Fe^{+/0}$ in THF, **Table 1.1**). At these potentials, weak acids must be employed to avoid proton reduction to H_2 directly at the electrode (see **Figure 1.18**).[127] As discussed earlier, most N_2-derived nitrides are also unreactive towards protonation at the nitride, with the exception of a few Mo examples.

It is evident that a vital challenge in achieving electrocatalytic NRR via N_2 cleavage is PCET reduction of the nitride. There existing research described above implies a few potential strategies to achieve this reactivity and unlock NRR: balancing the thermodynamic driving force of N_2 splitting to facilitate N–H bond formation at the nitride, developing new concerted PCET methods for nitride reduction to NH_3, and incorporating concerted PCET reduction into electrochemical systems.

1.6.2. Towards balancing thermodynamics of N_2 cleavage and PCET nitride reduction

The thermodynamic penalty of an exergonic N–N bond cleavage step in NRR to form stable metal nitrides must be paid with endergonic N–H bond forming steps, as outlined previously. To flatten the overall energy surface of electrocatalysis, systems that feature roughly ergoneutral steps along the NRR pathway should be targeted. Detailed mechanistic and thermochemical analysis of the existing molecular N_2 reduction catalysts that proceed through bimetallic N_2 cleavage may give insight into the key to their reactivity. Systems that can photochemically cleave N_2 [71, 84, 101, 153, 154] offer a promising opportunity: cleavage of the N–N bond in $[(^{iPr}P^{H}NP)ReCl_2]_2(\mu\text{-}N_2)$ is *uphill* by 2 kcal/mol but rapidly occurs upon UV-Vis irradiation. In this case, light-driven N_2 cleavage overcomes a substantial kinetic barrier ($\Delta G^{\ddagger}$ = 42 kcal/mol) and provides the extra energy input necessary to drive nitride formation.[71] The resulting Re nitride can incorporate N into benzonitrile, and the precursor to the $\mu\text{-}N_2$ dimer can be regenerated electrochemically in an overall stoichiometric cycle (see **Figure 1.10**, right). This provides inspiring evidence that less favorable nitride formation, perhaps utilizing photolysis or protonation to facilitate N_2 splitting, may generating more reactive nitride products.[69, 71]

In contrast to our growing understanding of the factors that dictate thermal and photolytic N_2 splitting, our understanding of what factors determine N–H bond strengths along the reduction pathway from nitride to NH_3 is underdeveloped. This is in part due to the small number of systems that can reduce nitrides to NH_3, limiting the ability to collect and compare thermochemical data to identify trends. Experimental determination of thermochemical values is particularly lacking in the field: no experimental thermochemical values involved with N_2-derived nitride conversion to NH_3 have been reported. This may

be due to the instability of intermediates along nitride reduction pathways. However, considering the growing number of pincer-supported systems that can achieve N_2 splitting at Mo[45-47, 73] and Re,[67, 71, 100] comparisons of computationally-derived N–H bond strengths may shed light on how more favorable PCET nitride reduction can occur (**Figure 1.20**, left). Analogous studies comparing the thermochemistry of N_2 reduction to NH_3 by (P_3^E)Fe complexes indicate that changing the anchoring atom of the supporting ligand can have a drastic effect on N–H BDFEs (**Figure 1.20**, right).[130] In this system, the relative N–H bond strengths of intermediates along the N_2 reduction cycle serves as an accurate predictor for trends in turnover and selectivity for catalytic NH_3 formation.[48-50] A similar understanding of N–H bond formation at metal nitrides will help guide the design of systems where PCET nitride formation is more favorable.

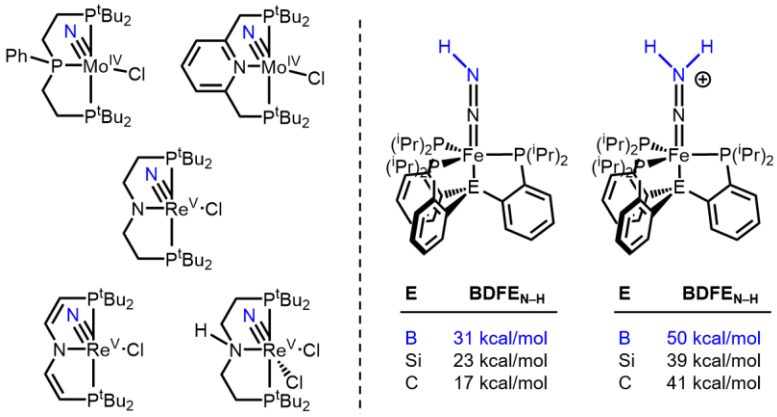

Figure 1.20. Left: Structurally similar N_2-derived Mo and Re nitrides amenable to computational comparison of thermochemistry involved with N–H bond formation. **Right:** Computational comparison of N–H BDFEs in structurally-related intermediates of N_2 reduction by (P_3^E)Fe. Complexes featuring a B anchor (blue) exhibit the strongest N–H bonds and highest activity for catalytic NH_3 formation. Adapted from ref.[130]

1.6.3. Exploring new concerted PCET methods for nitride reduction

The success of the PCET reagents summarized in Section 1.5 in achieving difficult nitride reductions to NH_3 merits the exploration of other HAT reagents for this

transformation (**Figure 1.21**). One opportunity exists in using photoexcitation to weaken coordinated X–H bonds in metal complexes.[140] For example, imidazole N–H bonds in a series of Ru complexes have been shown to weaken considerably upon photoexcitation, generating bonds as weak as 41 kcal/mol.[140, 155-157] The use of "milder" HAT reagents, containing higher effective BDFEs closer to the thermodynamic energy of NH_3 bond formation from N_2 and H_2 (*ca.* 50 kcal/mol), should also be explored in order to keep the catalytic cycle as ergoneutral as possible. Coordination of H_2O to reduced titanocene complexes to form $[Cp_2Ti(H_2O)_2]^+$ can generate O–H bonds as weak as 53 kcal/mol.[132] These complexes have been demonstrated as capable HAT reagents for the reduction of carbon-centered radicals and epoxides, but they have not yet been assessed for PCET nitride reduction.[158] Alternatively, anthracenediols contain O–H bonds as weak as 55 kcal/mol.[131, 159] Use of these milder reagents may prevent unproductive HAT reactions, such reduction of the supporting ligand to deactivate the catalyst or metal center to generate hydrides, while also reducing the chemical overpotential for reduction of N_2 to NH_3.

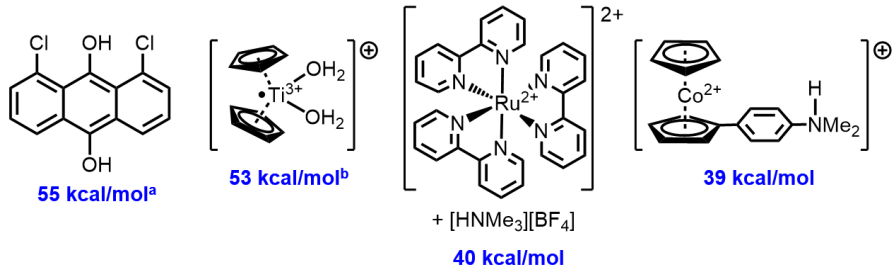

Figure 1.21. Reported PCET reagents that have not been assessed for N_2-derived nitride reduction, with $BDFE_{eff}$ values in blue. [a]Average O–H BDFE.[131] [b]Bond dissociation enthalpy reported.[132]

Beyond identifying new methodologies for concerted PCET nitride reduction, it is important to understand the deleterious pathways of strong HAT reagents to reduce metal nitride complexes. While tentative relationships between driving force for N–H bond

formation and efficiency of NH_3 generation have been established, some systems are inherently more selective for the production of NH_3 over H_2 than others despite utilizing similar reagents. It is important to understand the potential pathways of H_2 formation in these systems, for example through hydride formation[70] or elimination of H_2 from particularly weak N–H bonds.[128, 130, 145] In the case of catalytic reduction of N_2 to NH_3 by (^{tBu}PNP)Mo(N)(X) (X = Cl, Br, I), the identity of the ancillary halide plays an enormous role in the efficiency of NH_3 production despite a relatively mild effect on redox potential.[46] Decrease in NH_3 production in this system is accompanied by a corresponding increase in H_2 generation, implying that the halide identity has kinetic influence over reduction pathways during catalysis, either through affecting the relative rates of N_2 cleavage or PCET nitride reduction to H_2 formation. Similarly, Mo complexes supported with different pincer ligands give different selectivity for NH_3 vs. H_2 generation using the same reductant-acid PCET pairs.[46, 47, 73] Investigating the potential mechanisms of H_2 production in these systems and others will help guide the design of systems that hinder these pathways.

1.6.4. Incorporating concerted PCET methods into electrochemical nitride reduction

The vast majority of homogeneous systems that can achieve efficient catalytic reduction of N_2 to NH_3 utilize conditions that allow concerted PCET reactions. However, concerted PCET during electrochemical reduction is fundamentally challenging and typically requires the use of an added HAT mediator[160, 161] or pre-organization of substrates prior to PCET, such as through hydrogen bonding.[150, 151] Despite the challenges, Peters and coworkers recently demonstrated that PCET steps in an electrocatalytic N_2 reduction cycle can be achieved through the use of a molecular PCET mediator.[137] Ideally, a PCET

mediator must be potent enough to form weak N–H imide bonds, and should operate catalytically, being regenerated under the reaction conditions.

Chemical studies of PCET nitride reduction identify some promising candidates for HAT mediation in NRR. Anthracenediols with relatively weak O–H bonds, such as 1,8-dichloro-9,10-anthracendiol (BDFE = 55 kcal/mol in H_2O, **Figure 1.14**) offer one possibility.[131] To provide a stronger thermodynamic driving force for N–H bond formation, reductant-acid PCET pairs should also be explored. In conjunction with dihydroacridine, the photoreductant-acid pair $[(bpy)_3Ru]^{2+}/HNMe_3^+$ has already been demonstrated to catalytically achieve difficult HAT to a nitride, with dihydroacridine serving a dual role of generating the highly reducing $[(bpy)_3Ru]^{1+}$ species upon photolysis and providing H-atom equivalents for subsequent PCET reductions following imide formation.[129] This system may be well-primed for adaptation to a photoelectrocatalytic system in which the photoreductant can be regenerated at the electrode instead. Photolytic N_2 splitting could also be incorporated into a photoelectrocatalytic NRR system, where photoelectroreduction of the resulting nitride by $[(bpy)_3Ru]^{2+}/HNMe_3^+$ can form NH_3. Chalkley and Peters also recently demonstrated that an aniline-tethered Cp_2Co complex can serve as a concerted PCET mediator in the electrocatalytic reduction of difficult carbonyls, achieving up to 40 turnovers (see **Figure 1.21**).[162] This serves as an exciting proof-of-concept for electrochemically generating concerted PCET mediators, which can be regenerated at the electrode in the presence of a weak acid.

The use of H_2O as an H atom source is ideal for sustainable NRR. Reductant-acid PCET pairs that utilize H_2O as the acid, such as SmI_2/H_2O or $[(Cp_2Ti(H_2O)_2]^+$, are thus particularly enticing as HAT mediators.[163] However, regeneration of these reductants from

the oxidized Sm- or Ti-hydroxide product following HAT is difficult, as formation of strong Sm–OH and Ti–OH bonds help thermodynamically drive their respective PCET reductions. Additionally, Sm^{III}-hydroxide salts are particularly insoluble and tend to precipitate out from the reaction. Despite these challenges, catalytic use of $SmCl_2$ for HAT reactions has been reported recently using tetraglyme to solubilize the Sm^{III} product.[164] However, the use of trimethylsilyl chloride is required to cleave the Sm–OR bond prior to reductive regeneration of $SmCl_2$. On the other hand, catalytic use of $[(Cp_2Ti(H_2O)_2]^+$ as a HAT reagent has not been reported, to the best of my knowledge. Nonetheless, development of catalytic systems utilizing HAT from SmI_2 or $[(Cp_2Ti(H_2O)_2]^+$ is of particular interest in the context of concerted PCET nitride reduction considering their ability to generate powerful HAT reagents from H_2O.

Another opportunity for facilitating N–H bond formation in NRR exists in ligand-assisted PCET nitride reduction. Redox non-innocence of aliphatic pincer supporting ligands, in which the ligand can supply H^+/e^- equivalents, has been demonstrated in the synthesis of NH_3 from a Ru nitride[123] and benzonitrile from a Re nitride.[71] In the latter case, the supporting ligand can be restored via electrochemical reduction of the complex at –1.85 V vs. $Cp_2Fe^{+/0}$ in the presence of 2,6-dichlorophenol as a weak acid. One can imagine combining the concepts of these two reactions to achieve electrosynthesis of NH_3 from a N_2-derived nitride with a mild acid: electrochemical N_2 cleavage can form the metal nitride, followed by ligand-assisted PCET reduction of the nitride to NH_3, then regeneration of the N_2-splitting precursor directly at the electrode. Utilizing mild acids with coordinating conjugate bases, such as benzoic acids, may help to orient intermediates to facilitate proton shuttling during NRR while minimizing direct reduction of protons at the electrode.

1.7 Conclusions

Despite recent progress in electrochemical N_2 reduction to NH_3, there is still no report of a molecular electrocatalyst that is demonstrated to achieve turnover of N_2 to NH_3 via N_2 cleavage. However, each of the individual steps has been demonstrated, confirming the promise of this approach. Further support for this notion comes from the observation that leading Mo catalysts for NH_3 synthesis using chemical reductants appear to proceed via an N_2 cleavage mechanism.[93]

Outline of this Thesis

The studies in this dissertation use model systems to investigate the individual steps involved in a hypothetical electrocatalytic NRR system in detail in an effort to understand the hurdles to difficult steps, the drivers for productive reactivity, and the potential of new methodologies. Chapter 2 investigates an associative approach to N_2 electroreduction using Ir- and Rh-dinitrogen complexes. Chapter 3 explores the reactivity of an intransigent Re nitride formed from the electrochemical cleavage of N_2 in an attempt to coax it towards new directions for nitrogen fixation to NO_x. Chapter 4 applies new concerted PCET methodologies to generate NH_3 from a Re nitride derived from photolytic N_2 cleavage. Finally, chapter 5 identifies the thermodynamic hurdles associated with the PCET nitride reduction half of NRR by studying the microscopic-reverse reaction, NH_3 oxidation to a nitride. These studies herein have led to exciting discoveries, including as an unprecedented *umpolung* of reactivity at an N_2-derived nitride, the first demonstration of N_2 fixation to NH_3 utilizing Re, and the first experimental measurement of N–H bond enthalpies relevant to nitride reduction to NH_3. Together, the work in this dissertation

provides a holistic snapshot of the direction of this exciting young field as it progresses towards successful electrocatalytic N_2 fixation. It is my hope that the lessons learned herein will guide the design of molecular electrocatalysts for NRR, and ultimately contribute to a more sustainable route to global nitrogen fixation.

1.8 References

1. Lee, C. C.; Ribbe, M. W.; Hu, Y., Cleaving the N,N Triple Bond: The Transformation of Dinitrogen to Ammonia by Nitrogenases. In *The Metal-Driven Biogeochemistry of Gaseous Compounds in the Environment*, Kroneck, P. M. H.; Torres, M. E. S., Eds. Springer Netherlands: Dordrecht, 2014; pp 147-176.

2. Vitousek, P. M.; Hattenschwiler, S.; Olander, L.; Allison, S., *Ambio* **2002,** *31*, 97-101.

3. Erisman, J. W.; Sutton, M. A.; Galloway, J.; Klimont, Z.; Winiwarter, W., *Nat. Geosci.* **2008,** *1*, 636-639.

4. Burgess Jr., D. R., Thermochemical Data. In *NIST Chemistry WebBook, NIST Standard Reference Database Number 69*, Linstrom, P. J. M., W. G., Ed. National Institute of Standards and Technology: Gaithersburg, MD, 20899, 2020.

5. Duveen, D. I.; Klickstein, H. S., *Isis* **1954,** *45*, 368-382.

6. Purkhold, U.; Pommerening-Röser, A.; Juretschko, S.; Schmid, M. C.; Koops, H.-P.; Wagner, M., *Appl. Environ. Microbiol.* **2000,** *66*, 5368.

7. Hatzenpichler, R., *Appl. Environ. Microbiol.* **2012,** *78*, 7501.

8. Hooper, A. B.; Arciero, D.; Bergmann, D.; Hendrich, M. P., Chapter 6: The Oxidation of Ammonia as an Engergy Source in Bacteria. In *Respiration in Archaea and Bacteria: Diversity of Prokaryotic Respiratory Systems*, Zannoni, D., Ed. Springer Netherlands: Dordrecht, 2004; pp 121-147.

9. Schuur, E. A. G., *Nature* **2011,** *477*, 39-40.

10. Hill, R. D.; Rinker, R. G.; Wilson, H. D., *J. Atmos. Sci.* **1980,** *37*, 179-92.

11. Haber, F. *The synthesis of ammonia from its elements*; 1918 Nobel Lecture, June 2, 1920.

12. Smil, V., *Enriching the Earth: Fritz Haber, Carl Bosch, and the Transformation of World Food Production*. MIT Press: Cambridge, MA, 2004.

13. Smil, V., *Nature* **1999,** *400*, 415.

14. Galloway, J. N.; Cowling, E. B., *Ambio* **2002,** *31*, 64-71.

15. Ritter, S. K., The Haber-Bosch Reaction: An Early Chemical Impact on Sustainability. *Chemical & Engineering News* **2008,** web exculsive August 18, 2008 (accessed August 19, 2020).

16. Appl, M., Ammonia. In *Ullmann's Encyclopedia of Industria Chemistry*, Wiley-VCH: Weinheim, 2006; pp 404-414.

17. Connor, G. P.; Holland, P. L., *Catal. Today* **2017,** *286*, 21-40.

18. Mittasch, A., *Geschichte der Ammoniaksynthese*. Verlag Chem.: 1951.

19. Vandervell, H. D.; Waugh, K. C., *Chem. Phys. Lett.* **1990,** *171*, 462-8.

20. Bosch, C., *The development of the chemical high pressure method during the establishment of the new ammonia industry*. 1931 Nobel Lecture, May 21, 1932.

21. Ertl, G., *Reactions at surfaces: from atoms to complexity*. 2007 Nobel Lecture, December 8, 2007.

22. Pattabathula, V. R., Jim, *Chem. Eng. Prog.* **2016,** *9*, 69-75.

23. Gruber, N.; Galloway, J. N., *Nature* **2008,** *451*, 293-296.

24. Giddey, S.; Badwal, S. P. S.; Munnings, C.; Dolan, M., *ACS Sustain. Chem. Eng.* **2017,** *5*, 10231-10239.

25. Jennings, J. R.; Editor, *Catalytic Ammonia Synthesis. Fundamentals and Practice*. Plenum: 1991.

26. Jewess, M.; Crabtree, R. H., *ACS Sustain. Chem. Eng.* **2016,** *4*, 5855-5858.

27. Renner, J. N.; Greenlee, L. F.; Ayres, K. E.; Herring, A. M., *Interface Magazine* **2015,** *24*, 51-57.

28. Hochman, G.; Goldman, A. S.; Felder, F. A.; Mayer, J. M.; Miller, A. J. M.; Holland, P. L.; Goldman, L. A.; Manocha, P.; Song, Z.; Aleti, S., *ACS Sustain. Chem. Eng.* **2020,** *8*, 8938-8948.

29. Suryanto, B. H. R.; Du, H.-L.; Wang, D.; Chen, J.; Simonov, A. N.; MacFarlane, D. R., *Nat. Catal.* **2019,** *2*, 290-296.

30. Foster, S. L.; Bakovic, S. I. P.; Duda, R. D.; Maheshwari, S.; Milton, R. D.; Minteer, S. D.; Janik, M. J.; Renner, J. N.; Greenlee, L. F., *Nat. Catal.* **2018,** *1*, 490-500.

31. Chen, J. G.; Crooks, R. M.; Seefeldt, L. C.; Bren, K. L.; Bullock, R. M.; Darensbourg, M. Y.; Holland, P. L.; Hoffman, B.; Janik, M. J.; Jones, A. K.; Kanatzidis, M. G.; King, P.; Lancaster, K. M.; Lymar, S. V.; Pfromm, P.; Schneider, W. F.; Schrock, R. R., *Science* **2018,** *360*, 873.

32. Schlögl, R., *Angew. Chem., Int. Ed.* **2003,** *42*, 2004-2008.

33. Tallaksen, J.; Bauer, F.; Hulteberg, C.; Reese, M.; Ahlgren, S., *J. Clean. Prod.* **2015,** *107*, 626-635.

34. Lindley, B. M.; Appel, A. M.; Krogh-Jespersen, K.; Mayer, J. M.; Miller, A. J. M., *ACS Energy Lett.* **2016,** *1*, 698-704.

35. Bard, A. J. J., Joseph; Parsons, Roger, *Standard potentials in aqueous solution*. M. Dekker: New York, NY, 1985.

36. Qing, G.; Ghazfar, R.; Jackowski, S. T.; Habibzadeh, F.; Ashtiani, M. M.; Chen, C.-P.; Smith, M. R.; Hamann, T. W., *Chem. Rev.* **2020,** *120*, 5437-5516.

37. Montoya, J. H.; Tsai, C.; Vojvodic, A.; Norskov, J. K., *ChemSusChem* **2015,** *8*, 2180-2186.

38. van der Ham, C. J. M.; Koper, M. T. M.; Hetterscheid, D. G. H., *Chem. Soc. Rev.* **2014,** *43*, 5183-5191.

39. Chalkley, M. J.; Drover, M. W.; Peters, J. C., *Chem. Rev.* **2020,** *120*, 5582-5636.

40. Yandulov, D. V.; Schrock, R. R., *Science* **2003,** *301*, 76-78.

41. Schrock, R. R., *Acc. Chem. Res.* **2005,** *38*, 955-962.

42. Arashiba, K.; Miyake, Y.; Nishibayashi, Y., *Nat. Chem.* **2011,** *3*, 120-125.

43. Kuriyama, S.; Arashiba, K.; Nakajima, K.; Tanaka, H.; Kamaru, N.; Yoshizawa, K.; Nishibayashi, Y., *J. Am. Chem. Soc.* **2014,** *136*, 9719-9731.

44. Tanaka, H.; Arashiba, K.; Kuriyama, S.; Nakajima, K.; Nishibayashi, Y.; Sasada, A.; Yoshizawa, K., *Nat. Commun.* **2014,** *5*, 3737.

45. Arashiba, K.; Kinoshita, E.; Kuriyama, S.; Eizawa, A.; Nakajima, K.; Tanaka, H.; Yoshizawa, K.; Nishibayashi, Y., *J. Am. Chem. Soc.* **2015,** *137*, 5666-5669.

46. Arashiba, K.; Eizawa, A.; Tanaka, H.; Nakajima, K.; Yoshizawa, K.; Nishibayashi, Y., *Bull. Chem. Soc. Jpn.* **2017,** *90*, 1111-1118.

47. Eizawa, A.; Arashiba, K.; Egi, A.; Tanaka, H.; Nakajima, K.; Yoshizawa, K.; Nishibayashi, Y., *Chem. - Asian J.* **2019,** *14*, 2091-2096.

48. Anderson, J. S.; Rittle, J.; Peters, J. C., *Nature* **2013,** *501*, 84-87.

49. Creutz, S. E.; Peters, J. C., *J. Am. Chem. Soc.* **2014,** *136*, 1105-1115.

50. Del Castillo, T. J.; Thompson, N. B.; Peters, J. C., *J. Am. Chem. Soc.* **2016,** *138*, 5341-5350.

51. Chalkley, M. J.; Del Castillo, T. J.; Matson, B. D.; Roddy, J. P.; Peters, J. C., *ACS Cent. Sci.* **2017,** *3*, 217-223.

52. Barney, B. M.; Lukoyanov, D.; Yang, T.-C.; Dean, D. R.; Hoffman, B. M.; Seefeldt, L. C., *Proc. Natl. Acad. Sci. U. S. A.* **2006,** *103*, 17113-17118.

53. Barney, B. M.; McClead, J.; Lukoyanov, D.; Laryukhin, M.; Yang, T.-C.; Dean, D. R.; Hoffman, B. M.; Seefeldt, L. C., *Biochem.* **2007,** *46*, 6784-6794.

54. Hoffman, B. M.; Lukoyanov, D.; Yang, Z.-Y.; Dean, D. R.; Seefeldt, L. C., *Chem. Rev.* **2014,** *114*, 4041-4062.

55. Hill, P. J.; Doyle, L. R.; Crawford, A. D.; Myers, W. K.; Ashley, A. E., *J. Am. Chem. Soc.* **2016,** *138*, 13521-13524.

56. Chatt, J.; Pearman, A. J.; Richards, R. L., *Nature* **1975,** *253*, 39-40.

57. Chatt, J.; Dilworth, J. R.; Richards, R. L., *Chem. Rev.* **1978,** *78*, 589-625.

58. Pickett, C. J., *J. Biol. Inorg. Chem.* **1996,** *1*, 601-606.

59. Chatt, J.; Heath, G. A.; Richards, R. L., *J. Chem. Soc., Dalton Trans.* **1974**, 2074-82.

60. Chatt, J.; Pearman, A. J.; Richards, R. L., *J. Chem. Soc., Dalton Trans.* **1977**, 1852-60.

61. Anderson, S. N.; Fakley, M. E.; Richards, R. L.; Chatt, J., *J. Chem. Soc., Dalton Trans.* **1981**, 1973-80.

62. Chatt, J.; Pearman, A. J.; Richards, R. L., *J. Chem. Soc., Dalton Trans.* **1976**, 1520-4.

63. Chatt, J.; Pearman, A. J.; Richards, R. L., *J. Organomet. Chem.* **1975,** *101*, C45-C47.

64. Galindo, A.; Hills, A.; Hughes, D. L.; Richards, R. L., *J. Chem. Soc., Chem. Commun.* **1987**, 1815-16.

65. Laplaza, C. E.; Cummins, C. C., *Science* **1995,** *268*, 861-3.

66. Hebden, T. J.; Schrock, R. R.; Takase, M. K.; Mueller, P., *Chem. Commun.* **2012,** *48*, 1851-1853.

67. Klopsch, I.; Finger, M.; Wuertele, C.; Milde, B.; Werz, D. B.; Schneider, S., *J. Am. Chem. Soc.* **2014,** *136*, 6881-6883.

68. Miyazaki, T.; Tanaka, H.; Tanabe, Y.; Yuki, M.; Nakajima, K.; Yoshizawa, K.; Nishibayashi, Y., *Angew. Chem., Int. Ed.* **2014,** *53*, 11488-11492.

69. Silantyev, G. A.; Foerster, M.; Schluschass, B.; Abbenseth, J.; Wuertele, C.; Volkmann, C.; Holthausen, M. C.; Schneider, S., *Angew. Chem., Int. Ed.* **2017,** *56*, 5872-5876.

70. Schluschass, B.; Abbenseth, J.; Demeshko, S.; Finger, M.; Franke, A.; Herwig, C.; Wuertele, C.; Ivanovic-Burmazovic, I.; Limberg, C.; Telser, J.; Schneider, S., *Chem. Sci.* **2019,** *10*, 10275-10282.

71. Schendzielorz, F.; Finger, M.; Abbenseth, J.; Würtele, C.; Krewald, V.; Schneider, S., *Angew. Chem., Inter. Ed.* **2019,** *58*, 830-834.

72. Itabashi, T.; Mori, I.; Arashiba, K.; Eizawa, A.; Nakajima, K.; Nishibayashi, Y., *Dalton Trans.* **2019,** *48*, 3182-3186.

73. Ashida, Y.; Arashiba, K.; Nakajima, K.; Nishibayashi, Y., *Nature* **2019,** *568*, 536-540.

74. Katayama, A.; Ohta, T.; Wasada-Tsutsui, Y.; Inomata, T.; Ozawa, T.; Ogura, T.; Masuda, H., *Angew. Chem., Int. Ed.* **2019,** *58*, 11279-11284.

75. Shima, T.; Hu, S.; Luo, G.; Kang, X.; Luo, Y.; Hou, Z., *Science* **2013,** *340*, 1549.

76. Clentsmith, G. K. B.; Bates, V. M. E.; Hitchcock, P. B.; Cloke, F. G. N., *J. Am. Chem. Soc.* **1999,** *121*, 10444-10445.

77. Caselli, A.; Solari, E.; Scopelliti, R.; Floriani, C.; Re, N.; Rizzoli, C.; Chiesi-Villa, A., *J. Am. Chem. Soc.* **2000,** *122*, 3652-3670.

78. Kawaguchi, H.; Matsuo, T., *Angew. Chem., Int. Ed.* **2002,** *41*, 2792-2794.

79. Rodriguez, M. M.; Bill, E.; Brennessel, W. W.; Holland, P. L., *Science* **2011,** *334*, 780-783.

80. Singh, D.; Buratto, W. R.; Torres, J. F.; Murray, L. J., *Chem. Rev.* **2020,** *120*, 5517-5581.

81. Chalkley, M. J.; Peters, J. C., *Eur. J. Inorg. Chem.* **2020,** *2020*, 1353-1357.

82. Ashida, Y.; Kondo, S.; Arashiba, K.; Kikuchi, T.; Nakajima, K.; Kakimoto, S.; Nishibayashi, Y., *Synthesis* **2019,** *51*, 3792-3795.

83. Laplaza, C. E.; Johnson, M. J. A.; Peters, J.; Odom, A. L.; Kim, E.; Cummins, C. C.; George, G. N.; Pickering, I. J., *J. Am. Chem. Soc.* **1996,** *118*, 8623-8638.

84. Bruch, Q. J.; Connor, G. P.; Chen, C.-H.; Holland, P. L.; Mayer, J. M.; Hasanayn, F.; Miller, A. J. M., *J. Am. Chem. Soc.* **2019,** *141*, 20198-20208.

85. Liao, Q.; Cavaille, A.; Saffon-Merceron, N.; Mezailles, N., *Angew. Chem., Int. Ed.* **2016,** *55*, 11212-11216.

86. Figueroa, J. S.; Piro, N. A.; Clough, C. R.; Cummins, C. C., *J. Am. Chem. Soc.* **2006,** *128*, 940-950.

87. Curley, J. J.; Sceats, E. L.; Cummins, C. C., *J. Am. Chem. Soc.* **2006,** *128*, 14036-14037.

88. Klopsch, I.; Kinauer, M.; Finger, M.; Wurtele, C.; Schneider, S., *Angew. Chem., Int. Ed.* **2016,** *55*, 4786-9.

89. Klopsch, I.; Schendzielorz, F.; Volkmann, C.; Würtele, C.; Schneider, S., *Z. Anorg. Allg. Chem.* **2018,** *644*, 916-919.

90. Sceats, E. L.; Figueroa, J. S.; Cummins, C. C.; Loening, N. M.; Van der Wel, P.; Griffin, R. G., *Polyhedron* **2004,** *23*, 2751-2768.

91. Espada, M. F.; Bennaamane, S.; Liao, Q.; Saffon-Merceron, N.; Massou, S.; Clot, E.; Nebra, N.; Fustier-Boutignon, M.; Mezailles, N., *Angew. Chem., Int. Ed.* **2018,** *57*, 12865-12868.

92. Duman, L. M.; Sita, L. R., *J. Am. Chem. Soc.* **2017,** *139*, 17241-17244.

93. Williams, D. S.; Meyer, T. J.; White, P. S., *J. Am. Chem. Soc.* **1995,** *117*, 823-4.

94. Coia, G. M.; Demadis, K. D.; Meyer, T. J., *Inorg. Chem.* **2000,** *39*, 2212-2223.

95. Crevier, T. J.; Lovell, S.; Mayer, J. M.; Rheingold, A. L.; Guzei, I. A., *J. Am. Chem. Soc.* **1998,** *120*, 6607-6608.

96. Walstrom, A.; Pink, M.; Fan, H.; Tomaszewski, J.; Caulton, K. G., *Inorg. Chem.* **2007,** *46*, 7704-7706.

97. Scheibel, M. G.; Askevold, B.; Heinemann, F. W.; Reijerse, E. J.; de Bruin, B.; Schneider, S., *Nat. Chem.* **2012,** *4*, 552-558.

98. Lindley, B. M.; van Alten, R. S.; Finger, M.; Schendzielorz, F.; Würtele, C.; Miller, A. J. M.; Siewert, I.; Schneider, S., *J. Am. Chem. Soc.* **2018,** *140*, 7922-7935.

99. Christian, G.; Stranger, R.; Yates, B. F., *Chem. - Eur. J.* **2009,** *15*, 646-655.

100. van Alten, R. S.; Wätjen, F.; Demeshko, S.; Miller, A. J. M.; Würtele, C.; Siewert, I.; Schneider, S., *Eur. J. Inorg. Chem.* **2020,** *15*, 1402-1410.

101. Curley, J. J.; Cook, T. R.; Reece, S. Y.; Muller, P.; Cummins, C. C., *J. Am. Chem. Soc.* **2008,** *130*, 9394-9405.

102. Klopsch, I.; Yuzik-Klimova, E. Y.; Schneider, S., Functionalization of N2 by Mid to Late Transition Metals via N–N Bond Cleavage. In *Nitrogen Fixation*, Nishibayashi, Y., Ed. Springer International Publishing: Cham, 2017; pp 71-112.

103. Cui, Q.; Musaev, D. G.; Svensson, M.; Sieber, S.; Morokuma, K., *J. Am. Chem. Soc.* **1995,** *117*, 12366-7.

104. Cherry, J.-P. F.; Johnson, A. R.; Baraldo, L. M.; Tsai, Y.-C.; Cummins, C. C.; Kryatov, S. V.; Rybak-Akimova, E. V.; Capps, K. B.; Hoff, C. D.; Haar, C. M.; Nolan, S. P., *J. Am. Chem. Soc.* **2001,** *123*, 7271-7286.

105. Mindiola, D. J.; Meyer, K.; Cherry, J.-P. F.; Baker, T. A.; Cummins, C. C., *Organomet.* **2000,** *19*, 1622-1624.

106. Shih, K.-Y.; Schrock, R. R.; Kempe, R., *J. Am. Chem. Soc.* **1994,** *116*, 8804-8805.

107. Solari, E.; Da Silva, C.; Iacono, B.; Hesschenbrouck, J.; Rizzoli, C.; Scopelliti, R.; Floriani, C., *Angew. Chem., Int. Ed.* **2001,** *40*, 3907-3909.

108. Tolmachev, Y. V.; Vorotyntsev, M. A., *Russ. J. Electrochem.* **2014,** *50*, 403-411.

109. Kuang, M.; Wang, Y.; Fang, W.; Tan, H.; Chen, M.; Yao, J.; Liu, C.; Xu, J.; Zhou, K.; Yan, Q., *Adv. Mater.* **2020,** *32*, 2002189.

110. Dai, C.; Sun, Y.; Chen, G.; Fisher, A. C.; Xu, Z. J., *Angew. Chem., Int. Ed.* **2020,** *59*, 9418-9422.

111. Bartholomew, C. H. F., Robert J., Catalytic Oxidations of Inorganic and Organic Compounds. In *Fundamentals of Industrial Catalytic Processes*, Wiley: 2006; pp 560-634.

112. Keane, A. J.; Farrell, W. S.; Yonke, B. L.; Zavalij, P. Y.; Sita, L. R., *Angew. Chem., Int. Ed.* **2015,** *54*, 10220-10224.

113. Abbenseth, J.; Finger, M.; Wuertele, C.; Kasanmascheff, M.; Schneider, S., *Inorg. Chem. Front.* **2016,** *3*, 469-477.

114. Keener, M.; Peterson, M.; Hernandez Sanchez, R.; Oswald, V. F.; Wu, G.; Menard, G., *Chem. - Eur. J.* **2017,** *23*, 11479-11484.

115. Berry, J. F., *Comments Inorg. Chem.* **2009,** *30*, 28-66.

116. Smith, J. M., *Prog. Inorg. Chem.* **2014,** *58*, 417-470.

117. Dehnicke, K.; Strähle, J., *Angew. Chem., Intern. Ed.* **1981,** *20*, 413-426.

118. Dehnicke, K.; Strähle, J., *Angew. Chem., Int. Ed.* **1992,** *31*, 955-978.

119. Eikey, R. A.; Abu-Omar, M. M., *Coord. Chem. Rev.* **2003,** *243*, 83-124.

120. Kim, J. C.; Lee, B. M.; Shin, J. I., *Polyhedron* **1995,** *14*, 2145-9.

121. Schendzielorz, F. S.; Finger, M.; Volkmann, C.; Wurtele, C.; Schneider, S., *Angew. Chem., Int. Ed.* **2016,** *55*, 11417-20.

122. Askevold, B.; Nieto, J. T.; Tussupbayev, S.; Diefenbach, M.; Herdtweck, E.; Holthausen, M. C.; Schneider, S., *Nat. Chem.* **2011,** *3*, 532-537.

123. Lindley, B. M.; Bruch, Q. J.; White, P. S.; Hasanayn, F.; Miller, A. J. M., *J. Am. Chem. Soc.* **2017,** *139*, 5305-5308.

124. Warren, J. J.; Tronic, T. A.; Mayer, J. M., *Chem. Rev.* **2010,** *110*, 6961-7001.

125. Bezdek, M. J.; Pappas, I.; Chirik, P. J., Determining and Understanding N-H Bond Strengths in Synthetic Nitrogen Fixation Cycles. In *Nitrogen Fixation*, Nishibayashi, Y., Ed. Springer International Publishing: Cham, 2017; pp 1-21.

126. Tshepelevitsh, S.; Kütt, A.; Lõkov, M.; Kaljurand, I.; Saame, J.; Heering, A.; Plieger, P. G.; Vianello, R.; Leito, I., *Eur. J. Org. Chem.* **2019,** *2019*, 6735-6748.

127. McCarthy, B. D.; Martin, D. J.; Rountree, E. S.; Ullman, A. C.; Dempsey, J. L., *Inorg. Chem.* **2014,** *53*, 8350-8361.

128. Bezdek, M. J.; Guo, S.; Chirik, P. J., *Science* **2016,** *354*, 730-733.

129. Wang, D.; Loose, F.; Chirik, P. J.; Knowles, R. R., *J. Am. Chem. Soc.* **2019,** *141*, 4795-4799.

130. Matson, B. D.; Peters, J. C., *ACS Catal.* **2018,** *8*, 1448-1455.

131. Wise, C. F.; Agarwal, R. G.; Mayer, J. M., *J. Am. Chem. Soc.* **2020,** *142*, 10681-10691.

132. Gansaeuer, A.; Behlendorf, M.; Cangoenuel, A.; Kube, C.; Cuerva, J. M.; Friedrich, J.; van Gastel, M., *Angew. Chem., Int. Ed.* **2012,** *51*, 3266-3270.

133. Scheibel, M. G.; Abbenseth, J.; Kinauer, M.; Heinemann, F. W.; Wuertele, C.; de Bruin, B.; Schneider, S., *Inorg. Chem.* **2015,** *54*, 9290-9302.

134. Scepaniak, J. J.; Young, J. A.; Bontchev, R. P.; Smith, J. M., *Angew. Chem., Int. Ed.* **2009,** *48*, 3158-3160.

135. Cheng, J.-P.; Lu, Y.; Zhu, X.-Q.; Sun, Y.; Bi, F.; He, J., *J. Org. Chem.* **2000,** *65*, 3853-3857.

136. Connelly, N. G.; Geiger, W. E., *Chem. Rev.* **1996,** *96*, 877-910.

137. Chalkley, M. J.; Del Castillo, T. J.; Matson, B. D.; Peters, J. C., *J. Am. Chem. Soc.* **2018,** *140*, 6122-6129.

138. Chalkley, M. J.; Oyala, P. H.; Peters, J. C., *J. Am. Chem. Soc.* **2019,** *141*, 4721-4729.

139. Wickramasinghe, L. A.; Ogawa, T.; Schrock, R. R.; Muller, P., *J. Am. Chem. Soc.* **2017,** *139*, 9132-9135.

140. Loose, F.; Wang, D.; Tian, L.; Scholes, G. D.; Knowles, R. R.; Chirik, P. J., *Chem. Commun.* **2019,** *55*, 5595-5598.

141. Kamochi, Y.; Kudo, T., *Chem. Lett.* **1993,** *22*, 1495-1498.

142. Chciuk, T. V.; Anderson, W. R.; Flowers, R. A., *J. Am. Chem. Soc.* **2016,** *138*, 8738-8741.

143. Kolmar, S. S.; Mayer, J. M., *J. Am. Chem. Soc.* **2017,** *139*, 10687-10692.

144. Chciuk, T. V.; Anderson, W. R.; Flowers, R. A., *J. Am. Chem. Soc.* **2018,** *140*, 15342-15352.

145. Margulieux, G. W.; Bezdek, M. J.; Turner, Z. R.; Chirik, P. J., *J. Am. Chem. Soc.* **2017,** *139*, 6110-6113.

146. Teprovich, J. A., Jr.; Balili, M. N.; Pintauer, T.; Flowers, R. A., II, *Angew. Chem., Int. Ed.* **2007,** *46*, 8160-8163.

147. Mayer, J. M., *Acc. Chem. Res.* **2011,** *44*, 36-46.

148. Nesbit, M. A.; Oyala, P. H.; Peters, J. C., *J. Am. Chem. Soc.* **2019,** *141*, 8116-8127.

149. Thompson, N. B.; Oyala, P. H.; Dong, H. T.; Chalkley, M. J.; Zhao, J.; Alp, E. E.; Hu, M.; Lehnert, N.; Peters, J. C., *Inorg. Chem.* **2019,** *58*, 3535-3549.

150. Weinberg, D. R.; Gagliardi, C. J.; Hull, J. F.; Murphy, C. F.; Kent, C. A.; Westlake, B. C.; Paul, A.; Ess, D. H.; McCafferty, D. G.; Meyer, T. J., *Chem. Rev.* **2012,** *112*, 4016-4093.

151. Costentin, C.; Robert, M.; Savéant, J.-M., *Chem. Rev.* **2010,** *110*, PR1-PR40.

152. Munisamy, T.; Schrock, R. R., *Dalton Trans.* **2012,** *41*, 130-137.

153. Kunkely, H.; Vogler, A., *Angew. Chem., Int. Ed.* **2010,** *49*, 1591-1593.

154. Rebreyend, C.; de Bruin, B., *Angew. Chem., Int. Ed.* **2015,** *54*, 42-44.

155. Hoenes, R.; Kuss-Petermann, M.; Wenger, O. S., *Photochem. Photobiol. Sci.* **2013,** *12*, 254-261.

156. Pannwitz, A.; Wenger, O. S., *Phys. Chem. Chem. Phys.* **2016,** *18*, 11374-82.

157. Pannwitz, A.; Prescimone, A.; Wenger, O. S., *Eur. J. Inorg. Chem.* **2017,** *2017*, 609-615.

158. Paradas, M.; Campana, A. G.; Jimenez, T.; Robles, R.; Oltra, J. E.; Bunuel, E.; Justicia, J.; Cardenas, D. J.; Cuerva, J. M., *J. Am. Chem. Soc.* **2010,** *132*, 12748-12756.

159. Huynh, M. T.; Anson, C. W.; Cavell, A. C.; Stahl, S. S.; Hammes-Schiffer, S., *J. Am. Chem. Soc.* **2016,** *138*, 15903-15910.

160. Nutting, J. E.; Rafiee, M.; Stahl, S. S., *Chem. Rev.* **2018,** *118*, 4834-4885.

161. Francke, R.; Little, R. D., *Chem. Soc. Rev.* **2014,** *43*, 2492-2521.

162. Chalkley, M. J.; Garrido-Barros, P.; Peters, J. C., *Science* **2020,** *369*, 850.

163. Sun, L.; Sahloul, K.; Mellah, M., *ACS Catal.* **2013,** *3*, 2568-2573.

164. Maity, S.; Flowers, R. A., *J. Am. Chem. Soc.* **2019,** *141*, 3207-3216.

2 Protonation and Electrochemical Reduction of Rhodium- and Iridium-dinitrogen Complexes in Organic Solution

This chapter is reproduced from Connor, G. P.; Lease, N.; Casuras, A.; Goldman, A. S.; Holland, P. L.; Mayer, J. M. *Dalton Trans.* **2017**, 46, 14325-14330. *NL and AS synthesized (PCP)Rh(N_2) and (PCP)IrH_2, and ASG provided helpful feedback and guidance for the project.*

2.1 Introduction

Large-scale processes for the conversion of N_2 to NH_3 involve hydride species. This is true for both the industrial Haber-Bosch process, where H_2 is readily dissociated on Fe and Ru surfaces,[1] and for the enzyme nitrogenase, where the mechanism involves hydride species that release H_2 only in the presence of N_2.[2] In contrast, homogeneous systems that reduce N_2 through an associative stepwise Chatt-like mechanism[3] often invoke high-energy intermediates such as metal-diazenido and hydrazido species.[4] Proton-coupled electrochemical N_2 reduction, in which varying the potential could overcome the high energetic barrier to formation of these intermediates, is an attractive goal for these systems.[5] To this end, advances have been made in both heterogeneous electrocatalytic N_2 reduction[6-9] and stoichiometric electrochemical N_2 reduction using molecular complexes,[10, 11] but these systems require highly reducing potentials and suffer from low efficiency. Additionally, while the conversion of N_2 to NH_3 via tandem protonation and reduction with transition-metal complexes has been extensively studied using chemical reductants, only a few studies explore the ability to electrochemically achieve this reaction.[12, 13]

One key to the success of electrochemical N_2 reduction is the regioselectivity of protonation, which can occur at the metal center to form a metal-hydride or at the distal nitrogen atom of the N_2 ligand to form a metal-diazenido complex. Under reducing and

acidic conditions, hydride formation is typically detrimental because it leads to diversion of electrons to H_2 rather than NH_3.[4] Therefore, regioselectivity of protonation may be particularly important in determining the overall selectivity of products for systems that can achieve proton-coupled electroreduction of N_2. We saw a special opportunity in studying the protonation and electrochemical reduction of rhodium(I) (**1**) and iridium(I) (**2**) pincer complexes that are known to bind N_2 under an atmosphere of N_2 (**Scheme 2.1**).[14] The corresponding hydride complexes (PCP)RhH_2 and (PCP)IrH_2 (PCP = 2,6-$(CH_2P^tBu_2)_2C_6H_3$) are both well-studied, and **2** forms slowly from disproportionation of (PCP)IrH_2 under N_2.[14-16] Their strong affinity for N_2[16, 17] inspired us to explore the ability of **1** and **2** to electrochemically reduce N_2 under acidic conditions. Since these complexes form both hydrides and N_2 adducts, they are especially well-suited to study N_2- vs. metal-centered reactivity in the context of electrochemical N_2 reduction.

Scheme 2.1: Structures of complexes **1** and **2**.

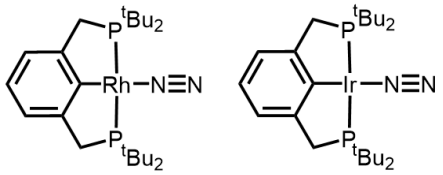

2.2 Results and Discussion

2.2.1. Protonation Studies

1 and **2** contain N_2 ligands with N-N stretching frequencies (ν_{NN}) of 2125 and 2078 cm^{-1}, respectively,[17] indicating very little activation of the N_2 ligands. To assess the regioselectivity of protonation, the reaction of **1** with 1 equiv of trifluoroacetic acid (TFA) under N_2 was monitored by ^1H and $^{31}P\{^1H\}$ NMR spectroscopies. The resulting spectra

show immediate and quantitative conversion to a new diamagnetic product. The formation of a rhodium-hydride complex (**1a**) was evident from a ^{1}H resonance with δ –25.6 ppm that appeared as a doublet of triplets ($^{1}J_{Rh,H}$ = 45.4, $^{2}J_{P,H}$ = 11.8 Hz), indicating initial metal-centered reactivity. Splitting of the methylene and ^{t}Bu resonances indicated the loss of C_{2v} symmetry, suggesting the formation of a five- or six-coordinate C_s-symmetric complex upon protonation. Binding of trifluoroacetate to **1a** was confirmed by the characteristic shift of ^{19}F NMR resonances.[29]

The formation of this product implies that N_2 could be displaced by trifluoroacetate upon protonation. The lability of the N_2 ligand upon protonation was tested by deprotonating **1a** with 1 equiv of 1,8-diazabicyclo[5.4.0]undec-7-ene (DBU) under N_2 and Ar while monitoring by ^{31}P{^{1}H} NMR spectroscopy. Under N_2, treatment of **1a** with DBU afforded **1** quantitatively, indicating a reversible protonation (**Figure 2.1A**). In contrast, treatment of **1a** with DBU under Ar gave only 4% reversion to **1**, indicating that N_2 was lost upon protonation of **1** with TFA (**Figure 2.1B**). Therefore, we assign **1a** as (PCP)Rh(H)(O_2CCF_3) (**Scheme 2.2**).

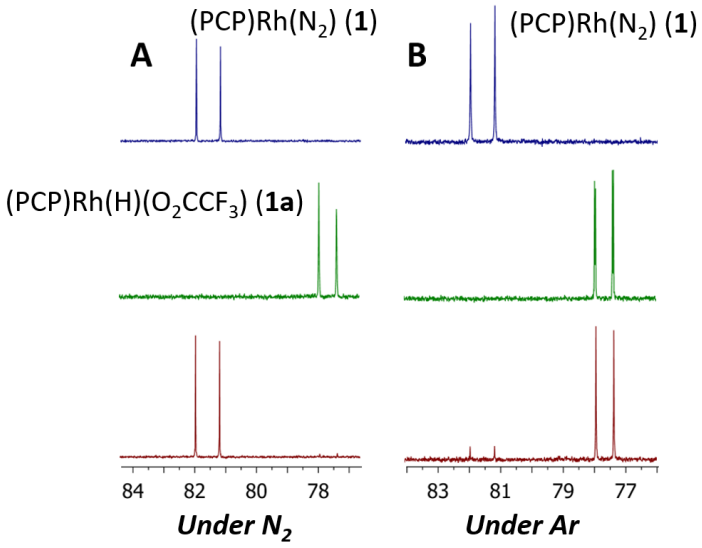

Figure 2.1: $^{31}P\{^{1}H\}$ NMR spectra of **1** (blue) upon protonation with TFA (green) in THF-d_8 and subsequent deprotonation with DBU (red) under N_2 (**A**) and under Ar (**B**) demonstrating reversible protonation under N_2 but no reversion to **1** under Ar.

Scheme 2.2: Protonation of **1** with stoichiometric acids in THF-d_8 at 25 °C.

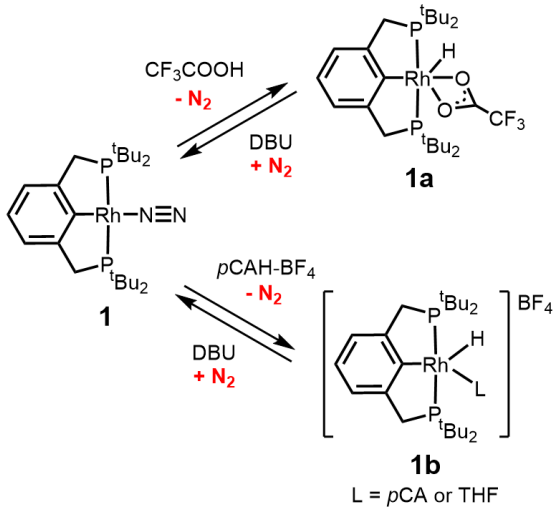

Considering that N_2 is both a poor σ-donor and π-acceptor ligand, and that late group transition metals such as Rh and Ir contain relatively low energy *d*-orbitals for *d*-π* backdonation, loss of N_2 upon protonation at the metal center of **1** is unsurprising. Protonation and oxidation of the metal centers of terminal N_2 complexes has long been identified as a roadblock to N_2 functionalization since it reduces the ability of the metal

complex to stabilize bound N_2.[18, 19] Despite this general trend in reactivity, there have been recent cases in which protonation of a terminal N_2 complex forms relatively stable metal-hydride species that retain N_2.[11, 20-22] These metal-hydride complexes are only able to coordinate N_2 at low temperatures; however, in some cases the addition of excess strong acid results in the generation of substoichiometric NH_4^+.[21, 22] Thus, formation of a metal-hydride complex that binds N_2 could still potentially lead to N_2 reduction under acidic and sufficiently reducing conditions. For example, Del Castillo *et al.* reported an off-cycle intermediate that contains a metal-hydride with bound N_2 in the catalytic reduction of N_2 to NH_3 by a tris(phosphino)borane supported iron complex.[11] The hydride complex is hypothesized to eliminate an equivalent of H_2 to return to the catalytic cycle. Relevantly, this iron system is also capable of generating at least 2 equiv of NH_3 from electrochemical reduction in the presence of strong acid.

We were thus interested in preventing N_2 loss upon protonation of **1** in the hopes of forming a metal-hydride with bound N_2, such as the mono-hydride iridium-N_2 complex reported by Millard *et al*.[23] To avoid the displacement of N_2 by trifluoroacetate, other acids with neutral, relatively non-coordinating, and sterically bulky conjugate-bases were employed. Upon protonation with *p*-chloroanilinium tetrafluoroborate (*p*CAH-BF_4) in THF, **1** converts to a new complex **1b** by NMR spectroscopy, which exhibits C_s symmetry and a hydride resonance at δ –26.5 ppm as a broadened doublet. As with **1a**, protonation with *p*CAH-BF_4 is reversible under N_2; however, treating **1b** with 1 equiv DBU under Ar gives very low conversion to **1**, again indicating that the N_2 ligand is lost upon protonation. Broadening of the hydride resonance in the ^{1}H NMR spectrum and phosphine resonance in

the $^{31}P\{^{1}H\}$ NMR spectrum suggests dynamic exchange of bound ligands, likely THF and/or *p*CA.

In analogy to the protonation studies with **1**, addition of 1 equiv of *N,N*-dimethylanilinium tetrafluoroborate (DMAH-BF_4) to the iridium-N_2 complex **2** shows clean conversion to a new diamagnetic C_s-symmetric complex **2a** by ^{1}H NMR spectroscopy. Curiously, neither the phosphine resonance nor any hydride resonance were resolved at ambient temperature in the $^{31}P\{^{1}H\}$ or ^{1}H NMR spectra. However, upon cooling the sample to –40 °C in THF-d_8, a broad singlet appeared in the $^{31}P\{^{1}H\}$ NMR spectrum at δ 69.2 ppm. The resonance sharpens and shifts upfield as temperature is decreased from 0 to –40 °C, but does not decoalesce. This implies two temperature-dependent processes, likely a fluxional exchange of ligands resulting in peak broadening as well as a temperature-dependent equilibrium favoring a single species at –40 °C. Additionally, a hydride resonance was visible in the ^{1}H NMR spectrum at δ –36.7 ppm. The hydride resonance sharpens and shifts downfield as the temperature is decreased from 0 to –40 °C, which suggests binding of a weak donor ligand (such as additional solvent) *trans* to the hydride at low temperature.[24-26] The shift of the hydride resonance as temperature is decreased supports the possibility of a temperature-dependent equilibrium that could favor a six-coordinate species at lower temperatures.

While protonation of **2** with DMAH-BF_4 was reversible at ambient conditions under N_2 upon the addition of 1 equiv DBU, adding 1 equiv of DBU to **2a** under Ar resulted in the formation of several uncharacterized products but no reversion to **2**. This suggests that **2a** does not contain N_2, leading us to conclude that protonation of **2** with DMAH-BF_4 forms the cationic Ir^{3+} complex $[(PCP)Ir(H)(THF)]^{+}$ (see **Scheme 2.3**).[27] When the sample

was spiked with excess pyridine-d_5, the hydride resonance in the ^{1}H NMR spectrum shifted to δ –22.8 ppm, and the phosphine resonance in the ^{31}P{^{1}H} spectrum shifted to δ 46.5 ppm. This is consistent with the previously reported behavior of [(PCP)Ir(H)(THF)]$^+$ in the presence of excess pyridine.[28] The loss of N_2 from **2** upon protonation with DMAH-BF_4 was confirmed by the solid-state IR spectrum of **2a**, isolated as a crude solid with DMA, which shows no N–N stretch.

The spectroscopic data monitoring protonation of **1** and **2** indicate a clear pattern of regioselectivity, as protonation occurs at the metal center rather than at an N_2 ligand in all cases. While formation of metal-hydride species does not prevent N_2 reduction in large-scale NH_3 generating processes, in this system N_2 is lost upon formation of the cationic Rh^{III}/Ir^{III}-hydride species even when using acids with sterically encumbered, non-coordinating conjugate-bases. These results suggest that, upon protonation, these metal centers are no longer electron-rich enough to stabilize bound N_2 through *d*-π* back-bonding interactions.

2.2.2. Electrochemical reduction

Having concluded that functionalization of bound N_2 via initial protonation is prevented by the formation of metal-hydrides resulting in the loss of the N_2 ligand, we next explored whether reduction of **1** and **2** could facilitate N_2-centered reactivity. Cyclic voltammetry (CV) of **1** and **2** in THF showed no reduction of either complex within the solvent window. The inability to reduce these complexes even at –3.4 V vs. ferrocene ($Fc^{+/0}$) demonstrates that **1** and **2** are quite electron-rich, which is likely key to the high stability of the Rh^I/Ir^I-N_2 adducts.

In contrast, CV of a solution containing **1** with 1 equiv TFA showed an irreversible reduction event at E_{pc} = –2.63 V vs. $Fc^{+/0}$ (**Figure 2.2**, blue). Considering the spectroscopic data discussed previously, this event likely corresponds to the reduction of the protonated **1a**. In an analogous experiment, CV of a solution of equimolar **2** and TFA showed an irreversible reduction event at E_{pc} = –2.42 V vs. $Fc^{+/0}$ (**Figure 2.2**, red). Integration of these irreversible reduction events against a Fc internal standard suggest that these are one-electron reductions with pre-wave features arising from background reduction of TFA at the working electrode. Additional equivalents of TFA increased the reductive current at E_{pc}, and catalytic waves were observed with a large excess of TFA.[29] These catalytic current enhancements imply that **1** and **2** are pre-catalysts for electrocatalytic proton reduction, but we did not further investigate their catalytic capabilities due to the high overpotentials and modest peak currents of these features. The current enhancement is unlikely to be attributable to the generation of a reduced N_2 species, considering that N_2 is lost upon formation of **1a**. Consequently, the observation of catalytic current passed in the presence of excess acid supports the general notion that protonation at the metal center can facilitate the undesired diversion of electrons to produce H_2.

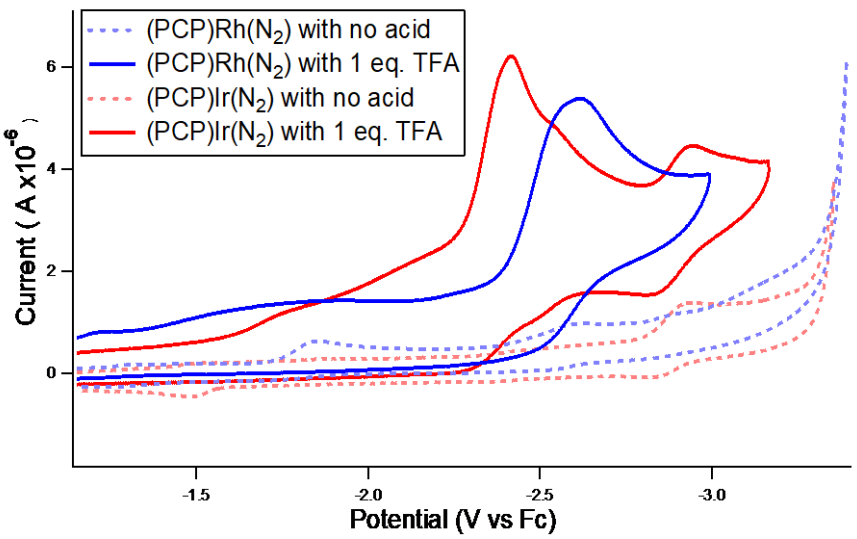

Figure 2.2: Cyclic voltammograms of **1** (blue) and **2** (red) before and after addition of 1 equiv TFA. The sub-stoichiometric feature in the absence of acid is due to a small impurity. Scans were taken at a scan rate of 50 mV/s with a glassy carbon working electrode, Pt wire auxiliary electrode, and Ag wire psuedoreference in THF with 0.1 M TBA-PF_6.

We considered the possibility that reduction of an Ir^{III}-hydride complex by one electron could result in N_2 binding to the more electron-rich metal center. To this end, we hoped to generate a metal-hydride complex that could bind N_2 upon electroreduction by replacing TFA with an acid featuring a non-coordinating conjugate base. CV of **2** in the presence of 1 equiv DMAH-BF_4 in THF showed that the protonated complex **2a** is irreversibly reduced by one electron with E_{pc} = –1.82 V vs. $Fc^{+/0}$. This irreversible reduction occurs at a significantly less cathodic potential than the irreversible reductions of **1** and **2** in the presence of TFA, likely because **2a** is cationic and is ligated by THF, a weaker donor than trifluoroacetate. Several additional substoichiometric reductions occur at more reducing potentials, including a reversible reduction occurring with $E_{1/2}$ = –2.89 V vs. $Fc^{+/0}$. The observation of an irreversible reduction feature is consistent with formation of one or more new products upon electroreduction; however, the nature of these products could not be determined.

2.2.3. Chemical protonation and reduction

To characterize the processes that occur following the electrochemical reduction of **2a**, the chemical reduction of **2a** was monitored by NMR spectroscopy (**Figure 2.3**). Mixing **2a** with 1.1 equiv of decamethylcobaltocene (Cp^*_2Co) in THF at ambient temperature results in immediate change of the brown Cp^*_2Co solution to orange, as well as formation of $[Cp^*_2Co][BF_4]$ as a yellow precipitate. Despite the addition of only one equivalent of reductant, diamagnetic products were observed by ^1H and $^{31}P\{^1H\}$ NMR spectroscopy, accounting for ~90% of the expected phosphorus signal intensity versus a capillary standard. The products were identified as a mixture of **2** and the known complexes (PCP)IrH_2 and (PCP)IrH_4 by their characteristic ^{31}P and ^1H hydride resonances.[14, 30] After 1 week under N_2 at ambient temperature, the (PCP)IrH_2 quantitatively converts to **2** and (PCP)IrH_4, according to the $^{31}P\{^1H\}$ NMR spectra. The fast formation of **2**, (PCP)IrH_2, and (PCP)IrH_4 implies that an Ir^{II} species formed upon reduction quickly disproportionates rather than bind N_2. The intermediate is likely an Ir^{II}-monohydride species (**Scheme 2.3**), which could disproportionate into (PCP)IrH_2 and a 14-electron (PCP)Ir^I species that is trapped by N_2 to regenerate **2**. Similar disproportionation reactivity has been reported upon electrochemical $1e^-$ oxidation of Ir/Rh^I-hydrides.[31] Ir^{II} species are typically stable only when they are dimers,[32-37] although a few Ir^{II} complexes employing bulky ligands have been characterized.[38-42] In this case, the transient Ir^{II} complex is likely not stable enough to form a N_2-ligated monohydride complex that could mediate N_2 reduction, or such a species is too short lived to perform further N_2 reduction.

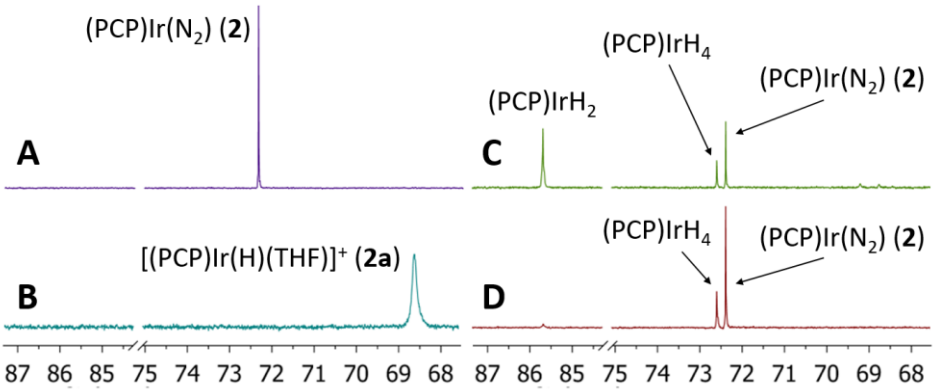

Figure 2.3: $^{31}P\{^{1}H\}$ NMR spectra of **2** (**A**) upon protonation with DMAH-BF_4 (**B**, spectrum at –40 °C) in THF-d_8, subsequent reduction with Cp^*_2Co (**C**), and 1 week after reduction with Cp^*_2Co (**D**).

Scheme 2.3: Stepwise protonation of **2** and reduction of **2a** in THF-d_8 at 25 °C followed by disproportionation to generate $(PCP)Ir(H)_2$, $(PCP)Ir(H)_4$, and **2**.

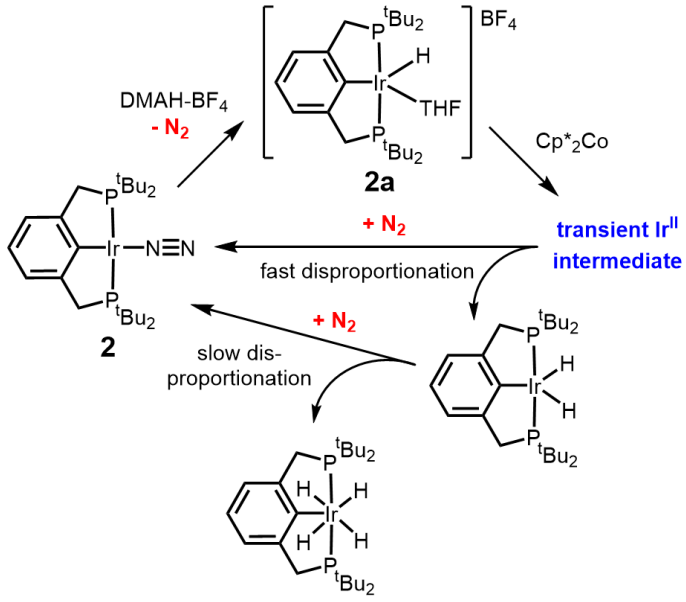

2.3 Conclusions

In summary, protonation of **1** and **2** with various acids and subsequent reduction does not lead to N_2-centered reactivity. The electron-rich nature of **1** and **2** that leads to their high affinity for N_2 also promotes metal-centered protonation to form metal-hydride

species. The formation of a metal-hydride results in the loss of N_2 from the metal center in all cases. N_2 is displaced from the cationic hydride complexes even by weak donor ligands such as THF, which is evident by formation of **2a**. The greater favorability of metal-center-based reactivity for **1** and **2** is further evident by the electrocatalytic hydrogen production observed in high concentrations of TFA. Additionally, reduction of **2a** in an effort to generate an electron-rich metal center that could bind N_2 results in disproportionation of a putative Ir^{II} species instead.

In these systems, the regioselectivity of protonation is a critical determinant of the ability for **1** and **2** to electrochemically reduce N_2. Specifically, the formation of metal-hydride complexes that cannot coordinate N_2 at ambient temperature prevents any subsequent N_2 functionalization. These results highlight two important reasons why preventing protonation of the metal center presents an important challenge in achieving the electrochemical reduction of N_2: a) formation of a metal-hydride in protic conditions can lead to loss of N_2, and b) metal-centered reactivity can heavily favor proton reduction over N_2 reduction even in systems that appear to strongly bind N_2.

2.4 Experimental

2.4.1. Materials and syntheses

All manipulations were conducted under an air- and moisture-free environment in an argon-filled M. Braun glovebox or a N_2-filled M. Braun glovebox. Tetrahydrofuran (THF) was distilled under N_2 from potassium and stored over molecular sieves prior to use. THF-d_8 was degassed and dried with calcium hydride then potassium benzophenone before storing over molecular sieves prior to use. Trifluoroacetic acid (TFA, Sigma-Aldrich), tert-butylethylene (TBE, Sigma-Aldrich), and 1,8-diazabicyclo[5.4.0]undec-7-ene (DBU, Alfa Aesar) were distilled under N_2 prior to use. (PCP)Rh(N_2) (**1**) and acids *p*-chloroanilinium tetrafluoroborate (*p*CAH-BF_4) and *N,N*-dimethylanilinium tetrafluoroborate (DMAH-BF_4) were prepared according to literature procedures.[43, 44]

Preparation of (PCP)Ir(N_2) (2): (PCP)Ir(N_2) (**2**) was prepared using a modified literature procedure.[16, 17] In a N_2-glovebox, 45.7 mg (PCP)IrH_2 (7.77 x 10^{-5} mol) was dissolved in 5 mL toluene to give a red-orange solution. 5 equiv TBE (0.05 mL, 4 x 10^{-4} mol) was added to the solution via syringe. The reaction was stirred at ambient temperature for 15 hours, at which point it had turned an orange color. The solvent was removed under vacuum, and 2 was extracted with 3 x 3 mL pentane. Removal of the solvent under vacuum from the combined extracts gave an orange solid (43.0 mg, 7.00 x 10^{-5} mol, 90% yield). ^{1}H NMR (500 MHz, THF-d_8, **2**): δ 6.83 (d, $^3J_{H,H}$ = 7.4 Hz, 2H, *m*-Ph), 6.54 (t, $^3J_{H,H}$ = 7.4 Hz, 1H, *p*-Ph), 3.25 (m, 4H, CH_2), 1.33 (m, $^2J_{P,H}$ = 6.4 Hz, 36H, C(CH_3)$_3$). ^{31}P NMR (202 MHz, THF-d_8**, 2**): δ 72.80 (s).

2.4.2. Methods and instrumentation

NMR spectra were obtained using an Agilent 400 MHz or 500 MHz spectrometer. ^{1}H NMR spectra were referenced to residual ^{1}H signals from THF-d_8, and ^{31}P{^{1}H} NMR spectra were referenced to PMe_3 (s, δ –62.44) in a capillary tube. IR spectra were obtained using a Bruker Alpha spectrometer fitted with a diamond ATR (attenuated total reflection) unit. Electrochemical measurements were collected using a CH Instruments 600D potentiostat in a N_2-filled M. Braun glovebox. Cyclic voltammetry (CV) experiments were conducted in 0.1 M tetrabutylammonium-hexafluorophosphate (TBA-PF_6) solution in THF with a glassy carbon disc working electrode (3.0 mm diameter), platinum wire auxiliary electrode, and silver wire psuedoreference electrode. Wire electrodes were cleaned using fine sandpaper and rinsed with THF prior to use. Glassy carbon disc electrodes were polished with 0.05 μm alumina powder and rinsed with THF prior to use. CV experiments were referenced to stoichiometric ferrocene from a 0.015 M stock solution in THF as an internal standard after completion.

2.5 References

1. Jennings, J. R.; Editor, *Catalytic Ammonia Synthesis. Fundamentals and Practice*. Plenum: 1991.

2. Lukoyanov, D.; Khadka, N.; Yang, Z.-Y.; Dean, D. R.; Seefeldt, L. C.; Hoffman, B. M., *J. Am. Chem. Soc.* **2016,** *138*, 10674-10683.

3. Schrock, R. R., *Acc. Chem. Res.* **2005,** *38*, 955-962.

4. van der Ham, C. J. M.; Koper, M. T. M.; Hetterscheid, D. G. H., *Chem. Soc. Rev.* **2014,** *43*, 5183-5191.

5. Lindley, B. M.; Appel, A. M.; Krogh-Jespersen, K.; Mayer, J. M.; Miller, A. J. M., *ACS Energy Lett.* **2016,** *1*, 698-704.

6. Licht, S.; Cui, B.; Wang, B.; Li, F.-F.; Lau, J.; Liu, S., *Science* **2014,** *345*, 637-640.

7. Kordali, V.; Kyriacou, G.; Lambrou, C., *Chem. Commun.* **2000**, 1673-1674.

8. Furuya, N.; Yoshiba, H., *J. Electroanal. Chem. Interfac. Electrochem.* **1989,** *263*, 171-174.

9. Pospisil, L.; Bulickova, J.; Hromadova, M.; Gal, M.; Civis, S.; Cihelka, J.; Tarabek, J., *Chem. Commun.* **2007**, 2270-2272.

10. Pickett, C. J.; Talarmin, J., *Nature* **1985,** *317*, 652-653.

11. Del Castillo, T. J.; Thompson, N. B.; Peters, J. C., *J. Am. Chem. Soc.* **2016,** *138*, 5341-5350.

12. Pickett, C. J.; Ryder, K. S.; Talarmin, J., *J. Chem. Soc., Dalton Trans.* **1986**, 1453-1457.

13. Munisamy, T.; Schrock, R. R., *Dalton Trans.* **2012,** *41*, 130-137.

14. Gupta, M.; Hagen, C.; Flesher, R. J.; Kaska, W. C.; Jensen, C. M., *Chem. Commun.* **1996**, 2083-2084.

15. Gupta, M.; Kaska, W. C.; Jensen, C. M., *Chem. Commun.* **1997**, 461-462.

16. Lee, D. W.; Kaska, W. C.; Jensen, C. M., *Organometallics* **1998,** *17*, 1-3.

17. Ghosh, R.; Kanzelberger, M.; Emge, T. J.; Hall, G. S.; Goldman, A. S., *Organometallics* **2006,** *25*, 5668-5671.

18. Chatt, J.; Leigh, G. J., *Chem. Soc. Rev.* **1972,** *1*, 121-144.

19. Hidai, M.; Mizobe, Y. In *Reactions of Coordinated Dinitrogen and Related Species*, 1989; Plenum: 1989; pp 53-114.

20. Heiden, Z. M.; Chen, S.; Mock, M. T.; Dougherty, W. G.; Kassel, W. S.; Rousseau, R.; Bullock, R. M., *Inorg. Chem.* **2013,** *52*, 4026-4039.

21. Weiss, C. J.; Egbert, J. D.; Chen, S.; Helm, M. L.; Bullock, R. M.; Mock, M. T., *Organometallics* **2014,** *33*, 2189-2200.

22. Mock, M. T.; Pierpont, A. W.; Egbert, J. D.; O'Hagan, M.; Chen, S.; Bullock, R. M.; Dougherty, W. G.; Kassel, W. S.; Rousseau, R., *Inorg. Chem.* **2015,** *54*, 4827-4839.

23. Millard, M. D.; Moore, C. E.; Rheingold, A. L.; Figueroa, J. S., *J. Am. Chem. Soc.* **2010,** *132*, 8921-8923.

24. Cooper, A. C.; Streib, W. E.; Eisenstein, O.; Caulton, K. G., *J. Am. Chem. Soc.* **1997,** *119*, 9069-9070.

25. Zhang, X.; Kanzelberger, M.; Emge, T. J.; Goldman, A. S., *J. Am. Chem. Soc.* **2004,** *126*, 13192-13193.

26. Titova, E. M.; Silantyev, G. A.; Filippov, O. A.; Gulyaeva, E. S.; Gutsul, E. I.; Dolgushin, F. M.; Belkova, N. V., *Eur. J. Inorg. Chem.* **2016,** *2016*, 56-63.

27. Walden, A. G.; Kumar, A.; Lease, N.; Goldman, A. S.; Miller, A. J., *Dalton Trans.* **2016,** *45*, 9766-9769.

28. Walden, A. G. *Oxidative Electrochemistry of Molecular Catalysts*. Thesis, **2016**, University of North Carolina, Chapel Hill.

29. Connor, G. P.; Lease, N.; Casuras, A.; Goldman, A. S.; Holland, P. L.; Mayer, J. M., *Dalton Trans.* **2017,** *46*, 14325-14330.

30. Hebden, T. J.; Goldberg, K. I.; Heinekey, D. M.; Zhang, X.; Emge, T. J.; Goldman, A. S.; Krogh-Jespersen, K., *Inorg. Chem.* **2010,** *49*, 1733-1742.

31. Pilloni, G.; Schiavon, G.; Zotti, G.; Zecchin, S., *J. Organomet. Chem.* **1977,** *134*, 305-318.

32. Rasmussen, P. G.; Anderson, J. E.; Bailey, O. H.; Tamres, M.; Bayon, J. C., *J. Am. Chem. Soc.* **1985,** *107*, 279-281.

33. Tejel, C.; Ciriano, M. A.; Lopez, J. A.; Lahoz, F. J.; Oro, L. A., *Organometallics* **1997,** *16*, 4718-4727.

34. Tejel, C.; Ciriano, M. A.; Lopez, J. A.; Lahoz, F. J.; Oro, L. A., *Organometallics* **2000,** *19*, 4977-4984.

35. Linck, R. C.; Pafford, R. J.; Rauchfuss, T. B., *J. Am. Chem. Soc.* **2001,** *123*, 8856-8857.

36. Patra, S. K.; Rahaman, S. M. W.; Majumdar, M.; Sinha, A.; Bera, J. K., *Chem. Commun.* **2008**, 2511-2513.

37. Brost, R. D.; Bushnell, G. W.; Harrison, D. G.; Stobart, S. R., *Inorg. Chem.* **2002,** *41*, 1412-1420.

38. Mason, R.; Thomas, K. M.; Empsall, H. D.; Fletcher, S. R.; Heys, P. N.; Hyde, E. M.; Jones, C. E.; Shaw, B. L., *J. Chem. Soc., Chem. Commun.* **1974**, 612-614.

39. Garcia, M. P.; Jimenez, M. V.; Oro, L. A.; Lahoz, F. J.; Alonso, P. J., *Angew. Chem., Int. Ed.* **1992,** *31*, 1527-1529.

40. Garcia, M. P.; Jimenez, M. V.; Oro, L. A.; Lahoz, F. J.; Tiripicchio, M. C.; Tiripicchio, A., *Organometallics* **1993,** *12*, 4660-4663.

41. Zhai, H.; Bunn, A.; Wayland, B., *Chem. Commun.* **2001**, 1294-1295.

42. Ionkin, A. S.; Marshall, W. J., *Organometallics* **2004,** *23*, 6031-6041.

43. van der Boom, M. E.; Liou, S.-Y.; Ben-David, Y.; Shimon, L. J. W.; Milstein, D., *J. Am. Chem. Soc.* **1998,** *120*, 6531-6541.

44. McCarthy, B. D.; Martin, D. J.; Rountree, E. S.; Ullman, A. C.; Dempsey, J. L., *Inorg. Chem.* **2014,** *53*, 8350-8361.

3 Effects of Chemical Oxidation of an N_2-derived Rhenium-nitride Complex on Reactivity at the Nitride Ligand

This chapter is reproduced from Connor, G. P.; Mercado, B. Q.; Lant, H. M. C.; Mayer, J. M.; Holland, P. L. *Inorg. Chem.* **2019**, 58, 10791-10801. *HMCL performed and interpreted the EPR experiments, and BQM performed the X-ray diffraction experiments, including solving all crystal structures and generating their corresponding data tables.*

3.1 Introduction

A growing number of systems can reductively cleave dinitrogen (N_2) to form metal nitride complexes.[1-13] In order to take advantage of these discoveries, it is now important to learn how to control the reactivity of metal-nitrido complexes. Functionalization of N_2-derived nitrides is particularly challenging because these systems tend to have strong metal-nitride bonds that are formed through thermodynamically favorable N_2 splitting. Despite this challenge, there are some examples where reductive functionalization of N_2-derived, metal-nitride complexes have been reported,[13-20] including some that feature pincer-type supporting ligands.[8-10, 21] However, in other cases, supporting ligands react preferentially to the nitride ligand.[5, 8] These disparate results highlight the difficulty of predicting the reactivity of N_2-derived metal-nitrido complexes and show the need for understanding how nitrides respond to the supporting ligand. Understanding how supporting ligands control reactivity at the nitride ligand of these complexes is therefore key to developing systems that can achieve both the difficult reductive cleavage of N_2 as well as subsequent functionalization of the nitride ligand to useful products. In addition, chemists need to contend with the selectivity of attack on the supporting ligand versus attack on the nitride, as described below.

Metal-bound nitrides are known to range from strongly nucleophilic to strongly electrophilic,[22-24] including some complexes in which the nitride ligand can react in an

ambiphilic fashion.[25] Here, we study the reactivity of (PNP)Re(N)(Cl) (1, PNP = $N(CH_2CH_2P^tBu_2)_2$), which forms from the reductive cleavage of N_2 by $(PNP)ReCl_2$.[8, 11] Schneider has reported that complex **1** reacts with H^+ at the supporting ligand to protonate the backbone amide but reacts with carbon electrophiles at the nitride ligand to form alkylimido complexes, suggesting a fine balance between nitride and supporting ligand reactivity (**Scheme 3.1**).[8, 21] We thus were interested to explore other electrophiles in efforts toward net N_2 functionalization to other products.

Scheme 3.1. Reactivity of **1** with acids and carbon electrophiles.[8]

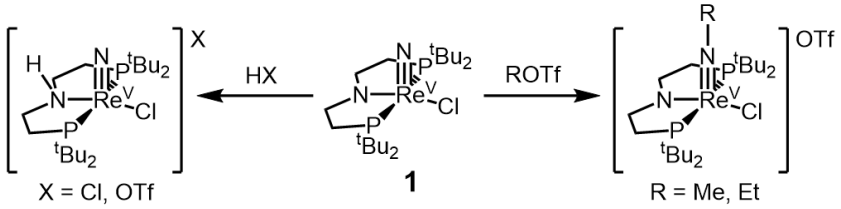

The $Re^{6+/5+}$potential for **1** in tetrahydrofuran (THF) is –0.08 V vs. $Cp_2Fe^{+/0}$,[8] which suggests that its formally Re^{5+} center is surprisingly electron-rich (**Figure 3.1**). We reasoned that **1** could display reactions toward O-atom donors that would form new N–O bonds to the N_2-derived nitride, giving interesting functionalized products such as nitrosyl or nitro complexes. The transformation of electrophilic nitride ligands to nitrosyl ligands has been reported in metal-nitrido complexes[26-30] and oxidation of nitrosyl to nitro ligands is also well precedented,[31-35] but neither has been observed in nitrides derived from N_2. To assess these possibilities, as well as to explore new methods to quantify and modulate the reactivity of metal-nitrido complexes, we experimentally evaluated the oxidative reactivity of **1** with O-atom transfer reagents and $1e^-$ chemical oxidants. These studies not only serve to help expand the understanding of supporting-ligand versus nitride-ligand reactivity in

systems that can cleave N_2, but could also address new pathways of transition-metal-mediated N_2 functionalization.

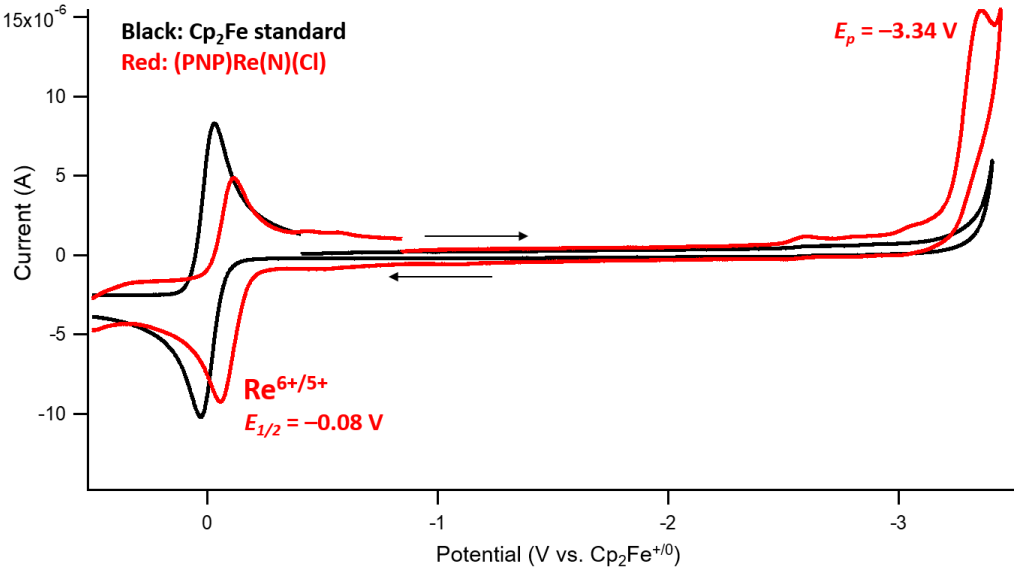

Figure 3.1. Cyclic voltammogram (CV) of 0.55 mM **1** in THF (red) demonstrating an irreversible reduction at –3.34 V vs. $Cp_2Fe^{+/0}$ and a reversible $Re^{6+/5+}$ couple at –0.08 V vs. $Cp_2Fe^{+/0}$, compared to a CV of just $Cp_2Fe^{+/0}$ (black). CVs obtained at a scan rate of 100 mV/s with a glassy carbon working electrode, Pt wire auxiliary electrode, and Ag wire pseudoreference electrode.

3.2 Results and Discussion

3.2.1. Synthesis and characterization of a novel nitroxide-pincer complex

Complex **1** reacts with 1.5 equiv of 3-chloroperbenzoic acid (mCPBA) to give a new diamagnetic complex **2** at ambient temperature in THF or diethyl ether (Et_2O). This reaction proceeds in >95% yield as judged by ^1H and $^{31}P\{^1H\}$ NMR spectroscopy. The oxidation of **1** to **2** leads to a slight shift in the ^{31}P resonance of the phosphine arms from δ 84.6 ppm for **1** to δ 64.6 ppm for **2** in the $^{31}P\{^1H\}$ NMR spectrum collected in THF-d_8. The solid-state crystal structure of **2** reveals that the oxidation occurs at the backbone amide of the pincer ligand rather than at the nitride ligand, forming a nitroxide moiety that binds η^2 to the metal center (**Scheme 3.2**). In the crystallographic structure of **2**, the nitroxide O

atom has a hydrogen bond to a molecule of 3-chlorobenzoic acid (mCBA) in the solid state, and **2** is isolated with one equivalent of mCBA as evident from the ^{1}H NMR spectrum of crystals of **2** (**Figure 3.2**). The H-atom involved in the hydrogen bond was not resolved by X-ray crystallography, but DFT calculations, structural parameters, and reduction potentials all suggest that the mCBA molecule is protonated rather than the Re-bound nitroxide (see below). Reaction of **1** with 1.5 equiv H_2O_2 (as a 30% w/w solution in H_2O) also forms **2** in 23% yield according to $^{31}P\{^{1}H\}$ NMR spectroscopy in THF-d_8 (**Figure 3.3**). Due to the low spectroscopic yield, we did not attempt to isolate **2** from the reaction of **1** with H_2O_2. Additionally, attempts to isolate **2** without a hydrogen-bonded mCBA equivalent were not successful. Although numerous transition metal complexes with nitroxide or hydroxylamine ligands have been reported,[36-38] only one other example of forming a nitroxide ligand via oxidation of a coordinated amide ligand has been reported with any transition metal.[39] No previous examples of a nitroxide coordinated to Re have been reported to our knowledge. Thus, this reaction represents a distinctive example of chemical oxidation of a coordinated pincer ligand to form a nitroxide ligand.

Scheme 3.2. Oxidative reactivity of Re-nitride complex **1** and formation of novel nitroxide complexes **2** and **4**.[8]

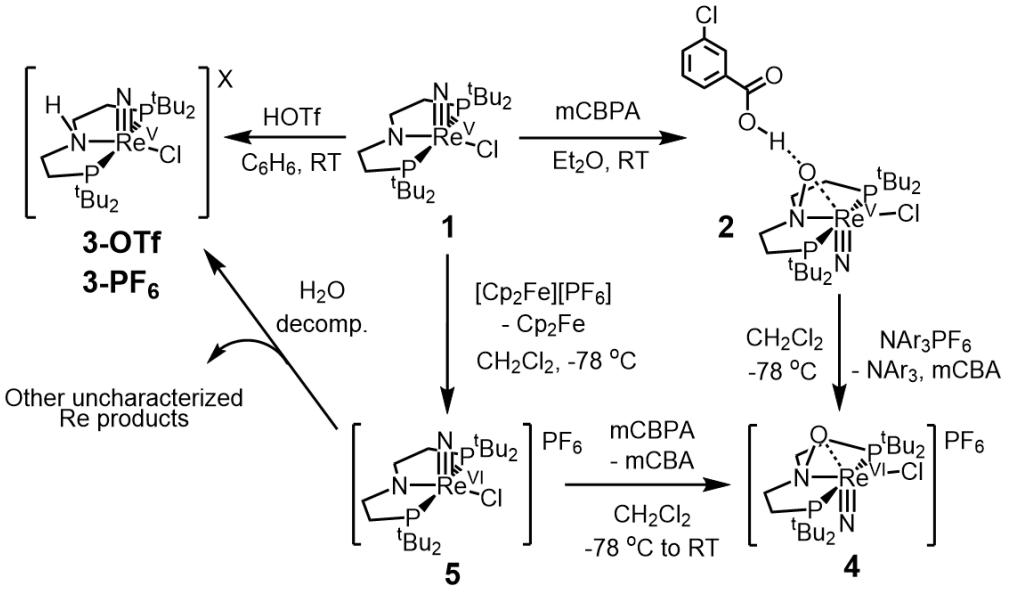

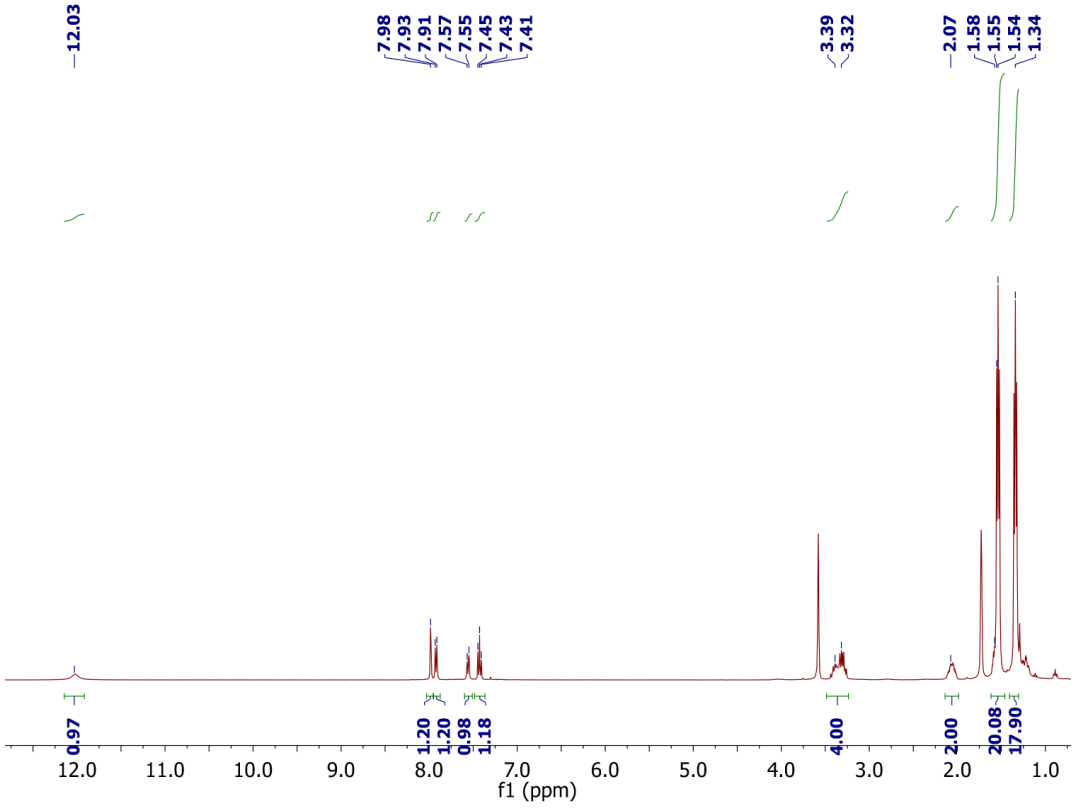

Figure 3.2. ^{1}H NMR spectrum of **2** in THF-d_8 shows isolation of the complex with one molecule of m-chlorobenzoic acid (mCBA).

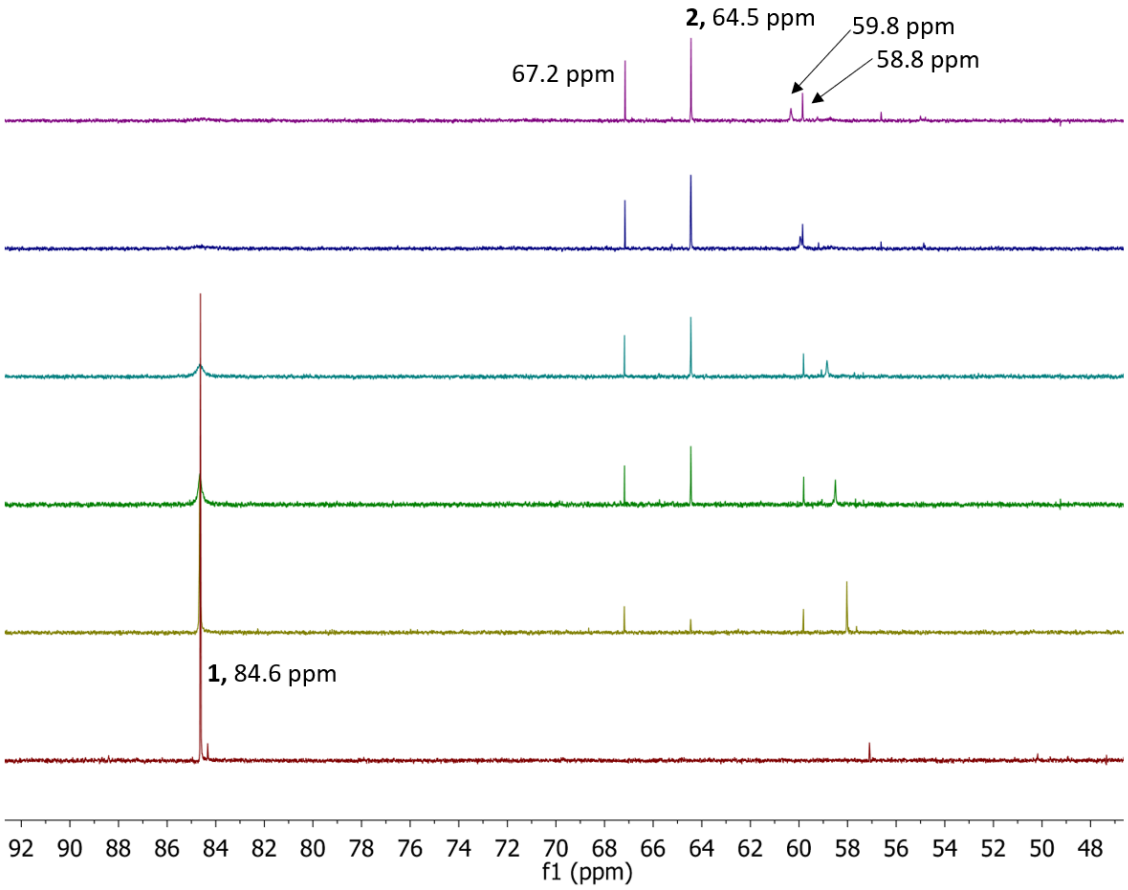

Figure 3.3. $^{31}P\{^{1}H\}$ NMR spectra of reaction of **1** with 1.5 equiv H_2O_2 (30% w/w in H_2O) in THF-d_8. Maroon (bottom): before addition. Light green: 30 min after addition. Green: 12 hr after addition. Teal: 36 hr after addition. Dark blue: 1 week after addition. Purple (top): 2 weeks after addition. After 2 weeks, **2** (δ 64.5 ppm) was formed in 23% spectroscopic yield.

In contrast, **2** is not formed when nucleophilic O-atom transfer reagents are employed. For example, reaction of **1** with excess trimethylamine-*N*-oxide, pyridine-*N*-oxide, or iodosobenzene gave no conversion to **2** by ^{1}H and $^{31}P\{^{1}H\}$ NMR spectroscopies, even after prolonged heating at 115 °C. Instead, these reactions gave an intractable mixture of multiple products, if any. IR spectra of the crude reaction products show no evidence of nitrosyl formation. These results suggest that oxidized products of these reactions involve O-atom transfer to neither the amide backbone nor the nitride ligand. The reactivity of **1** with an oxygen electrophile (mCPBA) at the backbone amide to form **2** differs from the

reactivity of **1** with carbon electrophiles, which react at the nitride ligand to form a new N–C bond.[8, 21] However, formation of **2** in this reaction is more reminiscent of ligand-based reactivity of **1** with hydrochloric or triflic acid (HOTf) to form cationic complexes with the amide protonated (see **Scheme 3.1**).[8]

While the amide backbones in PNP-pincer ligands[40-48] are strong σ- and π-donors, it is not obvious how to view the bonding nature of the new "$P^{O}NP$"-pincer ligand that features a nitroxide backbone. The solid-state structure of **2** exhibits a long Re–O interaction of 2.306(6) Å, and the Re-amide bond length elongates slightly from 2.033(6) to 2.080(7) Å going from **1** to **2**, respectively (**Figure 3.4**). There is also a slight shortening of the Re–Cl bond length from 2.441(2) Å to 2.409(2) Å upon oxidation of the supporting ligand, which is consistent with a loss of electron density at the metal center. Otherwise, the coordination geometry around Re deviates little from **1** to **2** (**Figure 3.5a**). To explore the change in electron density at Re, cyclic voltammetry (CV) experiments on **1** and **2** were performed in THF. These experiments show an anodic shift of the $Re^{6+/5+}$ couple of 80 mV from –0.08 V vs. $Cp_2Fe^{+/0}$ for **1** to 0.00 V vs. $Cp_2Fe^{+/0}$ for **2** (**Figure 3.6**).[8] This represents quite a small shift in electron-richness between **1** and **2** despite chemical oxidation of the supporting ligand. This observation agrees with the lack of change in the coordination geometry around Re. For comparison, protonation of **1** with HOTf to form the cationic amide-protonated complex [($P^{H}NP$)Re(N)(Cl)][OTf] (**3-OTf**) has a much larger effect, shifting the Re^{5+} to Re^{6+} reduction potential to 0.60 V vs. $Cp_2Fe^{+/0}$. These data show that there are only subtle electronic changes between **1** and **2**, supporting the conclusion that the ligand in **2** is a nitroxide anion with a hydrogen-bonded carboxylic acid, rather than a hydroxylamine ligand. The small changes between **1** and **2** indicate that oxidation of the

amide of a PNP-pincer complex to a nitroxide may offer an opportunity to "fine-tune" the electronics of the complex to improve reactivity without changing its overall charge or requiring the synthesis of a separate ligand.

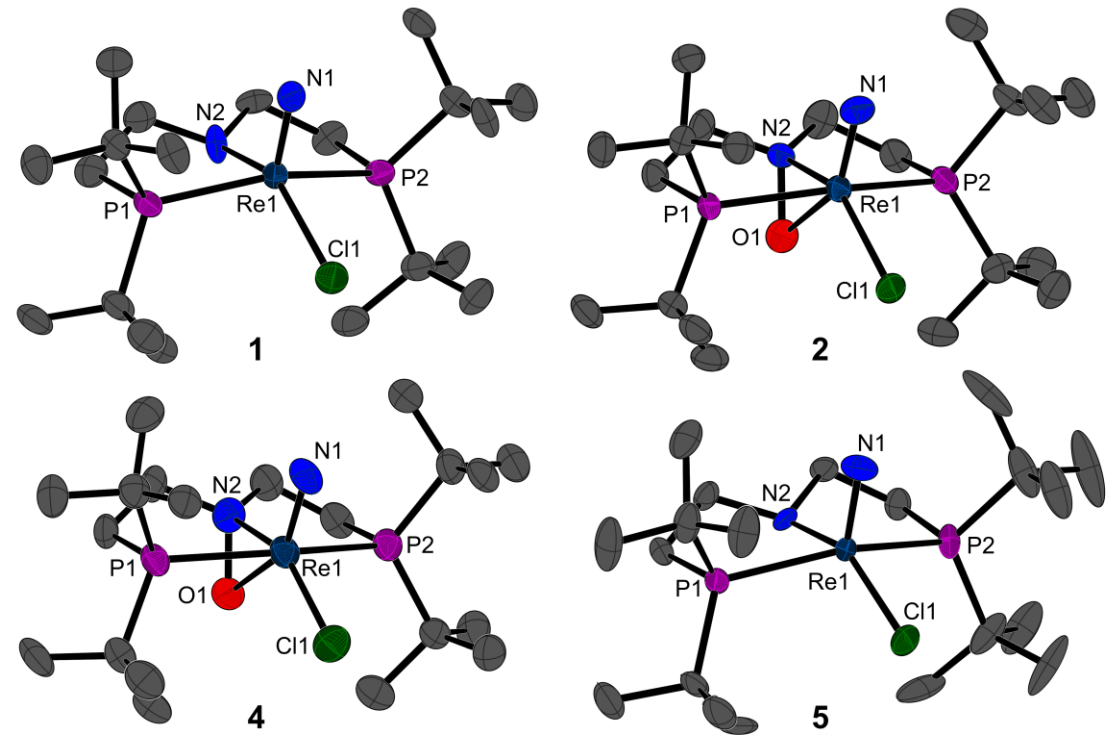

Figure 3.4. Solid-state structures of parent nitride complex **1** (left, matches previously reported DFT structure[8]), Re^{5+}-nitroxide complex **2** (mCBA molecule omitted), Re^{6+}-nitroxide complex **4** (PF_6 ion omitted), and Re^{6+}-nitride complex **5** (PF_6 ion omitted) with thermal ellipsoids at 50% probability. Hydrogen atoms are omitted for clarity.

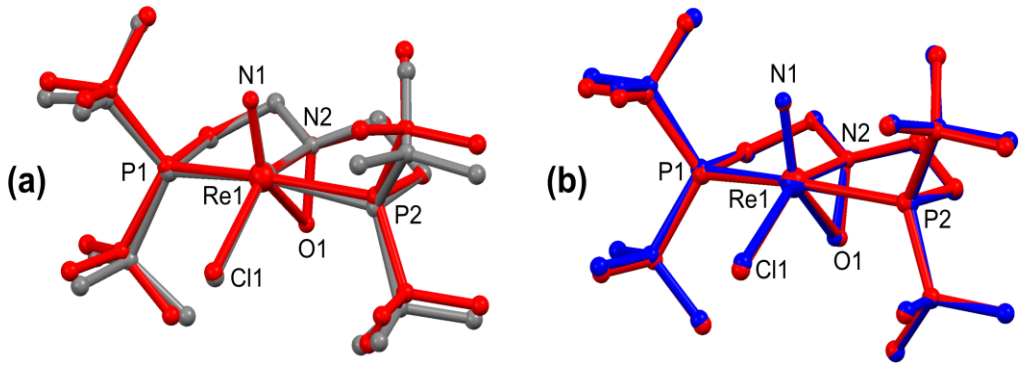

Figure 3.5. (a) Overlay of solid-state structures for Re^{5+}-nitride (**1**, gray), and Re^{5+}-nitroxide (**2**, red). **(b)** Overlay of solid-state structures for Re^{5+}-nitroxide (**2**, red) and Re^{6+}-nitroxide (**4**, blue).

Table 3.1. Selected bond lengths (Å) and bond angles (°) of complexes **1**, **2**, **4**, and **5**.

Bond/Angle	**1**	**2**	**4**	**5**
Re1–N1	1.643(6)	1.638(7)	1.665(7)	1.650(5)
Re1–N2	2.033(6)	2.080(7)	2.097(8)	2.054(5)
Re1–Cl1	2.441(2)	2.409(2)	2.295(3)	2.339(2)
Re1–O1	-	2.306(6)	2.200(6)	-
Re1–P1	2.443(2)	2.443(2)	2.516(2)	2.476(2)
Re1–P2	2.435(2)	2.460(2)	2.507(2)	2.479(2)
O1–N2	-	1.436(9)	1.433(1)	-
N1–Re1–N2	105.8(3)	105.3(3)	105.0(4)	103.4(2)
N1–Re1–Cl1	106.5(2)	105.3(2)	103.1(3)	105.6(2)
N2–Re1–Cl1	147.7(2)	149.5(2)	151.9(2)	151.0(1)
N1–Re1–P1	100.4(2)	96.1(3)	95.8(3)	98.9(2)
N1–Re1–P2	99.9(2)	97.6(3)	96.5(3)	100.8(2)
O1–N2–Re1	-	79.7(4)	74.5(4)	-
O1–Re1–N2	-	37.8(2)	38.8(3)	-
O1–Re1–Cl1	-	111.7(2)	113.1(2)	-

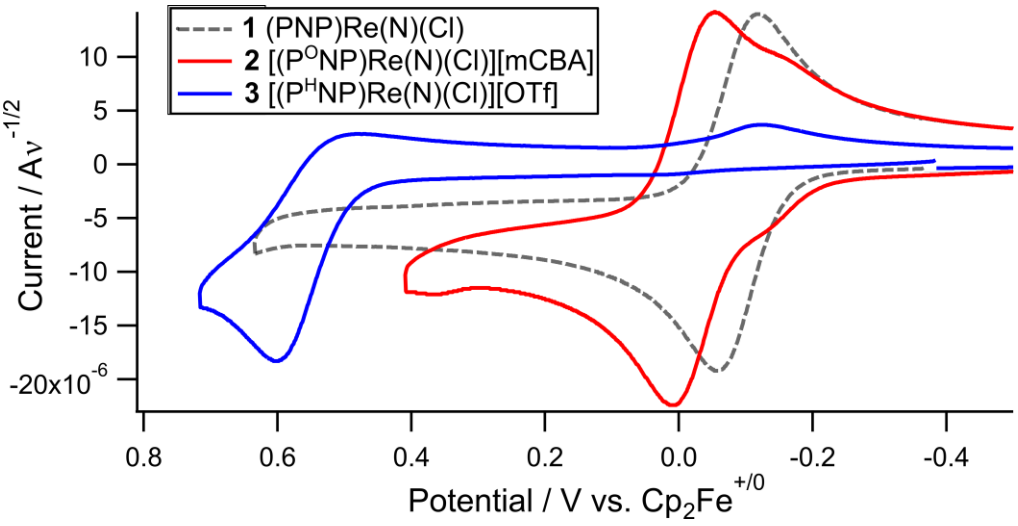

Figure 3.6. Cyclic voltammograms of **1** (gray, dashed), **2** (red), and **3-OTf** (blue) demonstrating effect of functionalizing the backbone amide on the $Re^{6+/5+}$ redox potential. Details: 100 mV/s scan rate, scanning anodically in 0.1 M tetrabutylammonium hexafluorophosphate solution in THF with glassy carbon disk working, Pt wire auxiliary, and Ag wire psuedoreference electrodes. An additional redox feature in the voltammogram of **2** may be from a minor adventitious impurity.

In order to elucidate the changes in bonding interactions arising from formation of the nitroxide, complexes **1** and **2** were modelled using DFT calculations. Complex **2** was modelled with and without a coordinated mCBA molecule, and the presence of mCBA did

not significantly affect any of the computational results (**Table 3.2**). Natural bond order (NBO) analysis of **2** (without mCBA) identifies a weak Re–O interaction with a Wiberg bond order[49] of 0.22, which is consistent with the long Re–O bond observed in the solid-state structure (**Figure 3.7**). The Wiberg bond order of the Re-amide decreases from 0.65 in **1** to 0.43 in **2**, suggesting loss of π-donation from the amide. Second-order perturbation theory (SOPT) analysis[50] identifies several donor-acceptor interactions between the nitroxide and Re-containing molecular orbitals. This analysis estimates the energy lowering in a molecule achieved by donation of electrons in a filled (bonding or lone pair) orbital into a vacant or antibonding orbital. The dominant interaction identified by SOPT analysis is the donation of lone pairs (LPs) on the O atom into antibonding d-π* Re-nitride orbitals (**Figure 3.7c**). These interactions replace analogous donation from the amide LP in **1** into the same antibonding d-π* Re-nitride orbitals. However, the donor-acceptor interactions from the O atom in **2** (see **Table 3.3**) are stronger than the analogous interactions from the amide in **1** (see **Table 3.4**), as evident by an approximately 30% increase in the calculated exchange energies for these interactions in **2** vs. **1**. Additionally, a weak donor-acceptor interaction between the N–O σ-bond and the overlapping antibonding Re-nitride orbital was identified in **2**.

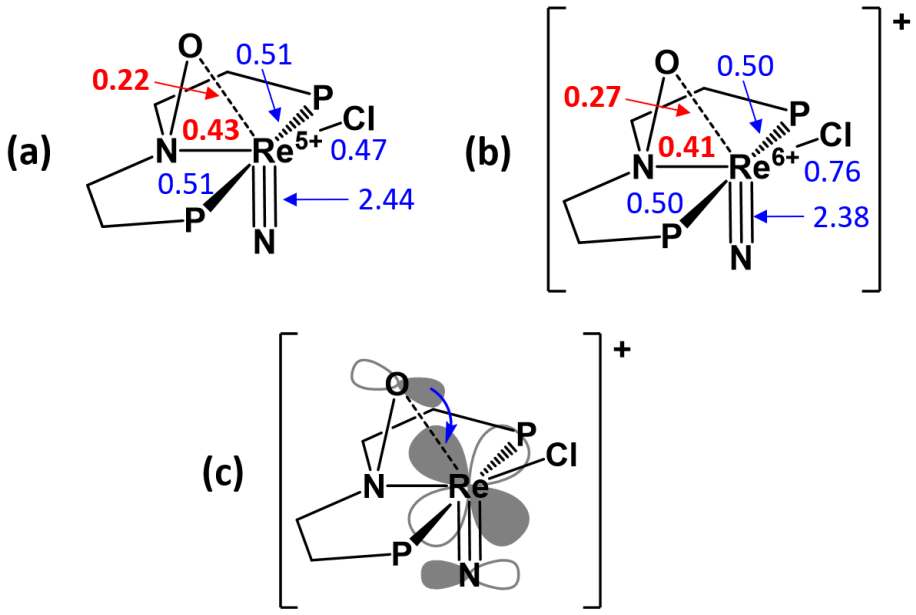

Figure 3.7. Calculated Wiberg bond orders of **(a)** Re^{5+}-nitroxide complex (**2**) and **(b)** Re^{6+}-nitroxide complex (**4**), and **(c)** representation of donor-acceptor interaction from O atom LP to antibonding *d*-π* Re-nitride orbital. For the purpose of clarity, the supporting ligand is truncated.

Table 3.2. Calculated structural parameters of **2** using different functionals. [a] Structure optimized without *m*-chlorobenzoic acid molecule.

Functional **Dispersion corr.**	**Exp. (2)** -	**PBE** -	**PBE0** -	**PBE0** **D3**	**PBE0**[a] **D3**
Re - N1	1.638(7)	1.666	1.643	1.641	1.646
Re - N2	2.080(7)	2.097	2.079	2.087	2.084
Re - Cl	2.409(2)	2.492	2.479	2.470	2.486
Re - O	2.306(6)	2.350	2.323	2.352	2.342
Re - P (avg)	2.452	2.464	2.458	2.446	2.441
O - N2	1.436(9)	1.418	1.395	1.395	1.388
N1 - Re - N2	105.3(3)	104.9	104.8	104.8	106.0
N1 - Re - Cl	105.3(2)	102.7	102.5	102.6	102.4
N2 - Re - Cl	149.5(2)	152.4	152.7	152.7	151.6
O - N2 - Re	79.7(4)	81.4	81.3	82.4	82.2
N2 - Re - O	37.8(2)	36.6	36.4	36.0	36.0

Table 3.3. Selected donor-acceptor interactions involving Re–N antibonding orbitals from SOPT analysis in NBO calculations for **2**. BD*(1–3) are Re–N antibonding orbitals and E(2) is the exchange energy.

Donor Orbital	Acceptor Orbital	E(2) (kcal/mol)	Sum (kcal/mol)
Oxygen lone pairs (LPs)	BD*(1)	28.34	
	BD*(2)	3.13	
	BD*(3)	19.7	51.17
Phosphorus LPs	BD*(1)	0	
	BD*(2)	47.48	
	BD*(3)	4.33	51.81
Chloride LPs	BD*(1)	21.2	
	BD*(2)	0	
	BD*(3)	7.23	28.43
Re–P bonds	BD*(1)	2.03	
	BD*(2)	7.53	
	BD*(3)	104.74	114.3
Re-amide bond	BD*(1)	0.66	
	BD*(2)	2.08	
	BD*(3)	86.91	89.65
N–O bond	BD*(1)	11.54	
	BD*(2)	0	
	BD*(3)	0	11.54

Table 3.4. Selected donor-acceptor interactions involving Re–N antibonding orbitals from SOPT analysis in NBO calculations for **1**. BD*(1–3) are Re–N antibonding orbitals and E(2) is the exchange energy.

Donor Orbital	Acceptor Orbital	E(2) (kcal/mol)	Sum (kcal/mol)
Amide lone pair (LP)	BD*(1)	36.58	
	BD*(2)	0	
	BD*(3)	3.13	39.71
Phosphorus LPs	BD*(1)	0	
	BD*(2)	61.26	
	BD*(3)	6.09	67.35
Chloride LPs	BD*(1)	18.98	
	BD*(2)	1.22	
	BD*(3)	9.22	29.42
Re–P bond	BD*(1)	9.05	
	BD*(2)	10.28	
	BD*(3)	88.14	107.47
Re-amide bond	BD*(1)	0	
	BD*(2)	3.17	
	BD*(3)	86.93	90.1

Overall, the change from **1** to **2** decreases the reactivity of the complex. Nitroxide complex **2** does not react with mCPBA, trimethylamine-*N*-oxide, pyridine-*N*-oxide, or iodosobenzene. In addition, **2** does not react with potential nucleophiles PMe_3 or PPh_3. Thus, it is apparent that introduction of the nitroxide moiety does not affect the strong Re-nitrido interaction enough to increase reactivity at the nitride ligand.

3.2.2. Synthesis of Re^{6+}-nitride complexes

The reversible anodic waves observed in CV experiments of **2** indicate that the $(P^{O}NP)Re^{6+}$ complex could be accessible. Oxidation of **2** at –78 °C in dry CH_2Cl_2 with tris(4-bromo-phenyl)aminium hexafluorophosphate affords $[(P^{O}NP)Re(N)(Cl)][PF_6]$ (**4**), a rare example of an isolable paramagnetic Re^{6+}-nitride species. Complex **4** shows several broad paramagnetic proton resonances in its ^1H NMR spectrum between δ 5.5 and δ 34.0 ppm in CD_2Cl_2 (**Figure 3.8**) and its EPR spectrum is reminiscent of the few other reported S = ½ Re^{6+}-nitride complexes (**Figure 3.9**).[51-53] The solid-state structure of **4** shows a shortening of the Re–O interaction by 0.1 Å to 2.200(6) Å (see **Figure 3.5b**). The Re-nitride and Re-amide bond distances remain similar between **2** and **4**, but the Re–Cl bond distance shortens by about 0.1 Å from 2.409(2) to 2.295(3) Å upon oxidation of the Re metal center. NBO analysis of the DFT model of **4** calculates a larger Wiberg bond order of 0.27 for the Re–O bond and diminished value of 0.41 for the Re-amide bond, in agreement with the shortening of the Re–O bond and slight lengthening of the Re-amide bond, respectively (see **Figure 3.7**). SOPT analysis identifies the same donor-acceptor interactions in **4** as in **2**; however, oxidation of the metal center in **4** results in a 60% increase in exchange energies of the donation from O atom LPs into the antibonding d-π* Re-nitride orbitals (**Table 3.5**).

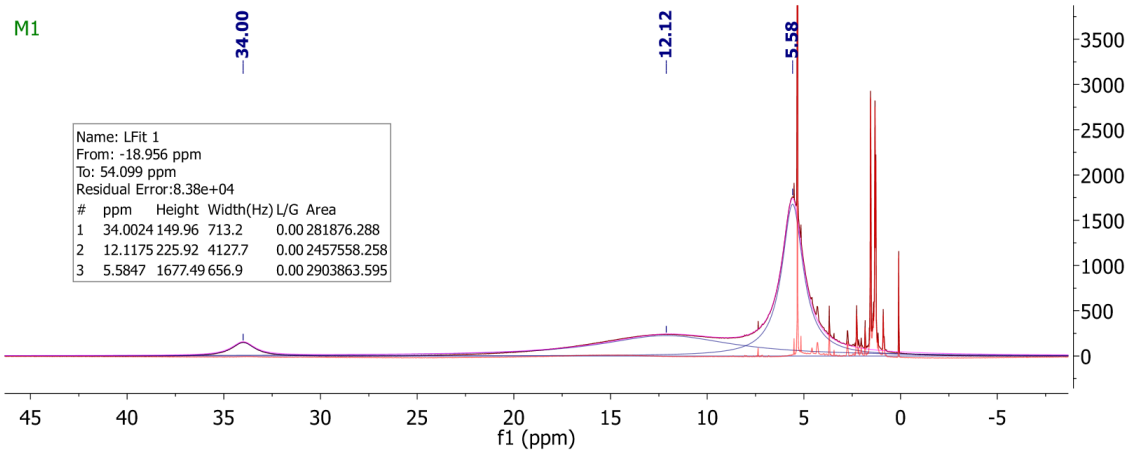

Figure 3.8. ^{1}H NMR (400 MHz, CD_2Cl_2) spectrum of **4** shows three broad paramagnetic resonances, and peak fitting gives relative integrations for each (See Experimental section). Spectrum contains **3-PF$_6$** as a 4% diamagnetic impurity (red residual peaks).

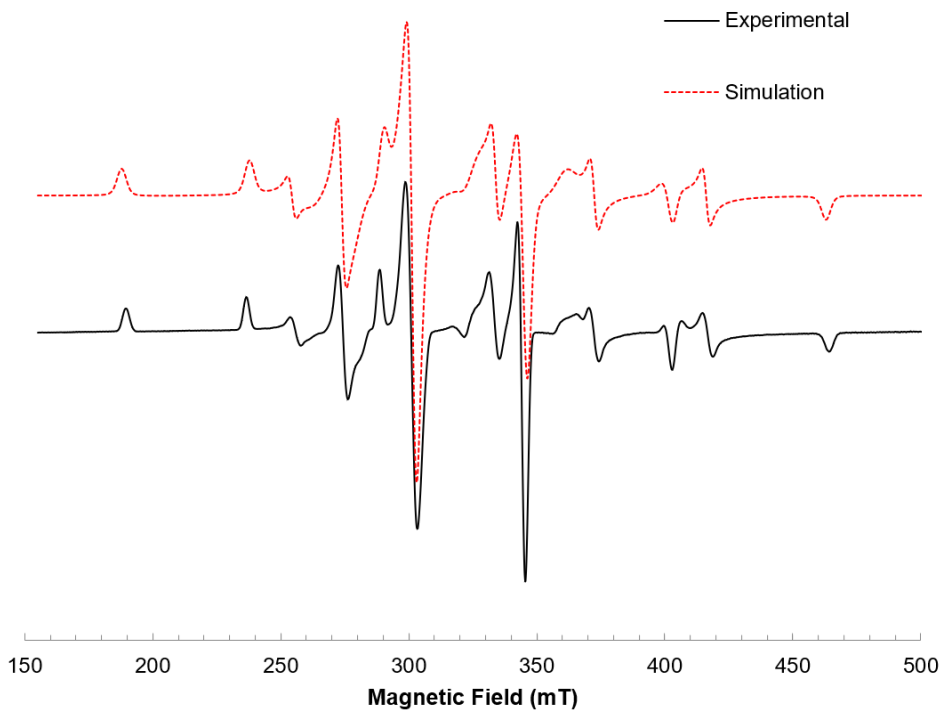

Figure 3.9. X-band EPR spectrum of 0.2 mM **4** in 1:1 CH_2Cl_2:toluene at 8–11 K (black). In red is a simulation using the following parameters: g_x = 1.951; g_y = 1.967; g_z = 2.037; A_{xx} = 87 MHz; A_{yy} = 748 MHz; A_{zz} = 1567 MHz. No phosphorus or nitrogen hyperfine couplings were resolved due to the large linewidth of the signal. Instrument parameters follow. Microwave frequency: 9.37 GHz; microwave power: 10 mW; modulation frequency 100 kHz; modulation amplitude: 19.49 G; conversion time: 5.12 ms; time constant: 1.28–2.56 ms.

Table 3.5. Selected donor-acceptor interactions involving Re–N antibonding orbitals from SOPT analysis in NBO calculations for **4**. BD*(1–3) are Re–N antibonding orbitals and E(2) is the exchange energy.

Donor Orbital	Acceptor Orbital	E2 (kcal/mol)	Sum (kcal/mol)
Oxygen lone pairs (LPs)	BD*(1)	5.48	
	BD*(2)	27.56	
	BD*(3)	49.14	82.18
Phosphorus LPs	BD*(1)	40.36	
	BD*(2)	1.28	
	BD*(3)	2.66	44.3
Chloride LPs/bond	BD*(1)	0	
	BD*(2)	9.4	
	BD*(3)	31.26	40.66
Re-P bonds	BD*(1)	2.96	
	BD*(2)	0	
	BD*(3)	61.26	64.22
Amide LP	BD*(1)	0	
	BD*(2)	21	
	BD*(3)	0	21
N–O bond	BD*(1)	0	
	BD*(2)	14.72	
	BD*(3)	0	14.72

CV analysis of parent nitride **1** shows a reversible $Re^{6+/5+}$ couple in dry CH_2Cl_2,[8] suggesting that the (PNP)Re^{6+} species is accessible in this case as well. This redox event becomes less reversible in dry acetonitrile and is only quasi-reversible in dry THF, becoming more irreversible with added aliquots of H_2O, indicating the instability of the Re^{6+} oxidation product (**Figure 3.10**). Oxidizing **1** in dry CH_2Cl_2 at –78 °C with $[Cp_2Fe][PF_6]$ results in a color change from orange to red, and the $1e^-$ oxidized complex $[(PNP)Re(N)(Cl)][PF_6]$ (**5**) was isolated from the reaction as a crystalline solid in 76% yield (**Figure 3.11**). EPR spectroscopy of the isolated crystals provides a spectrum similar to that of **4** (**Figure 3.12**).[51-53] However, ^1H and $^{31}P\{^1H\}$ NMR spectroscopies indicate that the crystals contain approximately 25% of a diamagnetic impurity, identified as $[(P^{H}NP)Re(N)(Cl)][PF_6]$ (**3-PF$_6$**), where $P^{H}NP$ indicates the pincer ligand with protonated

nitrogen. Upon further investigation, **5** was found to be extremely sensitive to decomposition in the presence of traces of moisture, forming **3-PF$_6$** as the major product (see **Figure 3.10c**). Complex **3-PF$_6$** is structurally and spectroscopically analogous to the related triflate salt **3-OTf** (**Figure 3.13**, **Table 3.6**).[8]

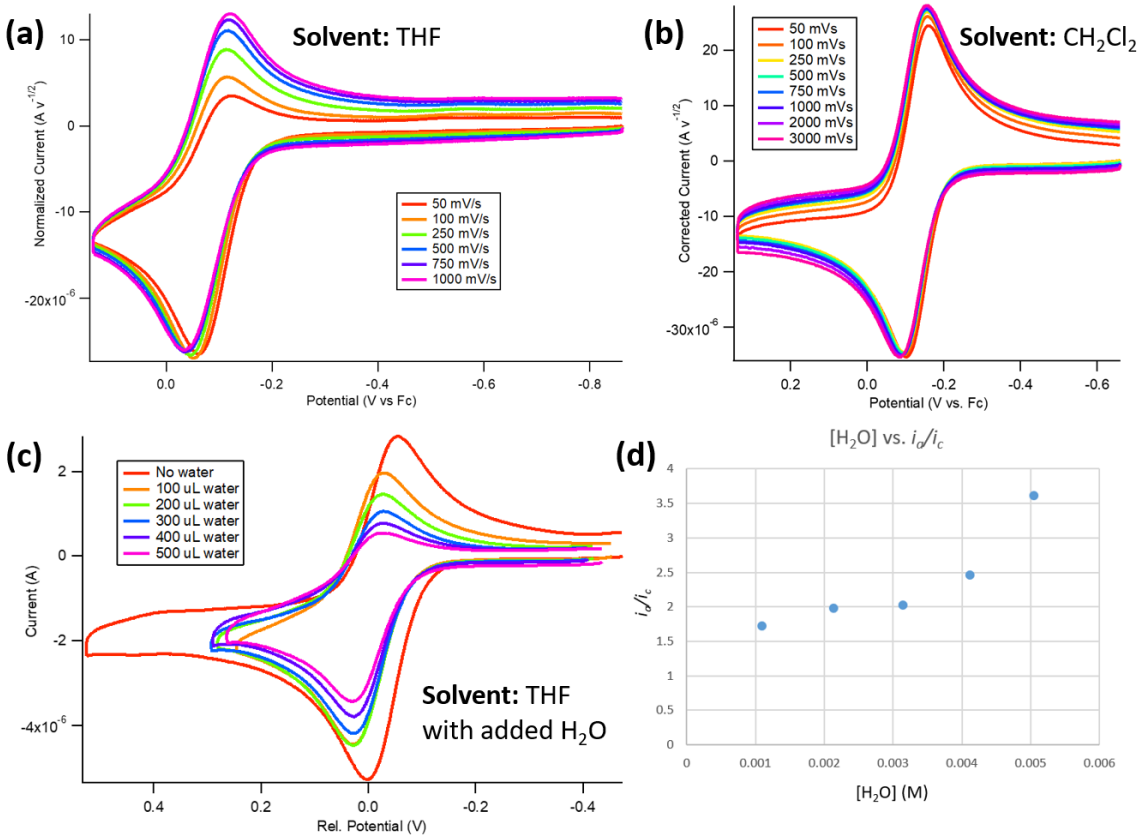

Figure 3.10. Cyclic voltammograms of **1** in different dry, N_2-sparged solvents with 0.1 M TBA-PF_6 electrolyte at various scan rates. **(a)** 0.5 mM **1** in 5 mL THF: complex shows a reversible oxidation at fast scan rates (1000 mV/s) that becomes less reversible at slower scan rates. **(b)** 0.6 mM **1** in CH_2Cl_2: complex shows a reversible oxidation at all scan rates. **(c)** 0.5 mM **1** in THF with added H_2O: the $Re^{6+/5+}$ couple becomes less reversible with more H_2O added. **(d)** Graphical representation of decreased reversibility with added H_2O as the ratio of peak anodic current (i_a) to peak cathodic current (i_c) for the couple, which should be 1 for a reversible redox event. The potentials are reported relative to the $Re^{6+/5+}$ couple with no H_2O added (set to 0 V) and do not change significantly upon addition of H_2O. All CVs taken with glassy carbon disc working electrode, Pt wire auxiliary electrode, and Ag wire psuedoreference. CVs referenced to $Cp_2Fe^{+/0}$ as an internal standard where indicated.

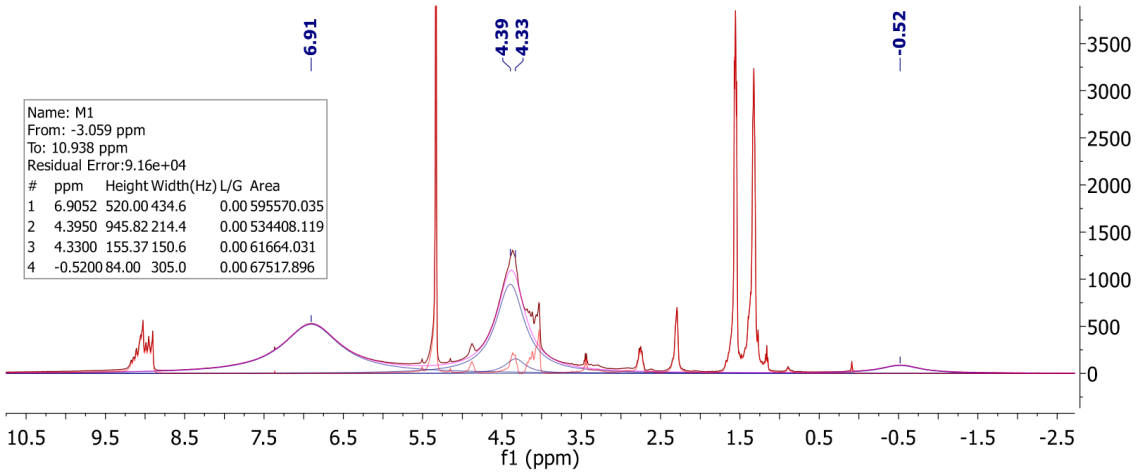

Figure 3.11. ^{1}H NMR (500 MHz, CD_2Cl_2) spectrum of **5** shows four broad paramagnetic resonances, and peak fitting gives relative integrations for each (see Experimental section). Spectrum contains **3-PF$_6$** as a 26% diamagnetic impurity (red residual peaks).

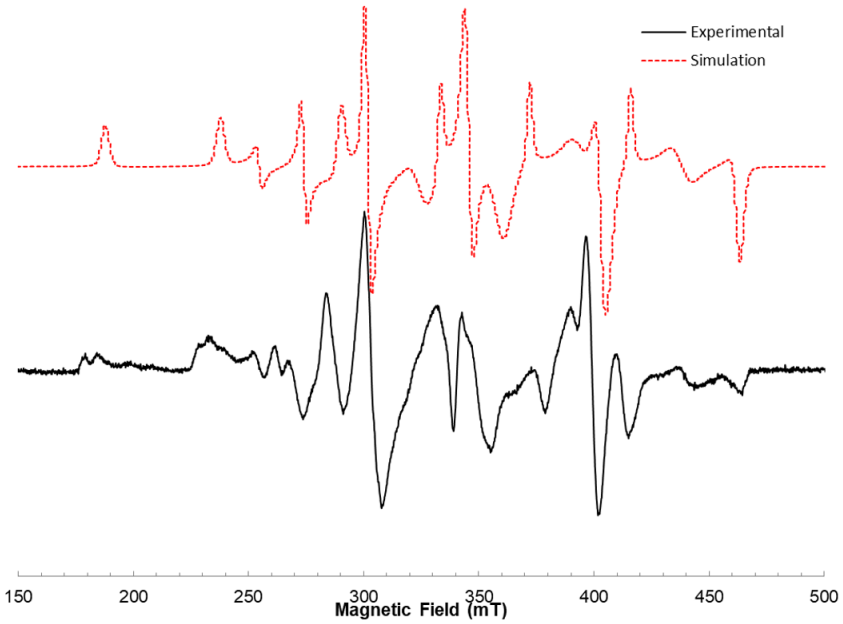

Figure 3.12. X-band EPR spectrum of 0.2 mM **5** in 1:1 CH_2Cl_2:toluene at 8–11 K. In red is a simulation using the following parameters: g_x = 1.80; g_y = 1.95; g_z = 2.04; A_{xx} = 750 MHz; A_{yy} = 880 MHz; A_{zz} = 1570 MHz. No phosphorus or nitrogen hyperfine couplings were resolved due to the large linewidth of the signal. Instrument parameters follow. Microwave frequency: 9.37 GHz; microwave power: 10 mW; modulation frequency 100 kHz; modulation amplitude: 19.49 G; conversion time: 5.12 ms; time constant: 1.28 ms.

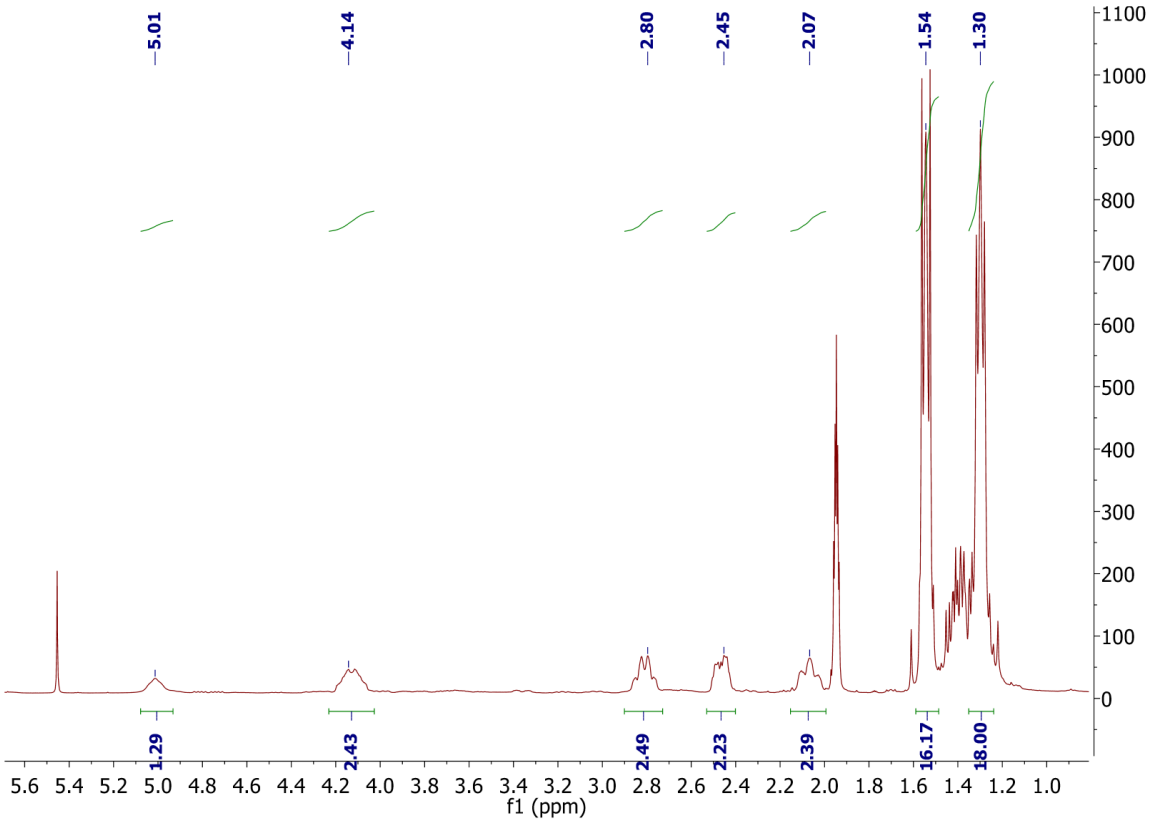

Figure 3.13. ^{1}H NMR spectrum (400 MHz, CD_3CN) of **3-PF$_6$**, formed from addition of stoichiometric H_2O to **5**. ^{1}H NMR (400 MHz, CD_3CN): δ 5.01 (br. s, 1H, N*H*), δ 4.14 (m, 2H, N(C*H*$_2$CH$_2$)$_2$), δ 2.80 (m, 2H, N(C*H*$_2$CH$_2$)$_2$), δ 2.45 (m, 2H, N(CH$_2$C*H*$_2$)$_2$), δ 2.07 (m, 2H, N(CH$_2$C*H*$_2$)$_2$), δ 1.54 (m, 18H, P(*tBu*)(tBu')), δ 1.30 (m, 18H, P(tBu)(*tBu'*)). ^{31}P{^{1}H} NMR (162 MHz, CD_3CN): δ 70.5 (s). ^{1}H-^{15}N HSQC (CD_3CN): {4.90, –336.35}. The spectroscopic data are reminiscent of those for **3-OTf**.[8]

Table 3.6. Selected bond lengths (Å) and angles (°) of complexes **3-PF$_6$** and **3-OTf**. [a] Geometric parameters from structure reported in this work. [b] Geometric parameters from previously reported structure.[8]

Bond/Angle	**3-PF$_6$**	**3-OTf** [a]	**3-OTf** [b]
Re1–N1	1.615(2)	1.624(7)	1.659(2)
Re1–N2	2.104(2)	2.138(7)	2.154(2)
Re1–Cl1	2.372(4)	2.385(2)	2.4078(9)
Re1–P1	2.462(5)	2.448(2)	2.4786(8)
Re1–P2	2.464(5)	2.455(2)	2.4694(7)
N1–Re1–N2	100.2(7)	99.9(3)	101.4(1)
N1–Re1–Cl1	105.5(6)	106.7(3)	106.8(1)
N2–Re1–Cl1	154.3(4)	153.4(2)	151.8(1)
N1–Re1–P1	99.2(7)	99.1(3)	99.4(1)
N1–Re1–P2	98.3(6)	98.5(3)	99.8(1)

3.2.3. Characterizing Re-nitrido interactions via ^{15}N-isotope labelling

With this series of Re-nitride complexes oxidized at the supporting ligand and/or metal center, we sought to quantitatively study the effects of these oxidations on the Re-nitrido bond via isotope labelling experiments. The ^{15}N-labeled parent nitride (**1-^{15}N**) was synthesized from reaction of (PNP)$ReCl_2$ with terminally labelled [PPN][N=N=^{15}N],[8] resulting in 50% labelling of the nitride ligand with ^{15}N. The 50% ^{15}N-labeled nitride complexes **2-^{15}N**, **3-^{15}N**,[8] **4-^{15}N**, and **5-^{15}N** were subsequently prepared from **1-^{15}N**. Isotopic labelling of the nitride ligand enables direct spectroscopic comparison of the Re-nitride stretching frequencies in the IR spectra of these complexes (**Figure 3.14**), and the ^{15}N resonance for the nitride is easily observed in the ^{15}N NMR spectra of the diamagnetic Re^{5+} complexes **1-^{15}N**, **2-^{15}N**, and **3-^{15}N** (**Figure 3.15**). Additionally, the Re-nitride bond lengths are available from the solid-state structures of the complexes. The data in **Table 3.7** show that Re-nitride interaction varies throughout the series of complexes, demonstrating small changes in Re-nitride bond lengths and notable changes in Re-nitride stretching frequencies. For example, the Re-nitride stretching frequency ranges from 1024 cm^{-1} in **4-^{15}N** to 1075 cm^{-1} in **3-^{15}N**, a difference of 51 cm^{-1}. In general, we see that functionalization of the backbone amide results in slightly higher Re-nitride stretching frequencies, while oxidation of the metal center results in slightly lower frequencies. However, the Re-nitride bond length ranges only from 1.624(7) Å in **3-OTf** to 1.665(7) Å in **4**. Excluding the protonated complex **3-OTf**, the complexes adhere well to Badger's rule, which predicts a correlation between bond length and stretching frequency (**Figure 3.16a**).[54] It is worth noting that the backbone- *and* metal-oxidized complex **4-^{15}N** demonstrates the lowest Re-nitride stretching frequency, likely resulting from stronger

donation from O atom LPs into the antibonding d-π* Re-nitride orbitals. Assuming that changes in stretching frequency parallel changes in bond strength, this implies that **4-^{15}N** has the weakest Re-nitride interaction.

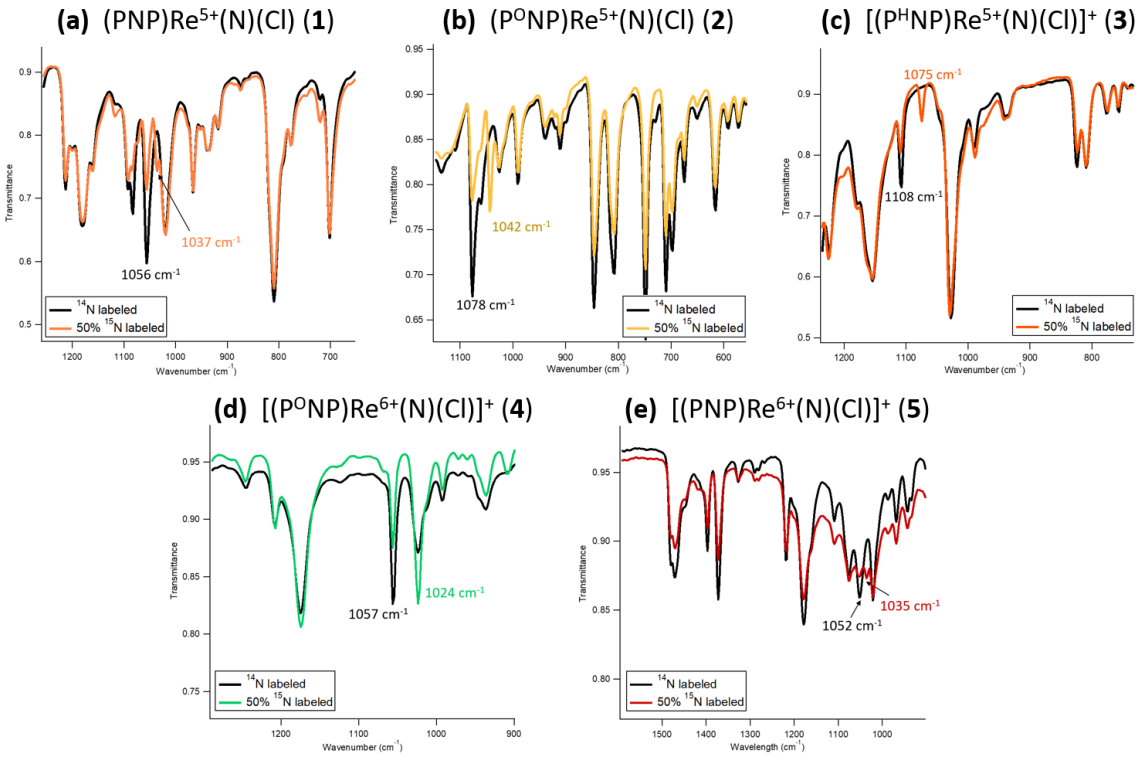

Figure 3.14. Comparison of FTIR spectra of ^{14}N- and ^{15}N-labeled complexes. **(a)** Band at 1056 cm^{-1} for **1** (solid, black trace) decreases in intensity and new band at 1037 cm^{-1} for **1-^{15}N** (solid, orange trace) appears upon 50% labeling with ^{15}N, demonstrating an isotope-dependent shift of the Re–N resonance of 19 cm^{-1}. The simple harmonic oscillator approximation predicts a shift of 33 cm^{-1}. **(b)** Band at 1078 cm^{-1} for **2** (solid, black trace) decreases in intensity and new band at 1042 cm^{-1} for **2-^{15}N** (solid, gold trace) appears upon 50% labeling with ^{15}N, demonstrating an isotope-dependent shift of the Re–N resonance of 36 cm^{-1} (34 cm^{-1} predicted). **(c)** Band at 1108 cm^{-1} for **3-OTf** (solid, black trace) decreases in intensity and new band at 1075 cm^{-1} for **3-^{15}N** (solid, red-orange trace) appears upon 50% labeling with ^{15}N, demonstrating an isotope-dependent shift of the Re–N resonance of 33 cm^{-1} (35 cm^{-1} predicted). **(d)** Band at 1057 cm^{-1} for **4** (solid, black trace) decreases in intensity and new band at 1024 cm^{-1} for **4-^{15}N** (solid, green trace) appears upon 50% labeling with ^{15}N, demonstrating an isotope-dependent shift of the Re–N resonance of 33 cm^{-1} (33 cm^{-1} predicted). **(e)** Band at 1052 cm^{-1} for **5** (solid, black trace) decreases in intensity and new band at 1035 cm^{-1} for **5-^{15}N** (solid, dark red trace) appears upon 50% labeling with ^{15}N, demonstrating an isotope-dependent shift of the Re–N resonance of 17 cm^{-1} (33 cm^{-1} predicted).

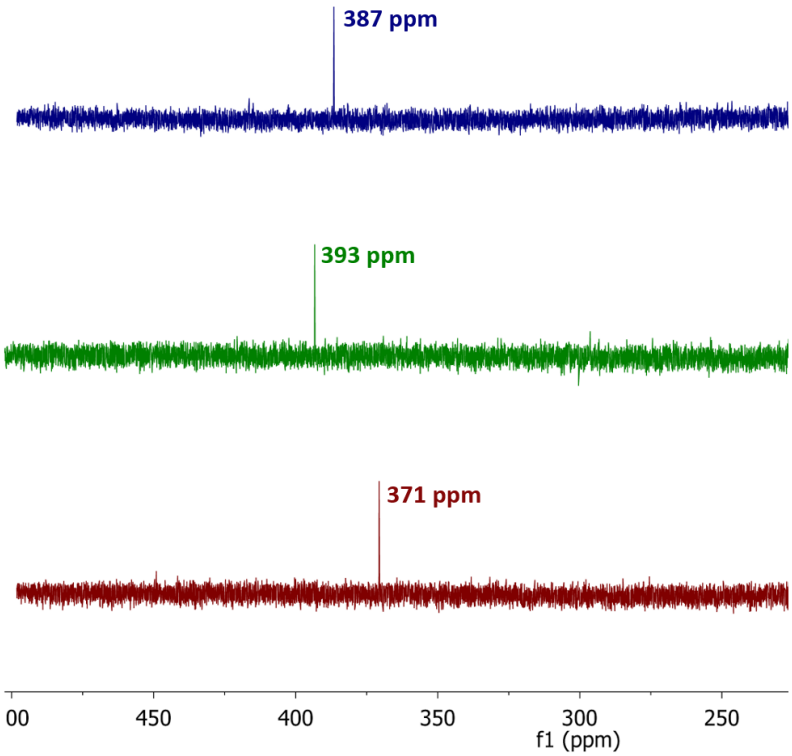

Figure 3.15. ^{15}N NMR spectra (51 MHz, C_6D_6) of **1-^{15}N** (bottom, maroon), **2-^{15}N** (middle, green), and **3-^{15}N** (top, blue).

Table 3.7. Re–^{15}N stretching frequencies, bond lengths, and ^{15}N NMR chemical shifts for Re-nitrido complexes. [a] Chemical shift reported vs. CH_3NO_2. [b] This distance has been previously reported as 1.659(2) Å.[8] The structure from this work gave a distance of 1.624(7) Å from a crystal with a different unit cell, and the shorter bond distance more closely corresponds to the high Re–N stretching frequency in this complex as well as its higher calculated Re–N Wiberg bond order.

Complex	Re–^{15}N stretch (cm^{-1})	Re–N bond length (Å)	Nitride ^{15}N NMR chemical shift[a] (ppm)
(PNP)Re(N)(Cl) (**1-^{15}N**)	1037	1.643(6)	371
[(P^ONP)Re(N)(Cl)][mCBA] (**2-^{15}N**)	1042	1.638(7)	393
[(P^HNP)Re(N)(Cl)][OTf] (**3-^{15}N**)	1075	1.624(7)[b]	387
[(P^ONP)Re(N)(Cl)][PF_6] (**4-^{15}N**)	1024	1.665(7)	-
[(PNP)Re(N)(Cl)][PF_6] (**5-^{15}N**)	1035	1.650(5)	-

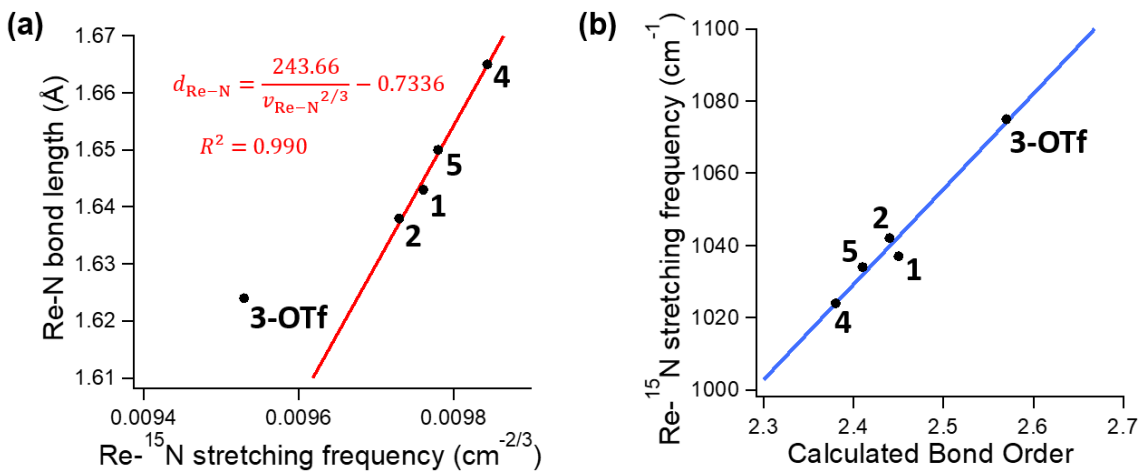

Figure 3.16. Re-nitride bond length vs. $1/\nu_{Re-N}{}^{2/3}$, with Badger's rule demonstrated as a linear fit for complexes **1**, **2**, **4**, and **5**. **(b)** Calculated Wiberg bond order of Re-nitride bonds vs. observed Re-nitride stretching frequencies in complexes **1**–**5**.

The chemical shifts of the ^{15}N nitride resonances in the ^{15}N NMR spectra of **1-^{15}N**, **2-^{15}N**, and **3-^{15}N** suggest the *relative* electron density of the nitride ligands, at least to a first approximation. In organic compounds, ^{15}N NMR chemical shifts have been shown to be correlated to various chemical properties, including Lewis basicity.[55-59] We wondered whether the ^{15}N NMR chemical shifts of the nitride ligands could thus be an estimate of the relative electron richness of these ligands and, by extension, be used to predict reactivity. Functionalization of the amide in 1-^{15}N to form a nitroxide (**2-^{15}N**) or protonated amide (**3-^{15}N**) both shift the nitride ^{15}N resonance downfield, suggesting a decrease in Lewis basicity. This can be rationalized partially from first principles, since oxidation or protonation of the complex should give a more electron-deficient Re center, which in turn should facilitate stronger donation from the nitride ligand. However, the changes in the nitride ^{15}N chemical shift from **1-^{15}N** to **2-^{15}N** (22 ppm) and from **1-^{15}N** to **3-^{15}N** (16 ppm) are very close. Despite the similar ^{15}N-nitride chemical shifts, there is a significant change in $Re^{6+/5+}$ reduction potential of +520 mV for **3** vs. **2**. Indeed, **2**, which has a more electron-

rich Re center than **3** based on their relative Re^{6+} reduction potentials, is predicted to have the most electron-*deficient* nitride by ^{15}N NMR spectroscopy, assuming that the chemical shifts show the same correlations with electron density in **1**–**3** as in organic compounds. This suggests that the electron-richness of the Re center may not be the only factor affecting the electron-richness of the nitride ligand. However, it is worth noting that difference in charge between **3** and **1–2** may also play a large role in the differences in redox potentials between the complexes; furthermore, since **1–3** are generally unreactive at the nitride, we could not experimentally test the Lewis basicity trends hinted by the ^{15}N NMR chemical shifts.

To supplement our spectroscopic studies, we compared the DFT models of complexes **1–5**. These models demonstrate that oxidation of the amide to form a nitroxide has an effect on the distribution and relative energy of the frontier molecular orbitals. The perturbation of molecular orbitals by replacing Re-amide interactions with Re-nitroxide interactions may be responsible for the decreased electron-richness of the nitride ligand in complex **2** vs. complex **3**. The redox trends between **1**, **2**, and **3** are reproduced with DFT calculations using these models, which validates the accuracy of the computational method (see **Tables 3.8–10**). NBO analysis of the series predicts changes in the Re-nitride Wiberg bond orders that match the experimentally observed trends in Re-nitride stretching frequencies (**Figure 3.16b** and **Figure 3.17**). These trends indicate that oxidation of the Re metal center results in a slight decrease in Re-nitride partial bond order, with **4** having the lowest Re-nitride bond order of 2.38.

Table 3.8. Calculated energies for complexes **1–5**, Cp_2Fe, $[Cp_2Fe]^+$, and theoretical complex $[(P^HNP)Re(N)(Cl)]^{2+}$ (PBE0/D3).

Complex	Free Energy (THF, hartrees)	Free Energy (gas-phase, hartrees)	Thermal correction to free energy (gas-phase, kcal/mol)
(PNP)Re(N)(Cl) (**1**)	–1673.557973	–1673.540488	0.560595
(P^ONP)Re(N)(Cl) (**2**)	–1748.689901	–1748.674239	0.567371
$[(P^HNP)Re(N)(Cl)]^+$ (**3**)	–1674.002372	–1673.934679	0.575024
$[(P^ONP)Re(N)(Cl)]^+$ (**4**)	–1748.508188	–1748.457007	0.565944
$[(PNP)Re(N)(Cl)]^+$ (**5**)	–1673.385201	–1673.329878	0.560574
$[(P^HNP)Re(N)(Cl)]^{2+}$	–1673.78884	–1673.589491	0.57444
Cp_2Fe	–510.057403	–510.053164	0.136952
$[Cp_2Fe]^+$	–509.86017	–509.797472	0.136092

Table 3.9. Calculated (PBE0/D3) $Re^{6+/5+}$ couples for complexes **1–3** and $[Cp_2Fe]^+/Cp_2Fe$ couple.

Complex	Corrected Free Energy (gas-phase, kcal/mol)	Free Energy (THF, kcal/mol)	Solvation Energy (kcal/mol)	Redox Energy (gas-phase, kcal/mol)	Redox Energy (THF, kcal/mol)	Redox Potential (V)
(PNP)Re(N)(Cl)	–1.0498E+06	–1.0502E+06	–362.75	–132.15	–108.42	4.70
$[(PNP)Re(N)(Cl)]^+$	–1.0497E+06	–1.0501E+06	–386.48			
(P^ONP)Re(N)(Cl)	–1.0970E+06	–1.0973E+06	–365.86	–135.42	–114.03	4.94
$[(P^ONP)Re(N)(Cl)]^+$	–1.0968E+06	–1.0972E+06	–387.25			
$[(P^HNP)Re(N)(Cl)]^+$	–1.0500E+06	–1.0505E+06	–403.31	–216.24	–133.99	5.81
$[(P^HNP)Re(N)(Cl)]^{2+}$	–1.0498E+06	–1.0503E+06	–485.56			
Cp_2Fe	–3.1998E+05	–3.2007E+05	–88.60	–159.91	–123.77	5.37
$[Cp_2Fe]^+$	–3.1982E+05	–3.1994E+05	–124.74			

Table 3.10. Calculated (PBE0/D3) vs. experimental $Re^{6+/5+}$ couples for complexes **1–3** vs. $[Cp_2Fe]^+/Cp_2Fe$. The absolute redox potentials vs. Fc are not accurately predicted by these calculations. However, the trends in redox potential are correct, though the magnitude of the difference in redox potential between these compounds is overestimated.

Redox Couple	Calculated Redox Potential (V vs. Fc.)	Experimental Redox Potential (V vs. Fc)	Relative Calculated Redox Potential	Relative Experimental Redox Potential
$[(PNP)Re(N)(Cl)]^+/(PNP)Re(N)(Cl)$	–0.67	–0.08	0.00	0.00
$[(P^ONP)Re(N)(Cl)]^+/(P^ONP)Re(N)(Cl)$	–0.43	0.00	0.24	0.08
$[(P^HNP)Re(N)(Cl)]^{2+}/[(P^HNP)Re(N)(Cl)]^+$	0.44	0.60	1.11	0.68

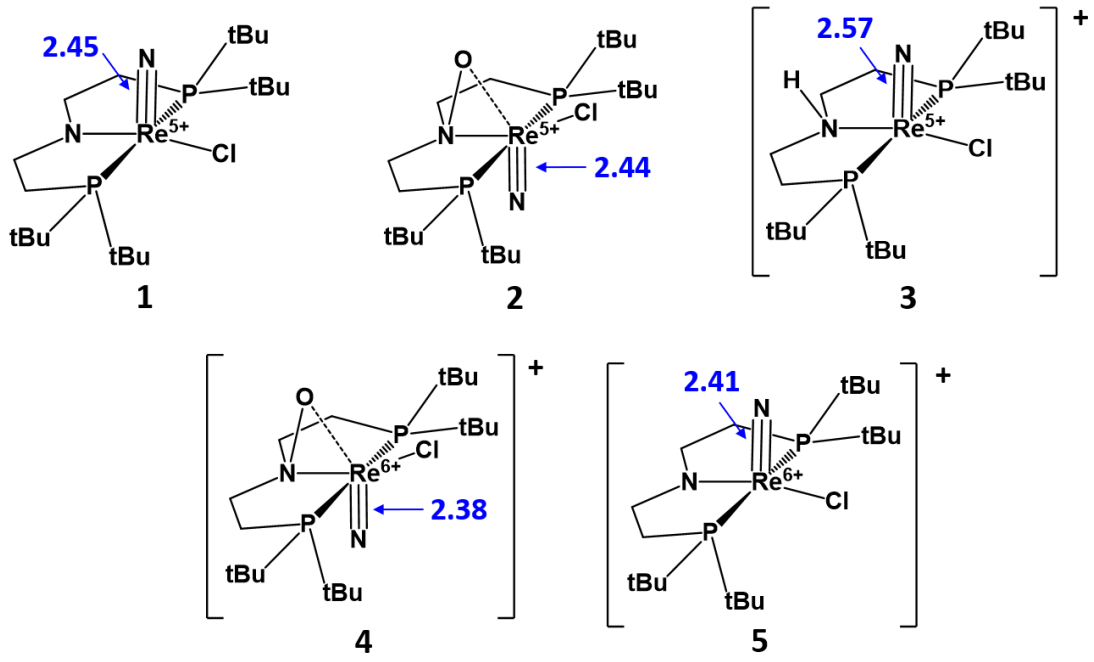

Figure 3.17. Calculated Wiberg bond order of Re-nitride bonds in complexes **1**–**5**.

3.2.4. Oxidation-induced change in nitride reactivity

At ambient temperature in CD_2Cl_2, addition of 1.2 equiv of PPh_3 to **4** leads to slow formation over the course of several hours of a new product (**Scheme 3.3**, drawn as **6**). The $^{31}P\{^1H\}$ NMR spectrum of the solution shows two singlets in a 2:1 ratio at δ 71.6 ppm and δ 54.6 ppm, respectively. Formation of this product is accompanied by loss of the PPh_3 signal, which is matched by an analogous change in the PPh_3 resonances in the corresponding ^1H NMR spectra. These data are consistent with formation of a diamagnetic Re^{3+}-phosphinimide complex, which would require an additional $1e^-$ reduction of the complex formed from initial $2e^-$ reduction of the nitride to phosphinimide. To determine whether **6** is indeed a phosphinimide complex, PPh_3 was reacted with **4-^{15}N**. This resulted in splitting of the ^{31}P resonance at δ 54.6 ppm into a doublet (J = 35.1 Hz), demonstrating that PPh_3 binds to the ^{15}N-labeled nitride (**Figure 3.18**, inset).

Scheme 3.3. Formation of phosphinimide complex **6** upon addition of PPh_3 to **4**.

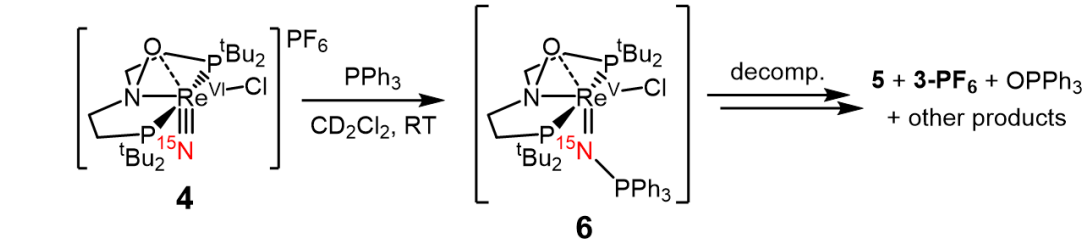

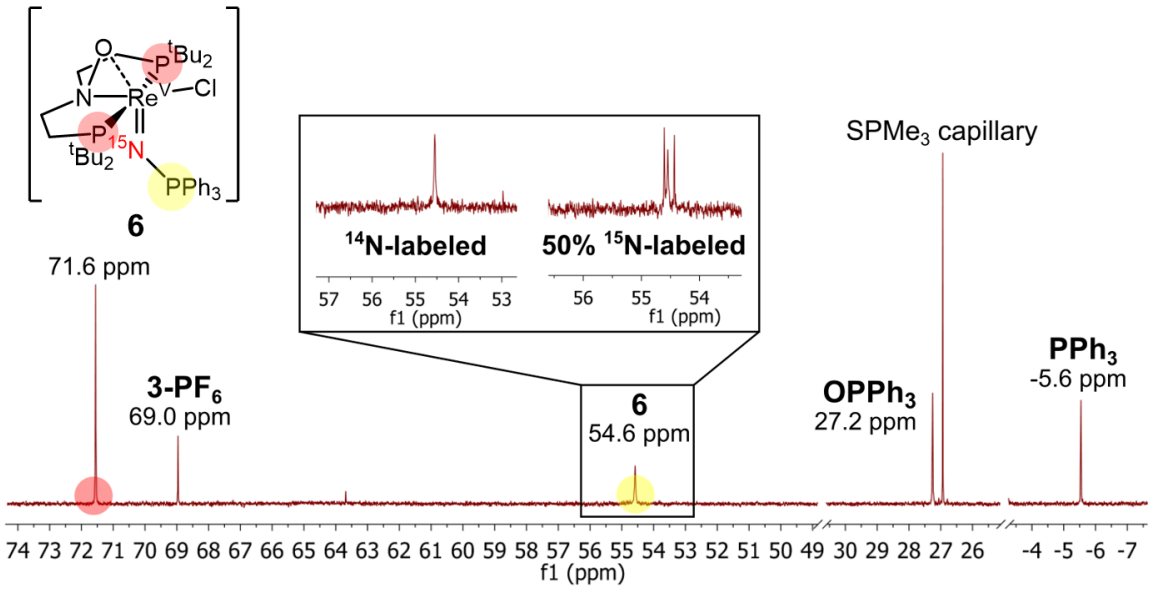

Figure 3.18. $^{31}P\{^1H\}$ NMR spectrum of **4** with PPh_3 in CD_2Cl_2 after 15 hours showing formation of a phosphinimide intermediate **6**. **Inset:** Difference in splitting of ^{31}P resonance at δ 54.6 ppm depending on N isotope used.

Formation of a phosphinimide from **4** with phosphines can involve the nitride acting either as an electrophile[24] or, less commonly, a nucleophile.[60] To assess the nature of the transition state during the reaction of the nitride ligand in **4** with phosphines, we varied the phosphines with substituents of differing electron richness. When **4** is mixed with stoichiometric tris-(*p*-tolyl)phosphine (P(*p*-tolyl)$_3$) or tris-(4-fluorophenyl)phosphine (P(4-^{F}Ph)$_3$), formation of phosphinimide complexes **6-P(*p*-tolyl)$_3$** (**Figures 3.19–20**) and **6-(4-^{F}Ph)$_3$**, (**Figure 3.21–22**) respectively, is observed by ^1H and $^{31}P\{^1H\}$ NMR spectroscopy. Since ^1H and $^{31}P\{^1H\}$ NMR spectra indicate that the phosphinimide complex

is the first product observed from reaction of **4** with phosphines, following the consumption of the distinct UV-Vis absorbance feature of **4** with λ_{max} = 668 nm allowed us to qualitatively compare the rates of phosphinimide complex formation. To determine the kinetic preference of **4** for phosphines of different electron-richness, we compared the consumption of **4** in the presence of P(4-^{F}Ph)$_3$, PPh$_3$, and P(*p*-tolyl)$_3$ under pseudo-first order conditions (10 equiv phosphine). Under identical reaction conditions, **4** reacts more quickly in the presence of P(*p*-tolyl)$_3$ than PPh$_3$, which in turn reacts more quickly than P(4-^{F}Ph)$_3$ (**Figure 3.23**). Assuming that consumption of **4** corresponds to formation of the phosphinimide complex **6**, which is consistent with NMR data (see **Figures 3.19-22**), we can conclude that the rate of P–N bond formation with the more nucleophilic phosphine is more rapid. We were unable to extract quantitative rate data in this system due to the perceived complicated mechanism of reaction, which results in multiple products formed by NMR spectroscopy and unexpected double-exponential behavior of the kinetic traces. However, this qualitative observation indicates that the nitride ligand in **4** behaves as an electrophile. Furthermore, in a competition experiment containing 1 equiv of both P(*p*-tolyl)$_3$ and P(4-^{F}Ph)$_3$, **4** reacts preferentially with P(*p*-tolyl)$_3$ to form **6-P(*p*-tolyl)$_3$** (**Scheme 3.4**), and no formation of **6-P(4-^{F}Ph)$_3$** is observed (**Figures 3.24–25**). The addition of excess P(*p*-tolyl)$_3$ to solution containing **6-P(4-^{F}Ph)$_3$** results in immediate conversion of the phosphinimide complex to **6-P(*p*-tolyl)$_3$**, suggesting a labile N–P interaction that favors the more electron-rich phosphinimide (**Figure 3.26**). This is evidence of a thermodynamic preference for formation of the more electron-rich phosphinimide due to a more stable N–P interaction, which further complicates the kinetic analysis of this reaction. It is significant that only complex **4**, in which both the backbone amide and metal center of **1** have been

oxidized, was found to react with phosphines to form transiently observed phosphinimide products. This demonstrates that the nitride in **4** is electrophilic enough to undergo reaction with nucleophiles, representing a reversal of reactivity at the nitride ligand relative to **1**, wherein the nitride reacts as a nucleophile with carbon electrophiles.[8, 21] Importantly, *umpolung* that makes the nitride electrophilic appears to require *both* oxidation of the backbone to form a nitroxide *and* 1e^- oxidation of the metal center to form a Re^{6+} complex, as neither **2** (just oxidized at ligand) nor **5** (just oxidized at Re) react with phosphine nucleophiles (**Figures 3.27** and **3.28**, respectively). Since **2** and **5** do not react with phosphines, it suggests that neither 1e^- reduction of **4** (to form **2**) nor O-atom abstraction from the nitroxide in **4** (to form **5**) occurs prior to phosphinimide formation.

Scheme 3.4. Competition reaction between P(*p*-tolyl)$_3$ and P(4-^{F}Ph)$_3$ with **4**.

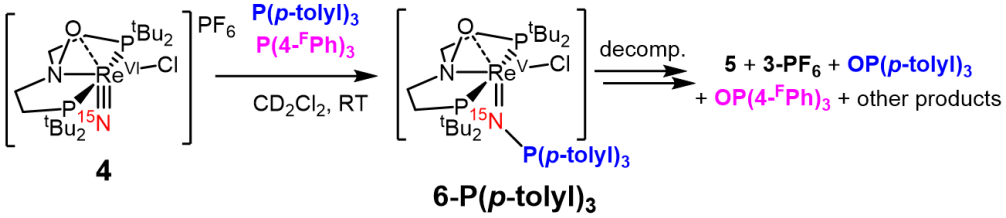

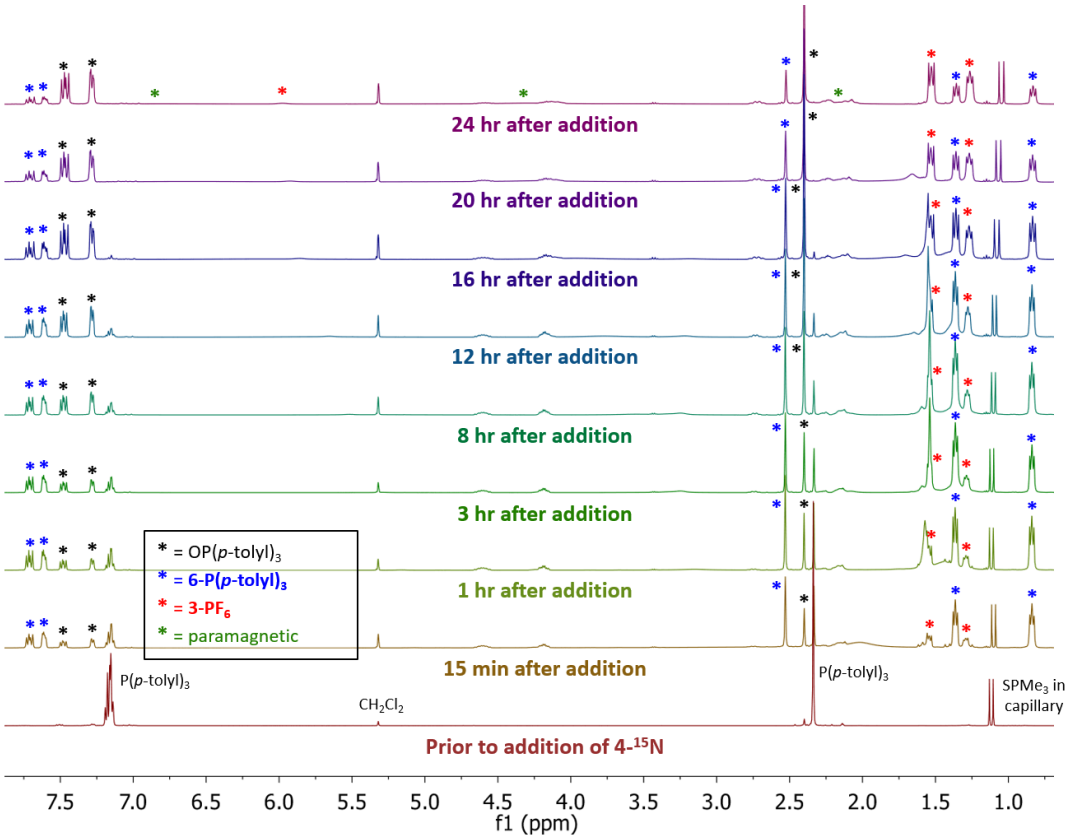

Figure 3.19. ^{1}H NMR spectra (500 MHz, CD_2Cl_2) of tris(*p*-tolyl)phosphine (P(*p*-tolyl)$_3$, 40 mM, 1 equiv) and **4-^{15}N** (40 mM, 1 equiv) at ambient temperature. The reaction demonstrated analogous color changes to the reaction of **4** with PPh_3. The formation of a phosphinimide complex analogous to **6** (**6-P(*p*-tolyl)$_3$**) is denoted by blue asterisks: δ 7.65–7.48 (m, 12H, *o,m*-C*H*), δ 2.53 (s, 9H, *p*-CH_3), δ 1.36 (m, 18H, P*t*Bu_2), δ 0.83 (m, 18H, P*t*Bu_2). Methylene resonances could not be confidently assigned due to the number of products generated. The formation of OP(*p*-tolyl)$_3$ is denoted by black asterisks, the formation of **3-PF$_6$** is denoted by red asterisks, and broad paramagnetic features (likely **5**) are denoted by green asterisks. Integration vs. the $SPMe_3$ capillary gives yields of **6-P(*p*-tolyl)$_3$**, OP(*p*-tolyl)$_3$, and unreacted P(*p*-tolyl)$_3$.

Table 3.11. Yields of compounds over time during the addition of P(p-tolyl)$_3$ to **4**, measured by ^{1}H NMR spectroscopy.

Time	*Yield of* ***6-P(p-tolyl)$_3$***	*Yield of OP(p-tolyl)$_3$*	*Unreacted P(p-tolyl)$_3$*
15 min	44%	24%	32%
1 h	42%	24%	23%
3 h	44%	31%	20%
8 h	35%	42%	13%
12 h	35%	51%	9%
16 h	30%	59%	3%
20 h	28%	71%	-
24 h	19%	78%	-

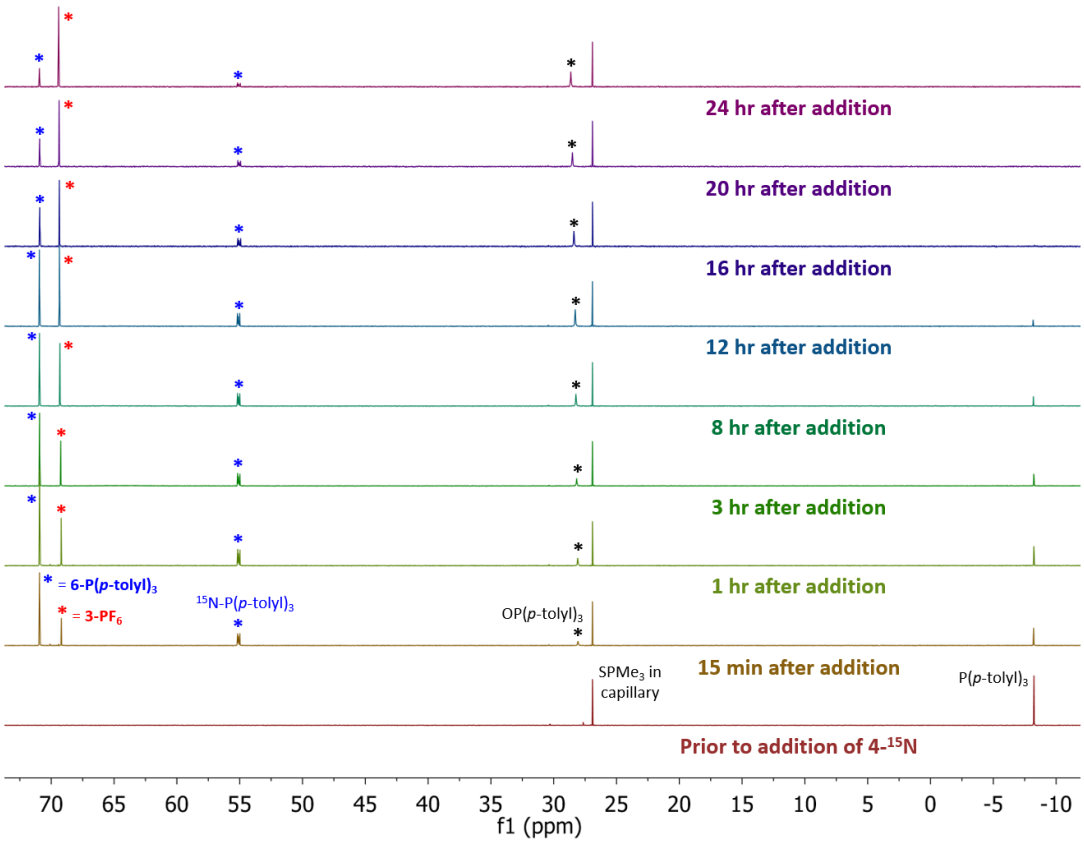

Figure 3.20. ^{31}P NMR spectra (202 MHz, CD_2Cl_2) of tris(*p*-tolyl)phosphine (P(*p*-tolyl)$_3$, 40 mM, 1 equiv) and **4-^{15}N** (40 mM, 1 equiv) at ambient temperature. The reaction demonstrated analogous color changes to the reaction of **4** with PPh_3. A complex analogous to **6** (**6-P(*p*-tolyl)$_3$**: δ 70.9, s, *P*tBu_2; δ 55.1, s, N-*P*(*p*-tolyl)$_3$) was observed after 15 min at ambient temperature, labeled with blue asterisks. The resonance at δ 55.1 is split into a doublet by the ^{15}N-labeled nitride (J = 35.2 Hz). Integration vs. the $SPMe_3$ capillary gives spectroscopic yields of **6-P(*p*-tolyl)$_3$**, OP(*p*-tolyl)$_3$ (δ 28.1, s, black asterisks), and **3-PF_6** (δ 68.9, s, *P*tBu_2, red asterisks) similar to those obtained from the ^{1}H NMR spectra (see **Figure 3.19**).

Table 3.12. Yields of compounds over time during the addition of P(p-tolyl)$_3$ to **4**, measured by ^{31}P{^{1}H} NMR spectroscopy.

Time	*Yield of* ***6-P(p-tolyl)$_3$***	*Yield of OP(p-tolyl)$_3$*	*Yield of* ***3-PF_6***
15 min	56%	22%	14%
1 h	57%	25%	19%
3 h	55%	32%	22%
8 h	49%	44%	27%
12 h	45%	51%	32%
16 h	38%	63%	29%
20 h	34%	70%	38%
24 h	22%	82%	46%

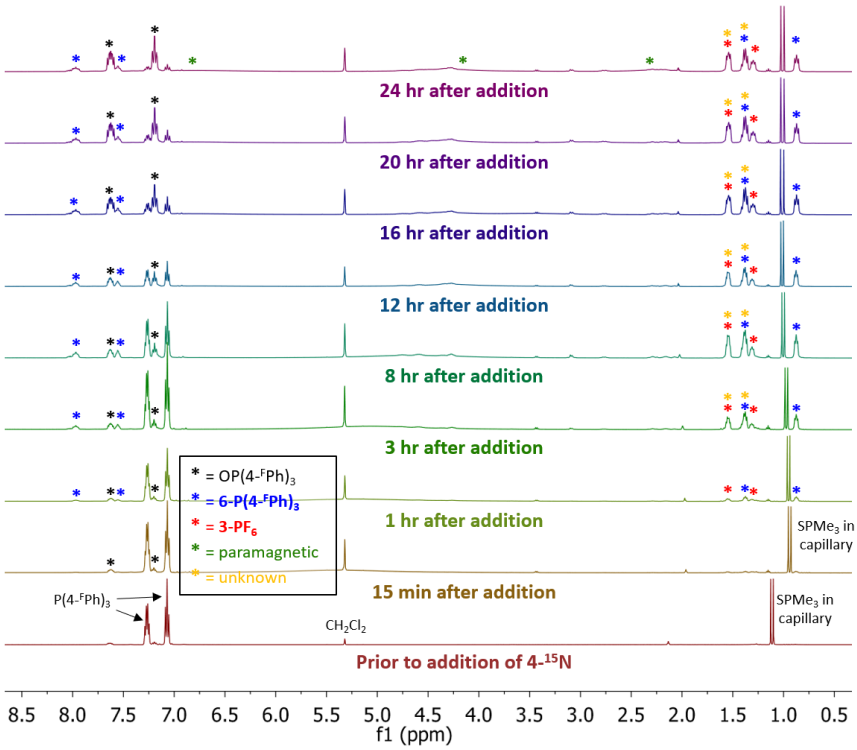

Figure 3.21. ^{1}H NMR spectra (500 MHz, CD_2Cl_2) of tris(4-fluorophenyl)phosphine (P(4-^{F}Ph)$_3$, 40 mM, 1 equiv) and **4-^{15}N** (40 mM, 1 equiv) at ambient temperature. The reaction demonstrated analogous color changes to the reaction of **4** with PPh_3, but these color changes occurred much more slowly. The formation of a phosphinimide complex analogous to **6** (**6-P(4-^{F}Ph)$_3$**) is denoted by blue asterisks: δ 7.27 (m, 6H, *m*-C*H*), δ 7.07 (m, 6H, *o*-C*H*), δ 1.38 (m, 18H, P*t*Bu$_2$), δ 0.87 (m, 18H, P*t*Bu$_2$). Methylene resonances could not be confidently assigned due to the number of products generated. Formation of OP(4-^{F}Ph)$_3$ is denoted by black asterisks, formation of **3-PF$_6$** is denoted by red asterisks, formation of an unknown diamagnetic product is denoted by orange asterisks, and broad paramagnetic features (likely **5**) are denoted by green asterisks. Integration vs. the $SPMe_3$ capillary gives yields of **6-P(4-^{F}Ph)$_3$**, OP(4-^{F}Ph)$_3$, and unreacted P(4-^{F}Ph)$_3$. Despite the same concentration of reagents as the analogous experiment with P(*p*-tolyl)$_3$ (see **Figures 3.19–20**), formation of **6-P(4-^{F}Ph)$_3$** and OP(4-^{F}Ph)$_3$, as well as consumption of P(4-^{F}Ph)$_3$, is much slower than formation of **6-P(*p*-tolyl)$_3$** and OP(*p*-tolyl)$_3$, and slower than consumption of P(*p*-tolyl)$_3$.

Table 3.13. Yields of compounds over time during the addition of P(4-^{F}Ph)$_3$ to **4**, measured by ^{1}H NMR spectroscopy.

Time	*Yield of* ***6-P(4-^{F}Ph)$_3$***	*Yield of OP(4-^{F}Ph)$_3$*	*Unreacted P(4-^{F}Ph)$_3$*
15 min	3%	9%	88%
1 h	5%	11%	85%
3 h	9%	14%	80%
8 h	14%	22%	61%
12 h	17%	34%	45%
16 h	19%	55%	28%
20 h	18%	64%	22%

24 h	17%	67%	15%

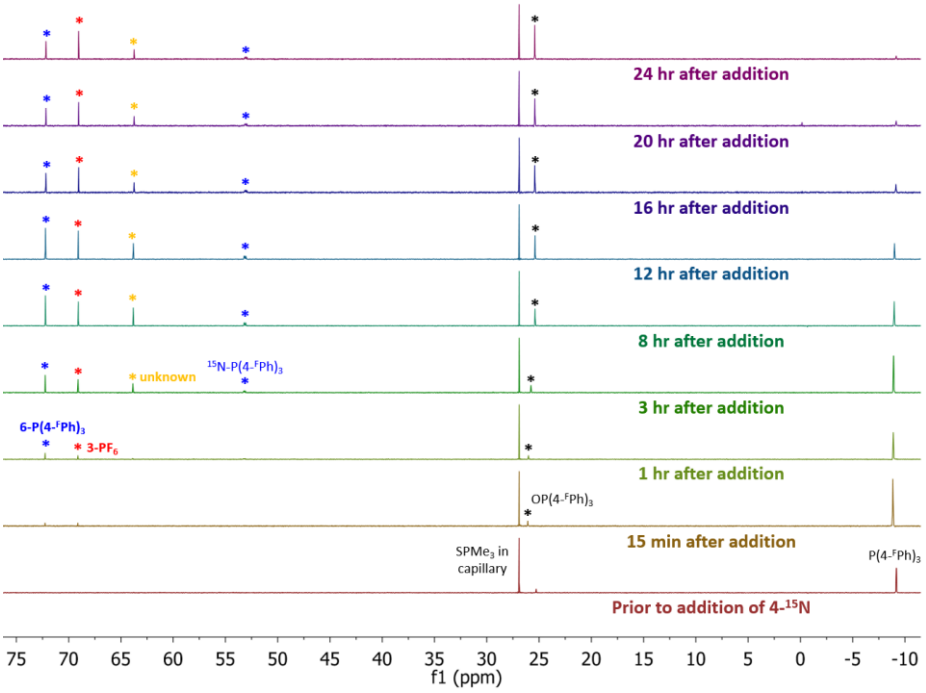

Figure 3.22. ^{31}P NMR spectra (202 MHz, CD_2Cl_2) of tris(4-fluorophenyl)phosphine (P(4-^{F}Ph)$_3$, 40 mM, 1 equiv) and **4-^{15}N** (40 mM, 1 equiv) at ambient temperature. The reaction demonstrated analogous color changes to the reaction of **4** with PPh_3. A complex analogous to **6** (**6-P(4-^{F}Ph)$_3$**: δ 72.2, s, *P*tBu_2; δ 53.3, s, N–*P*(4-^{F}Ph)$_3$) was observed in small spectroscopic yield after 1 h at ambient temperature, labeled with blue asterisks. The resonance at δ 53.3 is split into a doublet by the ^{15}N-labeled nitride (J = 35.6 Hz). Formation of OP(4-^{F}Ph)$_3$ is denoted by black asterisks, formation of **3-PF$_6$** is denoted by red asterisks, and formation of an unknown diamagnetic product is denoted by orange asterisks. Integration vs. the $SPMe_3$ capillary gives spectroscopic yields of **6-P(4-^{F}Ph)$_3$**, OP(4-^{F}Ph)$_3$ (δ 25.8, s), unreacted P(4-^{F}Ph)$_3$ (δ –8.9, s), and **3-PF$_6$** (δ 69.1, s, *P*tBu_2) similar to those obtained from the ^{1}H NMR spectra (see **Figure 3.21**). Despite the same concentration of reagents as the analogous experiment with P(*p*-tolyl)$_3$ (see **Figures 3.19–20**), formation of **6-P(4-^{F}Ph)$_3$** and OP(4-^{F}Ph)$_3$, as well as consumption of P(4-^{F}Ph)$_3$, is much slower than formation of **6-P(*p*-tolyl)$_3$** and OP(*p*-tolyl)$_3$, and slower than consumption of P(*p*-tolyl)$_3$.

Table 3.14. Yields of compounds over time during the addition of P(4-^{F}Ph)$_3$ to **4**, measured by ^{31}P{^{1}H} NMR spectroscopy.

Time	*Yield of* ***6-P(4-^{F}Ph)$_3$***	*Yield of OP(4-^{F}Ph)$_3$*	*Yield of* ***3-PF$_6$***
15 min	0%	7%	0%
1 h	4%	9%	2%
3 h	8%	11%	4%
8 h	15%	21%	8%
12 h	18%	37%	10%
16 h	17%	56%	11%
20 h	18%	64%	11%
24 h	16%	74%	12%

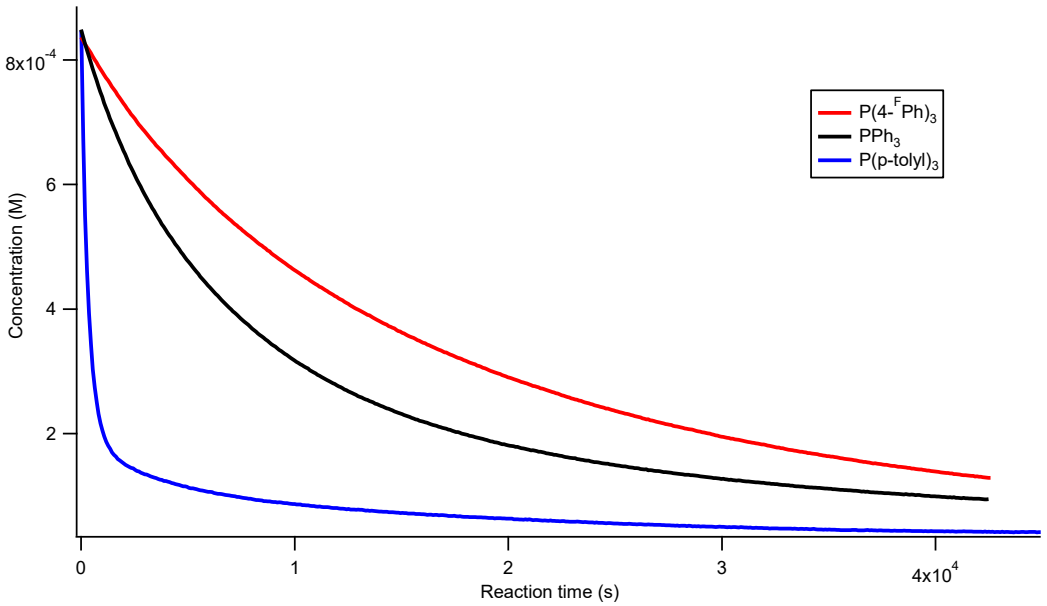

Figure 3.23. Consumption of **4** over time in the presence of 10 equiv P(4-^{F}Ph)$_3$ (red), PPh$_3$ (black), or P(*p*-tolyl)$_3$ (blue). For each reaction, a 0.40 mL solution of 69.5 mM phosphine (2.78 x 10^{-5} mol, 10 equiv.) was added to a cuvette containing a 1.80 mL solution of 1.55 mM **4** (2.78 x 10^{-6} mol, 1 equiv.). The cuvettes were capped, shaken vigorously, and the absorbance at λ = 668 nm was monitored for 12.5 hours by UV-Vis spectroscopy. Due to the procedure used, some of **4** was consumed prior to monitoring the reaction. To more directly compare the reaction traces, the traces above were time-normalized to have t = 0 at the same concentration of **4** (8.3 mM).

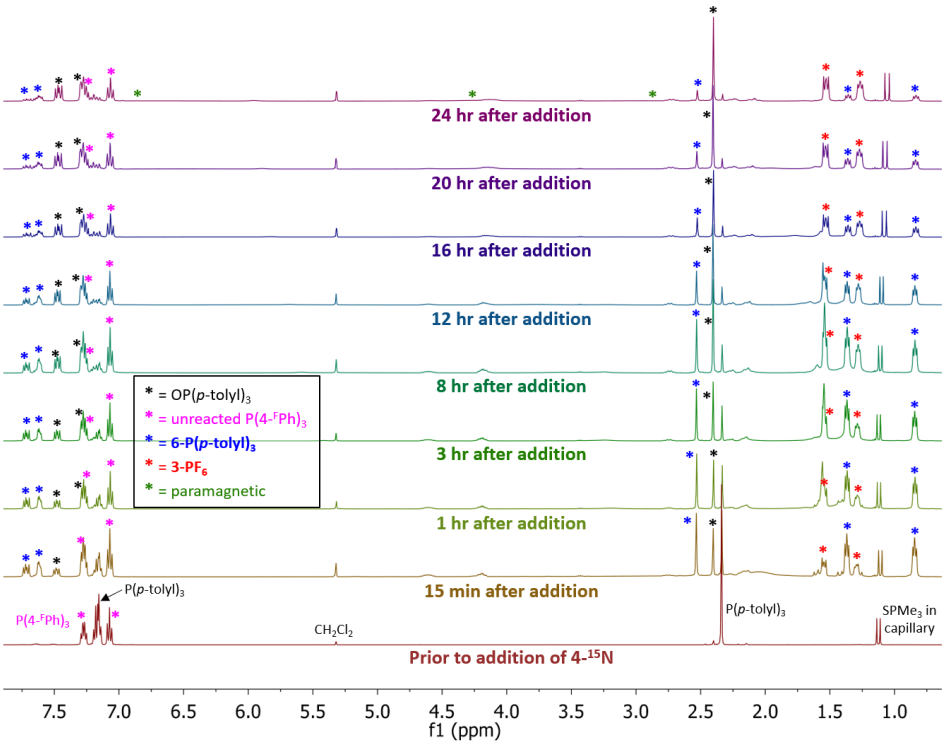

Figure 3.24. ^{1}H NMR spectra (500 MHz, CD_2Cl_2) of P(*p*-tolyl)$_3$ (40 mM, 1 equiv), P(4-^{F}Ph)$_3$ (40 mM, 1 equiv), and **4-^{15}N** (40 mM, 1 equiv) at ambient temperature. The reaction demonstrated analogous color changes to the reaction of **4** with PPh_3. **4-^{15}N** reacts preferentially with P(*p*-tolyl)$_3$ to form **6-P(*p*-tolyl)$_3$**, with no formation of **6-P(4-^{F}Ph)$_3$** observed in the ^{1}H NMR spectra. Formation of phosphinimide complex **6-P(*p*-tolyl)$_3$** is denoted by blue asterisks: δ 7.65–7.48 (m, 12H, *o,m*-C*H*), δ 2.53 (s, 9H, *p*-CH_3), δ 1.36 (m, 18H, P*t*Bu$_2$), δ 0.83 (m, 18H, P*t*Bu$_2$). Methylene resonances could not be confidently assigned due to the number of products generated. Unreacted P(4-^{F}Ph)$_3$ is denoted by magenta asterisks, formation of OP(*p*-tolyl)$_3$ is denoted by black asterisks, formation of **3-PF_6** is denoted by red asterisks, and broad paramagnetic features (likely **5**) are denoted by green asterisks. Integration of *p*-tolyl peaks vs. the $SPMe_3$ capillary gives yields of **6-P(*p*-tolyl)$_3$**, OP(*p*-tolyl)$_3$, and unreacted P(*p*-tolyl)$_3$; and integration of *o*-C*H* peaks gives the relative amount of unreacted P(4-^{F}Ph)$_3$. After 24 h, only roughly ~10% of P(*p*-tolyl)$_3$ remained unreacted, while more than 90% P(4-^{F}Ph)$_3$ remained unreacted.

Table 3.15. Yields of compounds over time during the addition of equimolar P(*p*-tolyl)$_3$ and P(4-^{F}Ph)$_3$ to **4**, measured by ^{1}H NMR spectroscopy.

Time	*Yield of* ***6-P(p-tolyl)$_3$***	*Yield of OP(p-tolyl)$_3$*	*Unreacted P(p-tolyl)$_3$*	*Unreacted P(4-^{F}Ph)$_3$*
15 min	39%	27%	34%	96%
1 h	41%	33%	26%	101%
3 h	39%	40%	21%	100%
8 h	32%	52%	16%	103%
12 h	28%	59%	13%	101%
16 h	23%	66%	10%	96%
20 h	19%	71%	10%	91%
24 h	14%	78%	9%	93%

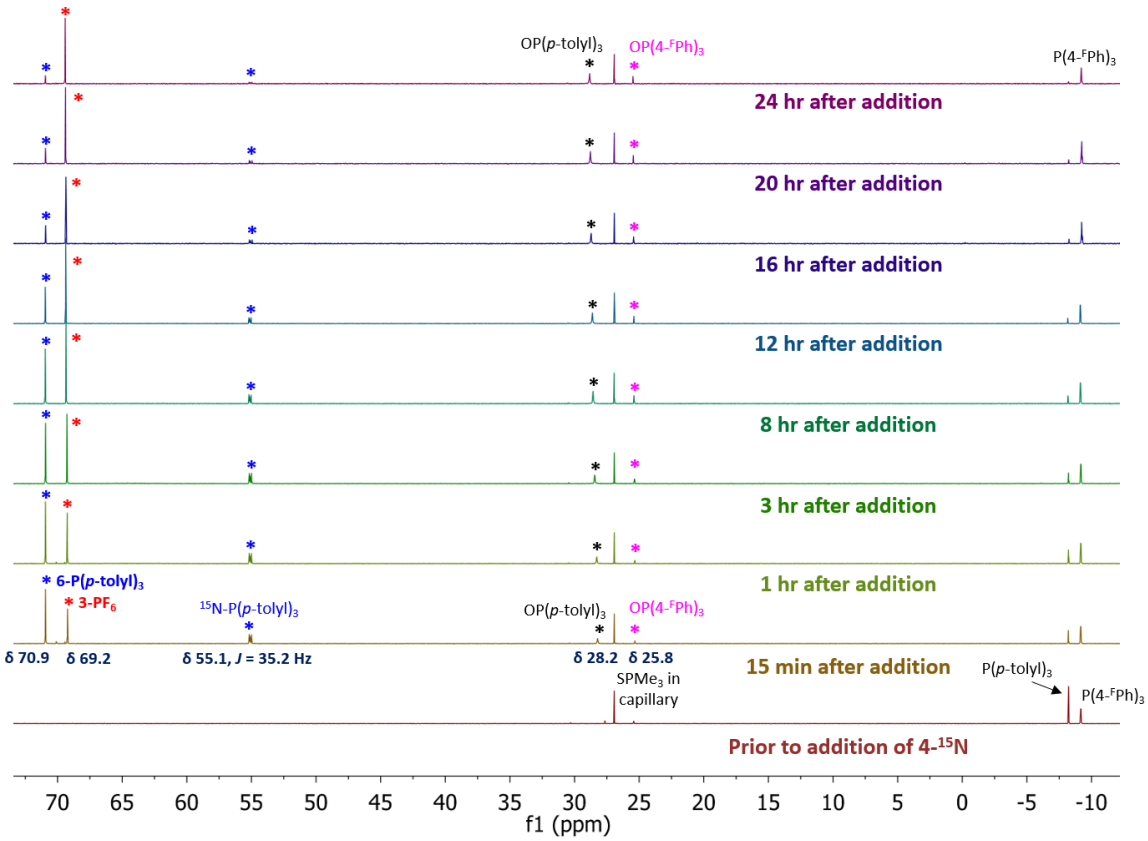

Figure 3.25. $^{31}P\{^{1}H\}$ NMR spectra (202 MHz, CD_2Cl_2) of P(*p*-tolyl)$_3$ (40 mM, 1 equiv), P(4-^{F}Ph)$_3$ (40 mM, 1 equiv), and **4-^{15}N** (40 mM, 1 equiv) at ambient temperature. The reaction demonstrated analogous color changes to the reaction of **4** with PPh_3. **4-^{15}N** reacts preferentially with P(*p*-tolyl)$_3$ to form **6-P(*p*-tolyl)$_3$**, with no formation of **6-P(4-^{F}Ph)$_3$** observed in the $^{31}P\{^{1}H\}$ NMR spectra. Formation of phosphinimide complex **6-P(*p*-tolyl)$_3$** (δ 70.9, s, *P*tBu$_2$; δ 55.1, s, N-*P*(*p*-tolyl)$_3$) is denoted by blue asterisks and occurs within the first 15 minutes. The resonance at δ 55.1 is split into a doublet by the ^{15}N-labeled nitride (J = 35.2 Hz). By integration vs. $SPMe_3$, only 6% P(*p*-tolyl)$_3$ remained unreacted after 24 h, while 80% P(4-^{F}Ph)$_3$ remained unreacted after 24 h. Note that both OP(*p*-tolyl)$_3$ (δ 28.2, s) and OP(4-^{F}Ph)$_3$ (δ 25.8, s) are formed during the reaction. The observation of OP(4-^{F}Ph)$_3$ indicates that one mechanism of decomposition is likely the abstraction of the nitroxide O-atom by free phosphine in solution, since **6-P(4-^{F}Ph)$_3$** is not observed under these conditions. This also provides an explanation for why some P(4-^{F}Ph)$_3$ is consumed during the reaction.

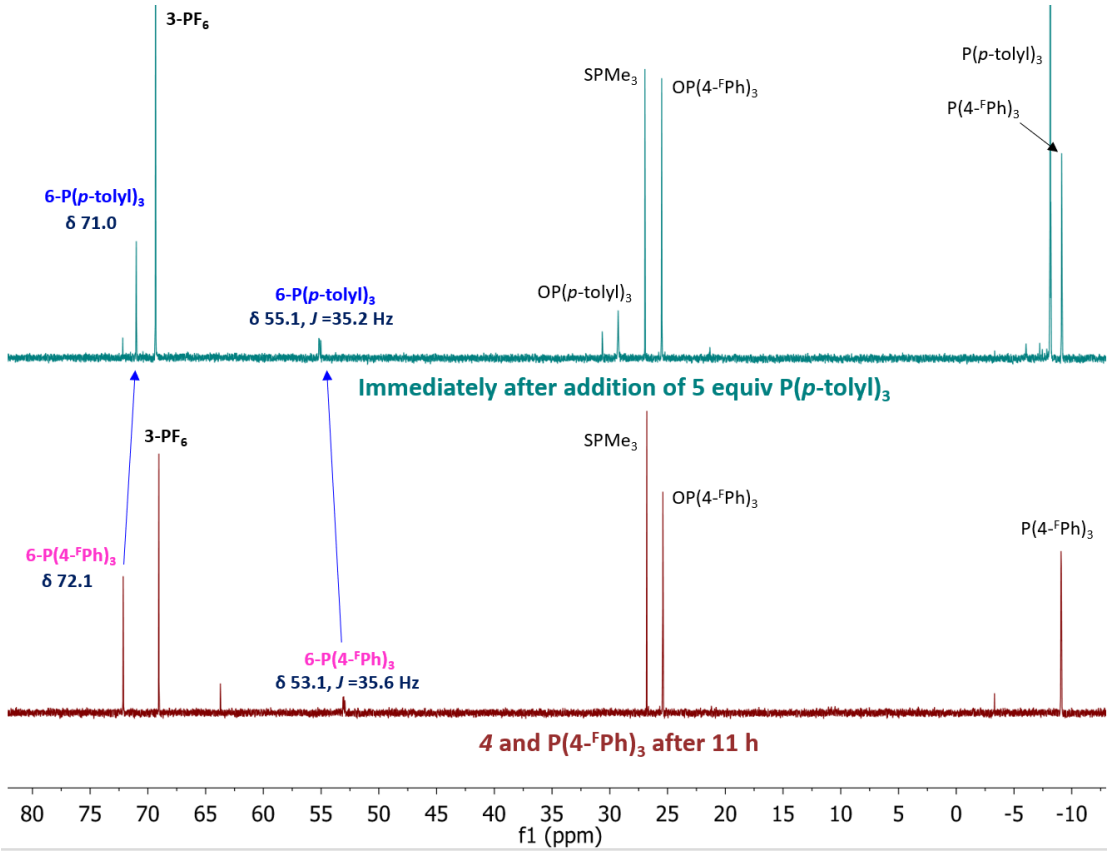

Figure 3.26. ^{31}P NMR spectra (202 MHz, CD_2Cl_2) of exchange reaction between **6-P(4-^{F}Ph)$_3$** and excess P(*p*-tolyl)$_3$ to form **6-P(*p*-tolyl)$_3$**. Bottom: Reaction of **6** (53 mM, 1 equiv) with P(4-^{F}Ph)$_3$ (80 mM, 1.5 equiv) in CD_2Cl_2 after 11 h at RT, showing buildup of phosphinimide complex **6-P(4-^{F}Ph)$_3$** (δ 72.1, s, *P*tBu$_2$; δ 53.1, s, N–*P*(4-^{F}Ph)$_3$) along with formation of **3-PF$_6$** (δ 69.1, s, *P*tBu$_2$) and OP(4-^{F}Ph)$_3$. Top: Spectrum immediately after addition of excess P(*p*-tolyl)$_3$ (5 equiv). All **6-P(4-^{F}Ph)$_3$** is converted to **6-P(*p*-tolyl)$_3$** (δ 71.0, s, *P*tBu$_2$; δ 55.1, s, N–*P*(*p*-tolyl)$_3$), indicating that phosphine exchange from the phosphinimide occurs. This exchange favors P(*p*-tolyl)$_3$ as the more electron-rich phosphine. $SPMe_3$ is from the internal capillary.

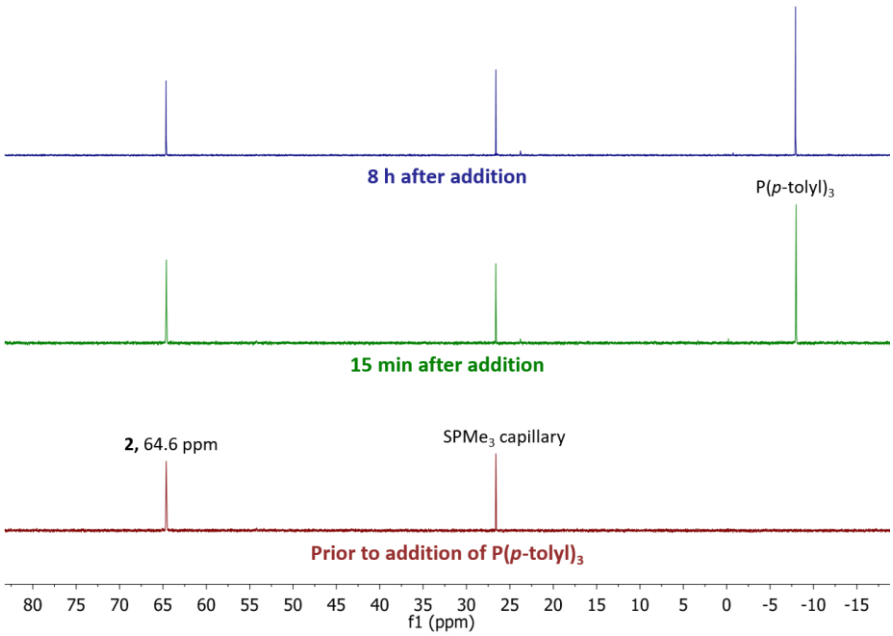

Figure 3.27. $^{31}P\{^{1}H\}$ NMR spectra (202 MHz, CD_2Cl_2) of **2** (15.6 mM, 1 equiv) prior to (bottom) and after the addition of P(*p*-tolyl)$_3$ (1.5 equiv), demonstrating no reaction even after 8 h at ambient temperature. $SPMe_3$ is from the internal capillary.

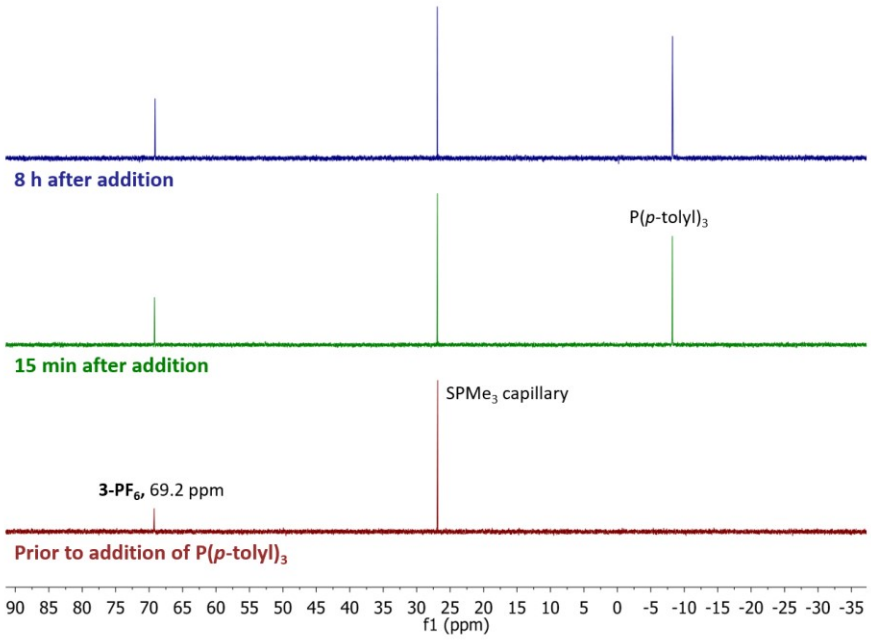

Figure 3.28. ^{1}H NMR spectra (202 MHz, CD_2Cl_2) of **5** (13.5 mM, 1 equiv) prior to (bottom) and after the addition of P(*p*-tolyl)$_3$ (1.5 equiv), demonstrating no formation of a phosphinimide complex even after 8 h at ambient temperature. **5** contains **3-PF$_6$** as an impurity (δ 69.2, s, *P*tBu_2), which also is formed slowly from decomposition of the unstable complex **5**. $SPMe_3$ is from the internal capillary.

The phosphinimide product **6** is unstable under the reaction conditions and decomposes to **3-PF$_6$** (^{31}P resonance at δ 69 ppm), a paramagnetic complex (which resembles **5** by ^{1}H NMR spectroscopy), and $OPPh_3$, among other unidentified phosphorus-containing products. The concentration of **6** during the reaction reached a maximum 15 hours into the reaction at approx. 31% spectroscopic yield by integration vs. an internal standard under these conditions (see **Figure 3.18**). The instability of **6** has precluded its isolation as a pure material. The formation of **3-PF$_6$**, the paramagnetic species, and $OPPh_3$ is observed only after **6** is formed, which suggests that $OPPh_3$ is formed by net O-atom abstraction from the nitroxide to a PPh_3. This could either be from the phosphinimide or free PPh_3 in the reaction. However, in phosphinimide-forming reactions that contain both P(*p*-tolyl)$_3$ and P(4-^{F}Ph)$_3$, phosphine oxides of both phosphines are observed as decomposition products (see **Figure 3.25**). The observation of OP(4-^{F}Ph)$_3$ indicates that one mechanism of decomposition is likely the abstraction of the nitroxide O-atom by free phosphine in solution, since **6-P(4-^{F}Ph)$_3$** is not observed under these conditions.

DFT analysis of the atomic contributions to the lowest-unoccupied molecular orbitals (LUMOs) of **1–5** provides a rationalization for this reversal in reactivity (**Tables 3.16–20**). In complex **4,** the LUMO and LUMO+1 are more localized at the nitride ligand than in the rest of the series, which is consistent with increased electrophilic behavior at the nitride (**Figure 3.29**). Thus, the cooperative effect of ligand-centered and metal-centered oxidations has a notable effect on nitride reactivity despite the strong Re-nitrido interaction.

Table 3.16. Calculated atomic contributions to selected molecular orbitals for **1** (PBE0/D3). Contributions from hydrogen and carbon atoms are omitted.

	(PNP)Re(N)(Cl) (1)									
	Energy vs. HOMO (kcal/mol)	**Atomic orbital contributions to molecular orbital**								
Orbital		**Re-*p***	**Re-*d***	**Cl-*p***	**N-*p*** **nitride**	**N-*p*** **(amide**	**P-*p***	**P-*d***	**P'-*p***	**P'-*d***
HOMO –4	–67.14	0.06	0.04	0.54	0.05	-	-	-	-	-
HOMO –3	–55.52	-	0.04	0.67	0.19	-	-	-	-	-
HOMO –2	–47.06	0.05	0.10	0.10	-	-	0.22	-	0.22	-
HOMO –1	–17.57	0.03	-	-	0.11	0.57	-	-	-	-
HOMO	0.00	-	0.71	0.13	-	-	-	-	-	-
LUMO	109.19	-	0.33	-	**0.35**	-	0.06	0.04	0.06	0.04
LUMO +1	113.58	0.20	0.17	-	**0.11**	-	0.12	0.05	0.12	0.05
LUMO +2	123.62	0.10	0.35	0.10	**0.17**	0.04	-	-	-	-
LUMO +3	135.54	0.30	0.09	-	**-**	-	0.17	-	0.17	-
LUMO +4	140.56	0.23	0.14	-	**0.04**	-	-	-	-	-

Table 3.17. Calculated atomic contributions to selected molecular orbitals for **2** (PBE0/D3, without mCBA molecule). Contributions from hydrogen and carbon atoms are omitted.

	(P^ONP)Re(N)(Cl) (2)										
	Energy vs. HOMO (kcal/mol)	**Atomic orbital contributions to molecular orbital**									
Orbital		**Re-*p***	**Re-*d***	**Cl-*p***	**N-*p*** **nitride**	**N-*p*** **amide**	**O-*p***	**P-*p***	**P-*d***	**P'-*p***	**P'-*d***
HOMO –4	–53.34	0.04	0.10	0.09	0.04	-	0.27	0.10	-	0.10	-
HOMO –3	–51.46	0.04	-	0.71	0.17	-	-	-	-	-	-
HOMO –2	–32.63	-	0.05	-	-	-	0.50	0.11	-	0.11	-
HOMO –1	–24.47	-	-	0.04	0.18	0.11	0.51	-	-	-	-
HOMO	0.00	-	0.67	0.16	-	-	-	-	-	-	-
LUMO	112.95	-	0.36	-	**0.37**	-	-	0.04	-	0.04	-
LUMO +1	121.11	0.20	0.38	0.06	**0.22**	-	-	0.04	-	0.04	-
LUMO +2	133.03	0.18	0.20	-	**0.09**	-	0.03	0.10	0.05	0.10	0.05
LUMO +3	135.54	0.14	0.31	0.07	**0.05**	0.04	-	0.10	-	0.10	-
LUMO +4	143.07	0.26	-	-	**-**	-	-	0.12	-	0.12	-

Table 3.18. Calculated atomic contributions to selected molecular orbitals for **3** (PBE0/D3). Contributions from hydrogen and carbon atoms are omitted.

	*[(P^{H}NP)Re(N)(Cl)]$^{+}$ (**3**)*									
	Energy vs. HOMO (kcal/mol)	**Atomic orbital contributions to molecular orbital**								
Orbital		**Re-*p***	**Re-*d***	**Cl-*p***	**N-*p*** **nitride**	**N-*p*** **(amide**	**P-*p***	**P-*d***	**P'-*p***	**P'-*d***
HOMO –4	–65.89	-	-	-	-	-	0.10	-	0.10	-
HOMO –3	–64.01	-	-	-	0.05	-	0.08	-	0.08	-
HOMO –2	–54.59	-	-	0.78	0.14	-	-	-	-	-
HOMO –1	–47.06	0.07	0.17	0.04	-	-	0.20	-	0.20	-
HOMO	0.00		0.63	0.19	-	-	-	-	-	-
LUMO	107.30	0.17	0.22	-	**0.20**	-	0.08	0.04	0.08	0.04
LUMO +1	108.56	-	0.36	-	**0.36**	-	0.05	0.03	0.05	0.03
LUMO +2	120.48	0.17	0.39	0.04	**0.24**	-	0.04	-	0.04	-
LUMO +3	130.52	-	0.39	0.08	**-**	0.03	0.06	-	0.06	-
LUMO +4	138.68	0.33	0.06	-	**-**	0.03	0.13	-	0.13	-

Table 3.19. Calculated atomic contributions to selected molecular orbitals for **4** (PBE0/D3). Contributions from hydrogen and carbon atoms are omitted.

	*[(P^{O}NP)Re(N)(Cl)]$^{+}$ (**4**)*										
	Energy vs. HOMO (kcal/mol)	**Atomic orbital contributions to molecular orbital**									
Orbital		**Re-*p***	**Re-*d***	**Cl-*p***	**N-*p*** **nitride**	**N-*p*** **amide**	**O-*p***	**P-*p***	**P-*d***	**P'-*p***	**P'-*d***
HOMO –4	–36.40	-	-	0.24	0.07	-	-	0.06	-	0.06	-
HOMO –3	–35.14	-	-	-	0.03	-	-	0.09	-	0.09	-
HOMO –2	–12.55	-	0.21	0.05	-	-	0.52	0.04	-	0.04	-
HOMO –1	–1.88	-	-	0.05	0.21	0.12	0.46	-	-	-	-
HOMO	0.00	0.04	0.29	0.21	-	-	-	0.12	-	0.12	-
LUMO	125.50	-	0.36	-	**0.46**	-	-	-	-	-	-
LUMO +1	132.40	0.10	0.43	0.04	**0.37**	-	-	-	-	-	-
LUMO +2	145.58	-	0.40	0.07	**-**	0.05	-	0.13	-	0.13	-
LUMO +3	162.52	0.15	0.20	0.03	**0.02**	-	0.05	0.10	0.04	0.10	0.04
LUMO +4	174.45	0.29	-	-	**-**	-	-	0.27	0.06	0.27	0.06

Table 3.20. Calculated atomic contributions to selected molecular orbitals for **5** (PBE0/D3). Contributions from hydrogen and carbon atoms are omitted.

	[(PNP)Re(N)(Cl)]⁺ (5)									
	Energy vs. HOMO (kcal/mol)	**Atomic orbital contributions to molecular orbital**								
Orbital		**Re-*p***	**Re-*d***	**Cl-*p***	**N-*p*** **nitride**	**N-*p*** **(amide**	**P-*p***	**P-*d***	**P'-*p***	**P'-*d***
HOMO –4	–45.18	-	-	-	-	-	0.09	-	0.09	-
HOMO –3	–44.55	-	0.04	0.54	0.19	-	-	-	-	-
HOMO –2	–34.51	0.08	0.27	-	-	-	0.17	-	0.17	-
HOMO –1	–8.79	0.03	0.40	0.26	-	-	0.07	-	0.07	-
HOMO	0.00	0.03	-	-	0.10	0.56	-	-	-	-
LUMO	117.97	-	0.35	-	**0.43**	-	0.04	-	0.04	-
LUMO +1	127.38	0.12	0.30	0.04	**0.20**	-	0.10	-	0.10	-
LUMO +2	133.66	0.04	0.35	0.03	**0.28**	0.04	0.04	-	0.04	-
LUMO +3	149.35	0.04	0.32	-	**0.04**	0.09	0.11	0.11	-	-
LUMO +4	166.92	0.37	-	-	-	-	0.23	0.05	0.23	0.05

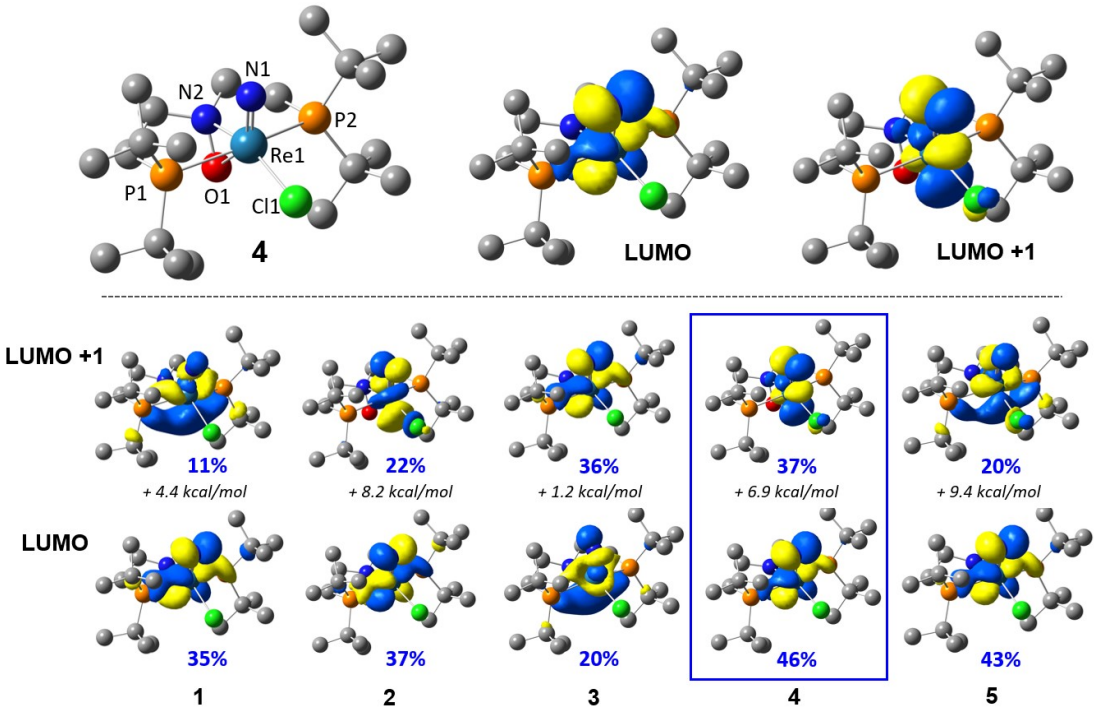

Figure 3.29. DFT model of complex **4** and visualizations of LUMO and LUMO+1 molecular orbitals (isosurface value = 0.05). **Bottom:** Drawings of the LUMO and LUMO+1 orbitals for **1**–**5** with atomic contributions of the nitride (blue percentages) showing that **4** demonstrates the highest combined nitride contribution to the lowest unoccupied frontier orbitals (energy difference between molecular orbitals denoted in italics).

3.3 Conclusions

This work describes the oxidative reactivity of an N_2-derived metal-nitrido complex, wherein two kinds of oxidations have been observed. Outer-sphere agents oxidize the metal center, forming unusual Re^{6+}-nitrido complexes. Electrophilic O-atom transfer agents, however, transfer O to the amide portion of the pincer ligand to form a nitroxide. Cooperative changes in oxidation state and ligand oxidation are required to induce electrophilic reactivity in the normally unreactive nitride complex. Our studies also uncover the unusual formation of Re complexes supported by nitroxide-containing pincer ligands that provide a new variant on a well-characterized PNP pincer. The O-atom transfer to the supporting ligand suggests that careful consideration of the supporting ligand is required for conversion of N_2 to oxidized N species.

Formation of the nitroxide moiety causes electronic changes at the metal center by replacing amide LP interactions with O atom LP interactions, resulting in a redistribution of molecular orbitals. These changes have a surprisingly small effect on the strong Re-nitride interaction in these complexes, but, when coupled with $1e^-$ oxidation of the metal center, cause the nitride ligand to become electrophilic. This *umpolung* in reactivity at the nitride ligand is achieved without exchanging any of the supporting ligands, potentially offering a new strategy for "fine-tuning" metal-center electronics via oxidation of a supporting amide ligand to a nitroxide.

3.4 Experimental

3.4.1. General Considerations

All manipulations were performed under an inert atmosphere of N_2 gas in a M. Braun glovebox or on a Schlenk line unless otherwise specified. Tetrahydrofuran (THF) was distilled under argon from potassium benzophenone ketyl and stored over molecular sieves prior to use. Unless otherwise noted, all other solvents were dried via passage through Q5 columns from Glass Contour Co. and stored over molecular sieves prior to use. Deuterated solvents were degassed and dried over calcium hydride before storing over molecular sieves prior to use, and THF-d_8 was dried additionally with potassium benzophenone ketyl. Ammonium perrhenate (Strem, 99+%), bis-[2-(di-tertbutylphosphino)ethyl)]amine (Strem, 10% w/w in hexanes), hydrogen peroxide (Fisher Chemicals, 30% in H_2O), trimethylamine-*N*-oxide (Sigma-Aldrich, 98%), pyridine-*N*-oxide (Sigma-Aldrich, 95%), iodosobenzene (TCI, 95+%), ferrocenium hexafluorophosphate (Santa Cruz Biotechnology, 97%), nitrosonium hexafluorophosphate (Alfa Aesar, 96%), tris-(4-bromophenyl)amine (Sigma-Aldrich, 98%), bis(triphenylphosphine)iminium chloride (Strem, 97%), sodium azide (terminal ^{15}N-labeled, Cambridge Isotope Laboratories, 98+%), trifluoromethanesulfonic acid (Sigma-Aldrich, 99+%), and trimethylphosphine (Sigma-Aldrich, 1.0 M in THF) were purchased and used without further purification. Triethylamine (Sigma-Aldrich, 99+%, distilled), triphenylphosphine (Aldrich, 99%, sublimed), tris(*p*-tolyl)phosphine (Aldrich, 98%, dried under high vacuum), tris(4-fluoro-phenyl)phosphine (Strem, 99%, dried under high vacuum), ferrocene (Aldrich, 98%, recrystallized), tetrabutylammonium hexafluorophosphate (Sigma-Aldrich, 99%, recrystallized x3), and *m*-chloroperbenzoic

acid (Aldrich, <77%, washed with pH 8.0 buffer and extracted with Et_2O) were purified prior to use. $ReOCl_3(PPh_3)_2$,[61] $(ReCl_3(MeCN)(PPh_3)_2$,[62] $(PNP)ReCl_2$,[8] and bis(triphenylphosphine)iminium azide[63] were synthesized and purified according to literature procedures.

3.4.2. Syntheses and Characterization

Preparation of ^{15}N-labelled bis(triphenylphosphine)iminium azide: Following a literature procedure,[64] 200 mg $Na(N{=}N{=}^{15}N)$ (3.03×10^{-3} mol, 1 equiv) and 1.74 g (PPN)Cl (3.03×10^{-3} mol, 1 equiv) were dissolved in 50 mL EtOH and stirred at ambient temperature for 6 h. The resulting mixture was filtered to remove NaCl, and the precipitate was washed with 15 mL EtOH. The filtrate was concentrated to dryness under vacuum to give a white solid. The residue was triturated with 3 x 10 mL Et_2O to give a white powder, which was dried in the vacuum oven at 120 °C for 24 h. *Caution: Azide salts can be explosive. Use extreme caution and allow the azide to cool to ambient temperature before handling after or during drying.* Isolated 1.56 g fine white powder (88% yield). IR stretches matched reported values.[64]

Preparation of (PNP)Re(N)(Cl) (1): Compound **1** was synthesized using a modified literature procedure.[8] Crystals suitable for X-ray diffraction were grown from a concentrated solution of **1** in pentane. ^{1}H and $^{31}P\{^1H\}$ NMR spectra matched previously reported data. FTIR (solid, cm^{-1}): 2983, 2942, 2922, 2897, 2861, 2814, 1467, 1390, 1368, 1326, 1281 (w), 1261 (w), 1213, 1180, 1161, 1092, 1083, 1056, 1020, 966, 939, 918, 874 (w), 809 (s), 116, 102, 612, 584, 544, 503, 478 (s), 424.

Preparation of (PNP)Re(^{15}N)(Cl) (1-^{15}N): This compound was synthesized analogous to **1** via a modified literature procedure,[8] in which 20.0 mg $(PNP)ReCl_2$ ($3.24 \times$

10^{-5} mol, 1.0 equiv) dissolved in 5 mL THF was added to 20.2 mg (PPN)(N=N=^{15}N) (3.47 x 10^{-5} mol, 1.07 equiv) slurried in 5 mL THF at –40 °C. The reaction was allowed to warm to ambient temperature and stirred for 12 h, accompanied by a color change from purple to orange and formation of a white precipitate. The solvent was removed under vacuum, and the product was extracted with 2 x 5 mL Et_2O and filtered through Celite. Removal of the solvent under vacuum gave an orange residue. To further purify the product, the residue was extracted with 4 x 5 mL pentane and filtered through Celite. The combined filtrates were evaporated to give 14.7 mg orange powder (76% yield). ^{1}H and ^{31}P{^{1}H} NMR spectra were identical to those of **1**. ^{15}N NMR (51 MHz, C_6D_6): δ 371 (s). FTIR (solid): matches 1 except for new bands at 1036 and 1074 cm^{-1}.

Preparation of [(P^{O}NP)Re(N)(Cl)][mCBA] (2): In separate 20 mL vials, 105.6 mg **1** (1.77 x 10^{-4} mol, 1.0 equiv) was suspended in 5 mL Et_2O to form an orange slurry, and 45.8 mg *m*-chloroperbenzoic acid (2.65 x 10^{-4} mol, 1.5 equiv) was dissolved in 3 mL Et_2O to give a colorless solution. The perbenzoic acid solution was quantitatively added to **1** dropwise via pipette while stirring at ambient temperature, resulting in a color change to a gold solution. The reaction was stirred at ambient temperature for 1 hour, after which the reaction was filtered through Celite to remove a brown precipitate. The gold filtrate was concentrated under vacuum to give a sticky yellow solid. This solid was triturated and washed with 4 x 3 mL pentane, then dried under vacuum to yield 114.5 mg **2** as a yellow powder (84% yield), which was pure by ^{1}H and ^{31}P{^{1}H} NMR spectroscopy. Crystals suitable for X-ray diffraction were grown from a concentrated solution of **2** in Et_2O at –40 °C. ^{1}H NMR (400 MHz, THF-d_8): δ 12.03 (br. s, 1H, O*H*), δ 7.98 (s, 1H, *o-H* of mCBA), δ 7.92 (d, *J* = 7.7 Hz, 1H, *o-H* of mCBA), 7.56 (d, *J* = 8.0 Hz, 1H, *p-H* of mCBA), 7.43 (t,

J = 7.9 Hz, 1H, *m-H* of mCBA), δ 3.39 (m, 2H, N(C*H*$_2$CH$_2$)$_2$), δ 3.32 (superimposed m, 2H, N(C*H*$_2$CH$_2$)$_2$), δ 2.07 (m, 2H, N(CH$_2$C*H*$_2$)$_2$), δ 1.58 (superimposed m, 2H, N(CH$_2$C*H*$_2$)$_2$), δ 1.54 (vt, 18H, P(*tBu*)(tBu')), δ 1.34 (vt, 18H, P(tBu)(*tBu'*)). ^{13}C{^{1}H} NMR (126 MHz, THF-d_8) δ 165.55, 133.95, 133.20, 132.18, 129.67, 129.31, 127.74, 66.37, 36.85, 34.64, 28.32, 24.29, 18.99. ^{31}P{^{1}H} NMR (162 MHz, THF-d_8): δ 64.60 (s). UV-vis (CH_2Cl_2 solution): λ = 332 nm (ε = 1300 M^{-1} cm^{-1}), 393 nm (shoulder, ε = 290 M^{-1} cm^{-1}), 458 nm (shoulder, ε = 160 M^{-1} cm^{-1}). FTIR (solid, cm^{-1}): 3073 (w), 2997, 2981, 2954, 2922, 2899, 2868, 1731 (br), 1607, 1574, 1470, 1429, 1394, 1367, 1278, 1263, 1248, 1210, 1179, 1136, 1077 (s), 1061, 1026, 990, 939, 911, 846 (s), 808 (s), 750 (s), 710 (s), 698, 675, 651, 616, 592 (w), 572 (w), 529, 484, 427. Anal. calcd.(found) for $C_{27}H_{49}Cl_2N_2O_3P_2Re$ (%): C, 42.18(43.04); H, 6.42(6.43); N, 3.64(3.33). We were unable to obtain elemental analysis with closer agreement in carbon.

Preparation of [(P^{O}NP)Re(^{15}N)(Cl)][mCBA] (2-^{15}N): The synthesis of **2-^{15}N** was completed analogously to the synthesis of **2** using **1-^{15}N** as the starting material. ^{1}H and ^{31}P{^{1}H} NMR spectra were identical to those of **2**. ^{15}N NMR (51 MHz, C_6D_6): δ 393 (s). FTIR (solid, cm^{-1}): matches **2** except for a new band at 1042 cm^{-1}.

Preparation of [(P^{H}NP)Re(N)(Cl)][OTf] (3-OTf): Compound **3-OTf** was synthesized from **1** according to a literature procedure.[8] ^{1}H and ^{31}P{^{1}H} NMR spectra matched previously reported data. FTIR (solid, cm^{-1}): 3048 (br), 2987, 2967, 2911, 2874, 1480, 1472, 1395, 1371, 1334, 1289 (s), 1241 (s), 1224 (s), 1154 (s), 1108, 1027 (s), 990, 940 (w), 824, 809, 776 (w), 757 (w), 742 (w), 727 (w), 691, 636 (s), 613, 575, 539 (w), 517, 497, 435, 426.

Preparation of [($P^{H}NP$)Re(^{15}N)(Cl)][OTf] (3-^{15}N): The synthesis of **3-^{15}N** was completed analogously to the synthesis of **3** using **1-^{15}N** as the starting material. ^{1}H and $^{31}P\{^{1}H\}$ NMR spectra were identical to those of **3**. ^{15}N NMR (51 MHz, C_6D_6): δ 387 (s). FTIR (solid, cm^{-1}): matches **3** except for new bands at 1037 and 1074 cm^{-1}.

Preparation of tris(4-bromo-phenyl)aminium hexafluorophosphate: This compound was synthesized according to a modified literature procedure,[65] in which 1.00 g tris(4-bromo-phenyl)amine (2.08 x 10^{-3} mol, 1.06 equiv) was dissolved in 8 mL CH_2Cl_2 and added via pipette to a slurry of 345 mg [NO][PF_6] (1.97 x 10^{-3} mol, 1 equiv) in 30 mL CH_2Cl_2 at –78 °C while stirring vigorously. Addition of the amine solution was accompanied by a distinct color change to deep blue. The reaction was stirred at –78 °C for 1 h, then allowed to warm to ambient temperature. Removal of the solvent under vacuum gave a dark indigo solid. This residue was slurried in 15 mL Et_2O and filtered. The solid was washed with 2 x 10 mL Et_2O and dried under vacuum for 30 min, resulting in 1.11 g of the compound as an indigo-purple solid (89% yield).

Preparation of [($P^{O}NP$)Re(N)(Cl)][PF_6] (4): In separate vials, 29.9 mg **2** (3.89 x 10^{-5} mol, 1.0 equiv) was dissolved in 3 mL CH_2Cl_2 to give a yellow solution, and 23.0 mg tris(4-bromo-phenyl)aminium hexafluorophosphate (3.67 x 10^{-5} mol, 0.94 equiv) was dissolved in 5 mL CH_2Cl_2 to give a dark blue solution. Both solutions were cooled to –78 °C, and the [Re] solution was added to the aminium dropwise via pipette while stirring. The reaction was stirred at –78 °C for 1 h, after which it had become bright green. The reaction was allowed to warm to ambient temperature, and the solvent was removed under vacuum to give a bright green residue. The product was washed with 4 x 5 mL Et_2O, re-dissolved in 4 mL DCM, layered with 12 mL Et_2O, and left at –40 °C overnight. Decanting

the mother liquor and evaporating residual solvent under vacuum gave 25.0 mg **4** as green feathery crystals (85% yield). The ^{1}H NMR spectrum of **4** demonstrates several broad paramagnetic resonances (see **Figure 3.8**). ^{1}H NMR (500 MHz, CD_2Cl_2): δ 34.00 (2H, C*H*$_2$), δ 12.12 (18H, P(*tBu*)(tBu')), δ 5.58 (20H, superimposed C*H*$_2$ and P(tBu)(*tBu'*)). UV-vis (CH_2Cl_2 solution): λ = 307 nm (ε = 5000 M^{-1} cm^{-1}), 350 nm (shoulder, ε = 2800 M^{-1} cm^{-1}), 417 nm (shoulder, ε = 580 M^{-1} cm^{-1}), 668 nm (ε = 390 M^{-1} cm^{-1}). FTIR (solid, cm^{-1}): 2971, 2939, 2907, 2873, 1478, 1468, 1445 (w), 1397, 1374, 1245 (w), 1209 (w), 1175, 1058, 1023, 992 (w), 936 (w), 874, 832 (s), 740, 709, 612 (w), 589 (w), 557, 485, 424. Anal. calcd.(found) for $C_{20}H_{44}ClF_6N_2OP_3Re$ (%): C, 31.73(31.75); H, 5.86(5.86); N, 3.70(3.65).

Preparation of [(P^{O}NP)Re(^{15}N)(Cl)][PF$_6$] (4-^{15}N): Synthesis of **4-^{15}N** was completed analogously to the synthesis of **4** using **2-^{15}N** as the starting material. FTIR (solid, cm^{-1}): matches **4** except for a new band at 1024 cm^{-1}.

Preparation of [(PNP)Re(N)(Cl)][PF$_6$] (5): In a 20 mL vial, 30.0 mg **1** (5.03 x 10^{-5} mol, 1.0 equiv) was dissolved in 5 mL CH_2Cl_2 to give an orange solution. The solution was cooled to –78 °C, at which point 15.8 mg $[Cp_2Fe][PF_6]$ (4.78 x 10^{-5} mol, 0.95 equiv) was slowly added as a solid while stirring. The solution darkened from orange to bright red. The solvent was removed under vacuum while the solution warmed to ambient temperature. The resulting residue was washed with 3 x 5 mL cold (–40 °C) Et_2O to remove Cp_2Fe and residual **1**, leaving behind a pink-red solid. The pink-red solid was dissolved in 3 mL cold (–40 °C) CH_2Cl_2 to give a red solution, which was layered with 10 mL cold (–40 °C) Et_2O and placed in a –40 °C freezer overnight. Decanting the mother liquor and evaporating residual solvent under vacuum gave 28.3 mg pink crystals suitable for X-ray

diffraction. ^{1}H NMR spectroscopy of the pink crystals showed that **5** was isolated with 26% 3-PF_6 as an impurity, giving an overall yield of 56% for **5**. The ^{1}H NMR spectrum of **5** demonstrates several broad paramagnetic resonances (see **Figure 3.11**). ^{1}H NMR (500 MHz, CD_2Cl_2): δ 6.91 (18H, P(*tBu*)(tBu')), δ 4.39 (18H, P(tBu)(*tBu'*)), δ 4.33 (2H, superimposed C*H*$_2$), δ –0.52 (2H, C*H*$_2$). UV-vis (CH_2Cl_2 solution with impurity of 3-PF_6): λ = 291 nm (shoulder, ε = 2500 M^{-1} cm^{-1}), 325 nm (shoulder, ε = 1700 M^{-1} cm^{-1}), 516 nm (ε = 290 M^{-1} cm^{-1}), 627 nm (ε = 90 M^{-1} cm^{-1}). FTIR (solid with impurity of **3-PF_6,** cm^{-1}): 3208 (w), 2987, 2969, 2908, 2874, 1480, 1471, 1397, 1372, 1327, 1290 (w), 1281 (w), 1218, 1178, 1109 (w), 1076, 1052, 1021, 988 (w), 968 (w), 943 (w), 832 (s), 782 (s), 740, 716, 693, 611, 583 (w), 557 (s), 519, 479 (s), 443, 422. Anal. calcd.(found) for $C_{20}H_{44}ClF_6N_2P_3Re$ (%): C, 32.41(33.19); H, 5.98(5.99); N, 3.78(3.61). We were unable to obtain elemental analysis with closer agreement in carbon.

Preparation of [(PNP)Re(^{15}N)(Cl)][PF_6] (5-^{15}N): Synthesis of **5-^{15}N** was completed analogously to synthesis of **5** using **1-^{15}N** as the starting material. FTIR (solid, cm^{-1}): matches **5** except for a new band at 1035 cm^{-1}.

3.4.3. Instrumentation and Methods

NMR spectra were acquired on an Agilent 400 MHz or 500 MHz spectrometer. ^{1}H spectra were referenced to residual ^{1}H signals from the deuterated solvent with which the sample was prepared,[66] and ^{13}C{^{1}H}, ^{31}P{^{1}H}, and ^{15}N spectra were absolute referenced to the corresponding ^{1}H spectra. Line fitting of paramagnetic resonances in ^{1}H NMR spectra was done using MestReNova 10.0.1. IR spectra were obtained using a Bruker Alpha spectrometer containing a diamond ATR unit with 2 cm^{-1} resolution.

Electrochemical measurements were collected using a CH Instruments 600D potentiostat in a N_2 glovebox or in solutions purged with dry N_2 gas. Cyclic voltammetry (CV) experiments were conducted in 0.1 M tetrabutylammonium hexafluorophosphate (TBA-PF_6) solutions in dry solvent using a glassy carbon disc working electrode (3.0 mm diameter), a platinum wire auxiliary electrode, and a silver wire psuedoreference. Wire electrodes were sanded and rinsed with dry solvent prior to use, and glassy carbon disc electrodes were polished using 0.05 μm alumina powder and rinsed with dry solvent prior to use. Measurements conducted in THF or CH_2Cl_2 were compensated for internal resistance prior to collecting data. CV experiments were referenced to ferrocene (Cp_2Fe) as an internal standard after completion.

Elemental analyses were obtained from the CENTC Elemental Analysis Facility at the University of Rochester. Microanalysis samples were weighed on a PerkinElmer Model AD-6 Autobalance, analyzed on a PerkinElmer 2400 Series II Analyzer, and handled in a VAC Atmospheres argon glovebox.

Differential EPR spectra were measured on a Bruker EXELSYS E500 spectrometer utilizing a super-high Q resonator and an Oxford ESR-900 helium-flow cryostat at 8–11 K. Instrument parameters: microwave frequency: 9.37 GHz; microwave power: 10 mW; modulation frequency 100 kHz; modulation amplitude: 19.49 G; conversion time: 5.12 ms; time constant: 1.28–2.56 ms. Samples of approximately 0.2 mM were dissolved in glassing solvent mixtures of 1:1 CH_2Cl_2:toluene. Simulations were performed using the 'pepper' function in EasySpin version 5.0.5. Line broadening was simulated using gStrain and Astrain to account for Gaussian distributions in *g* principal values and corresponding *A* values.

3.4.4. Computational Details

Density Functional Theory (DFT) calculations were performed using GAUSSIAN09 (revision D.01).[67] All calculations were performed by the clusters at the Yale University Faculty of Arts and Sciences High Performance Computing Center. Structures were optimized using the GGA functional PBE[68] and the hybrid functional PBE0[69], with basis sets def2-TZVP used for light atoms (H, C, N, O, P), LANL08(d) used for Cl, and LANL08(f) used for Re. Unless otherwise noted, all calculations include the D3 version of Grimme's dispersion correction[70] and a conductor-like polarizable continuum model (CPCM) for THF solvent. Frequency calculations were performed to confirm that the optimized structures were minima; the optimized structures for **1**–**5** showed no negative frequencies. Mulliken population analysis to determine atomic contributions to molecular orbitals in **1**–**5** was completed for the five highest energy occupied orbitals and the five lowest energy unoccupied orbitals with a minimum contribution percentage of 3%. Redox potentials were calculated from the free energy change and solvation free energies of the oxidized and reduced complexes and compared to ferrocene.[71, 72] Natural Bond Order (NBO) calculations including second-order perturbation theory analysis[50] were performed using the NBO6.0 package[73, 74] in GAUSSIAN09. NBO calculations were modified to include Wiberg[49] and Mayer-Mulliken[75, 76] partial bond orders.

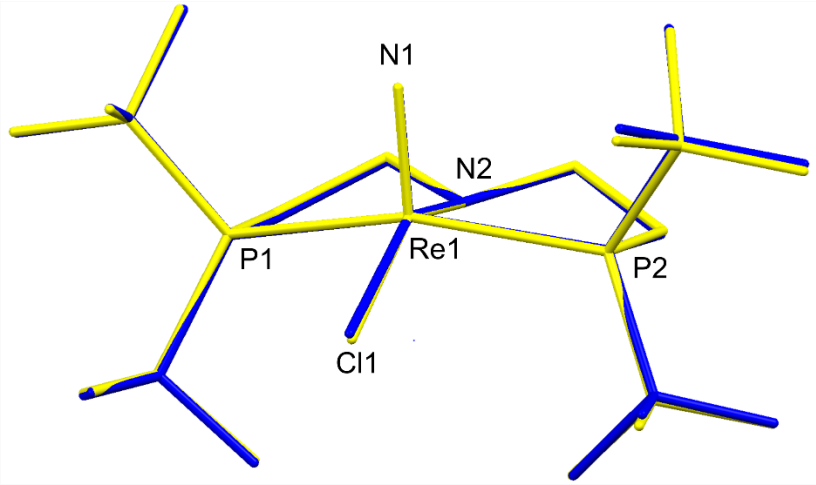

Figure 3.30. Overlay of crystal structure (yellow) and calculated structure (PBE0/D3, blue) of **1**. Hydrogen atoms are omitted for clarity.

Table 3.21. Calculated structural parameters of **1** using different functionals.

Functional **Dispersion corr.**	**Exp. (1)** **-**	**PBE** **-**	**PBE0** **-**	**PBE0** **D3**
Re - N1	1.643(6)	1.666	1.642	1.643
Re - N2	2.033(6)	2.008	1.999	2.000
Re - Cl	2.441(2)	2.534	2.516	2.507
Re - P (avg)	2.439	2.453	2.449	2.436
N1 - Re - N2	105.8(3)	106.2	106.1	106.5
N1 - Re - Cl	106.5(2)	103.3	103.1	103.1
N2 - Re - Cl	147.7(2)	150.5	150.8	150.8

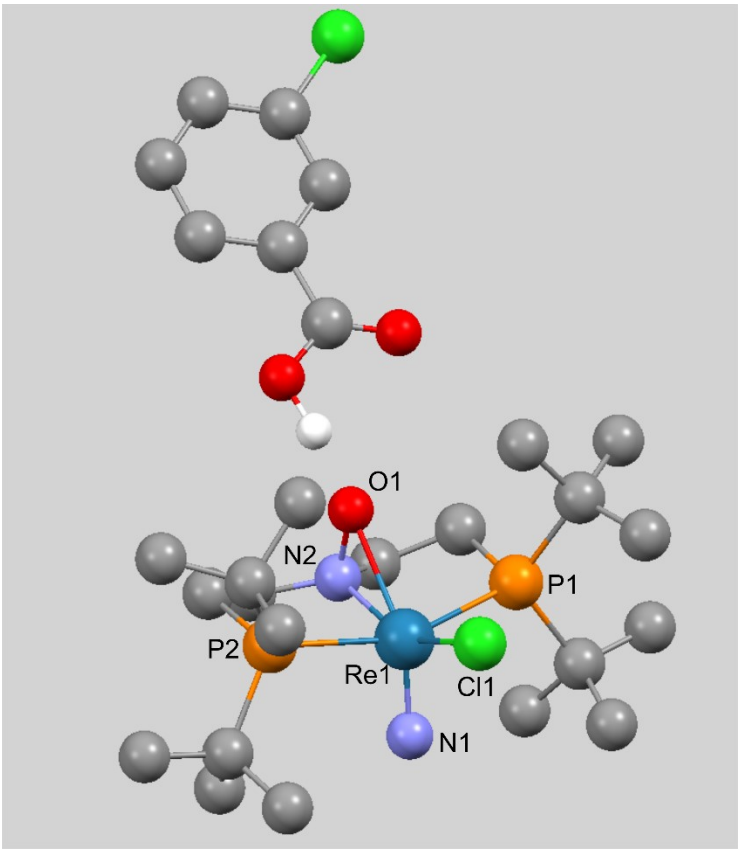

Figure 3.31. Calculated structure (PBE0/D3) of 2 with mCBA molecule hydrogen bound, showing preferential protonation of mCBA rather than the nitroxide. All other hydrogen atoms are omitted for clarity.

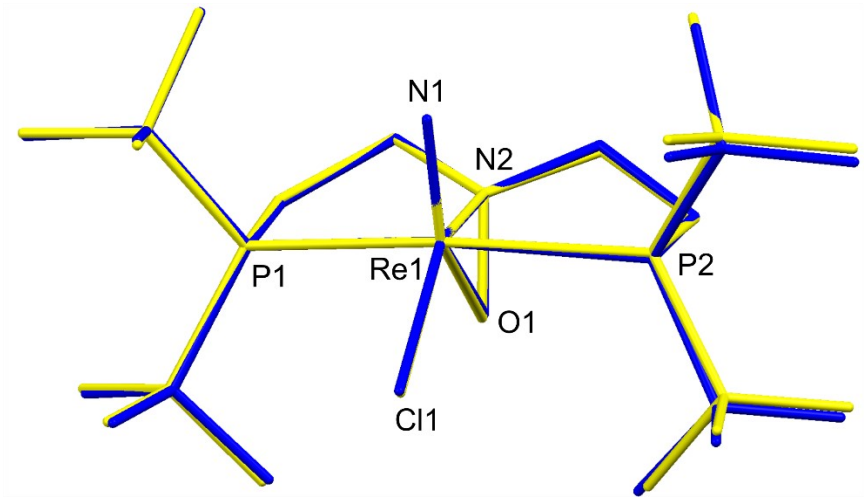

Figure 3.32. Overlay of crystal structure (yellow) and calculated structures (PBE0/D3 without mCBA molecule, blue) of **2**. Hydrogen atoms and mCBA molecules are omitted for clarity. See **Table 3.2** for calculated structural parameters of **2** using different functionals.

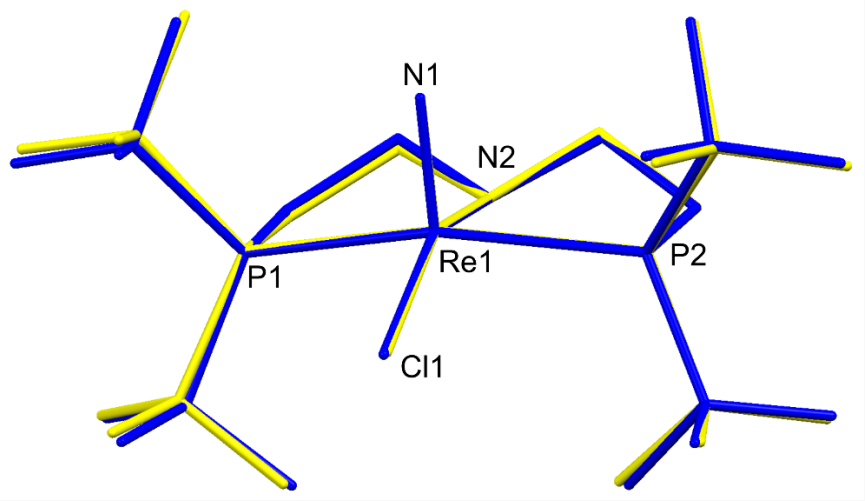

Figure 3.33. Overlay of crystal structure (yellow) and calculated structure (PBE0/D3, blue) of **3**. Hydrogen atoms are omitted for clarity.

Table 3.22. Calculated structural parameters of **3** using different functionals.

Functional **Dispersion corr.**	**Exp. (3-OTf)** -	**Exp. (3-PF_6)** -	**PBE** -	**PBE0** -	**PBE0** **D3**
Re - N1	1.624(7)	1.6215(16)	1.648	1.626	1.625
Re - N2	2.138(7)	2.104(16)	2.168	2.153	2.153
Re - Cl	2.385(2)	2.372(4)	2.437	2.423	2.413
Re - P (avg)	2.452	2.463	2.474	2.469	2.456
N1 - Re - N2	99.9(3)	100.2(7)	99.4	99.3	99.4
N1 - Re - Cl	106.7(3)	105.5(6)	106.0	106.1	106.1
N2 - Re - Cl	153.4(2)	154.3(4)	154.6	154.7	154.6

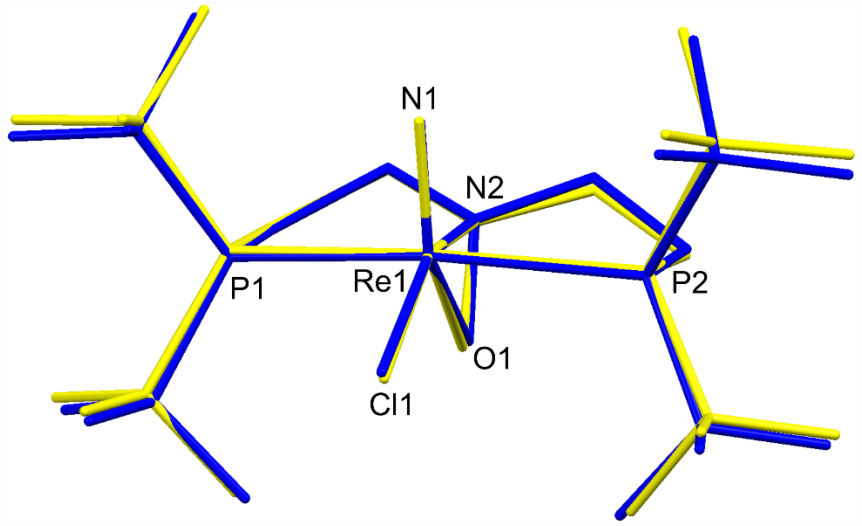

Figure 3.34. Overlay of crystal structure (yellow) and calculated structure (PBE0/D3, blue) of **4**. Hydrogen atoms are omitted for clarity.

Table 3.23. Calculated structural parameters of **4** using different functionals.

Functional **Dispersion corr.**	**Exp. (4)** **-**	**PBE** **-**	**PBE0** **-**	**PBE0** **D3**
Re - N1	1.665(7)	1.670	1.645	1.646
Re - N2	2.097(8)	2.104	2.079	2.080
Re - Cl	2.295(3)	2.355	2.347	2.340
Re - O	2.200(6)	2.239	2.219	2.229
Re - P (avg)	2.512	2.528	2.518	2.502
O - N2	1.433(1)	1.412	1.389	1.388
N1 - Re - N2	105.0(4)	101.7	102.1	101.8
N1 - Re - Cl	103.1(3)	102.0	101.5	101.5
N2 - Re - Cl	151.9(2)	156.3	156.4	156.7
O - N2 - Re	74.5(4)	76.3	76.7	77.2
N2 - Re - O	38.8(3)	37.8	37.5	37.4

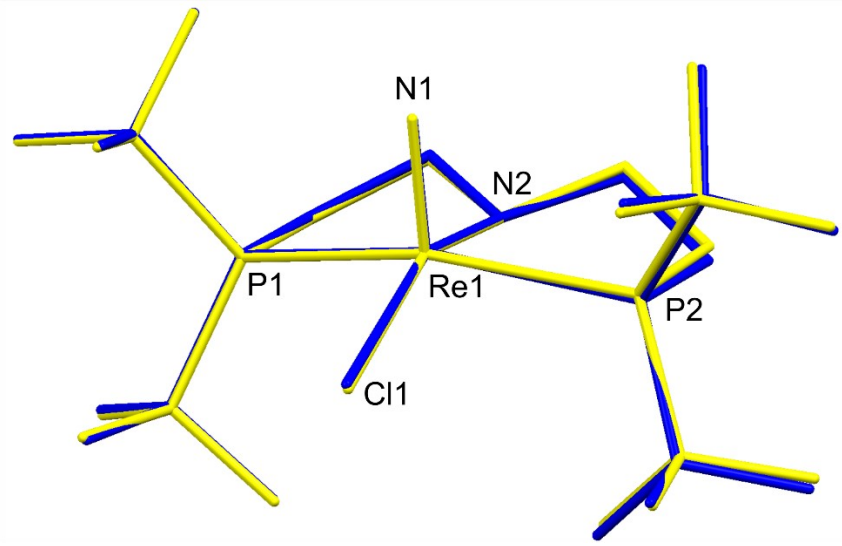

Figure 3.35. Overlay of crystal structure (yellow) and calculated structure (PBE0/D3, blue) of **5**. Hydrogen atoms are omitted for clarity.

Table 3.24. Calculated structural parameters of **5** using different functionals.

Functional **Dispersion corr.**	**Exp. (5)** **-**	**PBE** **-**	**PBE0** **-**	**PBE0** **D3**
Re - N1	1.650(5)	1.659	1.636	1.635
Re - N2	2.054(5)	1.985	1.987	1.988
Re - Cl	2.339(2)	2.392	2.360	2.355
Re - P (avg)	2.478	2.516	2.520	2.507
N1 - Re - N2	103.4(2)	101.9	104.4	104.2
N1 - Re - Cl	105.6(2)	101.6	103.2	103.3
N2 - Re - Cl	151.0(1)	156.5	152.5	152.5

Table 3.25. Calculated Wiberg partial bond orders for complexes **1–5** (PBE0/D3).

Bond	1	2	3	4	5
Re–N (nitride)	2.45	2.44	2.57	2.38	2.41
Re–N (amide)	0.65	0.43	0.39	0.41	0.66
Re–P1	0.53	0.51	0.52	0.50	0.50
Re–P2	0.53	0.51	0.52	0.50	0.50
Re–Cl	0.43	0.47	0.55	0.76	0.70
Re–O	-	0.22	-	0.27	-

Table 3.26. Calculated Mayer-Mulliken partial bond orders for complexes **1–5** (PBE0/D3).

Bond	1	2	3	4	5
Re–N (nitride)	2.56	2.56	2.69	2.52	2.56
Re–N (amide)	0.76	0.55	0.48	0.49	0.72
Re–P1	0.79	0.78	0.79	0.76	0.77
Re–P2	0.79	0.78	0.79	0.76	0.77
Re–Cl	0.57	0.56	0.66	0.78	0.78
Re–O	-	0.39	-	0.46	-

3.4.5. Crystallographic Details

Crystals were isolated in an N_2 glovebox by decanting the mother liquor from the crystals before transferring and submerging them in high-viscosity petroleum oil on a microscope slide. Single crystals suitable for X-ray diffraction were identified under a polarizing microscope and mounted on 200 μm MiTeGen Dual-Thickness MicroLoops in a mixture of high-viscosity petroleum, then mounted on the diffractometer instrument. Low-temperature (100 K) diffraction data (ω-scans) were collected on a Rigaku SCX Mini diffractometer coupled to a Rigaku Mercury275R CCD with Mo Kα radiation (λ = 0.71073 Å) for the structures of mini-16037 (**1**), mini-16064 (**5**), and mini-16096 (**3-PF$_6$**). Low-temperature (100 K) diffraction data (ω-scans) were collected on a Rigaku MicroMax-007HF diffractometer coupled to a Saturn994+ CCD detector with Cu Kα (λ = 1.54178 Å) for the structure of 007-16099 (**2**), 007-16141 (**3-OTf**), and 007-17024 (**4**). The diffraction images were processed and scaled using either Rigaku CrystalClear software (CrystalClear

and CrystalStructure; Rigaku/MSC: The Woodlands, TX, 2005) or Rigaku Oxford Diffraction software (CrysAlisPro; Rigaku OD: The Woodlands, TX, 2015). The structure was solved with SHELXT and was refined against F^2 on all data by full-matrix least squares with SHELXL (Sheldrick, G. M. Acta Cryst. 2008, A64, 112–122). The full numbering schemes of all compounds can be found in the full details of the X-ray structure determination (CIF) files, which are included as Supporting Information. CCDC numbers 1893092 (**1**), 1893093 (**2**), 1893094 (**3-OTf**), 1893095 (**4**), 1893096 (**5**), and 1893097 (**3-PF_6**) contain the supplementary crystallographic data for this paper. These data can be obtained free of charge from The Cambridge Crystallographic Data Center via www.ccdc.cam.ac.uk/data_request/cif.

(PNP)Re(N)(Cl) (1, mini-16037): All non-hydrogen atoms were refined anisotropically. Hydrogen atoms were included in the model at geometrically calculated positions and refined using a riding model. The isotropic displacement parameters of all hydrogen atoms were fixed to 1.2 times the U value of the atoms to which they are linked (1.5 times for methyl groups).

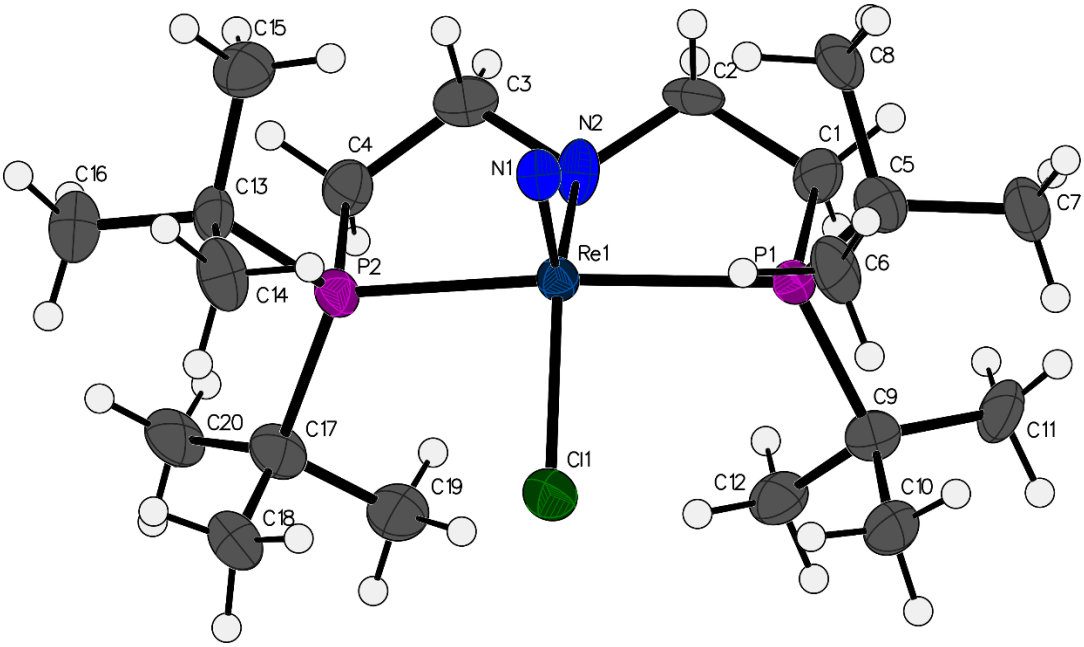

Figure 3.36. The complete numbering scheme of mini-16037 (**1**) with 50% thermal ellipsoid probability levels. The hydrogen atoms are shown as circles for clarity.

Table 3.27. Crystal data and structure refinement for mini-16037 (**1**).

Identification code	mini-16037	
Empirical formula	C20 H44 Cl N2 P2 Re	
Formula weight	596.16	
Temperature	93(2) K	
Wavelength	0.71073 Å	
Crystal system	Orthorhombic	
Space group	Pbca	
Unit cell dimensions	a = 11.9608(4) Å	α = 90°.
	b = 15.4844(5) Å	β = 90°.
	c = 26.3977(9) Å	γ = 90°.
Volume	4889.0(3) $Å^3$	
Z	8	
Density (calculated)	1.620 Mg/m^3	
Absorption coefficient	5.219 mm^{-1}	
F(000)	2400	
Crystal size	0.200 x 0.200 x 0.020 mm^3	
Theta range for data collection	2.742 to 25.025°.	
Index ranges	–14<=h<=14, –18<=k<=18, –31<=l<=31	
Reflections collected	66589	
Independent reflections	4317 [R(int) = 0.1091]	
Completeness to theta = 25.025°	99.9 %	

Absorption correction	Semi-empirical from equivalents
Max. and min. transmission	1.00000 and 0.84553
Refinement method	Full-matrix least-squares on F^2
Data / restraints / parameters	4317 / 0 / 247
Goodness-of-fit on F^2	1.053
Final R indices [I>2sigma(I)]	R1 = 0.0410, wR2 = 0.0850
R indices (all data)	R1 = 0.0635, wR2 = 0.0934
Largest diff. peak and hole	2.135 and –0.694 e.Å^{-3}

[($P^{O}NP$)Re(N)(Cl)][mCBA] (2, 007-16099): All non-hydrogen atoms were refined anisotropically. Hydrogen atoms were included in the model at geometrically calculated positions and refined using a riding model. The isotropic displacement parameters of all hydrogen atoms were fixed to 1.2 times the U value of the atoms to which they are linked (1.5 times for methyl groups). Several reflections were improperly recorded due to instrument artifacts. These reflections were omitted from the least squares refinement. A proton from mCBA is likely present in the difference map but was not located. This proton's existence is proposed for charge balancing and corresponding spectroscopic data.

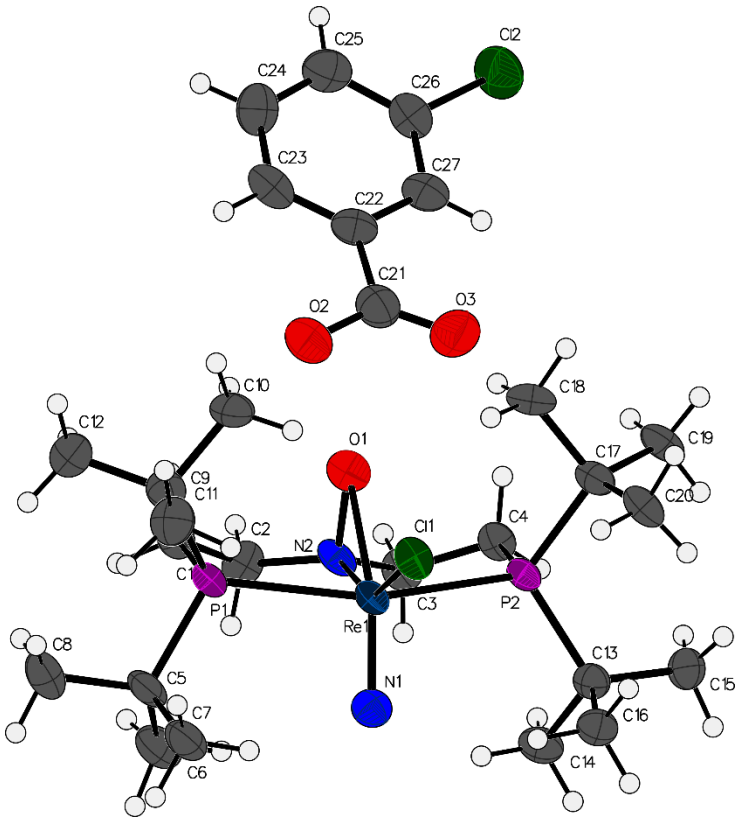

Figure 3.37. The complete numbering scheme of 077-16099 (**2**) with 50% thermal ellipsoid probability levels. The hydrogen atoms are shown as circles for clarity.

Table 3.28. Crystal data and structure refinement for 007-16099 (**2**).

Identification code	007-16099	
Empirical formula	C27 H48 Cl2 N2 O3 P2 Re	
Formula weight	767.71	
Temperature	93(2) K	
Wavelength	1.54178 Å	
Crystal system	Monoclinic	
Space group	$P2_1/c$	
Unit cell dimensions	a = 18.5246(13) Å	α = 90°.
	b = 12.1879(9) Å	β = 112.515(2)°.
	c = 15.4568(11) Å	γ = 90°.
Volume	3223.8(4) $Å^3$	
Z	4	
Density (calculated)	1.582 Mg/m^3	
Absorption coefficient	10.070 mm^{-1}	
F(000)	1548	
Crystal size	0.100 x 0.080 x 0.040 mm^3	
Theta range for data collection	2.582 to 67.954°.	

Index ranges	–22<=h<=22, –14<=k<=14, –18<=l<=18
Reflections collected	110848
Independent reflections	5848 [R(int) = 0.1138]
Completeness to theta = 67.679°	99.8 %
Absorption correction	Semi-empirical from equivalents
Max. and min. transmission	1.000 and 0.730
Refinement method	Full-matrix least-squares on F^2
Data / restraints / parameters	5848 / 0 / 346
Goodness-of-fit on F^2	1.072
Final R indices [I>2sigma(I)]	R1 = 0.0492, wR2 = 0.1297
R indices (all data)	R1 = 0.0636, wR2 = 0.1414
Largest diff. peak and hole	3.490 and –1.868 e.Å^{-3}

[(P^HNP)Re(N)(Cl)][OTf] (3-OTf, 007-16141): All non-hydrogen atoms were refined anisotropically. Hydrogen atoms were included in the model at geometrically calculated positions and refined using a riding model. The isotropic displacement parameters of all hydrogen atoms were fixed to 1.2 times the U value of the atoms to which they are linked (1.5 times for methyl groups). The only exception is H2, which was semi-freely refined. The triflate counter ion is disordered over two positions. The site occupancies of the fluorines within the model were freely refined and converged at values of 0.63(5) and 0.37(5) for the major (labels F#A) and minor (labels F#B) components, respectively. A similar approach was used for the oxygen atoms; their site occupancies converged at values of 0.59(6) and 0.41(6) for the major (labels O#A) and minor (labels O#B) components, respectively. The disordered models were refined with the aid of ridged bond and distance restraints. Restraints were only applied between areas of the model that were anticipated to be chemically similar.

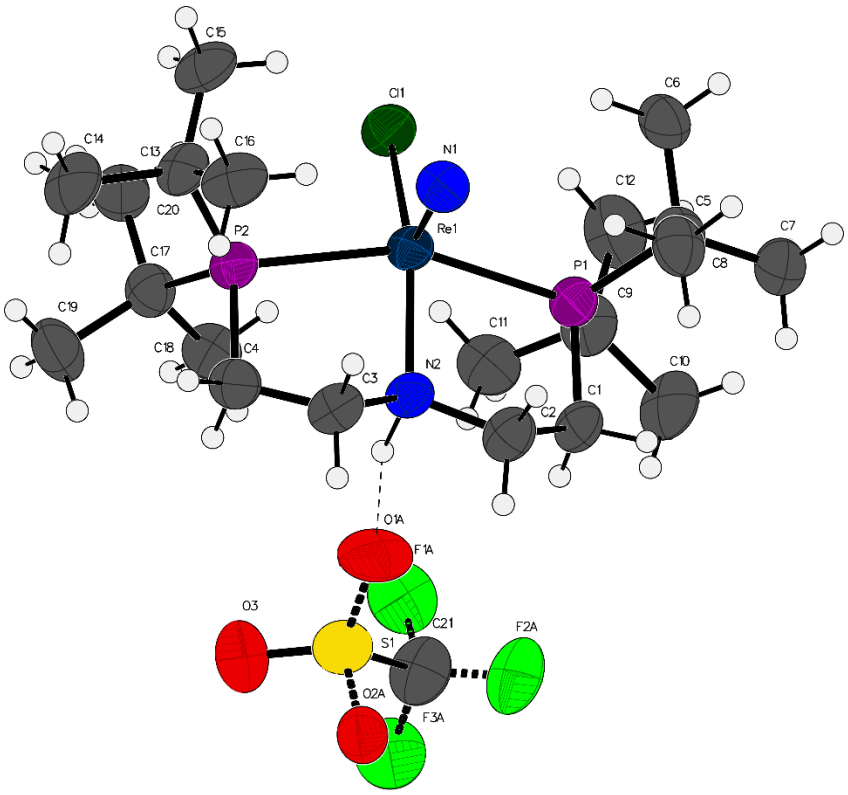

Figure 3.38. The complete numbering scheme of 077-16141 (**3-OTf**) with 50% thermal ellipsoid probability levels. The hydrogen atoms are shown as circles for clarity. Dashed lines highlight the hydrogen bond; dashed bonds denote disordered atoms.

Table 3.29. Crystal data and structure refinement for 007-16141 (**3-OTf**).

Identification code	007-16141	
Empirical formula	C21 H45 Cl F3 N2 O3 P2 Re S	
Formula weight	746.24	
Temperature	93(2) K	
Wavelength	1.54178 Å	
Crystal system	Monoclinic	
Space group	C2/c	
Unit cell dimensions	a = 32.617(2) Å	α = 90°.
	b = 14.2560(10) Å	β = 116.715(2)°.
	c = 14.9751(10) Å	γ = 90°.
Volume	6219.9(8) $Å^3$	
Z	8	
Density (calculated)	1.594 Mg/m^3	
Absorption coefficient	10.397 mm^{-1}	

F(000)	2992
Crystal size	0.200 x 0.200 x 0.020 mm^3
Theta range for data collection	3.033 to 68.240°.
Index ranges	–39<=h<=38, –17<=k<=17, –17<=l<=17
Reflections collected	109099
Independent reflections	5632 [R(int) = 0.1860]
Completeness to theta = 67.679°	99.8 %
Absorption correction	Semi-empirical from equivalents
Max. and min. transmission	1.000 and 0.641
Refinement method	Full-matrix least-squares on F^2
Data / restraints / parameters	5632 / 76 / 370
Goodness-of-fit on F^2	1.093
Final R indices [I>2sigma(I)]	R1 = 0.0516, wR2 = 0.1290
R indices (all data)	R1 = 0.0801, wR2 = 0.1419
Largest diff. peak and hole	1.967 and –0.633 e.$Å^{-3}$

[(P^{O}NP)Re(N)(Cl)][PF_6] (4, 007-17024): All non-hydrogen atoms were refined anisotropically. Hydrogen atoms were included in the model at geometrically calculated positions and refined using a riding model. The isotropic displacement parameters of all hydrogen atoms were fixed to 1.2 times the U value of the atoms to which they are linked (1.5 times for methyl groups).

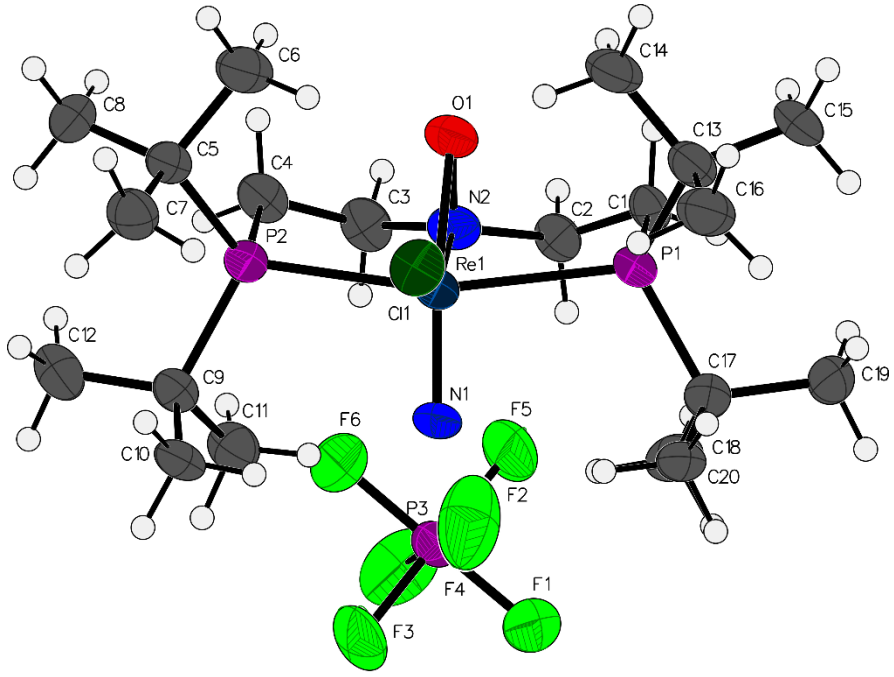

Figure 3.39. The complete numbering scheme of 007-17024 (**4**) with 50% thermal ellipsoid probability levels. The hydrogen atoms are shown as circles for clarity.

Table 3.30. Crystal data and structure refinement for 007-17024 (**4**).

Identification code	007-17024	
Empirical formula	C20 H44 Cl F6 N2 O P3 Re	
Formula weight	757.13	
Temperature	93(2) K	
Wavelength	1.54184 Å	
Crystal system	Monoclinic	
Space group	$P2_1/n$	
Unit cell dimensions	a = 8.5717(3) Å	α = 90°.
	b = 20.8417(9) Å	β = 100.224(3)°.
	c = 16.1218(5) Å	γ = 90°.
Volume	2834.41(18) $Å^3$	
Z	4	
Density (calculated)	1.774 Mg/m^3	
Absorption coefficient	11.367 mm^{-1}	
F(000)	1508	
Crystal size	0.040 x 0.040 x 0.020 mm^3	
Theta range for data collection	3.501 to 68.088°.	

Index ranges	–10<=h<=10, –24<=k<=24, –19<=l<=19
Reflections collected	98715
Independent reflections	5172 [R(int) = 0.1799]
Completeness to theta = 67.684°	100.0 %
Absorption correction	Semi-empirical from equivalents
Max. and min. transmission	1.00000 and 0.42402
Refinement method	Full-matrix least-squares on F^2
Data / restraints / parameters	5172 / 0 / 319
Goodness-of-fit on F^2	1.082
Final R indices [I>2sigma(I)]	R1 = 0.0605, wR2 = 0.1271
R indices (all data)	R1 = 0.0909, wR2 = 0.1403
Extinction coefficient	n/a
Largest diff. peak and hole	1.409 and –2.057 e.Å^{-3}

[(PNP)Re(N)(Cl)][PF$_6$] (5, mini-16064): All non-hydrogen atoms were refined anisotropically. Hydrogen atoms were included in the model at geometrically calculated positions and refined using a riding model. The isotropic displacement parameters of all hydrogen atoms were fixed to 1.2 times the U value of the atoms to which they are linked (1.5 times for methyl groups). Several low angle reflections were obscured by the beam stop and subsequently omitted. The program SQUEEZE was used to compensate for the contribution of disordered solvents contained in voids within the crystal lattice from the diffraction intensities (A.L.Spek, Acta Cryst. 2009, D65, 148-155). This procedure was applied to the data file and the submitted model is based on the solvent removed data. Based on the total electron density found in the voids (87.9 e/Å^3), it is likely that ~2 tetrahydrofuran molecules are present in the unit cell. Cyclopentane was also considered. See "_platon_squeeze_details" in the .cif for more information.

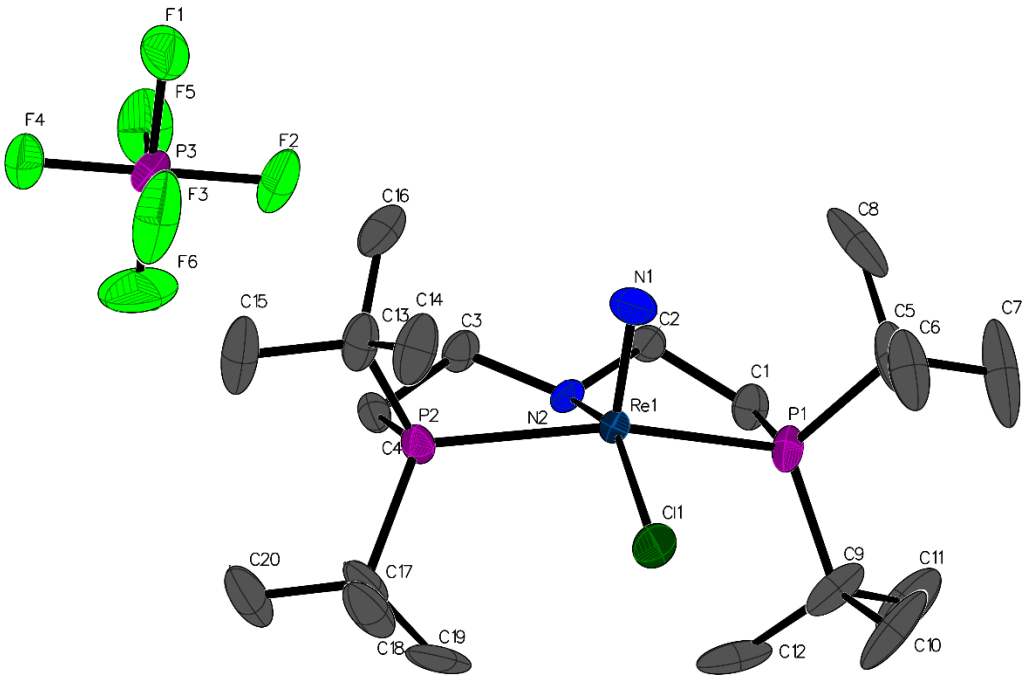

Figure 3.40. The complete numbering scheme of mini-16064 (**5**) with 50% thermal ellipsoid probability levels. The hydrogen atoms have been removed for clarity.

Table 3.31. Crystal data and structure refinement for mini-16064 (**5**).

Identification code	mini-16064	
Empirical formula	C20 H44 Cl F6 N2 P3 Re	
Formula weight	741.13	
Temperature	93(2) K	
Wavelength	0.71073 Å	
Crystal system	Monoclinic	
Space group	P2/c	
Unit cell dimensions	a = 16.0071(11) Å	α = 90°.
	b = 14.4897(8) Å	β = 115.838(9)°.
	c = 14.8364(10) Å	γ = 90°.
Volume	3097.1(4) $Å^3$	
Z	4	
Density (calculated)	1.589 Mg/m^3	
Absorption coefficient	4.212 mm^{-1}	
F(000)	1476	
Crystal size	0.220 x 0.210 x 0.080 mm^3	
Theta range for data collection	2.860 to 27.130°.	

Index ranges	–20<=h<=20, –18<=k<=18, –19<=l<=19
Reflections collected	28704
Independent reflections	6836 [R(int) = 0.0963]
Completeness to theta = 25.242°	99.8 %
Absorption correction	Semi-empirical from equivalents
Max. and min. transmission	1.00000 and 0.64023
Refinement method	Full-matrix least-squares on F^2
Data / restraints / parameters	6836 / 0 / 310
Goodness-of-fit on F^2	1.046
Final R indices [I>2sigma(I)]	R1 = 0.0445, wR2 = 0.1044
R indices (all data)	R1 = 0.0625, wR2 = 0.1170
Largest diff. peak and hole	1.635 and –1.762 e.Å^{-3}

[(P^HNP)Re(N)(Cl)][PF_6] (3-PF_6, mini-16096): All non-hydrogen atoms were refined anisotropically. Hydrogen atoms were included in the model at geometrically calculated positions and refined using a riding model. The isotropic displacement parameters of all hydrogen atoms were fixed to 1.2 times the U value of the atoms to which they are linked (1.5 times for methyl groups).

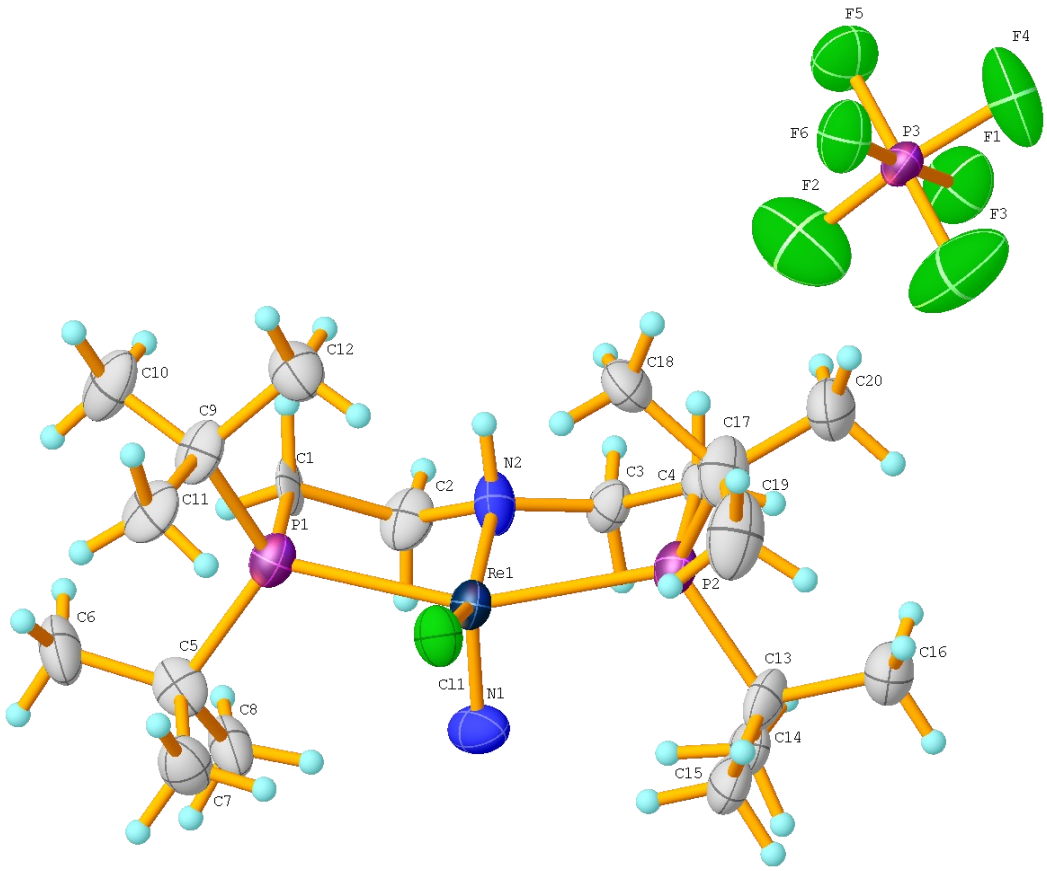

Figure 3.41. The complete numbering scheme of mini-16069 (**3-PF$_6$**) with 50% thermal ellipsoid probability levels. The hydrogen atoms are shown as circles for clarity.

Table 3.32. Crystal data and structure refinement for mini-16096 (**3-PF$_6$**).

Identification code	mini-16096	
Empirical formula	C20 H45 Cl F6 N2 P3 Re	
Formula weight	742.14	
Temperature	93(2) K	
Wavelength	0.71073 Å	
Crystal system	Monoclinic	
Space group	I2/a	
Unit cell dimensions	a = 14.5911(9) Å	α = 90°.
	b = 14.2947(8) Å	β = 95.276(6)°.
	c = 28.2101(19) Å	γ = 90°.
Volume	5859.0(6) Å^3	
Z	8	
Density (calculated)	1.683 Mg/m^3	

Absorption coefficient	4.453 mm^{-1}
F(000)	2960
Crystal size	0.200 x 0.150 x 0.050 mm^3
Crystal color and habit	Orange Plate
Diffractometer	Rigaku Mercury275R CCD
Theta range for data collection	1.598 to 25.019°.
Index ranges	–17<=h<=17, –17<=k<=17, –33<=l<=33
Reflections collected	40982
Independent reflections	5171 [R(int) = 0.1615]
Observed reflections (I > 2sigma(I))	3466
Completeness to theta = 25.019°	99.9 %
Absorption correction	Semi-empirical from equivalents
Max. and min. transmission	1.00000 and 0.83567
Solution method	SHELXT-2014/5 (Sheldrick, 2014)
Refinement method	SHELXL-2014/7 (Sheldrick, 2014)
Data / restraints / parameters	5171 / 0 / 310
Goodness-of-fit on F^2	1.047
Final R indices [I>2sigma(I)]	R1 = 0.0914, wR2 = 0.2095
R indices (all data)	R1 = 0.1335, wR2 = 0.2331
Largest diff. peak and hole	4.858 and –1.326 e.$Å^{-3}$

3.5 References

1. Klopsch, I.; Yuzik-Klimova, E. Y.; Schneider, S., Functionalization of N2 by Mid to Late Transition Metals via N–N Bond Cleavage. In *Nitrogen Fixation*, Nishibayashi, Y., Ed. Springer International Publishing: Cham, 2017; pp 71-112.

2. Laplaza, C. E.; Cummins, C. C., *Science* **1995,** *268*, 861.

3. Laplaza, C. E.; Johnson, M. J. A.; Peters, J.; Odom, A. L.; Kim, E.; Cummins, C. C.; George, G. N.; Pickering, I. J., *J. Am. Chem. Soc.* **1996,** *118*, 8623-8638.

4. Bezdek, M. J.; Chirik, P. J., *Angew. Chem., Int. Ed.* **2016,** *55*, 7892-7896.

5. Hebden, T. J.; Schrock, R. R.; Takase, M. K.; Mueller, P., *Chem. Commun.* **2012,** *48*, 1851-1853.

6. Silantyev, G. A.; Foerster, M.; Schluschass, B.; Abbenseth, J.; Wuertele, C.; Volkmann, C.; Holthausen, M. C.; Schneider, S., *Angew. Chem., Int. Ed.* **2017,** *56*, 5872-5876.

7. Ishida, Y.; Kawaguchi, H., *J. Am. Chem. Soc.* **2014,** *136*, 16990-3.

8. Klopsch, I.; Finger, M.; Wuertele, C.; Milde, B.; Werz, D. B.; Schneider, S., *J. Am. Chem. Soc.* **2014,** *136*, 6881-6883.

9. Liao, Q.; Cavaille, A.; Saffon-Merceron, N.; Mezailles, N., *Angew. Chem., Int. Ed.* **2016,** *55*, 11212-11216.

10. Arashiba, K.; Eizawa, A.; Tanaka, H.; Nakajima, K.; Yoshizawa, K.; Nishibayashi, Y., *Bull. Chem. Soc. Jpn.* **2017,** *90*, 1111-1118.

11. Lindley, B. M.; van Alten, R. S.; Finger, M.; Schendzielorz, F.; Würtele, C.; Miller, A. J. M.; Siewert, I.; Schneider, S., *J. Am. Chem. Soc.* **2018,** *140*, 7922-7935.

12. Rodriguez, M. M.; Bill, E.; Brennessel, W. W.; Holland, P. L., *Science* **2011,** *334*, 780-783.

13. Miyazaki, T.; Tanaka, H.; Tanabe, Y.; Yuki, M.; Nakajima, K.; Yoshizawa, K.; Nishibayashi, Y., *Angew. Chem., Int. Ed.* **2014,** *53*, 11488-11492.

14. MacLeod, K. C.; McWilliams, S. F.; Mercado, B. Q.; Holland, P. L., *Chem. Sci.* **2016,** *7*, 5736-5746.

15. Lee, Y.; Sloane, F. T.; Blondin, G.; Abboud, K. A.; García-Serres, R.; Murray, L. J., *Angew. Chem., Int. Ed.* **2014,** *54*, 1499-1503.

16. Nikiforov, G. B.; Vidyaratne, I.; Gambarotta, S.; Korobkov, I., *Angew. Chem., Int. Ed.* **2009,** *48*, 7415-7419.

17. Akagi, F.; Matsuo, T.; Kawaguchi, H., *Angew. Chem., Int. Ed.* **2007,** *46*, 8778-8781.

18. Shima, T.; Hu, S.; Luo, G.; Kang, X.; Luo, Y.; Hou, Z., *Science* **2013,** *340*, 1549.

19. Curley, J. J.; Sceats, E. L.; Cummins, C. C., *J. Am. Chem. Soc.* **2006,** *128*, 14036-14037.

20. Guru, M. M.; Shima, T.; Hou, Z., *Angew. Chem., Int. Ed.* **2016,** *55*, 12316-12320.

21. Klopsch, I.; Kinauer, M.; Finger, M.; Wurtele, C.; Schneider, S., *Angew. Chem., Int. Ed.* **2016,** *55*, 4786-9.

22. Man, W.-L.; Lam, W. W. Y.; Lau, T.-C., *Acc. Chem. Res.* **2014,** *47*, 427-439.

23. Berry, J. F., *Comments Inorg. Chem.* **2009,** *30*, 28-66.

24. Smith, J. M., *Prog. Inorg. Chem.* **2014,** *58*, 417-470.

25. Schendzielorz, F. S.; Finger, M.; Volkmann, C.; Wurtele, C.; Schneider, S., *Angew. Chem., Int. Ed.* **2016,** *55*, 11417-20.

26. Williams, D. S.; Meyer, T. J.; White, P. S., *J. Am. Chem. Soc.* **1995,** *117*, 823-4.

27. Coia, G. M.; Demadis, K. D.; Meyer, T. J., *Inorg. Chem.* **2000,** *39*, 2212-2223.

28. Crevier, T. J.; Lovell, S.; Mayer, J. M.; Rheingold, A. L.; Guzei, I. A., *J. Am. Chem. Soc.* **1998,** *120*, 6607-6608.

29. Walstrom, A.; Pink, M.; Fan, H.; Tomaszewski, J.; Caulton, K. G., *Inorg. Chem.* **2007,** *46*, 7704-7706.

30. Scheibel, M. G.; Askevold, B.; Heinemann, F. W.; Reijerse, E. J.; de Bruin, B.; Schneider, S., *Nat. Chem.* **2012,** *4*, 552-558.

31. Clarkson, S. G.; Basolo, F., *Inorg. Chem.* **1973,** *12*, 1528-34.

32. Ugo, R.; Bhaduri, S.; Johnson, B. F. G.; Khair, A.; Pickard, A.; Benn-Taarit, Y., *J. Chem. Soc., Chem. Commun.* **1976**, 694-5.

33. Tovrog, B. S.; Diamond, S. E.; Mares, F., *J. Am. Chem. Soc.* **1979,** *101*, 270-2.

34. Pipes, D. W.; Meyer, T. J., *Inorg. Chem.* **1984,** *23*, 2466-72.

35. Fernandez, B. O.; Lorkovic, I. M.; Ford, P. C., *Inorg. Chem.* **2004,** *43*, 5393-5402.

36. Zhang, J.-Y.; Liu, C.-M.; Zhang, D.-Q.; Gao, S.; Zhu, D.-B., *Inorg. Chim. Acta* **2007,** *360*, 3553-3559.

37. Okamura, Y.; Ishii, N.; Nogami, T.; Ishida, T., *Bull. Chem. Soc. Jpn.* **2010,** *83*, 716-725.

38. Boreen, M. A.; Bogart, J. A.; Carroll, P. J.; Schelter, E. J., *Inorg. Chem.* **2015,** *54*, 9588-9593.

39. Chen, S.-J.; Zhang, X.-H.; Yu, X.; Qiu, H.; Yap, G. P. A.; Guzei, I. A.; Lin, Z.; Wu, Y.-D.; Xue, Z.-L., *J. Am. Chem. Soc.* **2007,** *129*, 14408-14421.

40. Graham, T. W.; Tsang, C.-W.; Chen, X.; Guo, R.; Jia, W.; Lu, S.-M.; Sui-Seng, C.; Ewart, C. B.; Lough, A.; Amoroso, D.; Abdur-Rashid, K., *Angew. Chem., Int. Ed.* **2010,** *49*, 8708-8711.

41. Nielsen, M.; Kammer, A.; Cozzula, D.; Junge, H.; Gladiali, S.; Beller, M., *Angew. Chem., Int. Ed.* **2011,** *50*, 9593-9597.

42. Han, Z.; Rong, L.; Wu, J.; Zhang, L.; Wang, Z.; Ding, K., *Angew. Chem., Int. Ed.* **2012,** *51*, 13041-13045.

43. Choi, J.-H.; Prechtl, M. H. G., *ChemCatChem* **2015,** *7*, 1023-1028.

44. Schiwek, C.; Meiners, J.; Foerster, M.; Wuertele, C.; Diefenbach, M.; Holthausen, M. C.; Schneider, S., *Angew. Chem., Int. Ed.* **2015,** *54*, 15271-15275.

45. Fu, S.; Chen, N.-Y.; Liu, X.; Shao, Z.; Luo, S.-P.; Liu, Q., *J. Am. Chem. Soc.* **2016,** *138*, 8588-8594.

46. Fu, S.; Shao, Z.; Wang, Y.; Liu, Q., *J. Am. Chem. Soc.* **2017,** *139*, 11941-11948.

47. Affan, M. A.; Jessop, P. G., *Inorg. Chem.* **2017,** *56*, 7301-7305.

48. Nguyen, D. H.; Trivelli, X.; Capet, F.; Paul, J.-F.; Dumeignil, F.; Gauvin, R. M., *ACS Catal.* **2017,** *7*, 2022-2032.

49. Wiberg, K. B., *Tetrahedron* **1968,** *24*, 1083-1096.

50. Reed, A. E.; Curtiss, L. A.; Weinhold, F., *Chem. Rev.* **1988,** *88*, 899-926.

51. Voigt, A.; Abram, U.; Kirmse, R., *Inorg. Chem. Commun.* **1998,** *1*, 141-142.

52. Voigt, A.; Abram, U.; Strauch, P.; Kirmse, R., *Inorg. Chim. Acta* **1998,** *271*, 199-202.

53. Abram, U.; Braun, M.; Abram, S.; Kirmse, R.; Voigt, A., *J. Chem. Soc., Dalton Trans.* **1998**, 231-238.

54. Badger, R. M., *J. Chem. Phys.* **1935,** *3*, 710-14.

55. Laihia, K.; Kolehmainen, E.; Kauppinen, R.; Lorenc, J.; Puszko, A., *Spectrochim. Acta, Part A* **2002,** *58A*, 1425-1435.

56. Wrackmeyer, B., *Z. Naturforsch., B: J. Chem. Sci.* **2011,** *66*, 1079-1082.

57. Perinu, C.; Saramakoon, G.; Arstad, B.; Jens, K.-J., *Energy Procedia* **2014,** *63*, 1144-1150.

58. Galajov, M.; Garcia, C.; Gomez, M., *Dalton Trans.* **2011,** *40*, 413-420.

59. Galajov, M.; Garcia, C.; Gomez, M.; Gomez-Sal, P.; Temprado, M., *Organometallics* **2014,** *33*, 2277-2286.

60. Scepaniak, J. J.; Margarit, C. G.; Harvey, J. N.; Smith, J. M., *Inorg. Chem.* **2011,** *50*, 9508-9517.

61. Johnson, N. P.; Lock, C. J. L.; Wilkinson, G., *J. Chem. Soc.* **1964**, 1054-66.

62. Rouschias, G.; Wilkinson, G., *J. Chem. Soc. A* **1967**, 993-1000.

63. Schulz, A.; Villinger, A., *Chem. - Eur. J.* **2015,** *21*, 3649-3663.

64. Demadis, K. D.; Meyer, T. J.; White, P. S., *Inorg. Chem.* **1998,** *37*, 3610-3619.

65. Rhile, I. J.; Markle, T. F.; Nagao, H.; DiPasquale, A. G.; Lam, O. P.; Lockwood, M. A.; Rotter, K.; Mayer, J. M., *J. Am. Chem. Soc.* **2006,** *128*, 6075-6088.

66. Fulmer, G. R.; Miller, A. J. M.; Sherden, N. H.; Gottlieb, H. E.; Nudelman, A.; Stoltz, B. M.; Bercaw, J. E.; Goldberg, K. I., *Organometallics* **2010,** *29*, 2176-2179.

67. Frisch, M. J.; Trucks, G. W.; Schlegel, H. B.; Scuseria, G. E.; Robb, M. A.; Cheeseman, J. R.; Scalmani, G.; Barone, V.; Mennucci, B.; Petersson, G. A.; Nakatsuji, H.; Caricato, M.; Li, X.; Hratchian, H. P.; Izmaylov, A. F.; Bloino, J.; Zheng, G.; Sonnenberg, J. L.; Hada, M.; Ehara, M.; Toyota, K.; Fukuda, R.; Hasegawa, J.; Ishida, M.; Nakajima, T.; Honda, Y.; Kitao, O.; Nakai, H.; Vreven, T.; Montgomery, J. A.; Peralta, J. E.; Ogliaro, F.; Bearpark, M.; Heyd, J. J.; Brothers, E.; Kudin, K. N.; Staroverov, V. N.; Kobayashi, R.; Normand, J.; Raghavachari, K.; Rendell, A.; Burant, J. C.; Iyengar, S. S.; Tomasi, J.; Cossi, M.; Rega, N.; Millam, J. M.; Klene, M.; Knox, J. E.; Cross, J. B.; Bakken, V.; Adamo, C.; Jaramillo, J.; Gomperts, R.; Stratmann, R. E.; Yazyev, O.; Austin, A. J.; Cammi, R.; Pomelli, C.; Ochterski, J. W.; Martin, R. L.; Morokuma, K.; Zakrzewski, V. G.; Voth, G. A.; Salvador, P.; Dannenberg, J. J.; Dapprich, S.; Daniels, A. D.; Farkas; Foresman, J. B.;

Ortiz, J. V.; Cioslowski, J.; Fox, D. J., Gaussian 09, Revision B.01. In Wallingford CT, 2009.

68. Perdew, J. P.; Burke, K.; Ernzerhof, M., *Phys. Rev. Lett.* **1996,** *77*, 3865-3868.

69. Perdew, J. P.; Ernzerhof, M.; Burke, K., *J. Chem. Phys.* **1996,** *105*, 9982-9985.

70. Grimme, S.; Antony, J.; Ehrlich, S.; Krieg, H., *J. Chem. Phys.* **2010,** *132*, 154104/1-154104/19.

71. Roy, L. E.; Jakubikova, E.; Guthrie, M. G.; Batista, E. R., *J. Phys. Chem. A* **2009,** *113*, 6745-6750.

72. Konezny, S. J.; Doherty, M. D.; Luca, O. R.; Crabtree, R. H.; Soloveichik, G. L.; Batista, V. S., *J. Phys. Chem. C* **2012,** *116*, 6349-6356.

73. Glendening, E. D.; Landis, C. R.; Weinhold, F., *J. Comput. Chem.* **2013,** *34*, 1429-1437.

74. E. D. Glendening, J. K. B., A. E. Reed, J. E. Carpenter, J. A. Bohmann, C. M. Morales, C. R. Landis, F. Weinhold.

75. Mayer, I., *Chem. Phys. Lett.* **1983,** *97*, 270-4.

76. Mayer, I., *Int. J. Quantum Chem.* **1984,** *26*, 151-4.

4 Reduction of N_2-derived Rhenium-nitride complexes via Proton-coupled Electron Transfer

This chapter is reproduced in part from Bruch, Q. J.; Connor, G. P.; Chen, C.-H.; Holland, P. L.; Mayer, J. M.; Hasanayn, F.; Miller, A. J. M. Dinitrogen reduction to ammonium at rhenium utilizing light and proton-coupled electron transfer. *J. Am. Chem. Soc.* **2019**, 141, 20198-20208.

4.1 Introduction

The overall electrochemical nitrogen reduction reaction (NRR) to NH_3 via an N_2 cleavage mechanism can be divided into two general processes: the reductive bimetallic cleavage of the N–N bond to form metal nitrides and the subsequent reduction of these nitride to NH_3. Although the former half has decades of precedence stemming from Cummins's seminal work with $[N(^tBu)(Ar)]_3Mo$ (Ar = 3,5-dimethylphenyl),[1] the ability to form NH_3 from nitrides formed via N_2 cleavage is very uncommon.[2-4] The conversion of a nitride to NH_3 requires a $3e^-/3H^+$ reduction, making it a proton-coupled electron transfer (PCET) process. The rarity of NH_3 formation from N_2-derived metal nitrides is due to both thermodynamic[5-8] and kinetic challenges.[9-11] Considering that overall N_2 conversion to NH_3 is approximately ergoneutral, and that bimetallic N_2 cleavage to metal nitrides is generally exergonic due to the strong driving force of M–N bond formation, subsequent formation of NH_3 from the nitride is usually endergonic to even out the cycle. Thus N–H bond formation at the nitride requires high-energy reagents, for example strong reductants and strong Brønsted acids (see Section 1.5).

Chapter 1 outlines how utilizing a concerted PCET mechanism, in which an e^- and H^+ equivalent is transferred in a single elementary step, can overcome some of the challenges associated with stepwise PCET reduction, such as very cathodic reduction potentials of electron-rich metal nitrides or insufficiently Brønsted-basic nitride ligands.

The studies herein apply PCET reduction strategies to N_2-derived Re nitrides in an attempt to close the NRR cycle from N_2 to NH_3.

4.1.1. (^{tBu}PNP)Re as a system for N_2 reduction

Klopsch and Schneider reported the first instance of bimetallic N_2 cleavage using Re with their complex (^{tBu}PNP)$ReCl_2$ (^{tBu}PNP = N((CH$_2$CH$_2$)P^{t}Bu$_2$)$_2$), which forms (^{tBu}PNP)Re(N)(Cl) upon 1e^- under an atmosphere of N_2.[12] In analogy with the D_{3h}-symmetric, N_2-splitting Mo complexes originally reported by Cummins,[1, 13] N_2 cleavage by (PNP)Re proceeds through a bridging N_2 complex, [(^{tBu}PNP)ReCl]$_2$(μ-N_2) (**Scheme 4.1**).[12, 14] According to DFT computations, the N–N bond cleavage step occurs upon thermally accessing a zig-zag transition state (see Section 1.3 for more details), which in this case requires temperatures above –30 °C.[14] The facile cleavage of N_2 at ambient temperature is rationalized by its low barrier ($\Delta G^{\ddagger}$ = 20.2 kcal/mol) and favorable thermodynamics (ΔG = –23.5 kcal/mol).[12]

Scheme 4.1. Reductive bimetallic N_2 cleavage by (^{tBu}PNP)$ReCl_2$.

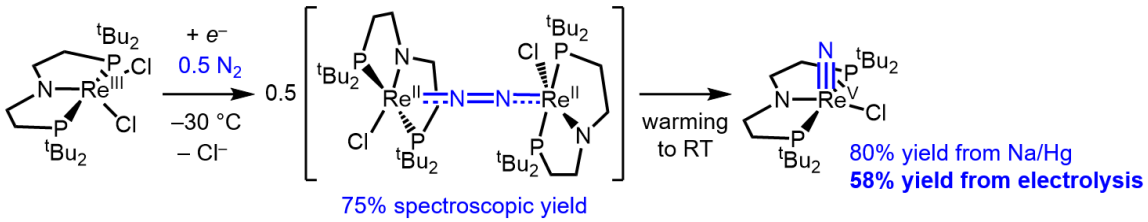

The inspiration for using this system as a model system for NRR lies in its remarkable ability to *electrochemically* split N_2. Electrolysis of (^{tBu}PNP)$ReCl_2$ at an applied potential of –1.9 V vs. $Cp_2Fe^{+/0}$ under 1 atm N_2 produces (^{tBu}PNP)Re(N)(Cl) in 58% yield. The mechanism of this transformation was elucidated using cyclic voltammetry (CV) experiments by Lindley *et al.*, who found that the rates of both the formation of the

N_2-bridging complex ($k^{298\ K}$ between 4×10^3 and 1×10^4 M^{-1} s^{-1}) and its subsequent cleavage into the nitride ($k^{298\ K} = 1.8 \times 10^{-2}$ s^{-1}) are rapid under electrolysis conditions.[14] This represents one half of the NRR reaction, justifying our investigation into the reduction of the nitride to NH_3 in an attempt to close the cycle.

In contrast to it its formation, (^{tBu}PNP)Re(N)(Cl) demonstrates a resilience to reactivity at the nitride. Initial reports indicated that stepwise PCET reduction of the nitride is not plausible: protonation of the complex occurs at the amide in the P*N*P backbone, and electrochemical reduction of the complex requires a highly cathodic potential (–3.34 V vs. $Cp_2Fe^{+/0}$).[12] Chapter 3 provides a summary of other efforts to cajole this nitride ligand into reactivity relevant to nitrogen fixation, with little success. However, the nitride does react with strong carbon electrophiles to form an N–C bond, which has led to stoichiometric cycles for the synthesis of acetonitrile and benzonitrile from N_2 (**Scheme 4.2**).[12, 15] This reactivity suggests that, if the driving force for bond formation at the nitride is sufficient, (^{tBu}PNP)Re could serve as a suitable scaffold for NRR.

Scheme 4.2. Stoichiometric cycle for nitrile synthesis from N_2 using (^{tBu}PNP)Re. [12, 15]

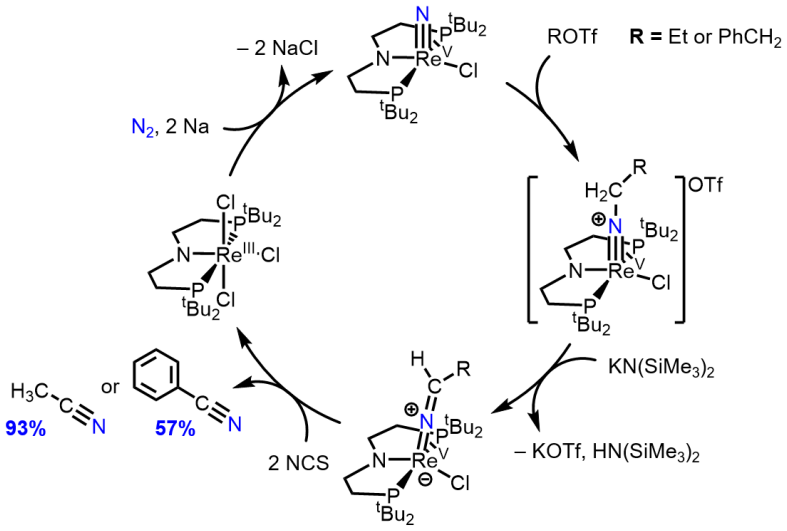

4.1.2. (^{iPr}PONOP)Re as system for N_2 reduction

In contrast to ^{tBu}PNP, the related pincer ligand ^{iPr}PONOP (2,6-bis-(diisopropyl-phosphinito)pyridine) does not contain a strongly Lewis basic amide.[16, 17] Additionally, the use of oxygen substituents in ^{iPr}PONOP provides a less electron-donating ligand, which should result in less cathodic reduction potentials for complexes along the NRR pathway. This led to the synthesis of (^{iPr}PONOP)$ReCl_3$ by Bruch and Miller, who demonstrated that the complex can bind N_2 in a bridging fashion upon $1e^-$ reduction and removal of a chloride (**Scheme 4.3**, top).[18]

Scheme 4.3. Reductive binding of N_2 (**top**) and subsequent thermal isomerization and photolytic N_2 cleavage (**bottom**) by (^{iPr}PONOP)Re.

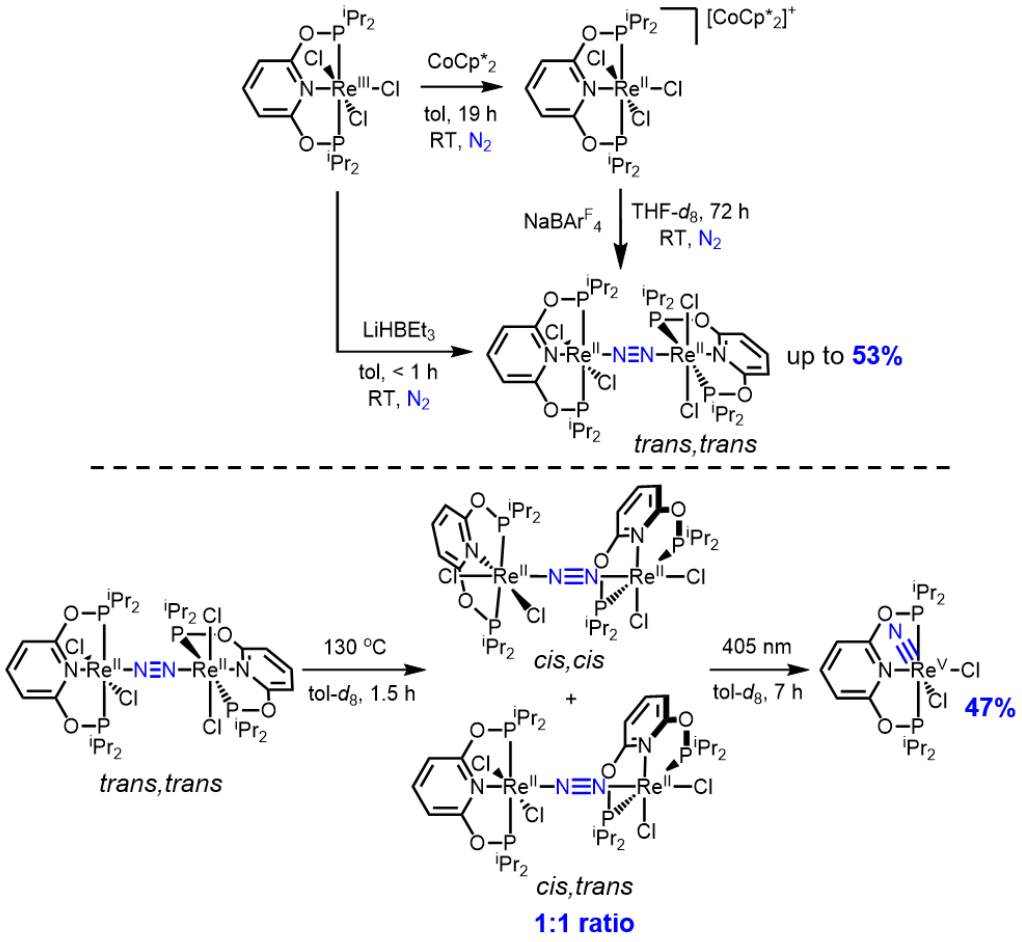

Bruch found that the resulting bridging N_2 complex [(^{iPr}PONOP)$ReCl_2$]$_2$(μ-N_2) is stable to thermal N_2 cleavage, despite its Re^{II}/Re^{II} "10-π" electron configuration. Instead, the μ-N_2 complex isomerizes into either a *cis,trans* or *cis,cis* confirmation. DFT calculations identified a prohibitively high barrier to thermal N–N bond cleavage ($\Delta G^{\ddagger}$ = 51–53 kcal/mol, isomer dependent) and unfavorable thermodynamics ($\Delta G°$ = +10–15 kcal/mol, isomer dependent). This is similar to the Re^{II}/Re^{II} complex reported by Schneider, [($^{iPr}P^{H}$NP)$ReCl_2$]$_2$(μ-N_2) ($^{iPr}P^{H}$NP = {HN[(CH_2CH_2)$P^{i}Pr_2$]$_2$}$^+$), which also demonstrates a high barrier to N–N bond cleavage and endergonic thermodynamics. However, Bruch found that photolysis of a 1:1 ratio of *cis,cis*/*cis,trans* [(^{iPr}PONOP)$ReCl_2$]$_2$(μ-N_2) at 405 nm results in formation of the Re^{V} nitride (^{iPr}PONOP)Re(N)$(Cl)_2$ in 47% yield (**Scheme 4.3**, bottom). This mirrors the reactivity of [($^{iPr}P^{H}$NP)$ReCl_2$]$_2$(μ-N_2), demonstrating another exciting example of using photon energy to drive N_2 cleavage to metal nitrides.

The lower driving force for N–N bond cleavage with (^{iPr}PONOP)Re implies that the (^{iPr}PONOP)Re nitride may be more reactive than that of (^{tBu}PNP)Re. For example, cyclic benzonitrile synthesis from (^{tBu}PNP)Re(N)(Cl) requires more steps and harsher reagents than benzonitrile synthesis from ($^{iPr}P^{H}$NP)Re(N)$(Cl)_2$.[19, 20] Furthermore, when considering the catalytic cycle of NRR more broadly, a less exergonic N_2 cleavage step should enable a less *endergonic* PCET nitride reduction step.

Bruch experimentally tested the stepwise PCET reduction of (^{iPr}PONOP)Re(N)$(Cl)_2$ using strong acids and electrochemical experiments. While the use of ^{iPr}PONOP did prevent protonation of the pincer ligand, the nitride remained stable to concentrated solutions of HCl in E_2O. Additionally, CV experiments showed that the

reduction potential of (^{iPr}PONOP)Re(N)(Cl)$_2$ is –2.4 V vs. $Cp_2Fe^{+/0}$ in THF. Although this represents a milder reduction potential than (^{tBu}PNP)Re(N)(Cl) by almost 1 V,[12] under the acidic conditions required for NRR, proton reduction to H_2 occurs directly at the electrode unless weak acids are employed. In order to better understand the thermodynamics of PCET reduction of the Re nitride to an imide, Hasanayn computed the stepwise and overall thermodynamics of the $1H^+/1e^-$ reduction of the nitride (**Figure 4.1**). This analysis shows that the N–H bond dissociation free energy ($BDFE_{N–H}$) of the imide is particularly weak (43 kcal/mol), and formation of the charged anionic nitride or cationic imide intermediates would require strong acids and reductants, respectively. However, a concerted PCET mechanism could bypass the high-energy charged intermediates, provided the effective BDFE ($BDFE_{eff}$) of the PCET reagent is less than 43 kcal/mol (see Section 1.5 for more details). Considering recent literature reports of concerted PCET reagents with suitably weak $BDFE_{eff}$ values, we reasoned that nitride reduction to NH_3 may be possible with (^{iPr}PONOP)Re(N)(Cl)$_2$.

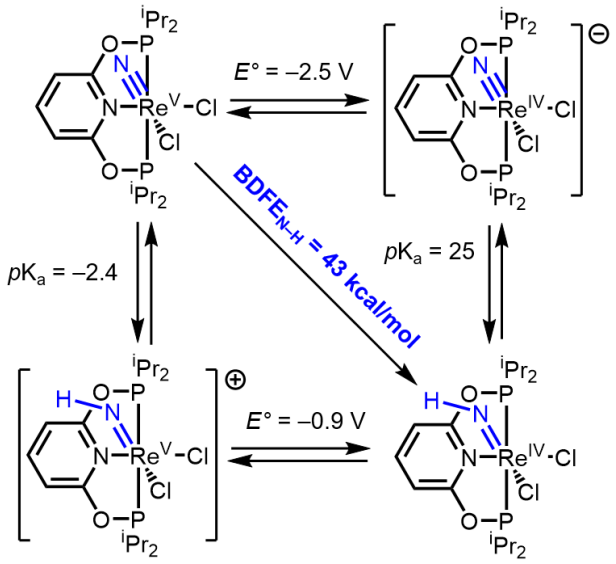

Figure 4.1. Computed PCET square scheme for the $1H^+/1e^-$ reduction of (^{iPr}PONOP)Re(N)(Cl)$_2$ to the imide complex in THF. $E°$ values are reported vs. $Cp_2Fe^{+/0}$. $BDFE_{N–H}$ is calculated from the Bordwell equation (see Section 1.5). Computations performed by F. Hasanayn.

4.2 Results and Discussion

4.2.1. PCET reduction of (^{iPr}PONOP)Re(N)(Cl)$_2$ with SmI$_2$

The combination of SmI_2 and H_2O has been used for PCET reduction of difficult organic substrates[21-23] and demonstrates the weakest $BDFE_{eff}$ of any PCET reagents currently known ($BDFE_{O–H}$ = 26 kcal/mol).[23] Concurrent with the studies herein, SmI_2 and H_2O were also used for the catalytic reduction of N_2 to NH_3 using Mo pincer complexes,[2-4] demonstrating the highest turnover and selectivity for NH_3 of any molecular N_2 reduction catalyst. We reasoned that SmI_2 and H_2O would provide sufficient driving force to form the imide N–H bond upon reaction with (^{iPr}PONOP)Re(N)(Cl)$_2$.

To test this idea, (^{iPr}PONOP)Re(N)(Cl)$_2$ was mixed with 3.3 equiv SmI_2 and 10 equiv H_2O in THF-d_8, resulting in an immediate color change from the deep blue of SmI_2

in THF to maroon. NMR spectroscopy revealed complete consumption of the (^{iPr}PONOP)Re(N)(Cl)$_2$ starting material and formation of new species by ^{31}P{^{1}H} NMR spectroscopy (**Figure 4.2**). The ^{1}NMR spectra of the reaction indicate the formation of hydride species (δ –5.99 and –7.64 ppm), as well as the formation of a broad 1:1:1 triplet at δ 7.13 ppm characteristic of NH_4^+ (J_{NH} = 51 Hz, **Figure 4.3**). Bruch confirmed that the 1:1:1 triplet was NH_4^+ using ion chromatography (IC),[24, 25] which determined that NH_4^+ was formed in 36% yield (compared to 35% yield by ^{1}H NMR spectroscopy). This represents the first example of N_2 fixation to NH_3 using Re.

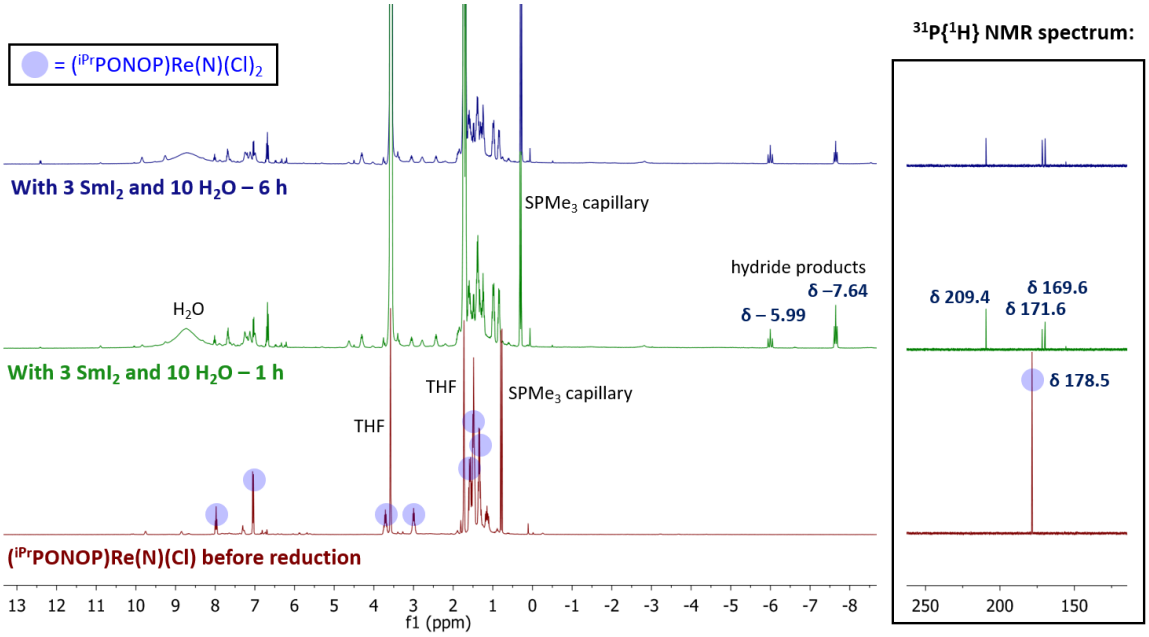

Figure 4.2. ^{1}H and ^{31}P{^{1}H} NMR spectra showing reduction of (^{iPr}PONOP)Re(N)(Cl)$_2$ with 3.3 equiv SmI$_2$ and 10 equiv H$_2$O in THF-d_8, showing full consumption of the nitride starting material and formation of new (^{iPr}PONOP)Re complexes (^{31}P{^{1}H} δ 209.4 (s), 171.6 (s), 169.6 (s) ppm) and hydrides (^{1}H δ –5.99 (t), –7.64 ppm (t)).

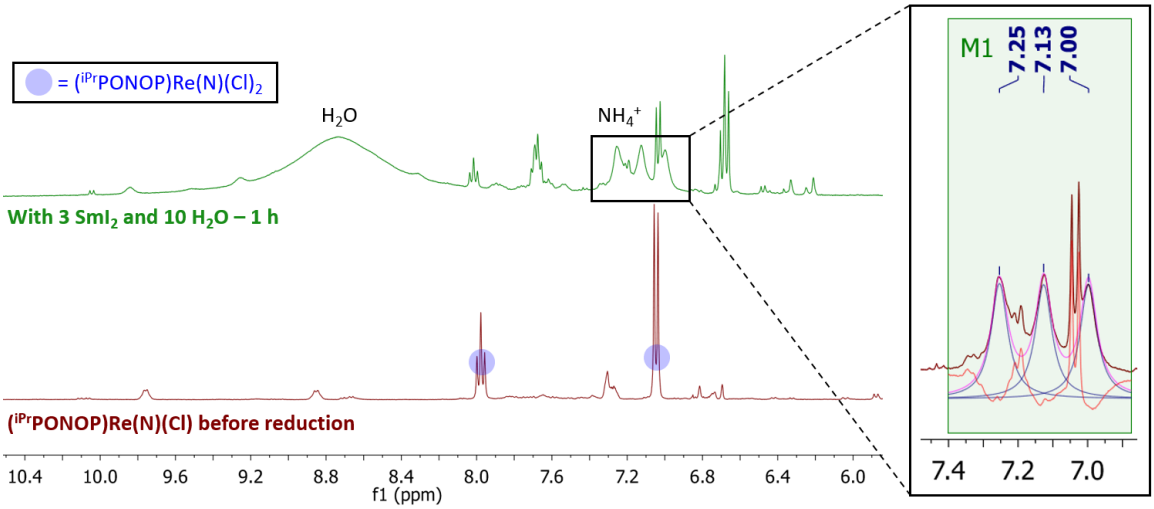

Figure 4.3. Zoomed ^{1}H NMR spectra showing 1:1:1 triplet corresponding to NH_4^+ (inset, δ 7.13 ppm, J_{NH} = 51 Hz) upon reduction of (^{iPr}PONOP)Re(N)(Cl)$_2$ with 3.3 equiv SmI_2 and 10 equiv H_2O.

The formation of NH_4^+ confirms that PCET reduction of the nitride in (^{iPr}PONOP)Re(N)(Cl)$_2$ can be achieved by SmI_2 and H_2O, presumably via initial formation of a N–H bond to form the imide complex. In order to probe the potential formation of a Re imide complex, (^{iPr}PONOP)Re(N)(Cl)$_2$ was reacted with 1 equiv SmI_2 and 10 equiv H_2O. Upon mixing, an immediate color change to amber-brown occurred and a white precipitate of Sm^{III} formed. Isolation of the colored product revealed a C_s-symmetric (^{iPr}PONOP)Re complex by ^{1}H NMR spectroscopy, with a ^{31}P{^{1}H} shift of δ 170.7 ppm (**Figure 4.4**). A [(^{iPr}PONOP)Re(N)(I)]$^+$ fragment dominates the high-resolution mass spectrum of the product, suggesting that reaction of the compound with SmI_2 first results in halide change (**Figure 4.5**). This hypothesis was confirmed by Bruch, who showed that reaction of (^{iPr}PONOP)Re(N)(Cl)$_2$ with LaI_3 gives (^{iPr}PONOP)Re(N)(I)$_2$,[18] which was crystallographically characterized and is spectroscopically identical to the product of (^{iPr}PONOP)Re(N)(Cl)$_2$ and 1 equiv SmI_2/10 equiv H_2O. Halide replacement upon reaction with SmI_2 has also been noted in Mo systems that can catalytically reduce N_2 to NH_3.

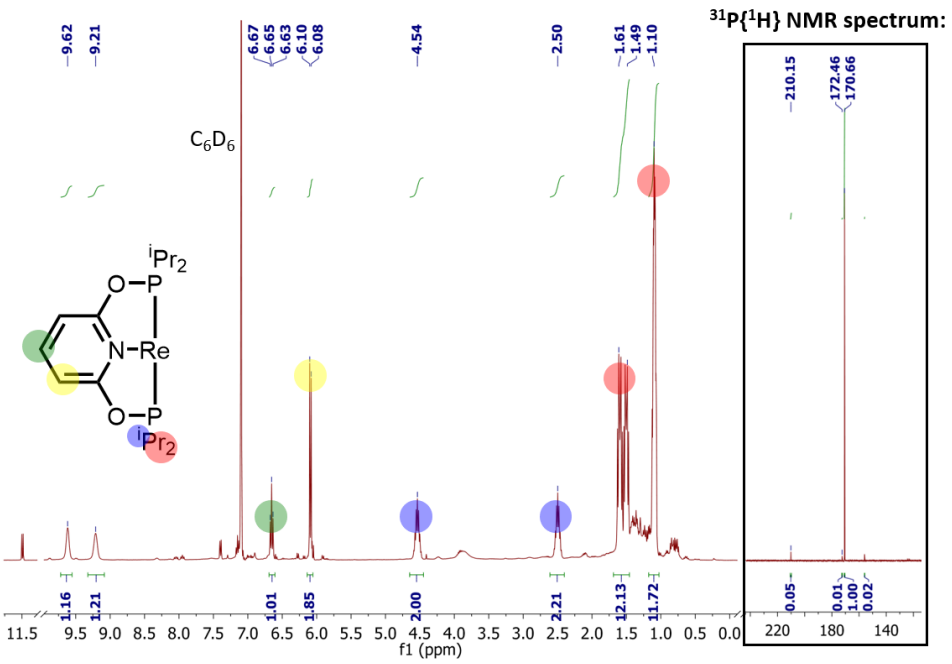

Figure 4.4. ^{1}H and $^{31}P\{^{1}H\}$ spectra (C_6D_6) of isolated product from the reduction of (^{iPr}PONOP)Re(N)(Cl)$_2$ with 1 equiv SmI_2 and 10 H_2O. The major product (^{31}P δ = 170.7 ppm (s)) corresponds to a C_s-symmetric (^{iPr}PONOP)Re complex, which can be identified by the splitting and relative integrations of ^{1}H resonances (colored dots).

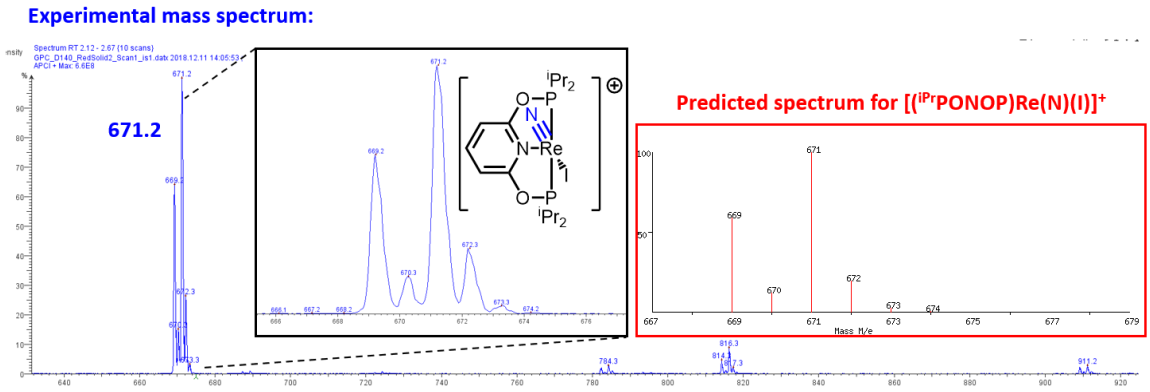

Figure 4.5. Mass spectrum (blue) of product isolated product from the reduction of (^{iPr}PONOP)Re(N)(Cl)$_2$ with 1 equiv SmI_2 and 10 H_2O, showing major mass fragment corresponding to [(^{iPr}PONOP)Re(N)(I)]$^+$. The experimental spectrum matches the predicted isotope pattern (red).

In order to optimize the reduction of nitride to NH_3, (^{iPr}PONOP)Re(N)(Cl)$_2$ was reacted with 10 equiv of SmI_2 and 100 equiv H_2O in THF-d_8, again resulting in a rapid reaction and the appearance of a broad 1:1:1 triplet in the ^{1}H NMR spectrum (δ 7.14 ppm,

J_{HN} = 48.6 Hz) characteristic of NH_4^+ (**Scheme 4.4**). The production of NH_4^+ was confirmed by IC (performed by Bruch, 74% ± 3%, average of three trials) and ^{1}H NMR spectroscopy (77% ± 9% yield, average of three trials, see **Figure 4.6** for example). Along with NH_4^+, one new dominant diamagnetic product was observed by ^{31}P NMR spectroscopy (δ 208.9 ppm, 38% yield, **Figure 4.7**). Unfortunately, the instability of the Re product to vacuum prevented its isolation (**Figure 4.8**). However, 2D ^{1}H–^{31}P HMBC, selectively coupled ^{31}P NMR, and mass spectrometry performed by Bruch enabled assignment of the product as (PONOP)Re(I)$(H)_4$, especially with the observation of a quintet for the proton-coupled ^{31}P resonance.[26] It is noteworthy that the ^{iPr}PONOP ligand successfully withstands the acidic conditions of NH_4^+ formation via SmI_2/H_2O reduction.

Scheme 4.4. PCET reduction of (^{iPr}PONOP)Re(N)$(Cl)_2$ with SmI_2/H_2O to form NH_4^+.

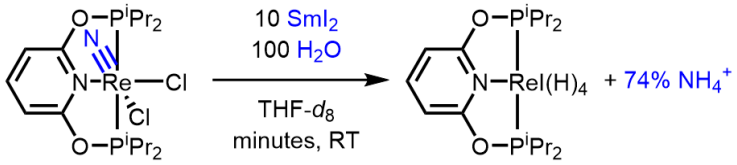

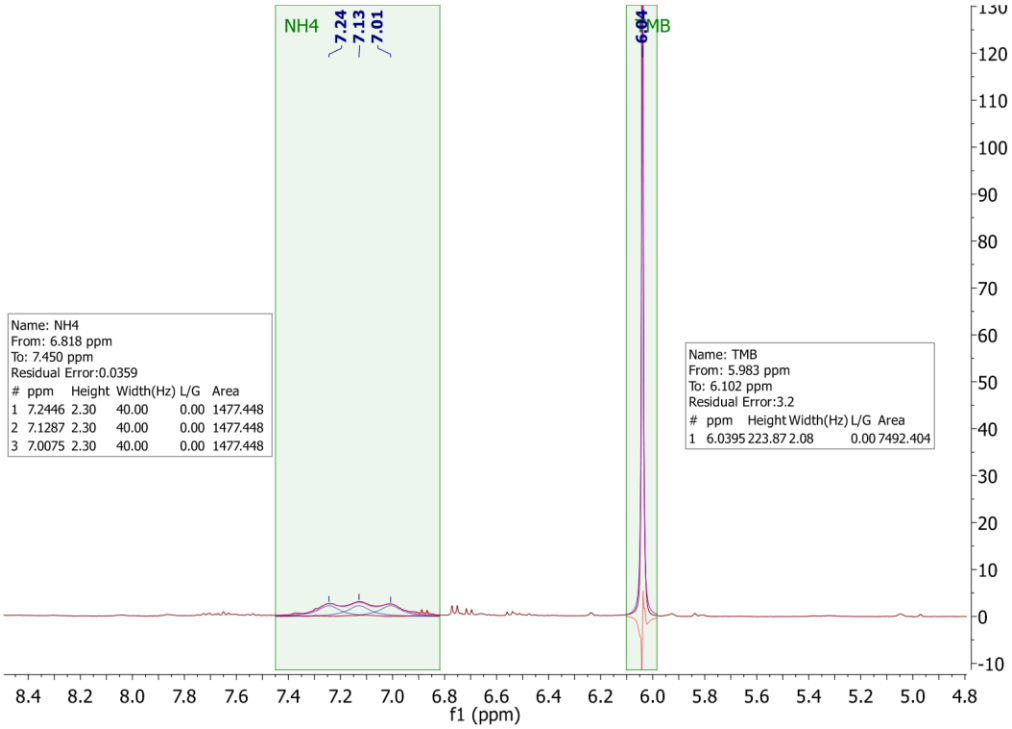

Figure 4.6. ^{1}H NMR spectrum (400 MHz, THF-d_8) of NH_4^+ isolated from reaction of (^{iPr}PONOP)Re(N)Cl_2 with 10 equiv SmI_2 and 100 equiv H_2O. NH_4^+ is detected as a broadened 1:1:1 triplet centered at δ 7.13 ppm (J = 47 Hz). Due to the significant broadening of the resonance, the peaks were fit as a 1:1:1 triplet and compared to 30.0 mM TMB as an internal standard (δ 6.04 ppm, s, 3H). Comparison of peak integrations shows a 70.0% yield of NH_4^+ based on Re. We hypothesize that the significant broadening of the NH_4^+ peak is due to hydrogen-bonding interactions with hydroxyl-containing Sm or Re products in the reaction mixture, as attempts to further dry the samples did not improve peak resolution.

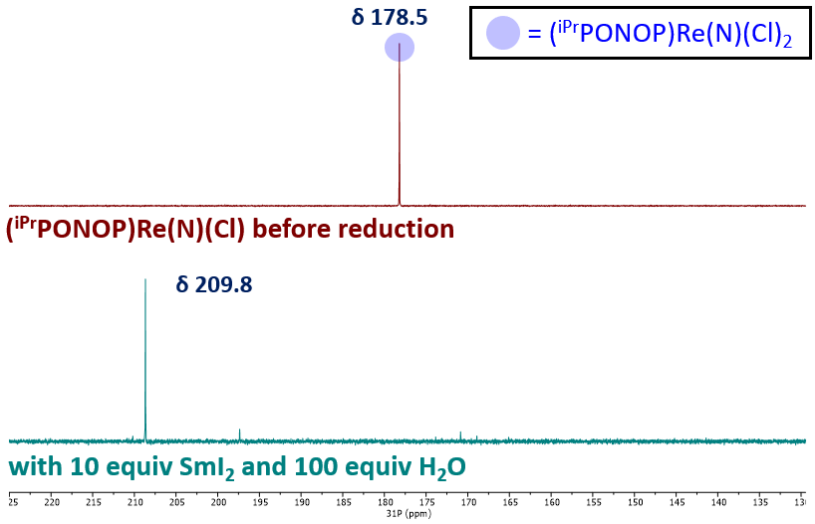

Figure 4.7. $^{31}P\{^{1}H\}$ NMR spectra (282 MHz, THF-d_8) of (^{iPr}PONOP)Re(N)Cl_2 before (maroon, top) and after (teal, bottom) addition of 10 equiv SmI_2 and 100 equiv H_2O, showing formation of a new diamagnetic complex (δ 209.8 ppm (s), 38% yield).

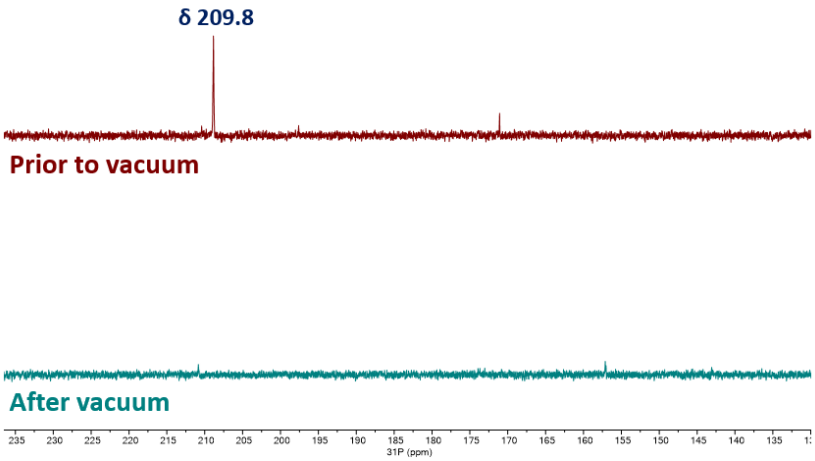

Figure 4.8. $^{31}P\{^{1}H\}$ NMR spectra (282 MHz, THF-d_8) of diamagnetic product from the reduction of (^{iPr}PONOP)Re(N)Cl_2 with 10 equiv SmI_2 and 100 H_2O before (top, maroon) and after (bottom, teal) exposure to vacuum, showing decomposition of the species under vacuum. The hydride resonance in the ^{1}H NMR spectrum also disappears.

The presence of SmI_2 is essential for NH_4^+ formation in this reaction. Treating (^{iPr}PONOP)Re(N)$(Cl)_2$ with 30 equiv of H_2O (and no SmI_2) resulted in complete decomposition over 5 h with no detectable NH_4^+. Treating (^{iPr}PONOP)Re(N)$(Cl)_2$ with LaI_3 and 45 equiv H_2O resulted in some chloride-iodide exchange but produced <1% NH_4^+.[18]

The use of SmI_2/H_2O, which can provide both H^+ and e^-, proved much more successful for nitride reduction as compared to attempts at stepwise protonation and reduction. The use of other O–H and C–H PCET reagents under conditions analogous to those described above (10 equiv, room temperature) was therefore tested. Treating nitride complex (^{iPr}PONOP)Re(N)$(Cl)_2$ with 2,4,6-tri-*tert*-butylphenol (^{t}Bu$_3$PhOH, $BDFE_{O–H}$ = 74.4 kcal/mol in THF, **Figure 4.9**),[27] TEMPOH ($BDFE_{O–H}$ = 65.5 kcal/mol in THF, **Figure 4.10**),[27] or 1,8-dichloro-9,10-anthracenediol (DCAD, average $BDFE_{O–H}$ = 55.4 kcal/mol in THF, **Figure 4.11**)[27] resulted in no reaction over 1 h. The lack of observed reactivity is consistent with a lack of driving force for N–H bond formation using these reagents, which have stronger O–H bonds compared to SmI_2/H_2O ($BDFE_{O–H}$ = 26 kcal/mol in H_2O).[23] In contrast, treating (^{iPr}PONOP)Re(N)$(Cl)_2$ with $CoCp_2$* and $Ph_2NH_2^+$ produces NH_4^+ in 24% yield (performed by Bruch).[18] These conditions can generate [Co(Cp*)(Cp*H)] ($BDFE_{C–H}$ ~ 29 kcal/mol in butyronitrile),[28-30] which features a $BDFE_{C–H}$ similar to the $BDFE_{O–H}$ of SmI_2/H_2O.

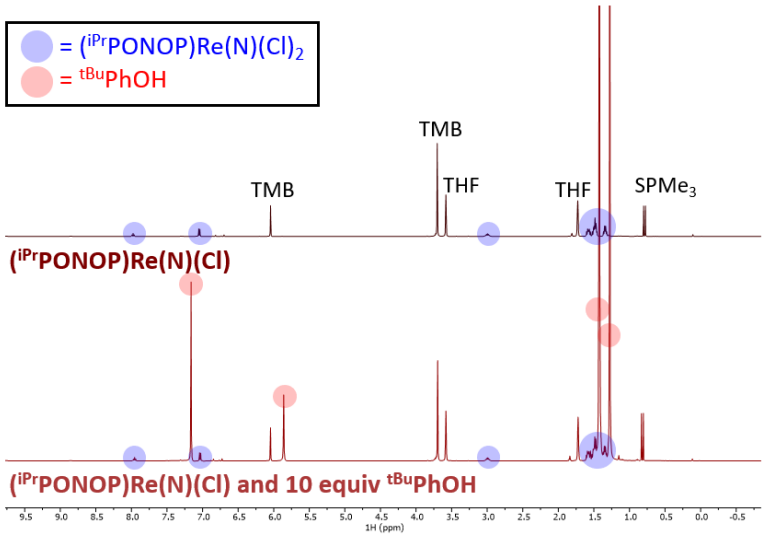

Figure 4.9. ^{1}H NMR spectra (500 MHz, THF-d_8) of (^{iPr}PONOP)Re(N)$(Cl)_2$ before (top, maroon) and 1 h after (bottom, red) mixture with 10 equiv ^{t}Bu$_3$PhOH, showing no reaction vs. TMB and $SPMe_3$ internal standards.

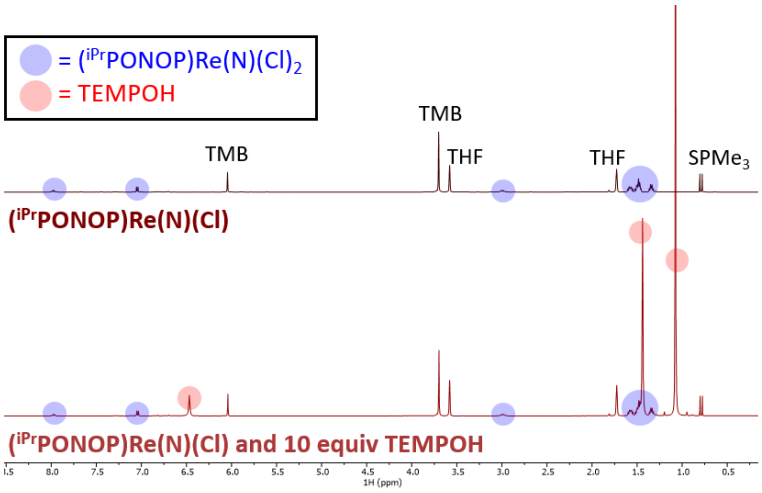

Figure 4.10. ^{1}H NMR spectra (500 MHz, THF-d_8) of (^{iPr}PONOP)Re(N)(Cl)$_2$ before (top, maroon) and 1 h after (bottom, red) mixture with 10 equiv TEMPOH, showing no reaction vs. TMB and $SPMe_3$ internal standards.

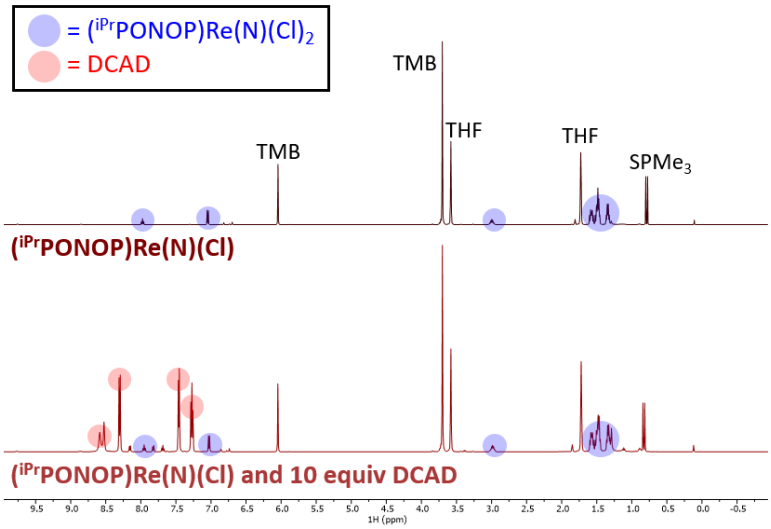

Figure 4.11. ^{1}H NMR spectra (500 MHz, THF-d_8) of (^{iPr}PONOP)Re(N)(Cl)$_2$ before (top, maroon) and 1 h after (bottom, red) mixture with 10 equiv 1,8-dichloro-9,10-anthracenediol, showing no reaction vs. TMB and $SPMe_3$ internal standards.

Formation of ammonia from nitride complex (^{iPr}PONOP)Re(N)(Cl)$_2$ was only observed using species having exceptionally weak BDFE values that provide at least –14 kcal/mol of thermodynamic driving force for initial N–H bond formation. The first N–H bond formation is often proposed to be the most difficult of the imide/amide/ammine

series,[6-8, 31] and the same trend is predicted computationally in the present system (**Figure 4.12**). In accord with this trend, the driving force for delivery of the *second* H^+/e^- equivalent was calculated to be quite large (*ca.* –52 kcal/mol), implicating rapid formation of the more stable amide species.

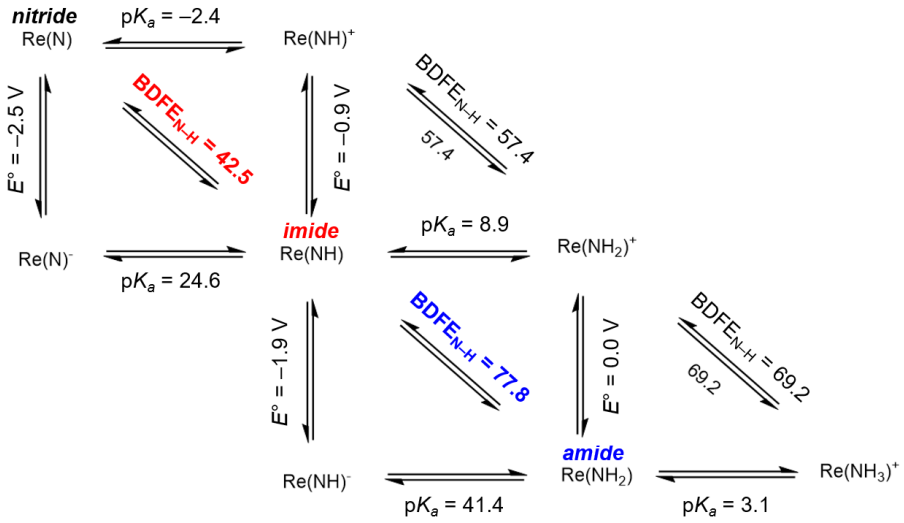

Figure 4.12. Computed PCET thermodynamic parameters for the sequential reduction of the nitride in (^{iPr}PONOP)Re(N)(Cl)$_2$ to an ammine, demonstrating formation of a weak imide N–H bond (red) followed by a more stable amide N–H bond (blue). BDFE values are given in kcal/mol, and *E*° values are vs. $Cp_2Fe^{+/0}$. Figure adapted from Q. Bruch; computations performed by F. Hasanayn.

4.2.2. Targeting a regenerable Sm PCET reagent

The reaction of (^{iPr}PONOP)Re(N)(Cl)$_2$ with SmI_2 and H_2O was accompanied by formation of a precipitate in every case, presumably an insoluble Sm^{III}-hydroxide product. Although the discovery that (^{iPr}PONOP)Re can fix N_2 to NH_3 is promising, the use of superstoichiometric SmI_2 is uneconomical. A more feasible system for electrocatalytic NRR would include a soluble Sm^{III} product from reduction of the nitride, which could be regenerated via reduction at the electrode and protonation from a weak acid, serving as a

potent PCET mediator (**Scheme 4.4**). The utility of soluble Sm^{III} in the catalytic use of SmI_2/H_2O as a reductant was recently demonstrated by Maity *et al*.[32]

Scheme 4.5. Simplified depiction of potential use of a soluble Sm source as a PCET mediator in electrocatalytic NRR, with e^- coming from the electrode and H^+ coming from a weak acid.

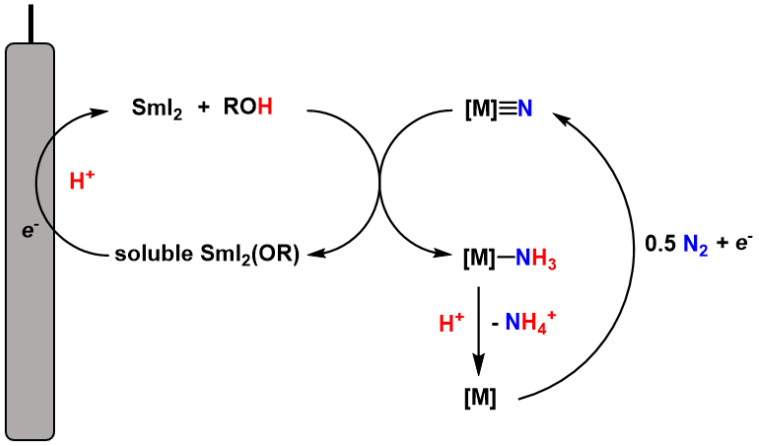

We reasoned that the bulky hydroxylamine TEMPOH could perform the role of an alcohol in classic SmI_2 PCET reactions while providing a more soluble Sm^{III} product. TEMPOH may also provide a strong enough PCET reagent ($BDFE_{O–H}$ = 65.5 kcal/mol in THF)[27] to perform the subsequent reductions of imide to amide or amide to ammine, and can also be regenerated at the electrode. To test this hypothesis, a combination of 2 equiv SmI_2 and 2 equiv TEMPOH was added to a solution of 5,10-phenazine in THF-d_8. Within minutes, the solution turned from deep blue to light green (no precipitate is formed), and 5,10-dihydrophenazine (average $BDFE_{N–H}$ = 58.7 kcal/mol in MeCN)[27] formed in near-quantitative yield (>95%) by ^{1}H NMR spectroscopy (**Figure 4.13**). Repeating the reaction in the absence of SmI_2 gave no reaction, as predicted by the unfavorable thermodynamics of PCET from 2 TEMPOH to phenazine ($\Delta G° \sim +14$ kcal/mol). Similarly, addition of 2 equiv ^{t}Bu$_3$PhOH ($BDFE_{O–H}$ = 74.4 kcal/mol in THF) and 2 equiv SmI_2 to phenazine also resulted in quantitative formation of 5,10-dihydrophenazine by ^{1}H NMR spectroscopy

(**Figure 4.14**); however, this reaction was accompanied by formation of a white precipitate.

Again, the reduction of phenazine by $^{t}Bu_3PhOH$ does not occur in the absence of SmI_2.

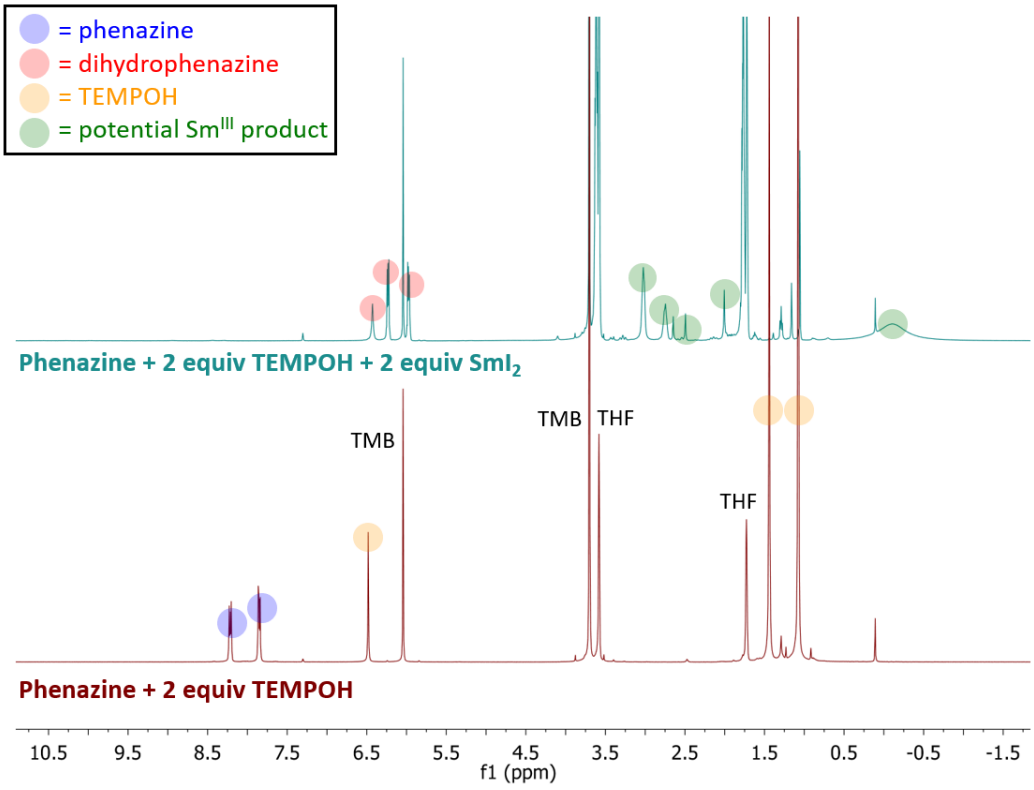

Figure 4.13. ^{1}H NMR spectra (400 MHz, THF-d_8) of the reduction of phenazine with 2 equiv TEMPOH and 2 equiv SmI_2. The reaction does not proceed without SmI_2 (bottom, maroon) but gives complete consumption of phenazine to give dihydrophenazine (top, teal; reaction after 3 hr at ambient temperature; >95% spectroscopic yield vs. TMB internal standard). TEMPOH is also consumed, and broad, unidentified peaks that may correspond to a soluble Sm^{III} product are observed (highlighted in green).

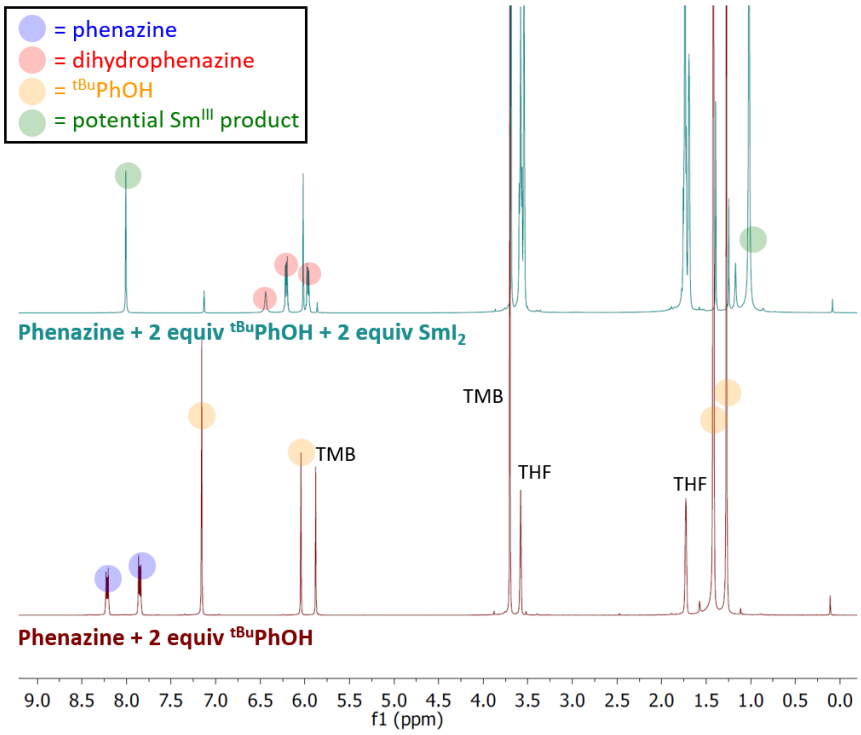

Figure 4.14. ^{1}H NMR spectra (400 MHz, THF-d_8) of the reduction of phenazine with 2 equiv ^{t}Bu$_3$PhOH and 2 equiv SmI_2. The reaction does not proceed without SmI_2 (bottom, maroon) but gives complete consumption of phenazine to give dihydrophenazine (top, teal; reaction after 16 h at ambient temperature; >95% spectroscopic yield vs. TMB internal standard). ^{t}Bu$_3$PhOH is also consumed, and unidentified peaks that may correspond to a soluble Sm^{III} product are observed (highlighted in green).

Regarding the SmI_2/TEMPOH reduction of phenazine, the lack of formation of a precipitate normally associated with SmI_2 reductions was encouraging. Cooling the crude reaction mixture to –40 °C resulted in the growth of small, yellow crystals. Single-crystal X-ray diffraction (XRD) of the crystals revealed a Sm^{III} TEMPO complex, $SmI_2(TEMPO)(THF)_2$ which is soluble in THF (**Figure 4.15**). Independent synthesis of the complex by addition of TEMPO$^\bullet$ to SmI_2 provides a yellow product featuring ^{1}H resonances that correlate to those present in the reduction of phenazine by SmI_2/TEMPOH (**Figure 4.16**). Unfortunately, the ^{1}H resonances of $SmI_2(TEMPO)(THF)_2$ could not be assigned accurately, potentially due to formation of multiple structural isomers. Regardless, the ability of SmI_2/TEMPOH to serve as potent PCET reagent and form a

soluble Sm^{III} product is promising for development of potential regenerable Sm PCET mediators.

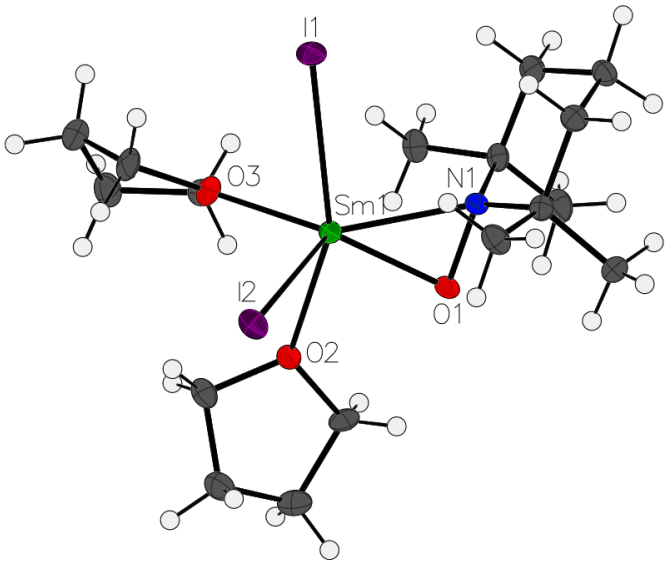

Figure 4.15. Solid-state structure of $SmI_2(TEMPO)(THF)_2$ complex with thermal ellipsoids at 50% probability. The complex displays a distorted trigonal bipyramidal coordination geometry (excluding O1 from TEMPO).

Table 4.1. Selected bond lengths (Å) and bond angles (°) of $SmI_2(TEMPO)(THF)_2$.

Bond/Angle	**$SmI_2(TEMPO)(THF)_2$**
Sm1–O1	2.163(3)
Sm1–N1	2.393(3)
Sm1–O2	2.451(3)
Sm1–O3	2.418(3)
Sm1–I1	3.0872(4)
Sm1–I2	3.0492(3)
O1–N2	1.440(4)
O1–Sm1–O3	128.5(1)
N1–Sm1–O1	36.4(1)
N1–Sm1–O2	109.4(1)
N1–Sm1–O3	130.2(1)
I1–Sm1–O2	156.8(1)

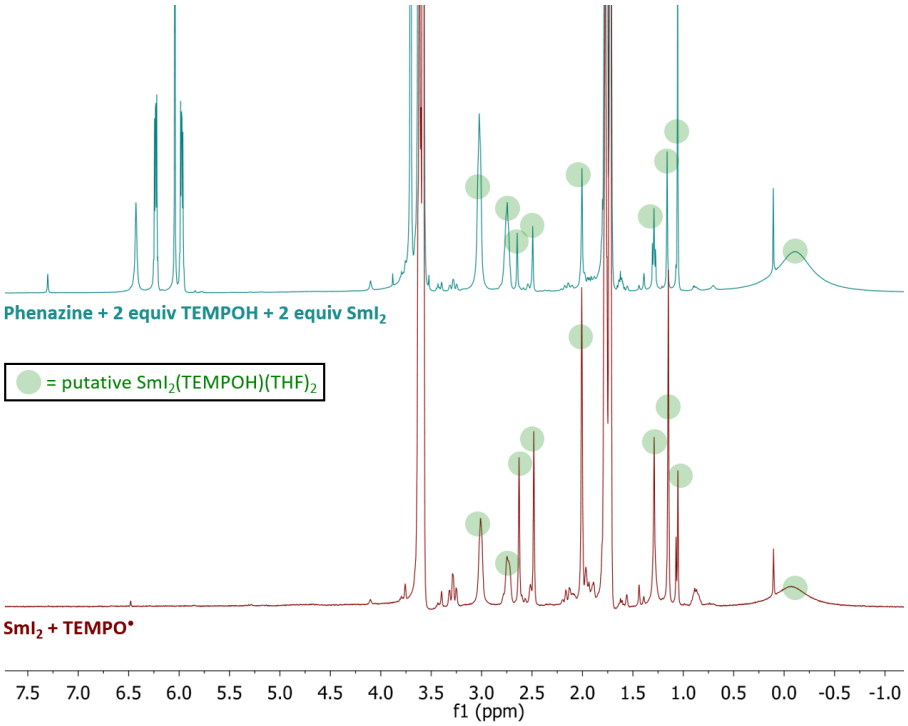

Figure 4.16. Conserved ^{1}H resonances (highlighted in green) between reaction of SmI_2 and TEMPO$^{\bullet}$ (bottom, maroon) and reduction of phenazine with 2 equiv TEMPOH and 2 equiv SmI_2 (top, maroon), potentially corresponding to soluble Sm^{III} product $SmI_2(TEMPO)(THF)_2$.

4.2.3. Exploring other PCET reagents for reduction of (^{iPr}PONOP)Re(N)(Cl)$_2$

The efficacy of SmI_2/TEMPOH and SmI_2/^{t}Bu$_3$PhOH to reduce (^{iPr}PONOP)Re(N)(Cl)$_2$ was tested as a proof of concept for PCET nitride reduction with these systems. The addition of 2 equiv SmI_2 and 20 equiv of TEMPOH to a solution of (^{iPr}PONOP)Re(N)(Cl)$_2$ resulted in an immediate color change to brown and consumption of the nitride complex by ^{1}H and ^{31}P{^{1}H} NMR spectroscopy (**Figure 4.17**). Notably, no precipitate was formed, and ^{1}H resonances correlating with those found in the spectrum of the product formed from addition of TEMPO$^{\bullet}$ to SmI_2 were also observed (**Figure 4.18**). Acidification of the reaction mixture with excess HCl and analysis by IC showed that 25% NH_4^+ per Re was formed from the reaction, which is significantly less than using SmI_2/H_2O (**Scheme 4.6**). When the reaction was repeated using ^{t}Bu$_3$PhOH instead of TEMPOH,

consumption of the nitride was slow, with ~10% remaining after 48 hr at ambient temperature. Acidification of the reaction mixture with excess HCl and analysis by IC showed on 8% NH_4^+ per Re was formed (see **Scheme 4.6**). Although the yields of these reactions are small compared to SmI_2/H_2O, the formation of any NH_4^+ at all implies that these systems can serve as PCET reagents to form weak N–H bonds. The formation of soluble Sm^{III} products merits further exploration into their potential use as electrochemical PCET mediators.

Scheme 4.6. PCET reduction of (^{iPr}PONOP)Re(N)(Cl)$_2$ with various PCET reagents to form NH_4^+.

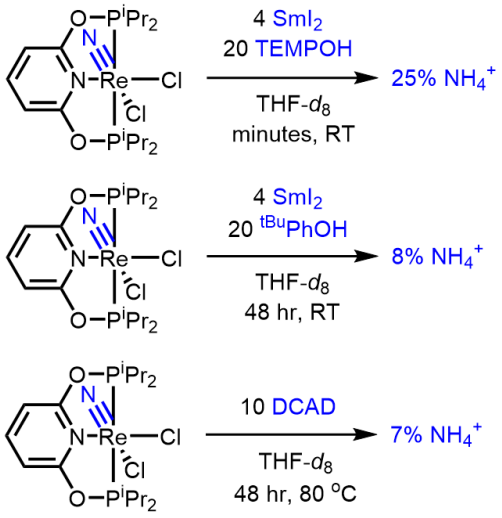

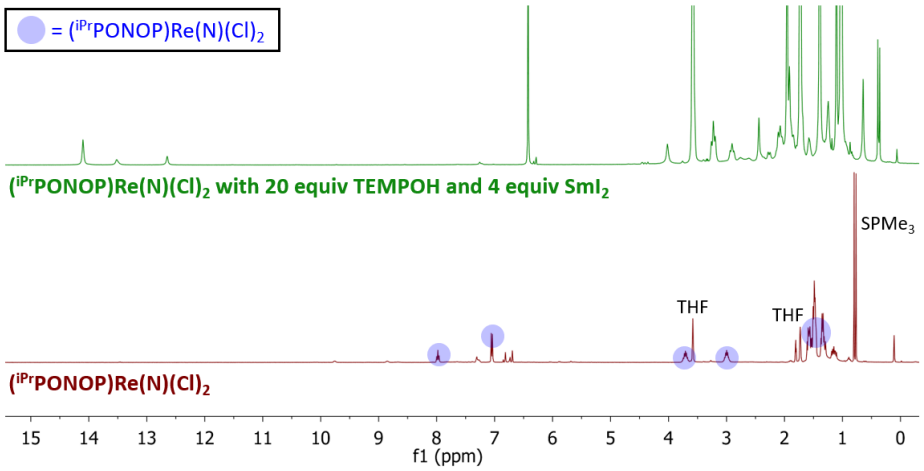

Figure 4.17. ^{1}H NMR spectra (400 MHz, THF-d_8) of (^{iPr}PONOP)Re(N)(Cl)$_2$ before (bottom, maroon) and 30 min reduction with 20 equiv TEMPOH and 4 equiv SmI_2 at ambient temperature.

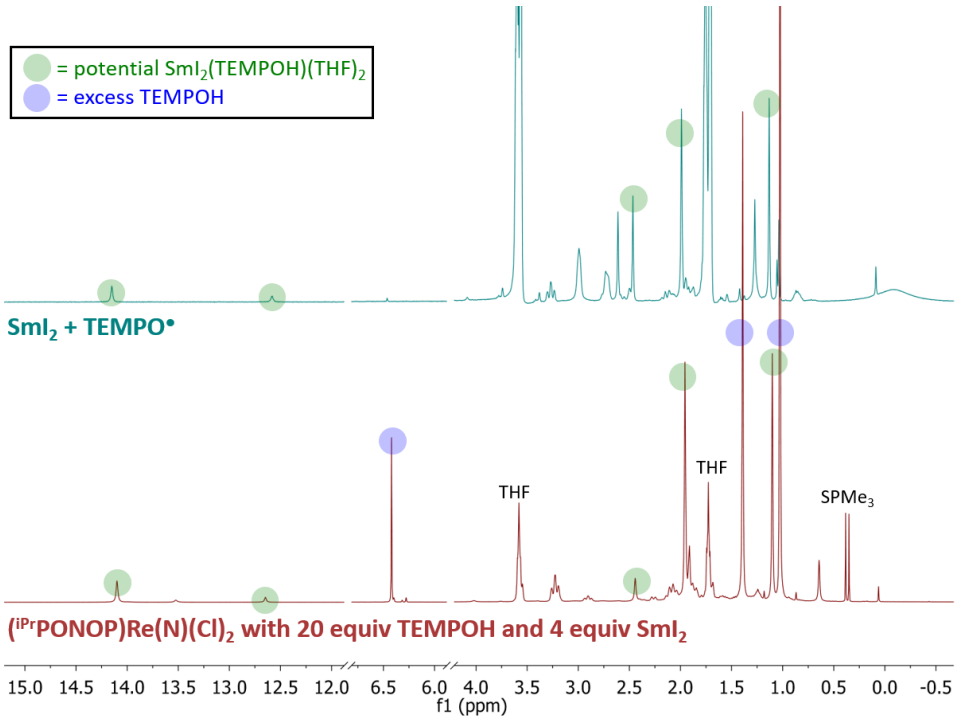

Figure 4.18. Correlation of ^{1}H resonances (highlighted in green) from the addition of TEMPO$^{\bullet}$ to SmI_2 (top, teal) and the reduction of (^{iPr}PONOP)Re(N)(Cl)$_2$ with 20 equiv TEMPOH and 4 equiv SmI_2 (bottom, maroon), potentially corresponding to soluble SmI_2(TEMPO)(THF)$_2$ species.

Another potential PCET mediator for electrocatalytic NRR is 1,8-dichloro-9,10-anthracenediol (DCAD, average $BDFE_{O–H}$ = 55.4 kcal/mol in THF).[27] Anthracenediols

have been evaluated for use as $2H^+/2e^-$ mediators in electrochemical reactions, and DCAD features particularly weak O–H bonds.[33] While reaction of (^{iPr}PONOP)Re(N)(Cl)$_2$ with 10 equiv DCAD gives no reaction at ambient temperature, heating the solution to 80 °C for 48 hr shows 70% consumption of the nitride by ^{1}H and ^{31}P{^{1}H} NMR spectroscopy (**Figure 4.19**). While no new diamagnetic (^{iPr}PONOP)Re products were observed in the ^{31}P{^{1}H} spectra over the course of the reaction, a product resonance was observed at δ –1904 ppm (**Figure 4.20**). Pincer-supported six-coordinate Re^{III} complexes, such as would be the case for a putative Re-amide complex (^{iPr}PONOP)Re(NH$_2$)(Cl)$_2$, have been reported to show similar large shifts due to temperature-independent paramagnetism (TIP).[18, 20] The ^{1}H spectra show the formation of 1,8-dichloroanthraquinone (DCAQ) during the reaction. Acidification of the reaction after 48 hr with excess HCl and analysis by IC showed that NH_4^+ was formed in 7% yield per Re consumed (see **Scheme 4.6**). The low yield of NH_4^+ from this reaction may be due to the thermodynamic mismatch of the DCAD reductant (average $BDFE_{N–H}$ = 55 kcal/mol) and the imide N–H bond formed ($BDFE_{N–H}$ = 43 kcal/mol), since initial N–H bond formation at the nitride is unfavorable. However, formation of NH_4^+ establishes DCAD as a potential candidate for PCET mediation, especially in N_2-cleaving systems that have milder thermodynamics for nitride reduction.

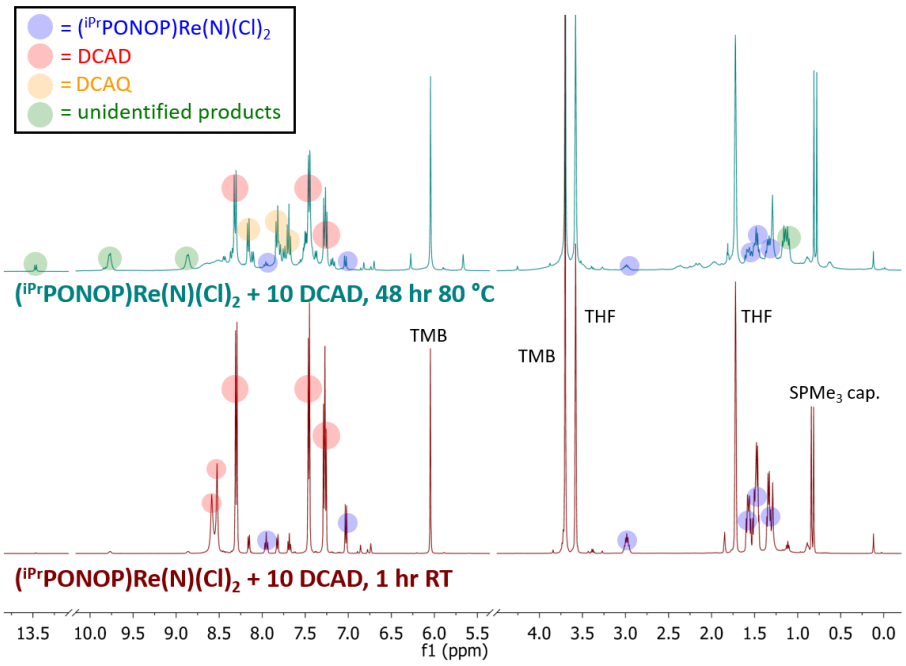

Figure 4.19. ^{1}H NMR spectra (400 MHz, THF-d_8) of the reduction of (^{iPr}PONOP)Re(N)(Cl)$_2$ with 10 equiv DCAD after 1 hr at RT (bottom, maroon) and 48 hr at 80 °C (top, teal). After 48 hr at 80 °C, 70% of the Re is consumed (vs. TMB internal standard), and 1,8-dichloroanthraquinone (DCAQ) is formed (highlighted in orange). Several unidentified ^{1}H resonances are also observed (highlighted in green).

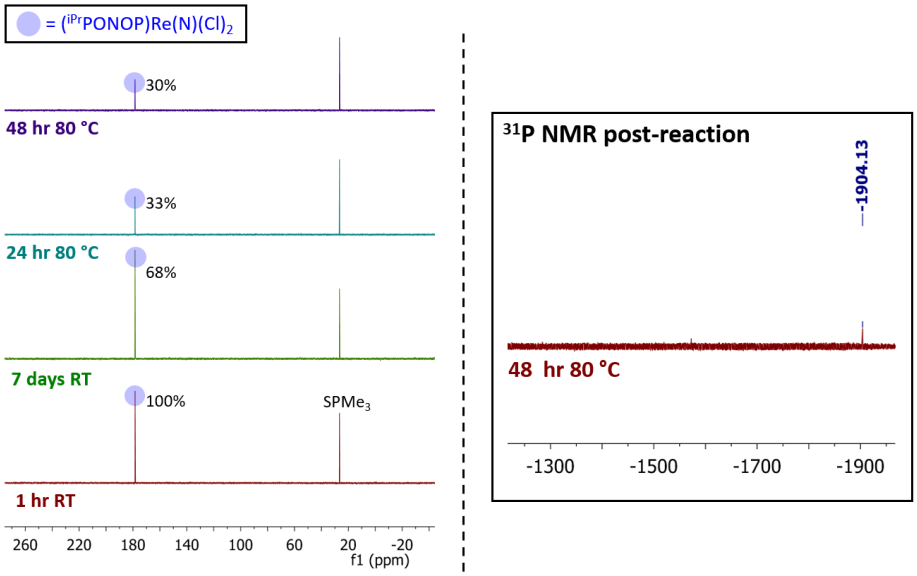

Figure 4.20. ^{31}P{^{1}H} spectra (162 MHz, THF-d_8) of the reduction of (^{iPr}PONOP)Re(N)(Cl)$_2$ with 10 equiv DCAD after 1 hr at RT (bottom, maroon), 7 days at RT (green), 24 hr at 80 °C (teal), and 48 hr at 80 °C (top, purple). After 48 hr at 80 °C, 70% of the Re is consumed (vs. SPMe$_3$ capillary), and a ^{31}P resonance at δ –1904 ppm is observed.

4.2.4. PCET reduction of (^{tBu}PNP)Re(N)(Cl) with SmI_2

Following the successful PCET reduction of (^{iPr}PONOP)Re(N)(Cl)$_2$ to form NH_3, which requires strong PCET reagents, we attempted the reduction of (^{tBu}PNP)Re(N)(Cl) with SmI_2 and H_2O in an attempt to close the NRR cycle. Following the reaction of (^{tBu}PNP)Re(N)(Cl) with 6 equiv SmI_2 and 60 equiv H_2O by UV-Vis spectroscopy shows steady consumption of SmI_2 beyond the 3 equiv necessary to reduce the nitride to ammonia (**Figure 4.21**). The stoichiometric reduction of (^{tBu}PNP)Re(N)(Cl) with 3 equiv SmI_2 and 30 equiv H_2O at a higher concentration proceeded with an immediate consumption of the deep blue SmI_2 and effervescence. Following the reaction by ^{1}H NMR spectroscopy showed the formation of a C_s-symmetric Re product, concurrent with the formation of H_2 as a singlet at δ 4.5 ppm (**Figure 4.22**). In contrast to (^{iPr}PONOP)Re(N)(Cl)$_2$, a 1:1:1 triplet corresponding to NH_4^+ was not observed in the ^{1}H NMR spectrum. These data imply that, rather than generating NH_3 from PCET nitride reduction, (^{tBu}PNP)Re(N)(Cl) catalytically decomposes SmI_2/H_2O to H_2.

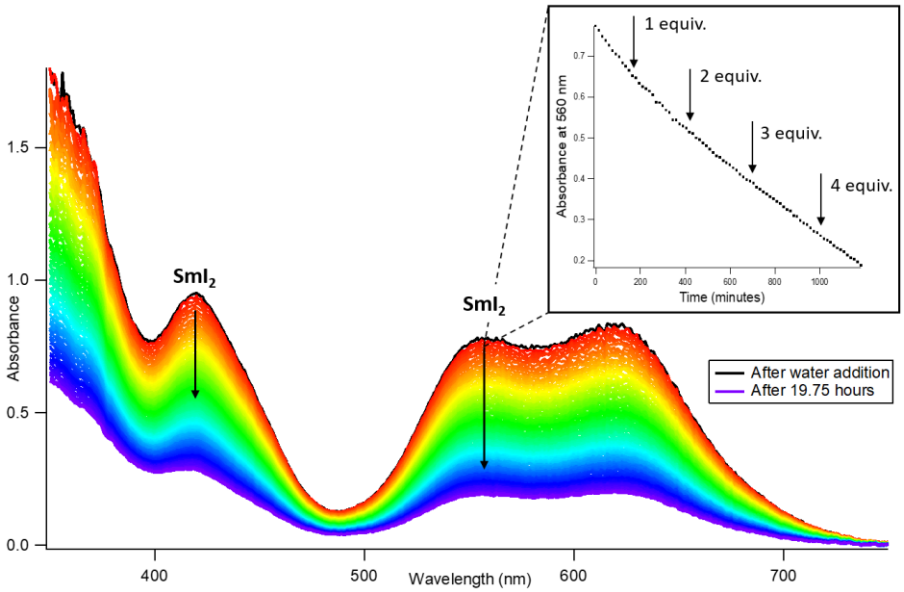

Figure 4.21. UV-Vis spectra of the reaction of (^{tBu}PNP)Re(N)(Cl) with 6 equiv SmI_2 and 60 H_2O in THF, showing the steady consumption of SmI_2 initiated by the addition of water (black trace). The reaction was stopped at 19.75 hours (purple trace). **Inset:** The absorbance at 560 nm over the course of the reaction, showing consumption of superstoichiometric SmI_2.

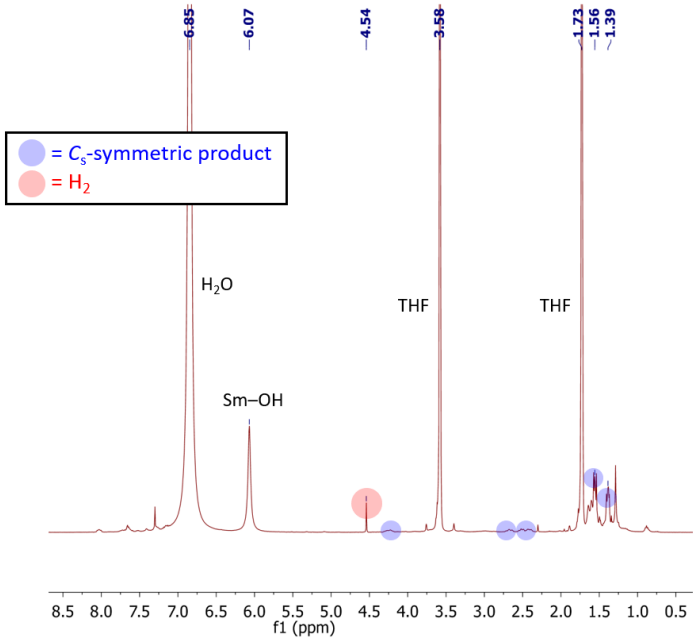

Figure 4.22. ^{1}H NMR spectrum (400 MHz, THF-d_8) of the reaction of (^{tBu}PNP)Re(N)(Cl) with 3 equiv SmI_2 and 30 equiv H_2O, showing formation of a C_s-symmetric Re product (highlighted in blue) and H_2 (δ 4.54, highlighted in red).

To probe the Re product of the initial reduction, (^{tBu}PNP)Re(N)(Cl) was mixed with 1 equiv SmI_2 and 10 equiv H_2O on a preparative scale, resulting in a color change from orange to red. A Re product, sparingly soluble in THF, was isolated from the reaction mixture via extraction with CH_2Cl_2. ^{1}H and ^{31}P{^{1}H} NMR spectra of the product showed a C_s-symmetric complex with identical ^{1}H resonances to the product formed from the 3 SmI_2/30 H_2O reduction of (^{tBu}PNP)Re(N)(Cl), with an additional ^{1}H resonance at δ 7.17 ppm integrating to 1H (**Figure 4.23**). The resonance at δ 7.17 ppm was confirmed to be a N–*H* resonance via a ^{1}H–^{15}N HSQC experiment (cross-peak at {δ 7.16, –331.46}), and the ^{1}H COSY spectrum shows cross-peaks between the C*H*$_2$ methylene resonances of the PNP backbone (**Figure 4.24**). The structure was confirmed by single-crystal XRD to be [(^{tBu}P^{H}NP)Re(N)(Cl)]I, closely resembling the protonated PNP complexes reported by Klopsch *et al.* (**Figure 4.25**, **Table 4.2**).[12, 34] Overall, the data for reduction of (^{tBu}PNP)Re(N)(Cl) with SmI_2/H_2O are consistent with the nitride staying intact throughout the reaction: rather than PCET reduction of the nitride to NH_3, the complex forms H_2 from the reducing equivalents, with [(^{tBu}P^{H}NP)Re(N)(X)]$^+$ (X = Cl or I) remaining at the end of the reaction (**Scheme 4.7**). This contrasts the reduction of (^{iPr}PONOP)Re(N)(Cl)$_2$ with SmI_2/H_2O to form NH_4^+ as the major product, as well as the recent reports of Mo-pincer complexes that can catalytically reduce N_2 to NH_3 with SmI_2/alcohols with extremely high selectivity for NH_3 vs. H_2.[2]

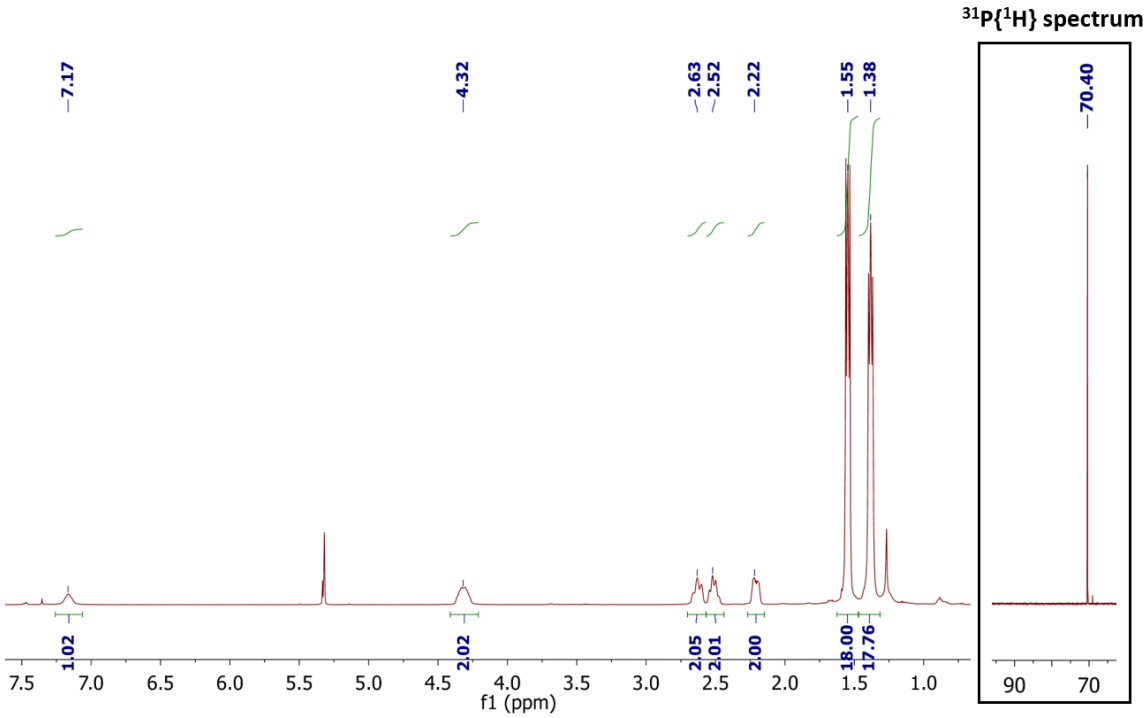

Figure 4.23. ^{1}H and $^{31}P\{^{1}H\}$ NMR spectra of [($^{tBu}P^{H}NP$)Re(N)(Cl)][I] isolated from the reduction of (^{tBu}PNP)Re(N)(Cl) with 1 equiv SmI_2 and 10 equiv H_2O. ^{1}H NMR (400 MHz, CD_2Cl_2): δ 7.17 (br s, 1H, N*H*), 4.32 (m, 2H, N(CH_2CH_2)$_2$), 2.63 (m, 2H, N(CH_2CH2)$_2$), 2.52 (m, 2H, N(CH_2CH_2)$_2$), 2.22 (m, 2H, N(CH_2CH_2)$_2$), 1.55 (vt, 18H, P(*'Bu*)(ᵗBu')), 1.38 (vt, 18H, P(ᵗBu)(*'Bu'*)). $^{31}P\{^{1}H\}$ NMR: (162 MHz, CD_2Cl_2): δ 70.4 (s).

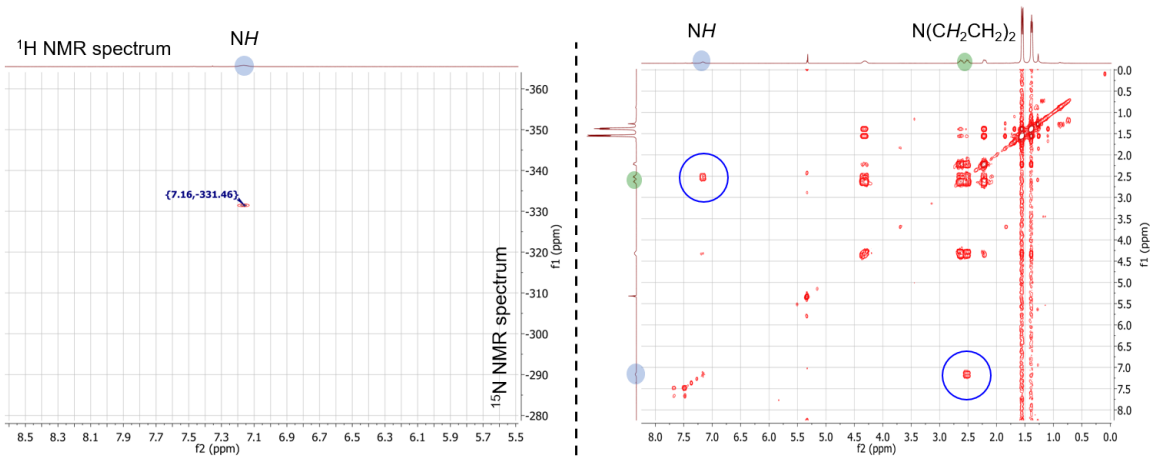

Figure 4.24. ^{1}H–^{15}N HSQC (500 MHz; 51 MHz, CD_2Cl_2) spectrum (left) and ^{1}H COSY (500 MHz, CD_2Cl_2) spectrum (right) of [($^{tBu}P^{H}NP$)Re(N)(Cl)][I] confirming protonation of the PNP amide.

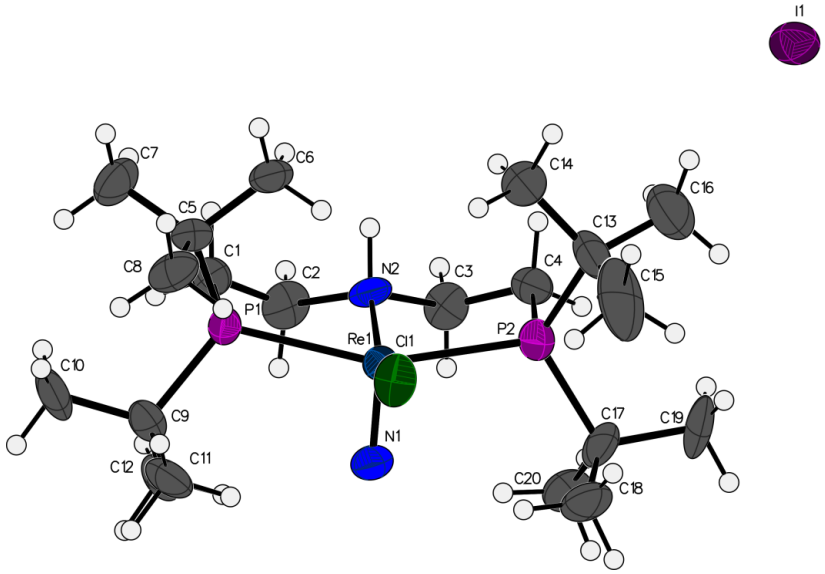

Figure 4.25. Solid-state structure of [(^{tBu}P^{H}NP)Re(N)(Cl)][I] with thermal ellipsoids at 50%.

Table 4.2. Selected bond lengths (Å) and bond angles (°) of [(^{tBu}P^{H}NP)Re(N)(Cl)][I] and comparison to related compound [(^{tBu}P^{H}NP)Re(N)(Cl)][OTf][34] (see **Section 3.4**).

Bond/Angle	**[(^{tBu}P^{H}NP)Re(N)(Cl)][I]**	**[(^{tBu}P^{H}NP)Re(N)(Cl)][OTf]**
Re1–N1	1.627(9)	1.624(7)
Re1–N2	2.11(1)	2.138(7)
Re1–Cl1	2.395(3)	2.385(2)
Re1–P1	2.441(3)	2.448(2)
Re1–P2	2.448(3)	2.455(2)
N1–Re1–N2	99.6(4)	99.9(3)
N1–Re1–Cl1	104.9(4)	106.7(3)
N2–Re1–Cl1	155.5(3)	153.4(2)
N1–Re1–P1	98.6(3)	99.1(3)
N1–Re1–P2	98.7(3)	98.5(3)
P1–Re1–P2	156.8(1)	156.3(1)

Scheme 4.7. Reduction of (^{tBu}PNP)Re(N)(Cl) with SmI_2 and H_2O.

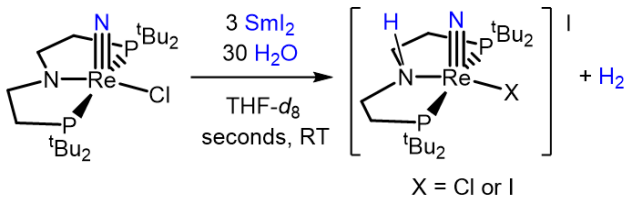

4.3 Conclusions

These studies establish the successful reduction of a N_2-derived Re nitride in (^{iPr}PONOP)Re(N)(Cl)$_2$ to NH_4^+, which completes the first reported fixation of N_2 to NH_3 using Re. Computational analysis of the thermodynamics associated with this transformation identify a major hurdle to PCET nitride reduction in this system: forming the initial imide N–H bond is particularly difficult ($BDFE_{N–H}$ = 43 kcal/mol). Stepwise PCET of the nitride to form this bond is unfavorable (calculated pK_a(imide) ~ –2.0; $E°$(nitride) = –2.5 V vs. $Cp_2Fe^{+/0}$). However, the use of SmI_2/H_2O as a potent concerted PCET reagent provides the necessary driving force to form the imide ($\Delta G°$ ~ –17 kcal/mol). Additionally, SmI_2/H_2O provides ample driving force to perform the subsequent PCET reduction of the imide to an amide ($\Delta G°$ ~ –52 kcal/mol), which may help contribute to selective formation of NH_3 (as opposed to formation of H_2) through rapid formation of the more stable amide species. The reduction of the nitride does not proceed with weaker PCET reagents, such as TEMPOH or $^tBu_3$PhOH, but does proceed with $[CoCp^*(Cp^*H)]^+$, which also provides a thermodynamic driving force for imide N–H bond formation ($\Delta G°$ ~ –14 kcal/mol).[30] This highlights the strategy of employing reductant-acid pairs that can generate strong PCET reagents to achieve difficult N–H bond formation during the reduction of N_2, as demonstrated by Peters' use of $[CoCp^*(Cp^*H)]^+$,[28-30] Knowles' use of $(bpy)_3Ru^{II}$/$HNMe_3$ ($BDFE_{eff}$ ~ 40 kcal/mol),[8, 35] and our use of SmI_2/H_2O. The utility of SmI_2/H_2O, in particular, is rapidly becoming clear, with recent examples of catalytic N_2 fixation by Mo complexes in addition to our example of NH_3 synthesis facilitated by a Re complex.[2, 3]

In contrast to (^{iPr}PONOP)Re(N)(Cl)$_2$, no NH_4^+ was observed from the reduction of (^{tBu}PNP)Re(N)(Cl) with SmI_2/H_2O. Instead, the nitride ligand stayed intact, and rapid effervescence was attributed to H_2 evolution by ^{1}H NMR spectroscopy. While H_2 is also evolved as a byproduct from reduction of (^{iPr}PONOP)Re(N)(Cl)$_2$ with SmI_2/H_2O, the difference in regioselectivity for NH_4^+ production between the two systems is stark. This difference is notable considering the similar supporting ligand and oxidation state of Re. It is unlikely that imide N–H bond formation from SmI_2/H_2O is thermodynamically unfavorable for (^{tBu}PNP)Re(N)(Cl) given its exceptionally weak O–H bond. However, elimination of H_2 from weak N–H bonds has been reported in some systems, provided the driving force for H_2 formation is sufficient ($BDFE_{H-H}$ = 97.2 kcal/mol in the gas phase).[36] SmI_2/H_2O may also provide a stronger driving force for Re hydride formation than imide N–H bond formation, which could result in subsequent H_2 elimination.[6, 9, 37] Tautomerization between the P*N*P-protonated ligand and a metal-hydride complex has been reported in a (^{tBu}PNP)W system, resulting in the production of H_2.[10] It is plausible that the lack of an open coordination site in the coordinatively-saturated (^{iPr}PONOP)Re(N)(Cl)$_2$ complex retards formation of a Re hydride that may form H_2, although hydrides are presumably formed at some point in this reaction. In any case, determining the pathways of unproductive H_2 production that out-compete nitride reduction to NH_3 in (^{tBu}PNP)Re(N)(Cl) vs. (^{iPr}PONOP)Re(N)(Cl)$_2$ may provide insight into methods for favoring selective N_2 reduction in later systems.

Formation of substoichiometric NH_3 from (^{iPr}PONOP)Re(N)(Cl)$_2$ using SmI_2/TEMPOH or DCAD represents initial progress towards developing new PCET mediators for the electrochemical reduction of N_2-derived nitrides. The thermochemistry

of PCET nitride reduction from (^{iPr}PONOP)Re(N)(Cl)$_2$ clearly indicates the need for strong reagents in order to achieve NH_3 production, which may be more easily achieved with the use of strong concerted PCET reagents as mediators.[38, 39] Inspiration for the usefulness of a concerted PCET mediator in electrocatalytic NRR comes from the lone molecular electrocatalytic system for this reaction, wherein the presence of CoCp*$_2$ to form [CoCp*(Cp*H)]$^+$ enhances turnover from 2.6 to 4.0 equiv NH_3 per catalyst.[29] However, it is unclear whether [CoCp*(Cp*H)]$^+$ can be regenerated under the electrochemical reaction conditions. The particularly successful use of SmI_2 in catalytic N_2 fixation[2] identifies it as a prime candidate for a PCET mediator, provided the Sm species remains and can be regenerated. To this end, pairing SmI_2 with TEMPOH has shown potential: the reagent pair performs the difficult reduction of phenazine to dihydrophenazine, generates a modest amount of NH_4^+ from (^{iPr}PONOP)Re(N)(Cl)$_2$, and the resulting Sm^{III} product remains soluble in THF. Future studies identifying the mechanism of PCET reduction with this reagent pair, as well as determining whether it can be regenerated, are needed to fully assess its utility as a PCET mediator. Using DCAD as a PCET mediator presents another opportunity, although only for systems where N–H bond formation at the nitride is less challenging than the Re nitrides studied here.

4.4 Experimental

4.4.1. General Considerations

All manipulations were performed under an inert atmosphere of N_2 gas in a M. Braun glovebox or on a Schlenk line unless otherwise specified. Tetrahydrofuran (THF) was distilled under argon from potassium benzophenone ketyl and stored over molecular sieves prior to use. Unless otherwise noted, all other solvents were dried via passage through Q5 columns from Glass Contour Co. and stored over molecular sieves prior to use. Deuterated solvents were degassed and dried over calcium hydride before storing over molecular sieves prior to use, and THF-d_8 was dried additionally with potassium benzophenone ketyl. Deionized water was degassed prior to use. Samarium diiodide (Sigma-Aldrich, >99.9%, dried over sieves as a solution in THF), hydrochloric acid (HCl, Sigma-Aldrich, 2.0 M solution in diethyl ether), TEMPO$^{\bullet}$ (Sigma-Aldrich, 98%), 2,4,6-tri-*tert*-butylphenol (Sigma-Aldrich, 97%), and phenazine (Sigma-Aldrich, 98%) were purchased and used without further purification unless noted. (PNP)Re(N)(Cl),[34] (PONOP)Re(N)$(Cl)_2$,[18] TEMPOH,[40] and 1,8-dichloro-9,10-anthracenediol[27] (DCAD) were synthesized according to literature procedures.

4.4.2. Instrumentation and Methods

NMR spectra were acquired on an Agilent 400 MHz or 500 MHz spectrometer. ^{1}H spectra were referenced to residual ^{1}H signals from the deuterated solvent with which the sample was prepared,[41] and $^{13}C\{^1H\}$, $^{31}P\{^1H\}$, and ^{15}N spectra were absolute referenced to the corresponding ^{1}H spectra. Line fitting of paramagnetic resonances in ^{1}H NMR spectra was done using MestReNova 10.0.1. Optical spectra and monitoring of reactions were done using an Agilent Cary 5000 UV-vis spectrometer, which was connected to sample holders

inside the N_2-filled glovebox via fiber optic cables. Ion Chromatography (IC) (performed by Q. Bruch) was carried out on a 930 Compact IC Flex from Metrohm equipped with a Metrosep C4 – 150/4.0 column for cation separation. A 1.7 mM nitric acid, 0.7 mM dipicolinic acid eluent was used. Samples for IC were run by dissolving solids in neat eluent or NERL high purity water. A calibration curve was generated using an analytic standard purchased from Sigma Aldrich based on the integrated peak areas of ammonium using the MagIC Net software package.

Quantification of NH_4^+ by ^{1}H NMR spectroscopy. In a N_2 glovebox, 7.0 mg (^{iPr}PONOP)Re(N)(Cl)$_2$ (1.14 x 10^{-5} mol) was dissolved in 1 mL THF to form a gold-colored solution. 20.5 µL degassed, deionized H_2O (100 equiv, 1.14 x 10^{-3} mol) was added to the Re solution via micropipet, which was then poured into a separate vial containing 85.0 mg solid $SmI_2(THF)_5$ (10 equiv, 1.14 x 10^{-4} mol). The mixture immediately effervesced and formed a deep red-maroon solution. The vial was capped and shaken vigorously to mix the components, forming a red-brown solution within seconds. Removal of the solvent under vacuum gave a maroon and white solid residues, which were dissolved in 5 mL 1:1 toluene:THF and filtered through Celite to remove an off-white precipitate. The maroon filtrate was dried under vacuum for several hours. 1.8 x 10^{-5} mol 1,3,5-trimethoxybenzene (TMB) was added to the sample from a stock solution, and the sample was further dried under vacuum for several more hours. Once completely dry, the resulting maroon and white solid residues were re-dissolved in 0.60 mL THF-d_8, and the solution was transferred into a Teflon-sealed NMR tube for ^{1}H NMR analysis. Each tube was centrifuged to separate an off-white solid from the maroon solution prior to NMR analysis.

Comparison of the relative peak integrations of the TMB internal standard peak (30 mM) and the NH_4^+ peak allowed calculation of NH_4^+ concentration within each sample, providing a yield of NH_4^+ per (PONOP)Re(N)Cl_2 equivalent. The average yield over three trials was 76.7% NH_4^+ per Re (σ = 8.9%).

Due to significant broadening of the NH_4^+ resonance and the significant deviation between trials, we consider our quantification by ^{1}H NMR spectroscopy as less accurate than IC analysis.

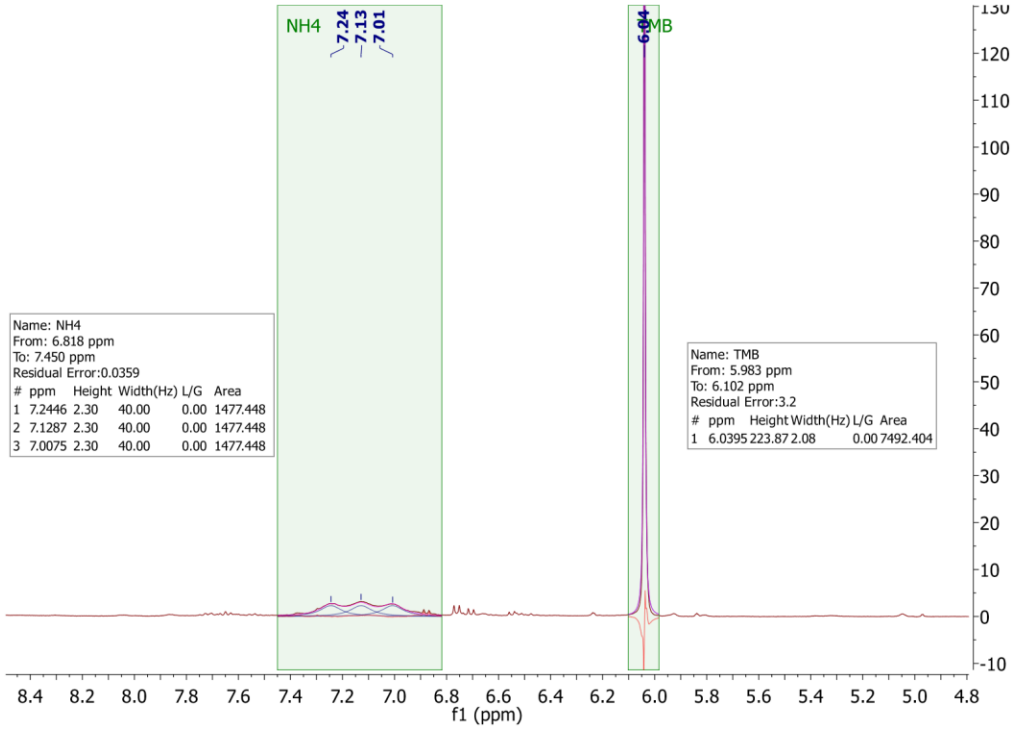

Figure 4.26. ^{1}H NMR spectrum of NH_4^+ from reaction of (PONOP)Re(N)Cl_2 with 10 equiv SmI_2 and 100 equiv H_2O (400 MHz, THF-d_8). NH_4^+ is detected as a broadened 1:1:1 triplet centered at δ 7.13 ppm (J = 47 Hz). Due to the significant broadening of the resonance, the peaks were fit as a 1:1:1 triplet and compared to 30.0 mM TMB as an internal standard (δ 6.04 ppm, s, 3H). We hypothesize that the significant broadening of the NH_4^+ peak is due to hydrogen-bonding interactions with hydroxyl-containing Sm or Re products in the reaction mixture, as attempts to further dry the samples did not improve peak resolution.

Quantification of NH_4^+ by ion chromatography (IC). As a general procedure, (^{iPr}PONOP)Re(N)$(Cl)_2$ was dissolved in 0.5 mL THF-d_8 to form a gold-colored solution,

which was poured over the desired PCET reagent. The reaction mixture was transferred to an NMR tube fitted with a Teflon cap. The reactions were mixed at room temperature or heated for the time as noted, and the reactions were monitored by ^{1}H and ^{31}P NMR spectroscopy. Once the reactions were stopped, the reaction mixture was acidified with 20 equiv HCl (as a 2.0 M solution in Et_2O), transferred to a 5 mL scintillation vial, and the solvent was removed under vacuum. The residual solids were sealed in a scintillation vial and sent to Q. Bruch for analysis. Extraction of solids into 2 mL of buffer (0.7 mM picolinic acid, 1.7 mM nitric acid) resulted in colorless solutions and a red or brown insoluble solid. Samples were filtered and diluted ten-fold before injection into the IC. The amount of NH_4^+ (in mg/L) was determined using a calibration curve, and yields were calculated based on (PONOP)Re(N)$(Cl)_2$ (in mg/L).

4.4.3. Crystallographic Details

Crystals were isolated in an N_2 glovebox by decanting the mother liquor from the crystals before transferring and submerging them in high-viscosity petroleum oil on a microscope slide. Single crystals suitable for X-ray diffraction were identified under a polarizing microscope and mounted on 200 μm MiTeGen Dual-Thickness MicroLoops in a mixture of high-viscosity petroleum, then mounted on the diffractometer instrument.

$SmI_2(TEMPO)(THF)_2$ (007c-19012). Low-temperature diffraction data (ω-scans) were collected on a Rigaku MicroMax-007HF diffractometer coupled to a Dectris Pilatus3R detector with Mo Kα (λ = 0.71073 Å) for the structure of 007c-19012. The diffraction images were processed and scaled using Rigaku Oxford Diffraction software (CrysAlisPro; Rigaku OD: The Woodlands, TX, 2015). The structure was solved with SHELXT and was refined against F^2 on all data by full-matrix least squares with SHELXL

(Sheldrick, G. M. Acta Cryst. 2008, A64, 112–122). All non-hydrogen atoms were refined anisotropically. Hydrogen atoms were included in the model at geometrically calculated positions and refined using a riding model. The isotropic displacement parameters of all hydrogen atoms were fixed to 1.2 times the U value of the atoms to which they are linked (1.5 times for methyl groups).

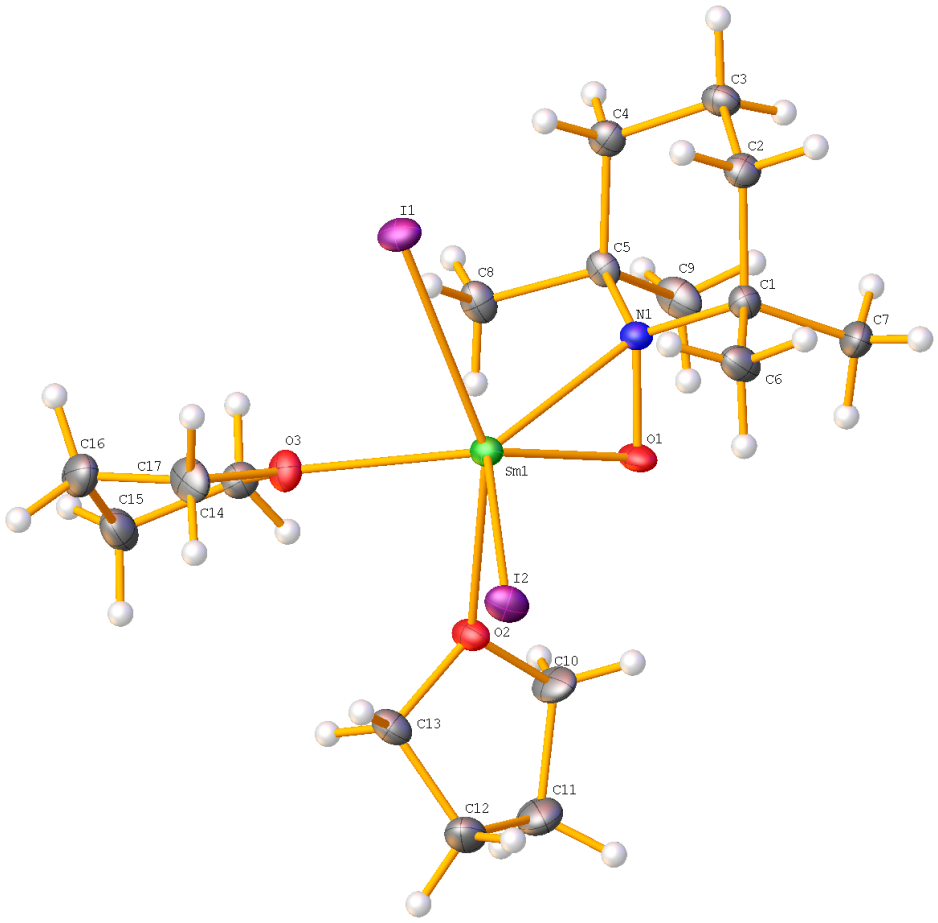

Figure 4.27. The complete numbering scheme of $SmI_2(TEMPO)(THF)_2$ (007c-19012) with 50% thermal ellipsoid probability levels. The hydrogen atoms are shown as circles for clarity.

Table 4.3. Crystal data and structure refinement for 007c-19012.

Identification code	007c-19012
Empirical formula	C17 H34 I2 N O3 Sm
Formula weight	704.60
Temperature	93(2) K

Wavelength	0.71073 Å	
Crystal system	Triclinic	
Space group	P-1	
Unit cell dimensions	a = 7.8007(3) Å	□= 76.008(3)°.
	b = 10.0133(4) Å	□= 81.388(3)°.
	c = 15.1637(6) Å	□ = 85.064(3)°.
Volume	1134.81(8) Å^3	
Z	2	
Density (calculated)	2.062 Mg/m^3	
Absorption coefficient	5.321 mm^{-1}	
F(000)	670	
Crystal size	0.200 x 0.200 x 0.120 mm^3	
Crystal color and habit	Colorless Block	
Diffractometer	Dectris Pilatus 3R	
Theta range for data collection	2.779 to 27.481°.	
Index ranges	-10<=h<=10, -13<=k<=12, -19<=l<=19	
Reflections collected	41699	
Independent reflections	5193 [R(int) = 0.0752]	
Observed reflections (I > 2sigma(I))	4734	
Completeness to theta = 25.242°	99.9 %	
Absorption correction	Semi-empirical from equivalents	
Max. and min. transmission	1.00000 and 0.42394	
Solution method	SHELXT-2014/5 (Sheldrick, 2014)	
Refinement method	SHELXL-2014/7 (Sheldrick, 2014)	
Data / restraints / parameters	5193 / 0 / 221	
Goodness-of-fit on F^2	1.080	
Final R indices [I>2sigma(I)]	R1 = 0.0348, wR2 = 0.0912	
R indices (all data)	R1 = 0.0384, wR2 = 0.0940	
Largest diff. peak and hole	3.826 and -1.439 e.Å^{-3}	

[(^{tBu}P^{H}NP)Re(N)(Cl)][I] (mini-17024). Low-temperature diffraction data (ω-scans) were collected on a Rigaku SCX Mini diffractometer coupled to a Rigaku Mercury275R CCD with Mo Kα radiation (λ = 0.71073 Å) for the structure of mini-17024. The diffraction images were processed and scaled using Rigaku Oxford Diffraction

software (CrysAlisPro; Rigaku OD: The Woodlands, TX, 2015). The structure was solved with SHELXT and was refined against F^2 on all data by full-matrix least squares with SHELXL (Sheldrick, G. M. Acta Cryst. 2008, A64, 112–122). All non-hydrogen atoms were refined anisotropically. Hydrogen atoms were included in the model at geometrically calculated positions and refined using a riding model. The isotropic displacement parameters of all hydrogen atoms were fixed to 1.2 times the U value of the atoms to which they are linked (1.5 times for methyl groups). The only exception is H2. The position was found in the difference map and refined as a riding atom on N2 with a distance restraint of 1.00(2) Å, which was suggested by the difference map. Two low angle reflections were recorded improperly and subsequently omitted from the refinement.

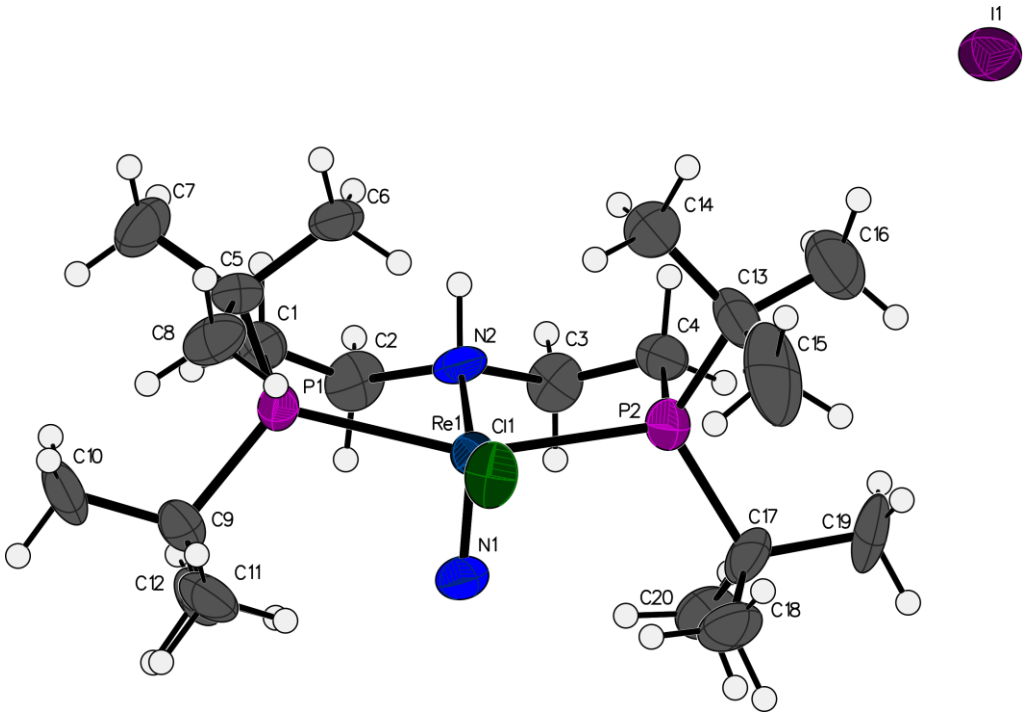

Figure 4.28. The complete numbering scheme of [($^{tBu}P^{H}NP$)Re(N)(Cl)][I] (mini-17024) with 50% thermal ellipsoid probability levels. The hydrogen atoms are shown as circles for clarity.

Table 4.4. Crystal data and structure refinement for [($^{tBu}P^{H}NP$)Re(N)(Cl)][I] (mini-17024).

Identification code	mini-17024	
Empirical formula	C20 H45 Cl I N2 P2 Re	
Formula weight	724.07	
Temperature	93(2) K	
Wavelength	0.71073 Å	
Crystal system	Monoclinic	
Space group	I2/a	
Unit cell dimensions	a = 14.6242(14) Å	□= 90°.
	b = 14.1559(12) Å	□= 96.874(8)°.
	c = 27.210(3) Å	□ = 90°.
Volume	5592.4(9) Å^3	
Z	8	
Density (calculated)	1.720 Mg/m^3	
Absorption coefficient	5.668 mm^{-1}	
F(000)	2832	
Crystal size	0.200 x 0.040 x 0.040 mm^3	
Theta range for data collection	2.409 to 26.377°.	
Index ranges	-18<=h<=17, -17<=k<=15, -34<=l<=21	
Reflections collected	10266	
Independent reflections	5681 [R(int) = 0.0889]	
Completeness to theta = 25.242°	99.4 %	
Absorption correction	Semi-empirical from equivalents	
Max. and min. transmission	1.00000 and 0.95223	
Refinement method	Full-matrix least-squares on F^2	
Data / restraints / parameters	5681 / 1 / 259	
Goodness-of-fit on F^2	0.960	
Final R indices [I>2sigma(I)]	R1 = 0.0634, wR2 = 0.0842	
R indices (all data)	R1 = 0.1339, wR2 = 0.1057	
Largest diff. peak and hole	1.729 and -1.236 e.Å^{-3}	

4.5 References

1. Laplaza, C. E.; Cummins, C. C., *Science* **1995,** *268*, 861-863.

2. Ashida, Y.; Arashiba, K.; Nakajima, K.; Nishibayashi, Y., *Nature* **2019,** *568*, 536-540.

3. Ashida, Y.; Arashiba, K.; Tanaka, H.; Egi, A.; Nakajima, K.; Yoshizawa, K.; Nishibayashi, Y., *Inorg. Chem.* **2019,** *58*, 8927-8932.

4. Ashida, Y.; Kondo, S.; Arashiba, K.; Kikuchi, T.; Nakajima, K.; Kakimoto, S.; Nishibayashi, Y., *Synthesis* **2019,** *51*, 3792-3795.

5. van der Ham, C. J. M.; Koper, M. T. M.; Hetterscheid, D. G. H., *Chem. Soc. Rev.* **2014,** *43*, 5183-5191.

6. Bezdek, M. J.; Guo, S.; Chirik, P. J., *Science* **2016,** *354*, 730-733.

7. Bezdek, M. J.; Pappas, I.; Chirik, P. J., Determining and Understanding N-H Bond Strengths in Synthetic Nitrogen Fixation Cycles. In *Nitrogen Fixation*, Nishibayashi, Y., Ed. Springer International Publishing: Cham, 2017; pp 1-21.

8. Wang, D.; Loose, F.; Chirik, P. J.; Knowles, R. R., *J. Am. Chem. Soc.***2019,** *141*, 4795-4799.

9. Margulieux, G. W.; Bezdek, M. J.; Turner, Z. R.; Chirik, P. J., *J. Am. Chem. Soc.* **2017,** *139*, 6110-6113.

10. Schluschass, B.; Abbenseth, J.; Demeshko, S.; Finger, M.; Franke, A.; Herwig, C.; Wuertele, C.; Ivanovic-Burmazovic, I.; Limberg, C.; Telser, J.; Schneider, S., *Chem. Sci.* **2019,** *10*, 10275-10282.

11. Lindley, B. M.; Appel, A. M.; Krogh-Jespersen, K.; Mayer, J. M.; Miller, A. J. M., *ACS Energy Lett.* **2016,** *1*, 698-704.

12. Klopsch, I.; Finger, M.; Wuertele, C.; Milde, B.; Werz, D. B.; Schneider, S., *J. Am. Chem. Soc.* **2014,** *136*, 6881-6883.

13. Laplaza, C. E.; Johnson, M. J. A.; Peters, J.; Odom, A. L.; Kim, E.; Cummins, C. C.; George, G. N.; Pickering, I. J., *J. Am. Chem. Soc.* **1996,** *118*, 8623-8638.

14. Lindley, B. M.; van Alten, R. S.; Finger, M.; Schendzielorz, F.; Würtele, C.; Miller, A. J. M.; Siewert, I.; Schneider, S., *J. Am. Chem. Soc.* **2018,** *140*, 7922-7935.

15. Klopsch, I.; Kinauer, M.; Finger, M.; Würtele, C.; Schneider, S., *Angew. Chem. Int. Ed.* **2016,** *55*, 4786-4789.

16. Salem, H.; Shimon, L. J. W.; Diskin-Posner, Y.; Leitus, G.; Ben-David, Y.; Milstein, D., *Organometallics* **2009,** *28*, 4791-4806.

17. Bernskoetter, W. H.; Hanson, S. K.; Buzak, S. K.; Davis, Z.; White, P. S.; Swartz, R.; Goldberg, K. I.; Brookhart, M., *J. Am. Chem. Soc.* **2009,** *131*, 8603-8613.

18. Bruch, Q. J.; Connor, G. P.; Chen, C.-H.; Holland, P. L.; Mayer, J. M.; Hasanayn, F.; Miller, A. J. M., *J. Am. Chem. Soc.* **2019,** *141*, 20198-20208.

19. Klopsch, I.; Schendzielorz, F.; Volkmann, C.; Würtele, C.; Schneider, S., *Z. Anorg. Allg. Chem.* **2018,** *644*, 916-919.

20. Schendzielorz, F.; Finger, M.; Abbenseth, J.; Würtele, C.; Krewald, V.; Schneider, S., *Angew. Chem., Inter. Ed.* **2019,** *58*, 830-834.

21. Kamochi, Y.; Kudo, T., *Chem. Lett.* **1993,** *22*, 1495-1498.

22. Chciuk, T. V.; Anderson, W. R.; Flowers, R. A., *J. Am. Chem. Soc.* **2016,** *138*, 8738-8741.

23. Kolmar, S. S.; Mayer, J. M., *J. Am. Chem. Soc.* **2017,** *139*, 10687-10692.

24. Pontes, F. V. M.; Carneiro, M. C.; Vaitsman, D. S.; da Rocha, G. P.; da Silva, L. I. D.; Neto, A. A.; Monteiro, M. I. C., *Anal. Chim. Acta* **2009,** *632*, 284-288.

25. Saigne, C.; Kirchner, S.; Legrand, M., *Anal. Chim. Acta* **1987,** *203*, 11-21.

26. Kim, Y.; Deng, H.; Gallucci, J. C.; Wojcicki, A., *Inorg. Chem.* **1996,** *35*, 7166-7173.

27. Wise, C. F.; Agarwal, R. G.; Mayer, J. M., *J. Am. Chem. Soc.* **2020,** *142*, 10681-10691.

28. Chalkley, M. J.; Del Castillo, T. J.; Matson, B. D.; Roddy, J. P.; Peters, J. C., *ACS Cent. Sci.* **2017,** *3*, 217-223.

29. Chalkley, M. J.; Del Castillo, T. J.; Matson, B. D.; Peters, J. C., *J. Am. Chem. Soc.* **2018,** *140*, 6122-6129.

30. Chalkley, M. J.; Oyala, P. H.; Peters, J. C., *J. Am. Chem. Soc.* **2019,** *141*, 4721-4729.

31. Scheibel, M. G.; Abbenseth, J.; Kinauer, M.; Heinemann, F. W.; Wuertele, C.; de Bruin, B.; Schneider, S., *Inorg. Chem.* **2015,** *54*, 9290-9302.

32. Maity, S.; Flowers, R. A., *J. Am. Chem. Soc.* **2019,** *141*, 3207-3216.

33. Huynh, M. T.; Anson, C. W.; Cavell, A. C.; Stahl, S. S.; Hammes-Schiffer, S., *J. Am. Chem. Soc.* **2016,** *138*, 15903-15910.

34. Connor, G. P.; Mercado, B. Q.; Lant, H. M. C.; Mayer, J. M.; Holland, P. L., *Inorg. Chem.* **2019,** *58*, 10791-10801.

35. Loose, F.; Wang, D.; Tian, L.; Scholes, G. D.; Knowles, R. R.; Chirik, P. J., *Chem. Commun.* **2019,** *55*, 5595-5598.

36. Warren, J. J.; Tronic, T. A.; Mayer, J. M., *Chem. Rev.* **2010,** *110*, 6961-7001.

37. Matson, B. D.; Peters, J. C., *ACS Catal.* **2018,** *8*, 1448-1455.

38. Nutting, J. E.; Rafiee, M.; Stahl, S. S., *Chem. Rev.* **2018,** *118*, 4834-4885.

39. Francke, R.; Little, R. D., *Chem. Soc. Rev.* **2014,** *43*, 2492-2521.

40. Mader, E. A.; Davidson, E. R.; Mayer, J. M., *J. Am. Chem. Soc.* **2007,** *129*, 5153-5166.

41. Fulmer, G. R.; Miller, A. J. M.; Sherden, N. H.; Gottlieb, H. E.; Nudelman, A.; Stoltz, B. M.; Bercaw, J. E.; Goldberg, K. I., *Organometallics* **2010,** *29*, 2176-2179.

5 Facile Conversion of Ammonia to a Nitride in a Rhenium System that Cleaves Dinitrogen

Dr. Brandon Q. Mercado solved the crystal structures presented in this chapter. Daniel Delony performed calorimetric measurements for experimentally-determined bond enthalpies. Julia Curley performed headspace analysis for H_2 quantification by gas chromatography.

5.1 Introduction

The interconversion of N_2 and NH_3 has widespread applications in agricultural and sustainable energy fields.[1, 2] The heavy use of NH_3 in fertilizer manufacturing has resulted in an extensive global infrastructure for its transportation and storage.[3] Coupled with its high energy density, this makes NH_3 an excellent candidate for a carbon-free chemical fuel, either through combustion or its use in direct NH_3 fuel cells.[4-7] However, in order to realize this potential, it is necessary to understand the individual steps through which N–N and N–H bonds can be formed and broken at transition-metal catalysts.

A promising route to form the N–H bonds in NH_3 from N_2 is to use proton-coupled electron transfer (PCET).[8] In a PCET mechanism, photo- or electrochemical energy may provide the necessary driving force to reduce N_2 using water as a source of protons and electrons, thus providing an attractive, sustainable strategy for NH_3 production.[9-15] Despite challenges including the stability of N_2, unstable N_xH_y intermediates, and competing reduction of protons to form H_2, a growing number of homogeneous systems can catalytically achieve this difficult transformation utilizing PCET strategies.[16-30]

It is also important to understand the reverse reaction, NH_3 oxidation to form N_2. The importance stems from the potential for both a) releasing energy in N–H bonds and b) better understanding of how to achieve PCET reduction of N_2. For example, the discovery of catalysts that can efficiently oxidize NH_3 to N_2 is vital for developing direct NH_3 fuel cells.[5, 7] Beyond furthering our understanding of NH_3 oxidation to N_2, the thermochemical

and mechanistic information unveiled from systems that can oxidize NH_3 is also relevant for identifying bottlenecks and opportunities for PCET reduction of N_2 to NH_3, with the ultimate goal of achieving facile interconversion between N_2 and NH_3 in either direction.

In the context of NH_3 oxidation to N_2, many examples of chemical N–H bond oxidation from NH_3-derived metal ammines have been reported to yield metal nitrides.[31-43] These systems can utilize either chemical oxidants under basic conditions or H-atom abstracting (HAA) reagents to achieve the necessary N–H bond oxidations for ammine-to-nitride transformation. In some systems, electrochemical oxidation of ammine complexes can also yield metal-nitride products.[38, 39, 41] Other systems can generate N_2 as a product from the oxidation of NH_3-derived ammine complexes, either through chemical[33, 37, 44-46] or electrochemical[46-49] methods. These include recently reported homogeneous systems that catalytically form N_2 from NH_3 through both chemical[40-42] or electrochemical[41, 50, 51] N–H bond oxidation. However, the mechanism of the $6e^-$, $6H^+$ oxidation of NH_3 to N_2 can be quite difficult to elucidate in these systems, especially since N–N bond formation can occur via bimetallic N–N coupling (*e.g.* between metal–NH_x species or metal nitrides)[37, 41, 42] or nucleophilic attack on a metal–NH_x intermediate by NH_3.[40, 50-52]

An important step towards understanding N_2 to NH_3 interconversion is to study NH_3 oxidation pathways in a well-defined system that is also capable of reductive functionalization of N_2 via an N_2-cleavage mechanism. Schneider and Miller have reported that electrochemical reduction of (PNP)$ReCl_2$ (**1**, PNP = $N((CH_2CH_2)P^tBu_2)_2$) cleaves N_2 to form the nitride complex (PNP)Re(N)(Cl) (**2**), which contains a nucleophilic nitride ligand (**Scheme 5.1**, black).[53, 54] This nitride can be incorporated into nitriles through a synthetic cycle that involves initial N–C bond formation;[55] however, PCET reduction of

the nitride in **2** to form NH_3 (**Scheme 5.1**, gray) has not been achieved. The difficulties vary: protonation of **2** occurs at the amide of the P*N*P-pincer ligand rather than the nitride ligand; the electron-richness of **2** prevents a reduction-first pathway; and, **2** is unreactive towards organic hydrogen-atom transfer (HAT) reagents or H_2.[53] We hoped that the oxidative reactivity of NH_3 with **1**, *i.e.* the microscopic reverse reactions (**Scheme 5.1**, blue), would provide us with an opportunity to identify and quantify the factors that prevent PCET nitride reduction in this system. This fundamental information aids in developing strategies to avoid bottlenecks to NH_3 generation in future N_2-cleaving systems.

Scheme 5.1. Reductive N_2 splitting by (PNP)Re and hypothetical PCET nitride reduction (gray) and NH_3 oxidation (blue) cycles.

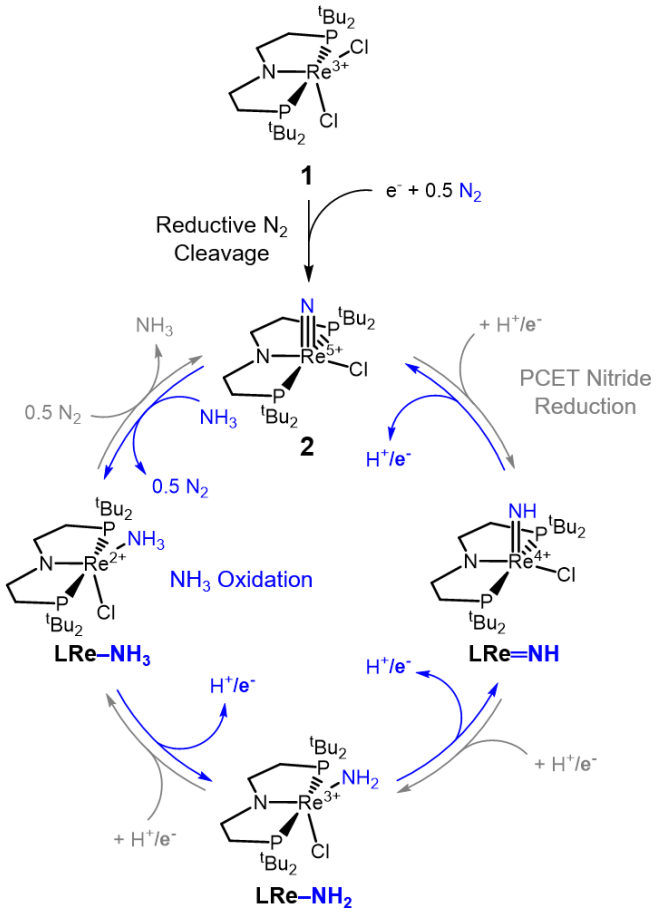

5.2 Results

5.2.1. Reactivity of (PNP)ReCl$_2$ with NH$_3$

Introduction of 1 atm of NH_3 gas to a solution of **1** in benzene-d_6 or tetrahydrofuran-d_8 (THF-d_8) in a Teflon-sealed NMR tube results in an immediate color change from purple to brown. ^{1}H and ^{31}P{^{1}H} NMR spectroscopy reveal the formation of a new C_s-symmetric diamagnetic product **3** in near quantitative yield (>95%), which displays a single ^{31}P resonance at δ 40.1 ppm (**Figure 5.1**). The number of resonances and integrations indicate the loss of a mirror plane, and the ^{1}H chemical shifts of **3** suggest a five-coordinate, trigonal-bipyramidal Re^{III} complex. In addition, **3** contains an additional ^{1}H resonance at δ 12.7 ppm integrating to 2 H, consistent with the formation of a Re–NH_2 complex (PNP)Re(NH_2)(Cl) (**Scheme 5.2**). A ^{1}H–^{15}N HSQC spectrum of a natural-abundance sample shows a ^{15}N cross-peak at δ –260 ppm (**Figure 5.2**), confirming that the ^{1}H resonance at δ 12.7 ppm corresponds to a proton that is bound to a N atom. This ^{15}N chemical shift is significantly upfield from related nitride complexes (371–393 ppm) but similar to the chemical shift of the ^{1}H–^{15}N cross-peak for the protonated P*N*P backbone of [(^{H}PNP)Re(N)(Cl)]$^+$ (–336 ppm).[56]

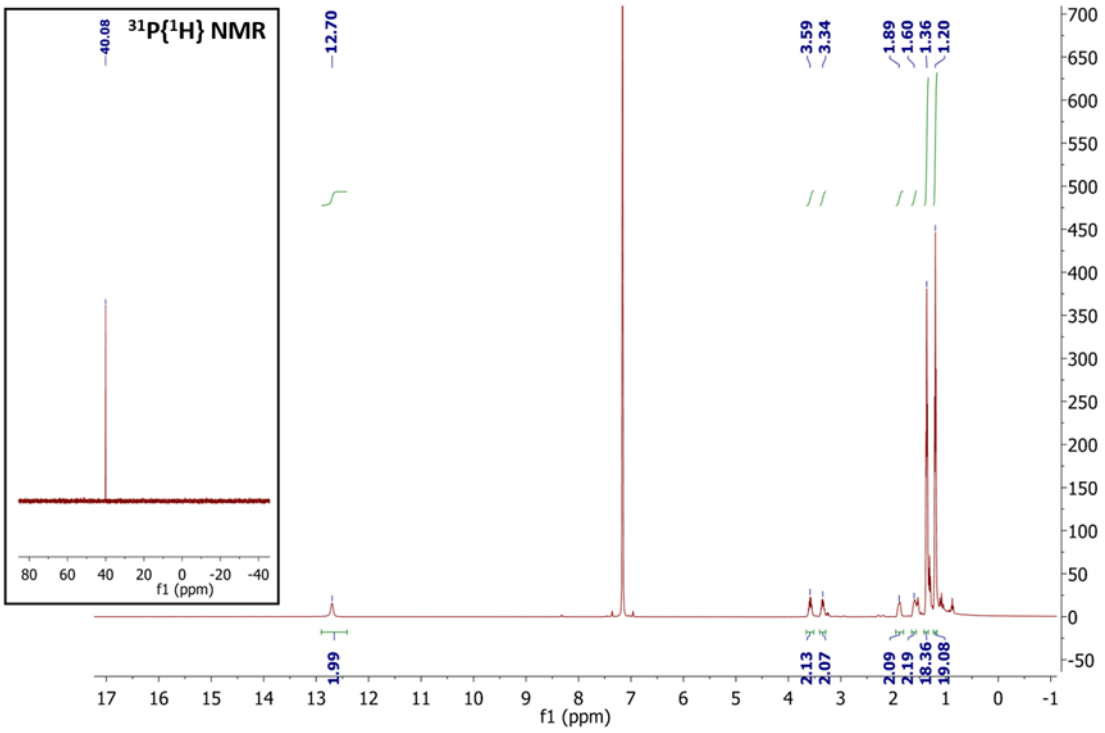

Figure 5.1. ^{1}H (400 MHz, C_6D_6) and $^{31}P\{^{1}H\}$ NMR spectra (162 MHz, C_6D_6, inset) of **3**. See Experimental section for more details.

Scheme 5.2. Reactivity of **1** with N_2 and NH_3.

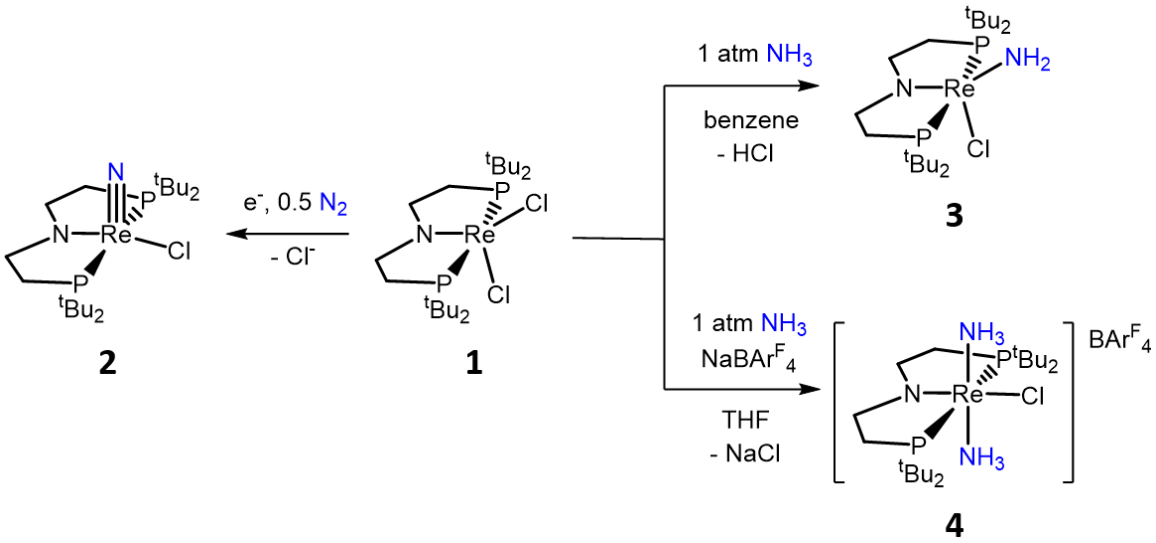

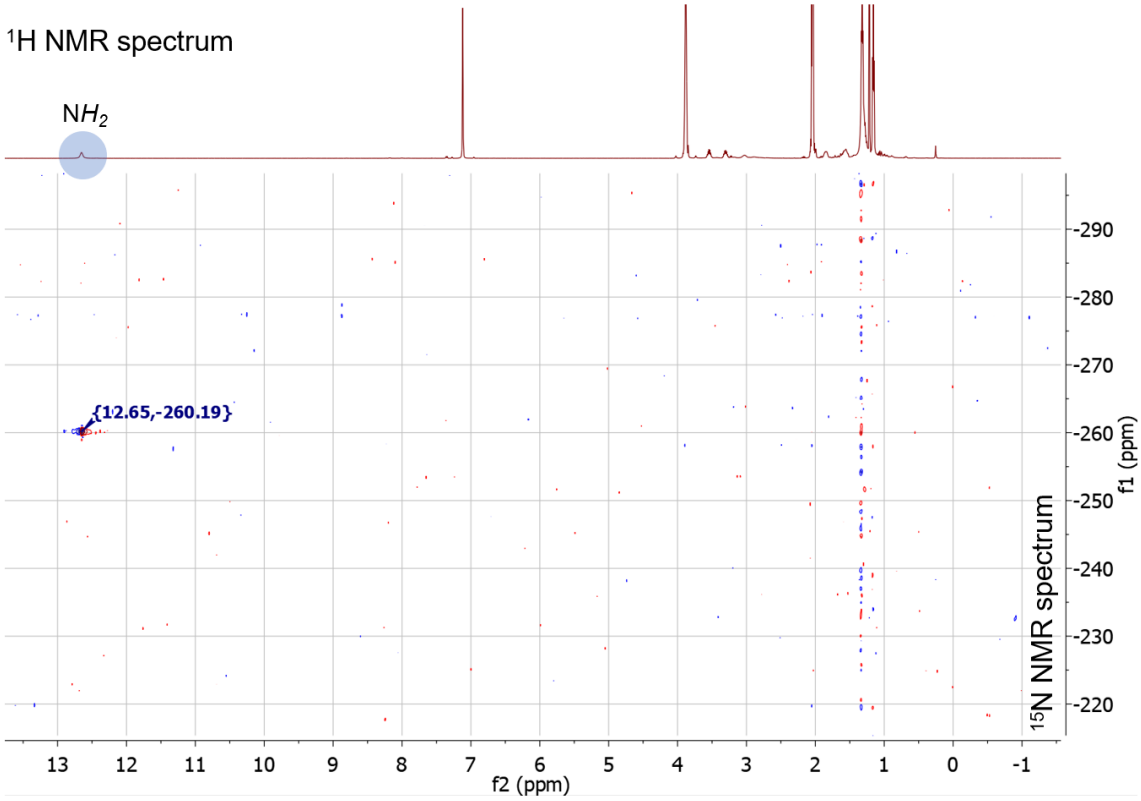

Figure 5.2. ^{1}H–^{15}N HSQC spectrum (400 MHz/51 MHz, C_6D_6) of **3** showing a ^{15}N cross-peak at δ –260 ppm corresponding to the 2 H resonance at δ 12.7 ppm.

On a preparative scale, addition of 1 atm NH_3 to a solution of **1** gives **3** as the major product, which is isolated from the reaction in 61% yield and purified by crystallization. The solid-state structure of **3** was elucidated via single crystal X-ray diffraction (XRD) and confirmed to be a Re–NH_2 complex in which the N-bound hydrogen atoms could be located (**Figure 5.3**). In a comparison of solid-state structures, **3** contains a Re–*N*H_2 bond 0.3 Å longer than the Re–*N* bond in the nitride complex **2**, consistent with a Re–N single bond in **3** (see **Table 5.1**).[56] Comparison of the metrics in the supporting ligand is also interesting: specifically, the (P*N*P)–Re bond is 0.1 Å shorter in **3** than in the Re-nitride complex **2**, indicating increased π-bonding from the N of the PNP ligand in **3**. The (P*N*P)–Re and Re–*N*H_2 amide bond lengths in **3** are within 0.02 Å of each other and both have planar N atoms

(Σ_{PNP} = 360°, Σ_{NH2} = 357°). The PNP and NH_2 amides are oriented such that they can π-donate into the same Re d orbital, which is reflected in a modest lengthening (0.04 Å) of the (P*N*P)–Re bond in **3** compared to in the Re-dichloride complex **1**.[57] In a similar manner, nitride complex **2** exhibits strong π-donation from the nitrido ligand that out-competes π-donation from the P*N*P amide. This results in a more pyramidalized amide (Σ_{PNP} = 348°) in **2**. These changes are accompanied by a change in the geometry of rhenium from trigonal bipyramidal in complex **3** to distorted square pyramidal in complex **2**, in which the coordination site *trans* to the nitride is open.

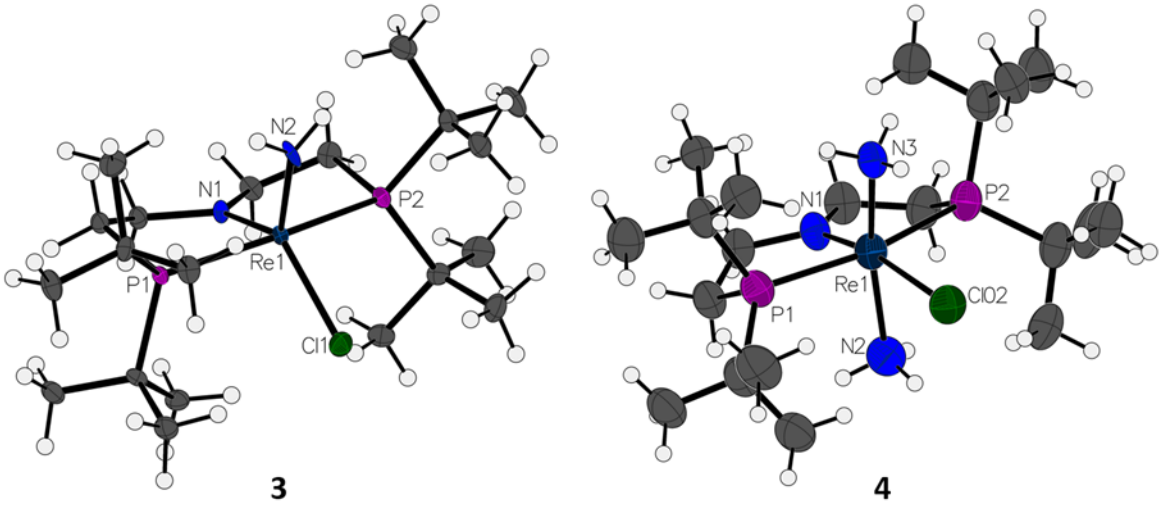

Figure 5.3. Solid-state structures of Re-amide complex **3** and $Re(NH_3)_2$ complex **4** (BAr^F_4 ion omitted) with thermal ellipsoids at 50% probability.

Table 5.1. Selected bond lengths (Å) and bond angles (°) of complexes **2**–**4**.

Bond/Angle	**2**	**3**	**4**
Re1–N1	2.033(6)	1.936(3)	1.894(5)
Re1–N2	1.643(6)	1.959(3)	2.150(5)
Re1–N3	-	-	2.193(6)
Re1–Cl1	2.441(2)	2.384(1)	2.495(2)
Re1–P1	2.443(2)	2.397(1)	2.424(2)
Re1–P2	2.435(2)	2.382(1)	2.425(2)
N1–Re1–N2	105.8(3)	115.5(1)	84.8(2)
N1–Re1–N3	-	-	165.6(2)
N2–Re1–N3			109.6(2)
N1–Re1–Cl1	106.5(2)	108.8(1)	83.4(1)
N2–Re1–Cl1	147.7(2)	135.6(1)	167.0(2)
N1–Re1–P1	100.4(2)	95.1(1)	91.0(1)
N1–Re1–P2	99.9(2)	95.5(1)	90.5(1)

When only 1 equiv of NH_3 gas was added to a solution of **1** in THF-d_8 at –80 °C, ^1H and $^{31}P\{^1H\}$ NMR spectra of the reaction showed a mixture of diamagnetic products, including some unreacted **1** (**Figure 5.4**, middle). Addition of another 4 equiv of NH_3 gas (for a total of 5 equiv NH_3 per Re) resulted in full consumption of **1** and observation of **3** in 71% yield (**Figure 5.4**, top). It is likely that dehydrohalogenation of the putative intermediate (PNP)Re(NH_3)$(Cl)_2$ by NH_3 to form NH_4Cl is required to drive the formation of **3**. This implies that coordination to Re^{III} significantly increases the acidity of the N-bound protons.[58]

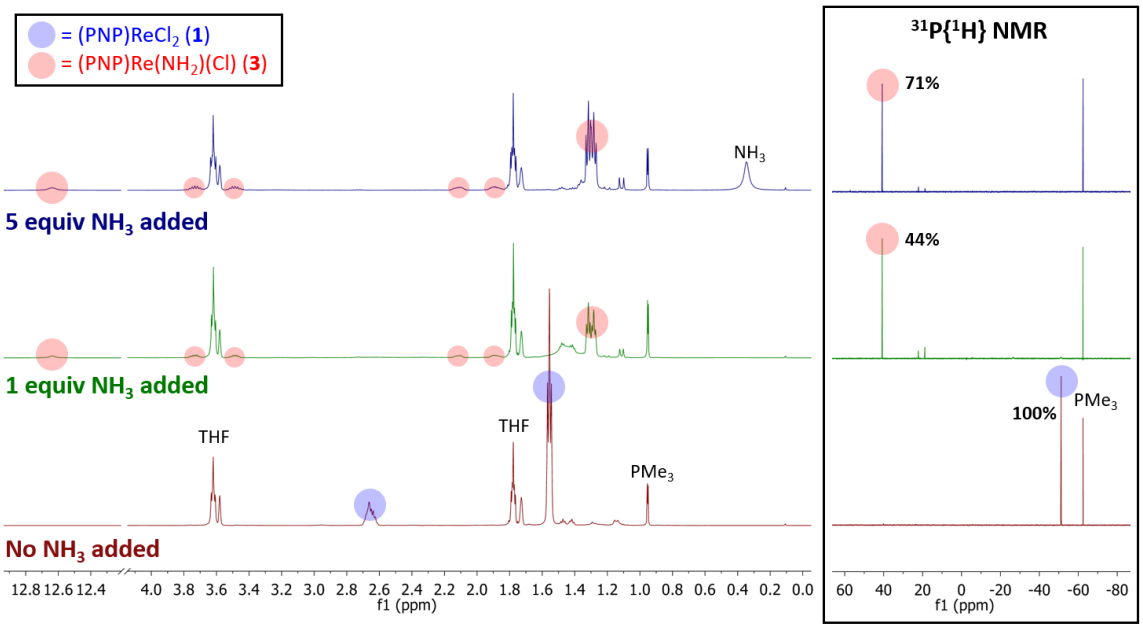

Figure 5.4. ^{1}H (400 MHz, THF-d_8) and ^{31}P{^{1}H} (162 MHz, THF-d_8) NMR spectra of **1** without NH_3 (bottom, maroon), with 1 equiv NH_3 added (middle, green), and with 5 equiv NH_3 added (top, blue). Addition of NH_3 was accompanied by a color change from purple to brown and the formation of a pale blue precipitate. Spectroscopic yields reported vs. PMe_3 in a capillary.

Although the putative intermediate (PNP)Re(NH_3)$(Cl)_2$ could not be isolated, addition of 1 atm NH_3 to a solution of **1** containing an equivalent of $NaBAr^F_4$ (Ar^F = 3,5-bis(trifluoromethyl)phenyl) in THF-d_8 at –80 °C results in a color change from purple to light green and formation of a new diamagnetic complex **4** by ^{1}H and ^{31}P{^{1}H} NMR spectroscopy (see **Scheme 5.2**). In contrast to **3**, complex **4** exhibits C_{2v} symmetry, with a singlet in the ^{31}P NMR spectrum at δ –10.0 ppm (**Figure 5.5**). Complex **3** also displays a broadened ^{1}H resonance with δ 5.47 ppm, integrating to 6 H. The XRD structure of **3** shows a six-coordinate, cationic bis-ammine adduct [(PNP)Re(NH_3)$_2$(Cl)][BAr^F_4] in a distorted octahedral geometry (see **Figure 5.3**). In comparison to **3**, complex **4** shows lengthened Re–*N* bonds to the ligands derived from NH_3, with **4** exhibiting an average Re–*N*H_3 bond length of 2.172(5) Å compared to the Re–*N*H_2 bond length of 1.959(3) Å (see **Table 5.1**). These bond lengths reflect the lack of π-donation from the ammine ligands in **4**. With no

strong π-donor ligands to compete with π-donation from the P*N*P amide, **4** contains a short Re–P*N*P bond distance of 1.894(5) Å (0.04 and 0.14 Å shorter than **3** and **2**, respectively). These trends in Re–N bond lengths in complexes **2**–**4** clearly illustrate the expected increase in Re–NH_x bond order as hydrogen atoms are removed. The flexibility of the P*N*P–Re interaction to accommodate the changes in ligand donor characteristics from ammine to nitride is also evident from the change in the P*N*P–Re bond lengths and P*N*P pyramidalization from **2**–**4**. This combined flexibility of the supporting PNP-pincer ligand and Re coordination geometries may enhance the ability to isolate stable $Re^{III}(NH_3)_2$, Re^{III}–NH_2, and $Re^{V}\equiv N$ complexes in this series.

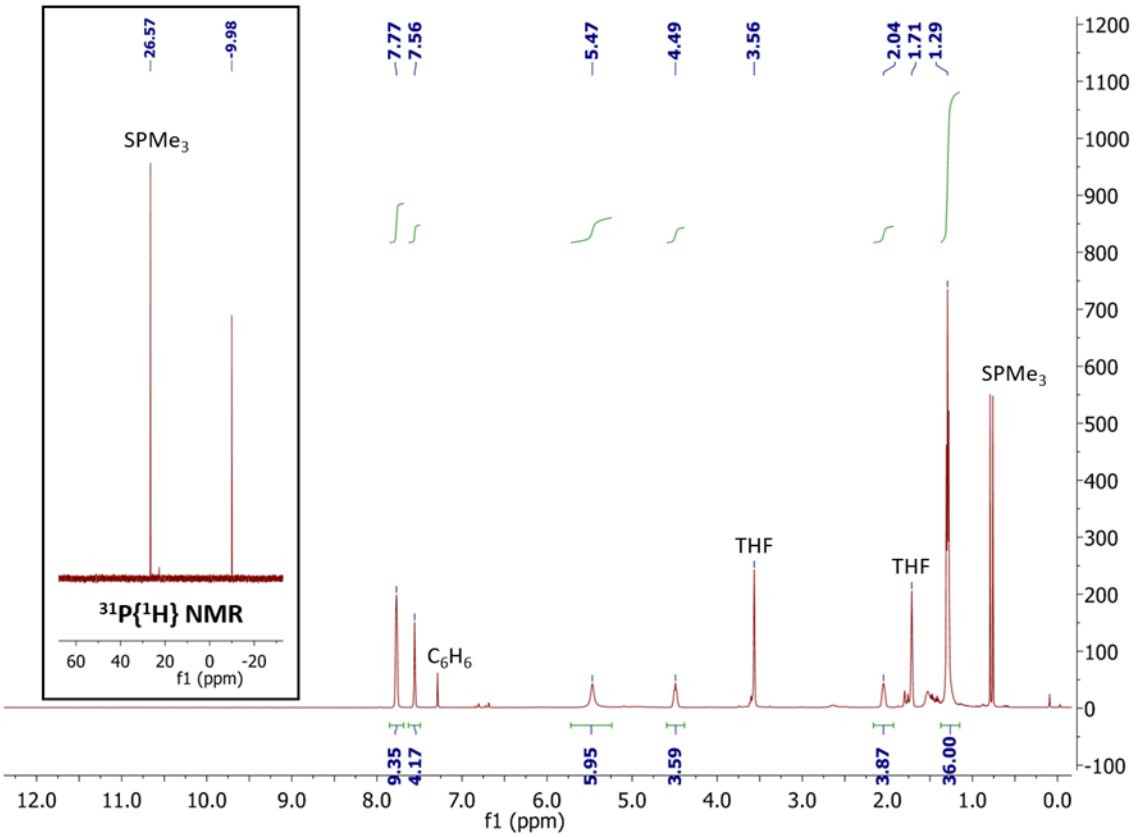

Figure 5.5. ^{1}H (400 MHz, THF-d_8) and $^{31}P\{^{1}H\}$ NMR spectra (162 MHz, THF-d_8, inset) of **4**. See Experimental section for more details.

5.2.2. *Reactivity of Re-ammine complex [(PNP)Re(NH$_3$)$_2$(Cl)]$^+$*

To assess the plausibility of **4** as an analogue of the intermediate during formation of **3**, a solution of **4** in THF-d_8 was treated with NH_3, which gave no reaction. However, addition of a slight excess of potassium hexamethyldisilazide (KHMDS) (**Scheme 5.3**) caused an immediate color change and formation of **3** as the major product (61% yield), as judged by ^{1}H and ^{31}P{^{1}H} spectroscopy (**Figure 5.6**).

Scheme 5.3. Reactivity of **4** with stoichiometric base and reductant.

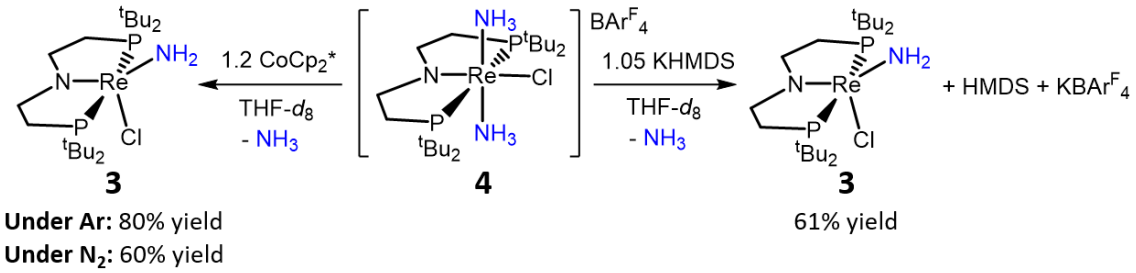

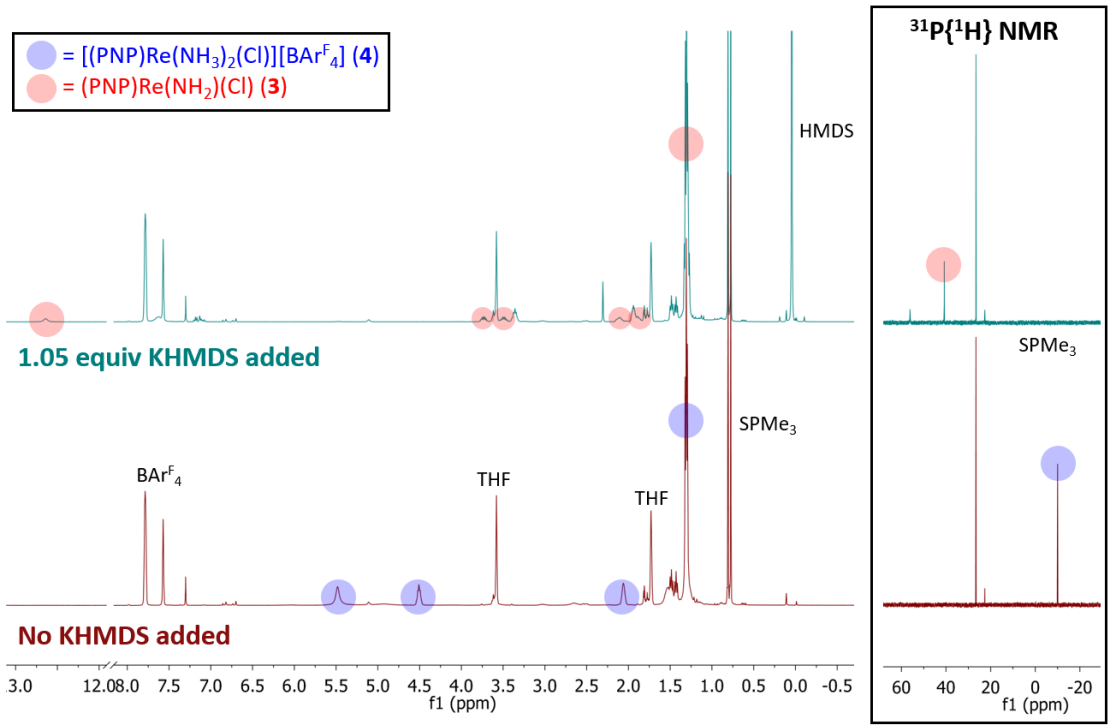

Figure 5.6. ^{1}H (400 MHz, THF-d_8) and ^{31}P{^{1}H} (162 MHz, THF-d_8) NMR spectra of **4** in THF-d_8 before (bottom, maroon) and after (top, teal) the addition of 1.05 equiv KHMDS. Complex **3** is formed in 61% spectroscopic yield vs. $SPMe_3$ in a capillary.

Isolation of **4** also provides the opportunity to explore the redox properties of a Re^{III}-ammine complex in this system. The ideal N_2 to NH_3 conversion pathway for (PNP)Re, proceeding through PCET nitride reduction following reductive N_2 cleavage, would likely involve a Re^{II}–NH_3 intermediate (left side of **Scheme 5.1**) that releases NH_3 and binds N_2 and in order to turn over. For example, the established electrochemical N_2 cleavage mechanism by (PNP)Re proceeds via initial $1e^-$ reduction of **1** to form $[(PNP)Re^{II}(Cl)_2]^-$, which binds N_2 and proceeds with subsequent reduction and comproportionation steps.[54] In the oxidative direction, $1e^-$ of a Re^{III}–NH_3 complex, followed by deprotonation of the NH_3 ligand, could provide a stepwise mechanism to N–H bond oxidation. In order to assess both of these possibilities in this system, we studied the electrochemistry of **4**.

Cyclic voltammetry (CV) of **4** in THF under Ar shows that it can be quasi-reversibly reduced at –1.95 V vs $Cp_2Fe^{+/0}$ and quasi-reversibly oxidized at –0.58 V vs. $Cp_2Fe^{+/0}$ (**Figure 5.7**). The initial quasi-reversible reduction of **4** (E_{pa} = –1.95 V vs. $Cp_2Fe^{+/0}$) is followed by a second irreversible reduction at –2.26 V vs. $Cp_2Fe^{+/0}$. This behavior is similar to that of **1** under Ar, which exhibits a quasi-reversible reduction at –2.00 V vs. $Cp_2Fe^{+/0}$ followed by an irreversible reduction at –2.29 V vs. $Cp_2Fe^{+/0}$.[59] Schneider and Miller attributed the first reduction of **1** under Ar to the formation of $[(PNP)Re^{II}(Cl)_2]^-$, which is followed by chloride dissociation to form $(PNP)Re^{II}(Cl)$. This monochloride complex is subsequently reduced by $1e^-$.[54] The very cathodic reduction potentials of **4** indicate that it is quite electron-rich despite its positive charge, and the similarity between CVs of **4** and **1** suggest that similar ligand dissociation events may occur upon electroreduction of **4**.

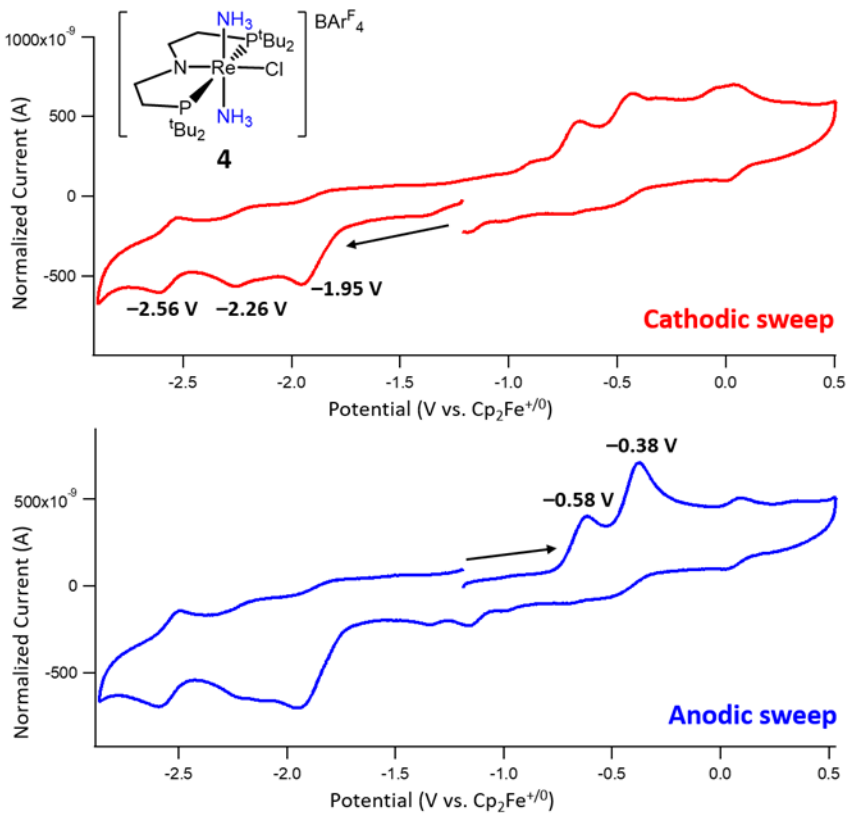

Figure 5.7. Cyclic voltammograms (CVs) of 0.4 mM **4** in 0.2 M tetrabutyl-ammonium hexafluorophosphate solution in THF under Ar, demonstrating irreversible 1e⁻ events sweeping in the cathodic (reductive) direction (top, red) and the anodic (oxidative) direction (bottom, blue). CVs measured at 100 mV/s with a glassy carbon disc working electrode, Pt wire auxiliary electrode, and Ag wire psuedoreference. Potentials referenced to $Cp_2Fe^{+/0}$ after the experiments.

To assess the species formed upon reduction, **4** was treated with a 1e^- chemical reductant. Addition of 1.2 equiv $CoCp_2$* to a solution of **4** in THF-d_8 under Ar resulted in an immediate color change to a darker brown. The ^{1}H and ^{31}P{^{1}H} NMR spectra show complete consumption of **4** and formation of **3** in 80% spectroscopic yield, indicating that reduction of **4** initiates N–H bond cleavage from coordinated NH_3 to form the Re amide (**Figure 5.8**, middle). Interestingly, when 1.2 equiv $CoCp_2$* was added to a solution of **4** in THF-d_8 under N_2 rather than Ar, the complete consumption of **4** gave **3** in a lower spectroscopic yield of 60% (**Figure 5.8**, top). No appreciable amount of Re-nitride

complex **2** was detected; however, numerous unidentified minor products were observed in the ^{1}H and $^{31}P\{^{1}H\}$ NMR spectra that were not formed in the analogous reaction under Ar. Thus, there is no binding of N_2 to give the bimetallic N_2 cleavage product, but the difference implies that N_2 probably interacts with some intermediate that has not been identified. The other products of the $1e^-$ reduction of **4** under either Ar or N_2 could not be identified.

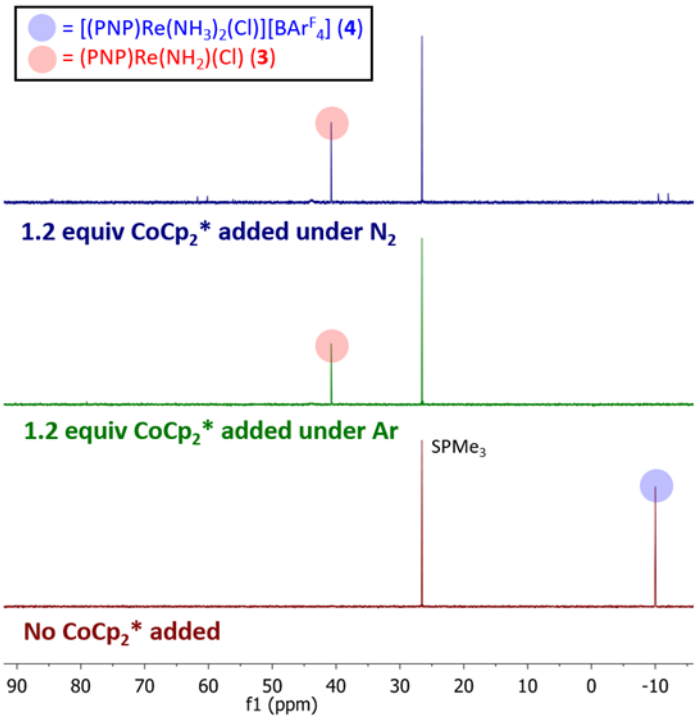

Figure 5.8. $^{31}P\{^{1}H\}$ NMR spectra (162 MHz, THF-d_8) of **4** in THF-d_8 prior to (bottom, maroon) and after addition of 1.2 equiv $CoCp_2$*. Under Ar, the reaction gave **3** in 80% spectroscopic yield (middle, green). Under N_2, the reaction gave **3** in 60% spectroscopic yield, along with numerous unidentified minor products. Spectroscopic yields measured vs. $SPMe_3$ in a capillary.

The relatively high yield of **3** from $1e^-$ reduction of **4** suggests that the "missing" H atom could be released as H_2. Such H_2 elimination from metal–NH_3 complexes is proposed to occur when coordination of NH_3 to the metal results in sufficient weakening of the ammine's N–H bonds to provide a thermodynamic preference for H_2 formation.[60] This

behavior is reported in NH_3-derived $Mo(NH_3)_2$ complexes, and $1e^-$ reduction of the Mo metal center enhances the weakening of N–H bonds in the NH_3 ligands.[36, 60] Similarly, H_2 elimination from unstable N_xH_y intermediates is hypothesized to be a mechanism for unproductive H_2 generation in systems that can achieve N_2 reduction to NH_3.[61] To test this possibility, the reaction of 1.1 equiv Cp^*_2Co with **4** was repeated on a larger scale. Complex **3** was isolated from the product mixture in 73% yield, but analysis of the headspace following the reaction showed no detectable amount of H_2 (<1% yield). This eliminates the possibility of bimetallic elimination of H_2 from weak N–H bonds upon reduction of **4**, and suggests that a dehydrohalogenation pathway similar to that of putative intermediate $(PNP)Re(NH_3)(Cl)_2$ is involved. The fate of the additional electron is unknown.

5.2.3. N–H bond oxidation from Re-amide complex (PNP)Re(NH_2)(Cl)

By analogy to other reported systems,[34-37, 40, 42, 43] we reasoned that abstraction of H atoms from complex **3** would lead to formation of the nitride complex **2** (see **Scheme 5.1**, blue). Addition of 2 equiv of either 2,4,6-tri-*tert*-butylphenoxyl radical ($^tBu_3PhO^\bullet$) or TEMPO$^\bullet$ as HAA reagents to a solution of **3** in THF-d_8 or benzene-d_6 at ambient temperature gives quantitative (>99%) formation of **2** within minutes, as judged by ^1H and $^{31}P\{^1H\}$ NMR spectroscopy (**Figure 5.9**). This is accompanied by the formation of 2 equiv of $^tBu_3PhOH$ ($BDFE_{O–H}$ = 74.4 kcal/mol in benzene) or TEMPOH ($BDFE_{O–H}$ = 65.5 kcal/mol in benzene),[62] respectively, supporting the idea that facile H-atom abstraction from the Re N–H bonds in **3** can form the Re-nitride complex **2**. When **3** is mixed with only 1 equiv of TEMPO$^\bullet$, **2** and **3** are observed as products in a ratio of *ca.* 1:1, showing that the second H-atom abstraction is faster and more favorable than the first (**Figure 5.10**).

To test the reverse reaction, **2** was mixed with excess $^{t}Bu_3PhOH$ or TEMPOH; however, no reaction was observed in either case even after prolonged heating. The indicates that formation of **2** from **3** is likely to reflect a strong thermodynamic preference for the O–H bonds over the N–H bonds in these reactions (see below).

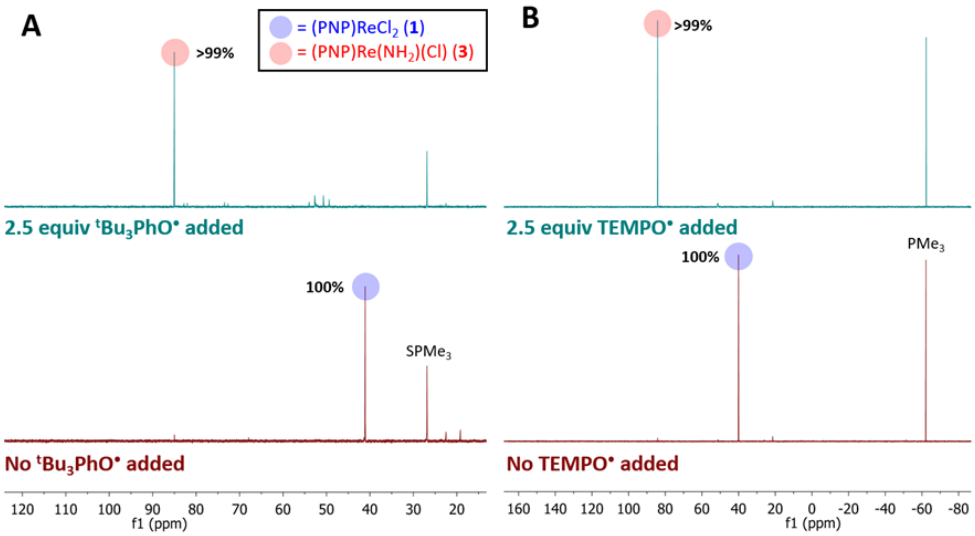

Figure 5.9. $^{31}P\{^{1}H\}$ NMR spectra (202 MHz, THF-d_8 or 162 MHz, C_6D_6) of the reaction of **3** with organic H-atom abstracting (HAA) reagents. **A:** Solution of **3** in THF-d_8 before (bottom, maroon) and after (top, teal) addition of 2.5 equiv $^{t}Bu_3PhO^{\bullet}$ at ambient temperature, showing quantitative conversion to nitride complex **2** within minutes. **B:** Solution of **3** in C_6D_6 before (bottom, maroon) and after (top, teal) addition of 2.5 equiv TEMPO$^{\bullet}$ at ambient temperature, showing quantitative conversion to nitride complex **2** within minutes. Spectroscopic yields were calculated vs. an internal standard of $SPMe_3$ or PMe_3 in a capillary.

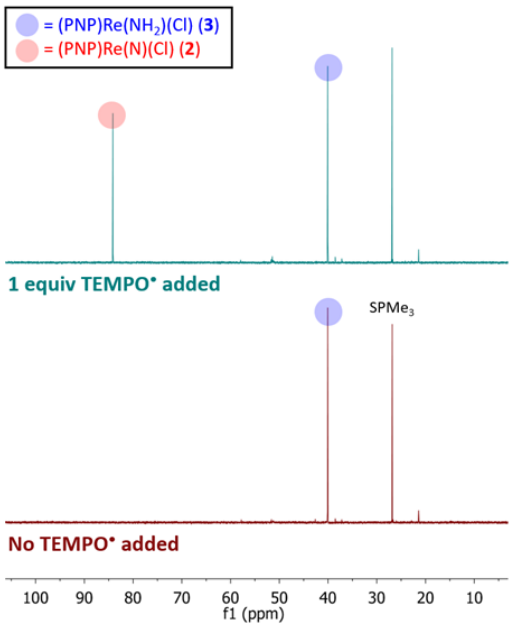

Figure 5.10. $^{31}P\{^{1}H\}$ NMR spectra (162 MHz, C_6D_6) of a solution of **3** in C_6D_6 before (bottom, maroon) and after (top, teal) addition of 1 equiv TEMPO•, resulting in formation of **2**.

We also surveyed potential H-atom abstraction from **3** to form weaker X–H bonds. Accordingly, **3** was mixed with 5 equiv of 5,10-phenazine in THF-d_8. Although no reaction was observed at ambient temperature, heating this mixture to 80 °C gave quantitative (>98%) conversion to **2** and 5,10-dihydrophenazine (average $BDFE_{N–H}$ = 58.7 kcal/mol in MeCN) after 21 h (**Figure 5.11**).[62] Conversely, no reaction was observed between **2** and 10 equiv of 5,10-dihydrophenazine even after prolonged heating at 80 °C, again indicating that the reverse reaction is unfavorable. Oxidation of the amide ligand in **3** to form **2** was also observed when using 1.5 equiv of azobenzene (54% yield of **2** after 72 h at 60 °C) and 1,8-dichloro-9,10-anthraquinone (67% yield of **2** after 4 d at ambient temperature). Formation of 1,2-diphenylhydrazine (average $BDFE_{N–H}$ = 60.9 kcal/mol in MeCN)[62] and 1,8-dichloro-9,10-anthracenediol (average $BDFE_{O–H}$ = 55.4 kcal/mol in THF),[62] respectively, was detected in these reactions by ^{1}H NMR spectroscopy; however, these

reactions form multiple products, so the product outcome does not give quantitative thermochemical information about the reactions in these cases. The reactivity of **3** with various HAA reagents to form **2** is summarized in **Scheme 5.4**.

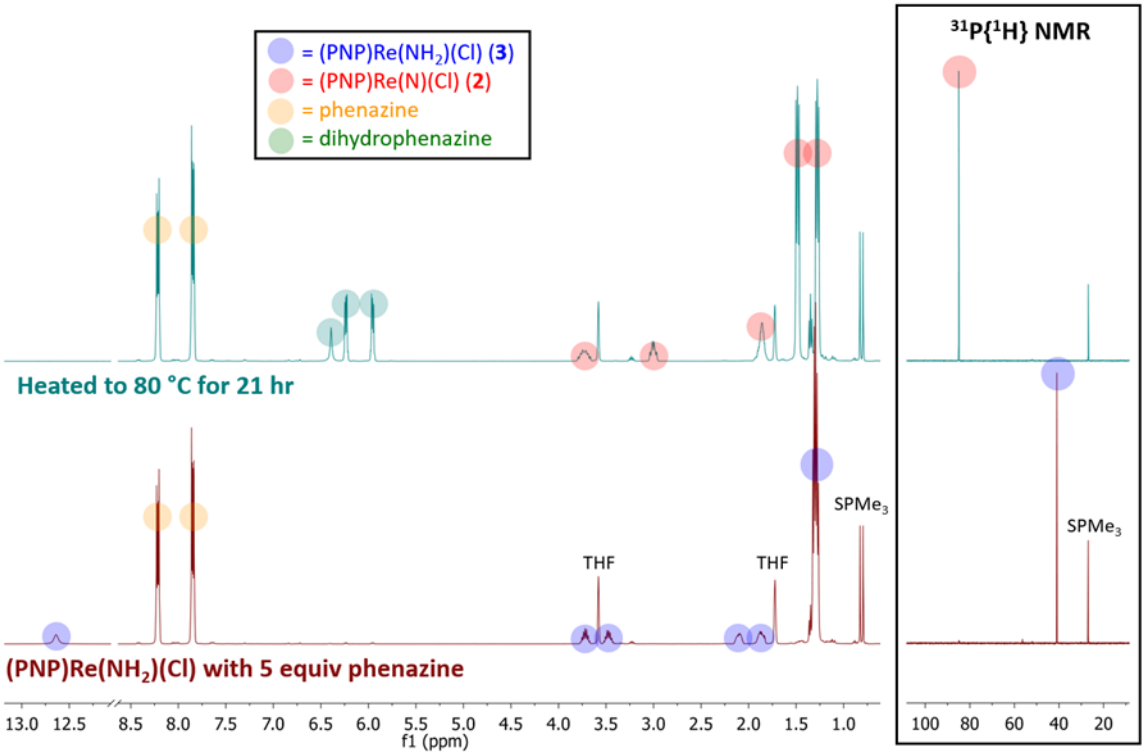

Figure 5.11. ^{1}H (400 MHz, THF-d_8) and ^{31}P{^{1}H} (162 MHz, THF-d_8) NMR spectra of **3** and 5 equiv phenazine in THF-d_8 before (bottom, maroon) and after (top, teal) heating at 80 °C for 21 h. Complex **2** is formed in 99% spectroscopic yield vs. $SPMe_3$ in a capillary.

Scheme 5.4. Reactivity of **3** with organic HAA reagents, with average $BDFE_{X–H}$ of the organic products reported in blue.

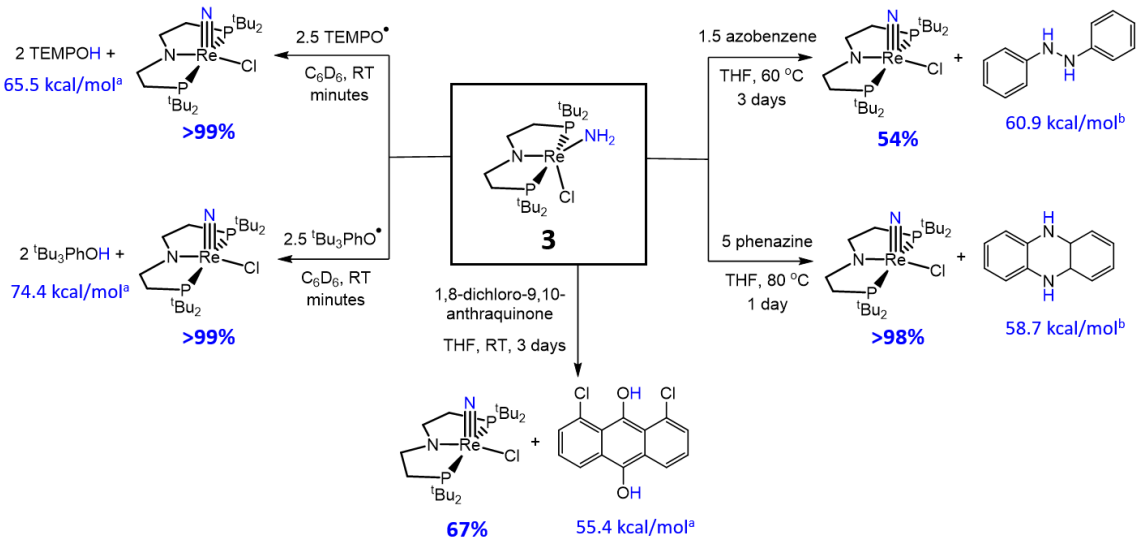

[a]$BDFE_{O–H}$ in THF. [b]Average $BDFE_{N–H}$ in MeCN.

5.2.4. Stepwise N–H bond oxidation from (PNP)Re(NH$_2$)(Cl)

The reactivity of **3** with HAA reagents demonstrates that the N–H bonds in the amide ligand can be easily oxidized via concerted removal of an H-atom.[8] However, it is important to consider that N–H bond oxidation could also occur through the stepwise $1e^-$ oxidation and deprotonation of **3**, since some reported systems for NH_3 oxidation proceed through $1e^-$ electrochemical oxidation followed by deprotonation by the electrolyte or an exogenous base.[38, 39, 41] We were therefore interested to determine whether a stepwise oxidation pathway for the conversion of **3** to **2** is possible.

To assess the feasibility of a deprotonation pathway, a solution of **3** was mixed with up to 12 equiv of 1,8-diazabicyclo[5.4.0]undec-7-ene (DBU, pK_a = 24.3 in MeCN),[63] phosphazene base P_1-tBu-tris(tetramethylene) (pK_a = 28.4 in MeCN),[64] or phosphazene base P_4-tBu (pK_a = 42.7 in MeCN)[65] in THF-d_8 at ambient temperature. No reaction of **3**

was observed by ^{1}H and $^{31}P\{^{1}H\}$ NMR spectroscopy with any of these strong bases, indicating that the amide ligand in **3** is not acidic; therefore, a deprotonation pathway towards stepwise N–H bond oxidation from **3** is not favorable. However, combining deprotonation with electrochemical oxidation showed more changes. CV of **3** in THF shows a quasi-reversible 1e^- oxidation at –0.61 V vs. $Cp_2Fe^{+/0}$, similar to both the dichloride complex **1** and the $Re(NH_3)_2$ complex **4** (**Figure 5.12**).[54] When 2,6-lutidine (pK_a = 14.2 in MeCN)[63] is added to a solution of **3**, this oxidation feature becomes less reversible, suggesting that a deprotonation follows the 1e^- oxidation of **3** (**Figure 5.13**). Assuming a stepwise 1e^- oxidation then deprotonation pathway, the Bordwell equation (**eq 1**) can be used to estimate the effective BDFE provided via oxidation at –0.61 V and deprotonation to form 2,6-lutidinium (**eq 2**, C_G = 66 kcal/mol for THF).[8, 66] This suggests an approximate upper limit for the N–H BDFE of **3** to be *ca.* 71 kcal/mol, although the Re^{IV} product from 1e^- oxidation of **3** could not be isolated for more accurate measurements. Complex **3** also exhibits an irreversible 1e^- reduction event at –3.05 V vs. $Cp_2Fe^{+/0}$, which is over 1 V more cathodic than complex **4**.

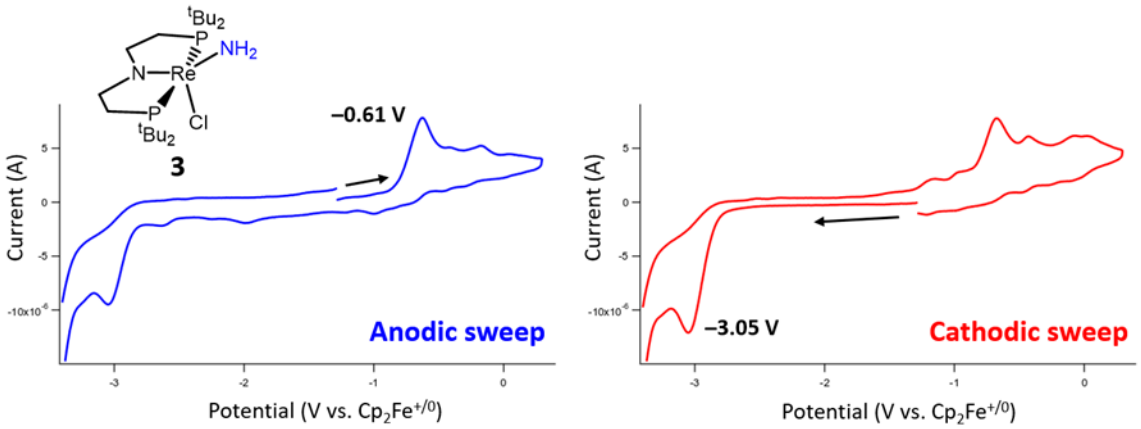

Figure 5.12. CV of **3** in 0.2 M tetrabutyl-ammonium hexafluorophosphate solution in THF under N_2, demonstrating irreversible 1e^- events sweeping in the anodic (oxidative) direction (left, blue) and the cathodic (reductive) direction (right, red). CVs measured at 100 mV/s with a glassy carbon

disc working electrode, Pt wire auxiliary electrode, and Ag wire psuedoreference. Potentials referenced to $Cp_2Fe^{+/0}$ after the experiments.

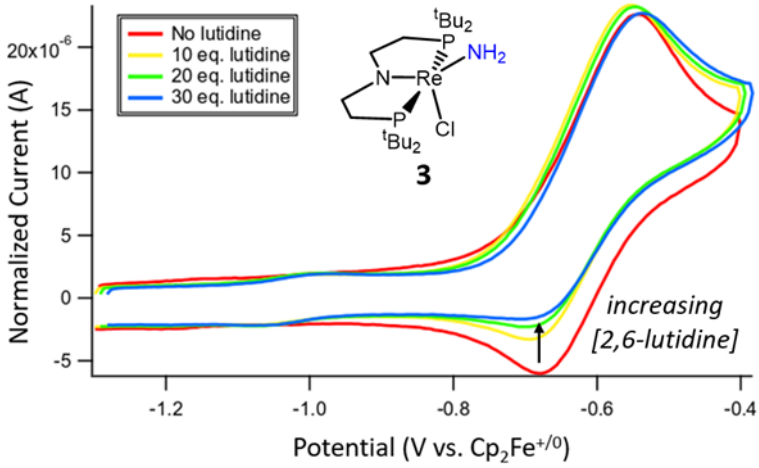

Figure 5.13. CVs of the first oxidation of **3** in 0.2 M tetrabutyl-ammonium hexafluorophosphate solution in THF under N_2 with various amounts of added 2,6-lutidine, showing a decrease in reversibility with higher [2,6-lutidine]. All scans taken at 1000 mV/s with a glassy carbon disc working electrode, Pt wire auxiliary electrode, and Ag wire pseudoreference. Potentials referenced to $Cp_2Fe^{+/0}$ after the experiments.

$$\mathrm{BDFE_{X-H}} = 1.37(\mathrm{p}K_a) + 23.06(E°) + C_G \qquad \textbf{(1)}$$

$$\mathrm{BDFE_{eff}} = 1.37(14.2) + 23.06(-0.61) + 66 = 71.4\ \mathrm{kcal/mol} \qquad \textbf{(2)}$$

To identify the products formed by $1e^-$ oxidation, 1.1 equiv of $[Cp_2Fe][PF_6]$ was added to a solution of **3** in THF-d_8. Interestingly, the major product identified from the resulting ^1H and $^{31}P\{^1H\}$ NMR spectra was the backbone-protonated Re-nitride complex $[(P^HNP)Re(N)(Cl)][PF_6]$ (**5**), which was formed in 50% yield (**Figure 5.14**).[56] The reaction also formed the Re^{III}-dichloride complex **1** in 25% yield, as well as a brown precipitate that could not be identified. The formation of both Re^{III} and Re^{V} complexes from the $1e^-$ oxidation of **3** implies that a disproportionation process occurs; however, these products are not formed in a 1:1 ratio, implicating other additional decomposition pathways. The

product mixture that can be identified spectroscopically does not account for all of the Re, N atoms, or H atoms present in the starting material. It is plausible that the remaining Re and N equivalents are contained in the intractable brown solid formed during the reaction. To test whether the missing H atoms could be released as H_2 from weakened N–H bonds during the reaction, the reaction was repeated on a larger scale. Analysis of the THF-soluble products from the reaction showed formation of **1** and **5** in 52% and 17% yield, respectively, and no H_2 was detected from analysis of the headspace (<1% yield).

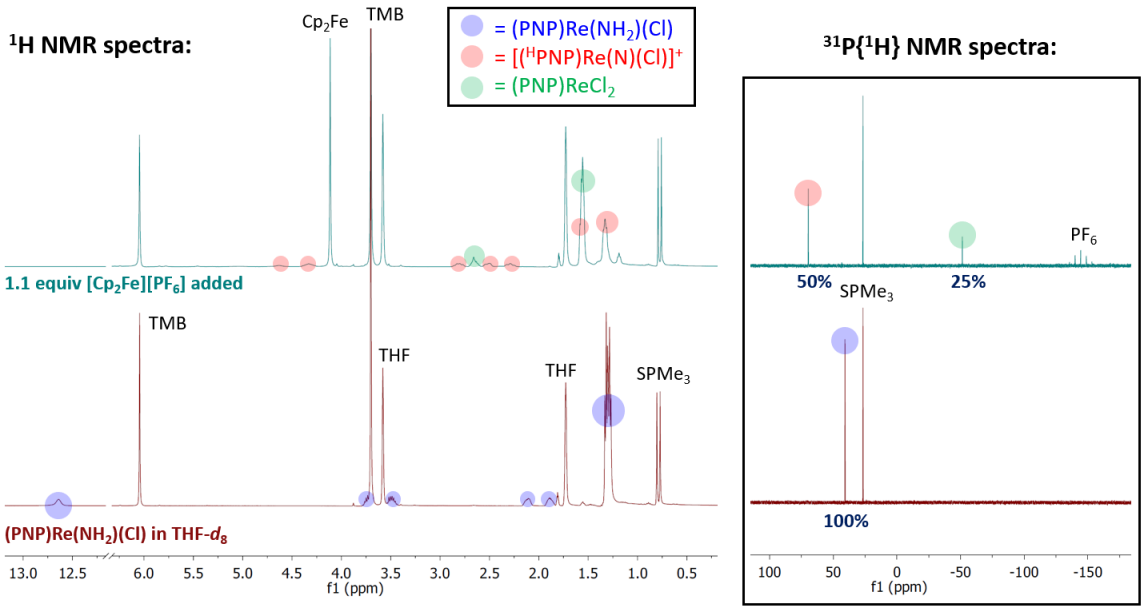

Figure 5.14. ^{1}H NMR (400 MHz, THF-d_8) and ^{31}P{^{1}H} NMR (162 MHz, THF-d_8) spectra of **3** before (bottom, maroon) and after the addition of 1.1 equiv [Cp_2Fe][PF_6] (top, teal), showing the formation of **5** and **1**. Spectroscopic yields are reported vs. TMB as an internal standard and a $SPMe_3$ capillary.

Formation of **5** from the 1e^- oxidation of **3** implies that: a) the amide in the P*N*P backbone may serve as an internal base following initial formation of [(PNP)Re(NH$_2$)(Cl)]$^+$ and b) the Re^{IV} imide intermediate is unstable towards subsequent decomposition to the nitride and other species. The CV data of **3** in the presence of added 2,6-lutidine indicates that a deprotonation step likely follows the formation of

$[(PNP)Re(NH_2)(Cl)]^+$ (see **Figure 5.13**). We therefore wondered if oxidation of **3** to a nitride could be facilitated by providing an exogenous base for the deprotonation steps and by using 2 equiv of oxidant in order to avoid the decomposition pathways of $[(PNP)Re(NH_2)(Cl)]^+$ implied by the $1e^-$ oxidation of **3**, such as disproportionation or formation of an intractable solid (**Scheme 5.5**). Accordingly, addition of 20 equiv 2,6-lutidine and 2.2 equiv $[Cp_2Fe][PF_6]$ to a solution of **3** in THF-d_8 forms **5** in 82% spectroscopic yield, with no formation of **1** observed (**Figure 5.15**). Similarly, electrolysis of a solution of **3** in the presence of 2,6-lutidine at the first oxidation event resulted in steady passing of charge up to 2.2 equiv e^- (**Figure 5.16**) and a change in color from brown to orange in the analyte solution. Nitride complex **5** was isolated from the post-electrolysis mixture in 69% isolated yield (**Figure 5.17**). These reactions indicate that the N–H bond oxidation from **3** to form a nitride can be achieved in stepwise $1e^-$ and deprotonation steps; however, an unidentified brown solid was formed as a byproduct in both reactions, suggesting that some decomposition pathways also occur.

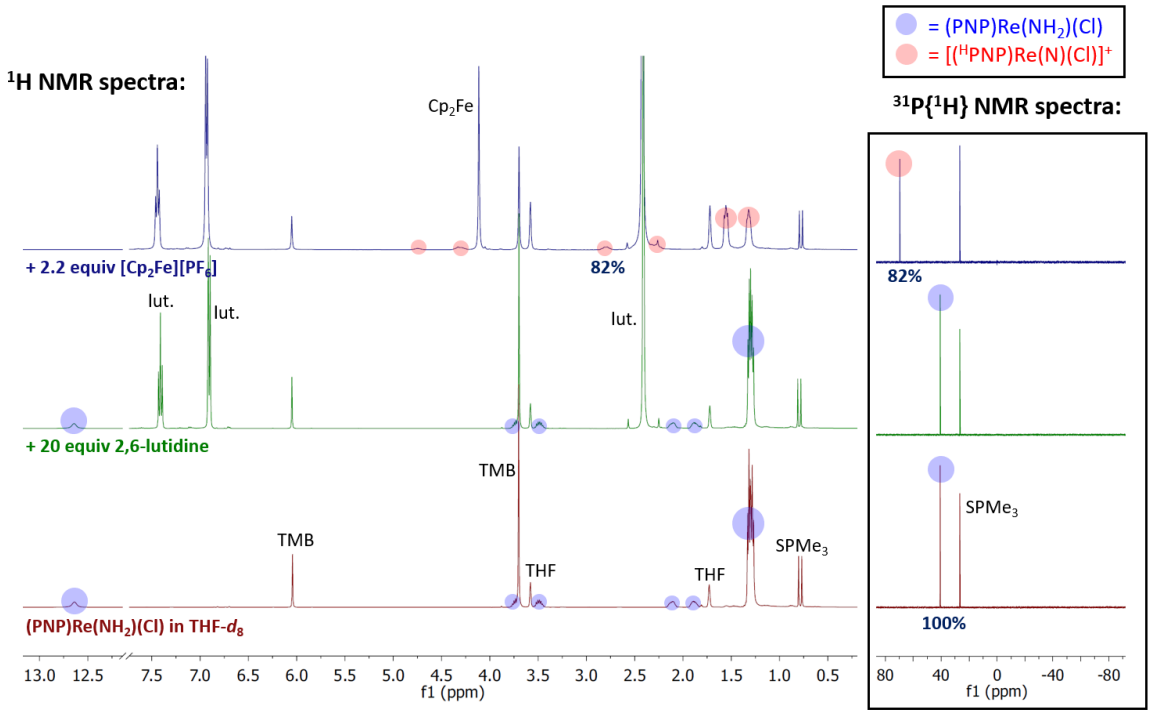

Figure 5.15. ^{1}H NMR (400 MHz, THF-d_8) and ^{31}P{^{1}H} NMR (162 MHz, THF-d_8) spectra of **3** (bottom, maroon) after the addition of 20 equiv 2,6-lutidine (middle, green), then after the addition of 2.2 equiv [Cp_2Fe][PF_6] (top, green). **3** shows no reaction with 2,6-lutidine, but reacts with 2.2 equiv [Cp_2Fe][PF_6] to give **5** in 82% yield, accompanied by formation of a brown precipitate. No **1** is formed in the reaction. Spectroscopic yields are reported vs. TMB as an internal standard and a $SPMe_3$ capillary.

Scheme 5.5. Oxidation of **3** with chemical oxidants.

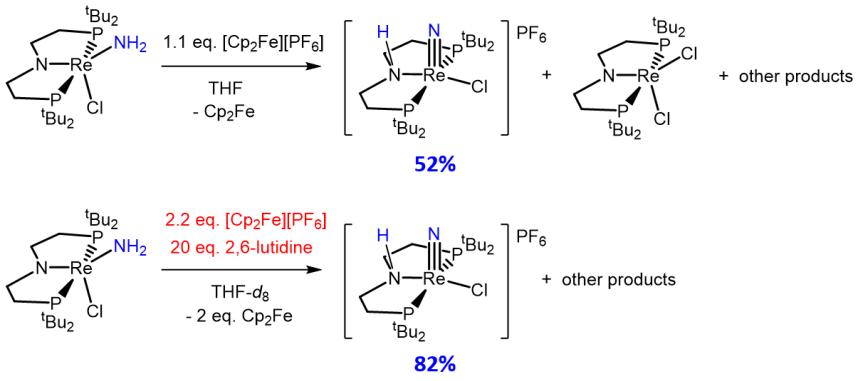

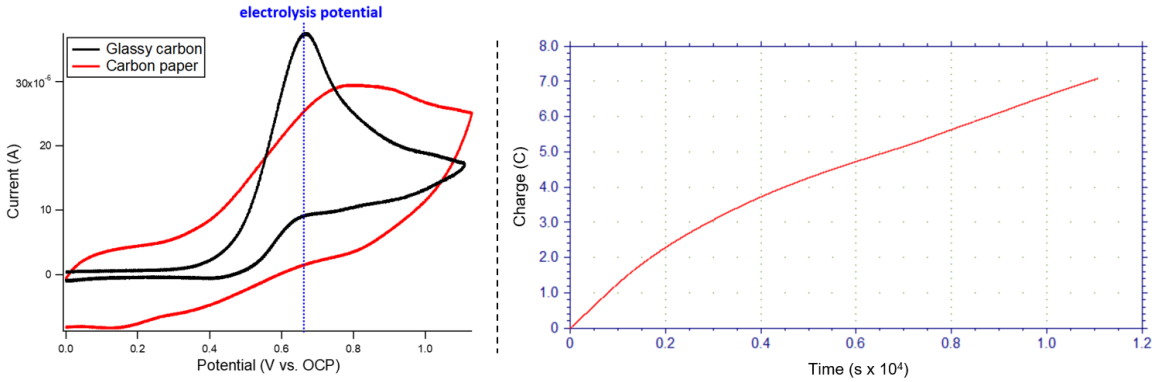

Figure 5.16. Left: Comparison of cyclic voltammograms of **3** (1.7 mM) prior to electrolysis, measured in 0.2 M tetrabutyl-ammonium hexafluorophosphate solution in THF containing excess 2,6-lutidine (34 mM) under Ar, using a glassy carbon (black) or carbon paper (red) working electrode, Pt mesh auxiliary electrode, and Ag wire pseudoreference electrode. The electrolysis potential (+0.66 V vs. open circuit potential) is noted in blue. **Right:** Charge passed vs. time during the electrolysis of **3**. The electrolysis was stopped after 2.2 equiv of charge per Re was passed. See Experimental Section for more details.

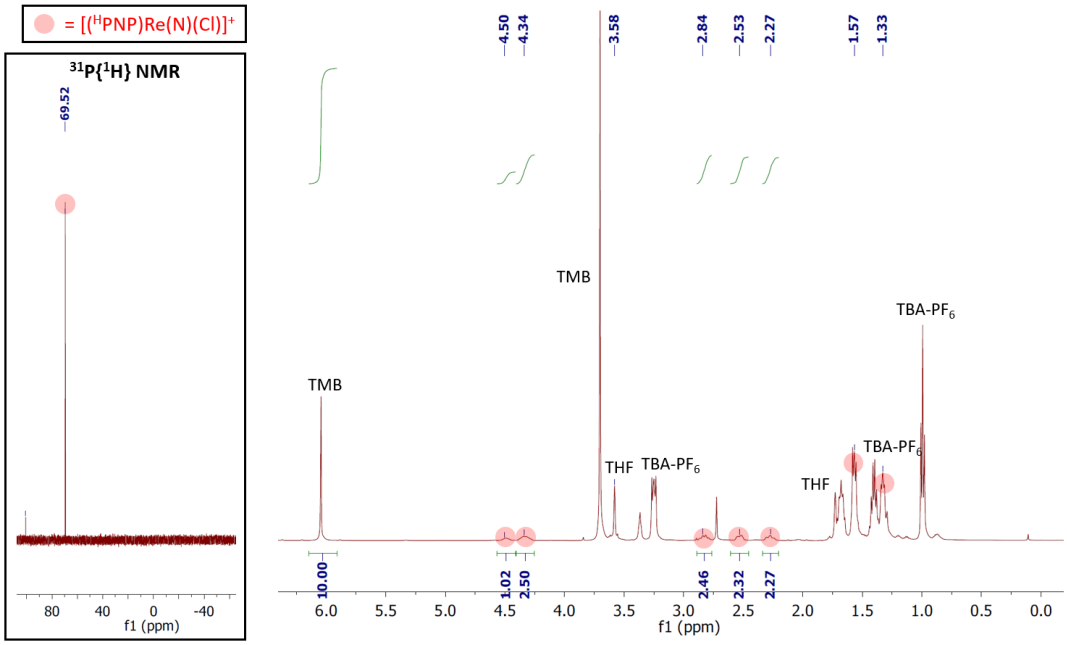

Figure 5.17. ^{1}H NMR (400 MHz, THF-d_8) and ^{31}P{^{1}H} NMR (162 MHz, THF-d_8) spectra of the THF-soluble products isolated from 2.2e^- electrolysis of **3** in the presence of 20 equiv 2,6-lutidine, showing formation of **5** in 69% yield. No **1** was isolated from the electrolysis. Yield reported vs. a TMB internal standard.

5.2.5. *Thermochemistry of N–H bond oxidation from (PNP)Re(NH$_2$)(Cl)*

Since **3** was found to react with all HAA reagents employed, we were unable to put a lower limit on the N–H BDE of **3**. However, since the reaction of **3** with 2 equiv ^{t}Bu$_3$PhO$^\bullet$ to form **2** and 2 equiv ^{t}Bu$_3$PhOH proceeds cleanly and quantitatively, we chose this reaction for calorimetric determination of the reaction enthalpy. The titration of **3** with ^{t}Bu$_3$PhO$^\bullet$ in THF using isothermal titration calorimetry (ITC) results in an exotherm of –50.9 kcal/mol until 2 equiv of ^{t}Bu$_3$PhO$^\bullet$ has been added (**Figure 5.18**). From these data, the average BDE$_{N–H}$ of **3** in THF was calculated to be 59.2 ± 0.2 kcal/mol.

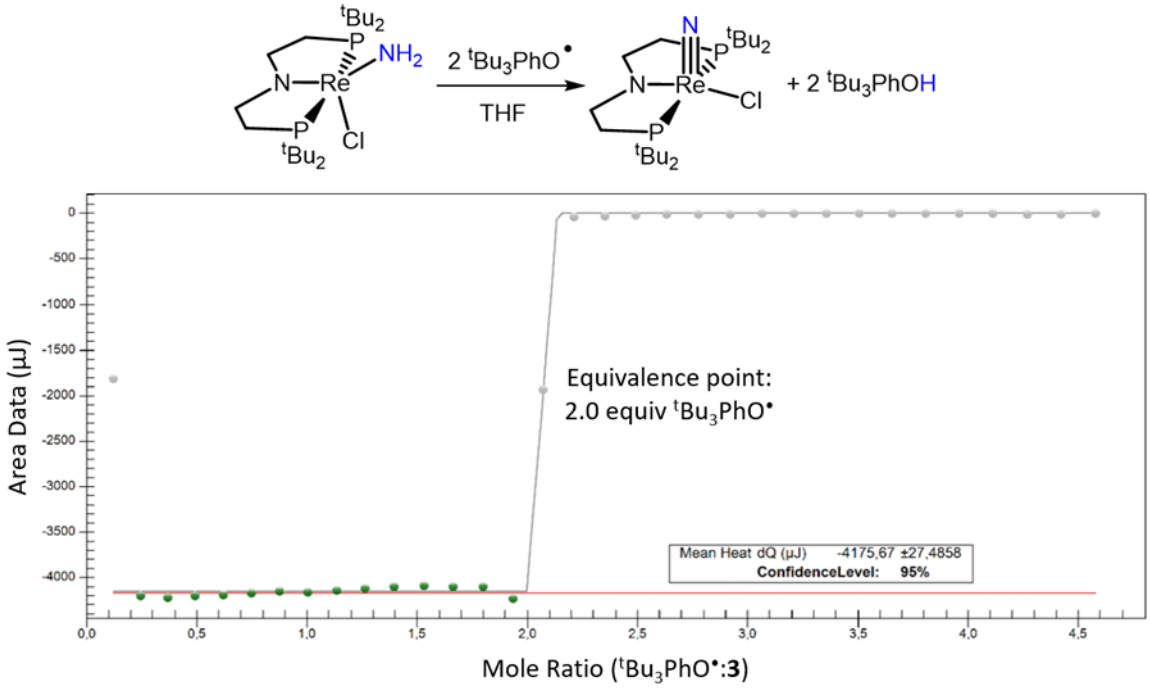

Figure 5.18. Top: Oxidation of **3** with 2 equiv ^{t}Bu$_3$PhO$^\bullet$. **Bottom:** Integrated heat titration curve for the reaction of **3** with 4.0 equiv ^{t}Bu$_3$PhO$^\bullet$ in THF, showing equivalence at 2.0 equiv of oxidant. The reaction exhibits an exotherm of –50.9 kcal/mol, calculated from the measured mean heat.

In order to understand the thermodynamics of each step in N–H bond oxidation from the –NH$_2$ ligand of **3**, the stepwise removal of a H atom from **3** to form **2** through the putative Re^{IV}-imide complex (PNP)Re(NH)(Cl) (**LRe–NH**) was evaluated

computationally (**Scheme 5.6**). This was achieved according to established methods by calculating the change in enthalpy associated with each sequential H-atom transfer from **3** to $^{t}Bu_3PhO^{\bullet}$ to form an equivalent of $^{t}Bu_3PhOH$ in THF.[35, 37, 67] The computational model predicts an average $BDE_{N–H}$ of 61.6 kcal/mol for **3**, which is in excellent agreement with the experimentally determined value of 59.2 kcal/mol. The overall conversion of amide complex **3** to nitride complex **2** via HAA from 2 equiv TEMPO$^{\bullet}$ was computed to be exergonic by 8.9 kcal/mol in THF, corresponding to an average $BDFE_{N–H}$ of 61.1 kcal/mol. The $BDFE_{N–H}$ of the amide ligand in **3** is calculated to be 79.5 kcal/mol, which is significantly higher than the computed $BDFE_{N–H}$ of **LRe–NH** (43.0 kcal/mol). The computations identify that the N–H bond in **LRe–NH** is particularly weak, which is consistent with both the facile, irreversible oxidation of **3** with HAA reagents and the proposed decomposition of putative Re^{IV}-imide intermediates to form **5** in stepwise oxidation pathways.

Scheme 5.6. Computed thermochemistry for the oxidation of **3** to **2** via stepwise H-atom removal. Models computed at the B3LYP/def2-TZVP level of theory (see Experimental Section for more details).

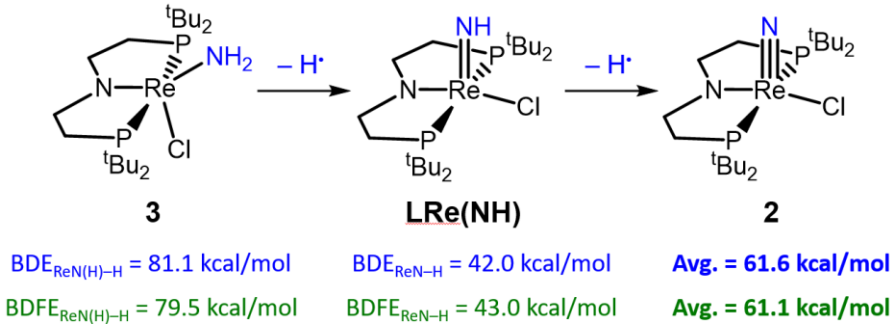

5.3 Discussion

5.3.1. NH_3 conversion to a nitride with (PNP)Re

The conversion of NH_3 to a nitride is quite facile in this system. Using excess NH_3, complex **1** goes directly to the Re–NH_2 complex **3**. The intermediate Re^{III}-ammine complex, potentially (PNP)Re$(NH_3)(Cl)_2$, has been neither spectroscopically observed nor isolated, which we attribute to rapid dehydrohalogenation by NH_3. This can be avoided through preparation of the analogous $Re^{III}(NH_3)_2$ complex **4**, which can be deprotonated with a different amide base to form complex **3**. Further oxidation of **3** to Re-nitride complexes is also facile, utilizing either HAA reagents to form **2** or via $2e^-$ oxidation in the presence of a weak base to form the nitride complex **5**. Thus, the complete conversion of NH_3 to a nitride in this system is achievable in good yield using a base (*i.e.* excess NH_3) and $2e^-$ oxidation at a mild potential (**Scheme 5.7**). From a functional standpoint, such facile formation of a nitride complex from NH_3 is attractive considering the mild oxidation potential used and the possibility for excess NH_3 to serve as an exogenous base.[7] However, turnover to achieve catalytic NH_3 oxidation to N_2 would require a nitride coupling step.[32, 33, 68] Although nitride coupling reactions between other late group transition-metal nitrides bearing similar supporting pincer ligands have been reported,[43, 69, 70] nitride coupling is not observed in this system due to the strong Re-nitride bond in complex **2**.[56] We can attribute this to a thermodynamic difficulty because the reverse reaction, reductive N_2 cleavage to form **2**, is exergonic by ~24 kcal/mol.[53]

Scheme 5.7. Full conversion of NH_3 by **1** to a nitride in complex **5**.

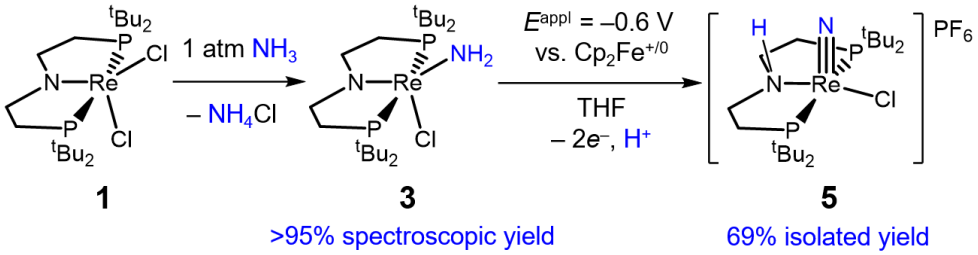

The oxidation of ammine complexes to form nitrides using HAA reagents is well precedented in other systems, but these systems typically utilize $^{t}Bu_3PhO^{\bullet}$ as the oxidant (forming $^{t}Bu_3PhOH$).[34-37, 40, 43] In contrast, H-atom abstraction from the amide in **3** can be achieved with HAA reagents to form X–H bonds that are >15 kcal/mol weaker than the O–H bond in $^{t}Bu_3PhOH$. The irreversibility of these reactions suggests that the average $BDFE_{N–H}$ of **3** is less than 65 kcal/mol, representing significant weakening from the $BDFE_{N–H}$ of NH_3 (99.4 kcal/mol in the gas phase).[8] Calorimetric titrations show that the average $BDE_{N–H}$ of **3** is 59.2 ± 0.2 kcal/mol in THF. This represents a rare example of experimentally-derived bond energies in the context of NH_3 oxidation.[60] In contrast, almost all other literature values are estimated through bracketing experiments or computational models. The computationally derived average $BDFE_{N–H}$ (61 kcal/mol) and average $BDE_{N–H}$ (62 kcal/mol) of **3** are in good agreement with the experimental average $BDE_{N–H}$ of 59 kcal/mol. The low average $BDFE_{N–H}$ and $BDE_{N–H}$ are driven by a particularly weak N–H bond in **LRe–NH** (43 kcal/mol), which is similar to the computed $BDFE_{N–H}$ of a putative pincer-supported (PONOP)Re^{IV}–NH (PONOP = 2,6-bis-(diisopropyl-phosphinito)pyridine) intermediate recently reported by Miller and coworkers (43 kcal/mol).[67]

Calculations also give insight into the relative energies during sequential removal of H atoms from **3**. The calculated first $BDFE_{N–H}$ of amido complex **3** (80 kcal/mol) is

almost 40 kcal/mol stronger than that of the second (removal of H from **LRe–NH**). Therefore, the initial HAA from **3** using organic reagents is thermodynamically unfavorable by up to 20 kcal/mol, and nitride formation is driven by the much more favorable second N–H oxidation.[34, 35, 42]

The thermochemistry of N–H bond forming and breaking is of particular interest for understanding how to achieve facile N_2 to NH_3 interconversion. We compare our experimental values to literature values (typically derived from computational modelling) in **Table 5.2**. Comparisons show that **3** and (PONOP)Re(NH_2)(Cl)$_2$, both pincer-supported Re^{III}–NH_2 complexes, have very similar $BDFE_{N–H}$ values. Interestingly, the Re–NH compounds exhibit much weaker imide N–H bonds than those of other metals. However, relatively weak N–H bonds were calculated for Mo–NH intermediates in the Chatt[71] (~23 kcal/mol) and Schrock[72] (~42 kcal/mol) systems for N_2 reduction.[73] Consistent with earlier systems, amide intermediates consistently exhibit stronger N–H bonds than their corresponding imide intermediates. However, the difference between these two bond energies is *significantly* larger in the Re systems, especially **3** ($\Delta_{BDFE(N–H)}$ = 37 kcal/mol).

Table 5.2. Selected computed N–H bond free energies of NH_x ligands derived from NH_3 (blue) or N_2 (green).

Complex	Solvent	$BDFE_{N–H}$ (kcal/mol)		
		NH_3	NH_2	NH
(PNP)Re(**NH_2**)(Cl) (**3**)[a]	THF	-	80[a]	43[a]
cis-(PONOP)Re(**NH_2**)$(Cl)_2$ [67]	THF	-	78	43
(PNP)Ir(**NH_2**) [43]	gas phase	-	95[b]	71[b]
trans-[(Ph-tpy)$(PPh_2Me)_2$Mo(**NH_3**)]$^+$ [60, 74]	THF	45.8[c]	64	-
cis-[(Cp)$(P^{Ph}{}_2N^{tBu}{}_2)$Mo(**NH_3**)(CO)]$^+$ [35]	Et_2O	84	61[c]	73[d]
[(PY5)Mo(**NH_3**)]$^{2+}$ [37]	MeCN	68	65	64
[(Cp*)$(P^{tBu}{}_2N^{Ph}{}_2)$Ru(**NH_3**)]$^+$ [40]	THF	83	89	72
[(tpy)(^{NMe2}bpy)Ru(**NH_3**)]$^{2+}$ [52]	THF	79	86	-
(TMP)Ru(**NH_3**)$_2$ [42]	C_6H_6	82	93	75
[(tpy)(^{NMe2}bpy)Fe(**NH_3**)]$^{2+}$ [52]	THF	82	90	-
[($^{Ph}NCH_2CH_2)_3$N]Mo(**NH_3**) [72]	-	52	64	42
[($P_3{}^B$)Fe(**NH_2**)]$^+$ [61]	Et_2O	-	80	65
(salen)Mn(**NH_3**) [73]	gas phase	85	84	60
(η^5-$C_5Me_4SiMe_3)_2$Ti(**NH_3**) [75]	gas phase	42	79	-

[a]This work. [b]Bond enthalpies reported. [c]Experimentally-obtained value from Bordwell equation. [d]Measured after loss of CO ligand following initial N–H bond oxidation.

5.3.2. Relevance to PCET nitride reduction step of NRR

Nitride complex **2** is readily formed via electrochemical N_2 cleavage,[54] so the conversion of NH_3 to the nitride ligand in **2** represents part of the reverse of a hypothetical pathway from N_2 to NH_3 where N_2 cleavage to form **2** is followed by PCET reduction of the nitride. Consequently, thermochemical data from this study can be used to identify specific challenges associated with steps during the conversion of N_2 to NH_3.

One challenge is that nitride complexes formed by N_2 cleavage are often relatively unreactive, and therefore few examples of NH_3 formation via reductive N_2 cleavage have been reported.[19, 20, 67, 76] The initial N–H bond formation via PCET reduction of **2** is one clear challenge, considering that the intermediate **LRe–NH** has a very weak calculated $BDFE_{N–H}$ of only 43 kcal/mol. This is a common problem encountered in N_2 to NH_3

reduction chemistry. [71-73] One way to overcome this is by using potent PCET reagent pairs to form the weak N–H bonds (see Section 1.5).[20, 28, 29, 67, 73, 76, 77] Elucidation of the thermodynamic challenge associated with converting **2**, which is readily formed from electrochemical N_2 splitting, into **LRe–NH** emphasizes the importance of continuing to develop new PCET methodology that can both achieve the formation of weak N–H bonds and integrate into an electrochemical N_2 reduction system.

Our inability to observe the presumed Re^{IV}-imide intermediates also implies that these intermediates are unstable. This is perhaps most evident from the formation of the backbone-protonated nitride complex **5** from the $1e^-$ oxidation of **3**, in which proton transfer from the putative $[Re^{IV}(NH_2)]^+$ complex to the backbone could form a cationic Re^{IV}-imide species. In a similar PNP-supported $W(N_2)$ system, protonation of the pincer-amide is in equilibrium with a transient W-hydride complex that can eliminate H_2 either via a bimetallic mechanism or via protonolysis.[78] A similar ligand-protonation to metal-hydride equilibrium is also hypothesized in an N_2-derived Mo-nitride complex.[79] However, we have no experimental evidence for the formation of a Re-hydride complex in this system. Additionally, decomposition of the Re^{IV}-imide is not accompanied by formation of H_2 gas, which indicates that the weak N–H bond does not eliminate H_2. While the precise mechanisms for decomposition of the imide to the nitride remain unclear, the instability of this intermediate and its preference to form the more stable nitride are problematic in the context of PCET nitride reduction, wherein the imide intermediate must be at least stable enough to persist until subsequent reduction to an amide.

5.4 Conclusions

The work outlined above provides a detailed examination of the thermochemistry and mechanism of NH_3 oxidation to a metal-nitride complex, which can also be generated via electrochemical N_2 cleavage. The conversion of NH_3 to a nitride by **1** to form **2** represents the first example of NH_3 to nitride transformation at Re. Initial deprotonation of NH_3 occurs upon coordination to **1** to form **3**, and subsequent oxidation of the complex can proceed through both concerted HAA pathways or via stepwise pathways following the $1e^-$ oxidation of **3**. In addition to determining individual $BDFE_{N–H}$ values for each N–H bond proceeding from **3** to **2** computationally, the average $BDE_{N–H}$ of **3** in THF (59.2 ± 0.2 kcal/mol) was measured experimentally via calorimetric titration. The particularly weak N–H bond in the **LRe–NH** intermediate (43 kcal/mol) identifies a crucial bottleneck in N_2 to NH_3 conversion for this system; however, the $BDFE_{N–H}$ of **3** is significantly stronger (80 kcal/mol). Additionally, the Re^{IV}-imide intermediates generated in these studies are unstable towards decomposition. Nitride complexes are evidently the most stable intermediates in N_2 cycle chemistry with (PNP)Re, representing a thermodynamic sink. This study demonstrates the utility of examining both directions of N_2 to NH_3 interconversion in the same system in order to identify barriers toward achieving facile conversion in the desired direction.

5.5 Experimental

5.5.1. General considerations

All manipulations were performed under an inert atmosphere of N_2 gas in a M. Braun glovebox or on a Schlenk line unless otherwise specified. Tetrahydrofuran (THF) was distilled under argon from potassium benzophenone ketyl and stored over molecular sieves prior to use. Unless otherwise noted, all other solvents were dried via passage through Q5 columns from Glass Contour Co. and stored over molecular sieves prior to use. Deuterated solvents were degassed and dried over calcium hydride before storing over molecular sieves prior to use, and THF-d_8 was dried additionally with potassium benzophenone ketyl. Deionized water was degassed prior to use. Anhydrous ammonia (Airgas, >99.9%), potassium hexamethyldisilazide (Sigma-Aldrich, 95%, recrystallized), decamethyl cobaltocene (Sigma-Aldrich, 95%, recrystallized), ferrocenium hexafluorophosphate (Santa Cruz Biotechnology, 97%), 2,6-lutidine (Sigma-Aldrich, 98%, distilled and dried over sieves), 2,4,6-tri-*tert*-butylphenol (Sigma-Aldrich, 97%), TEMPO$^{\bullet}$ (Sigma-Aldrich, 98%), phenazine (Sigma-Aldrich, 98%), azobenzene (Sigma-Aldrich, 98%), 1,8-diazabicyclo[5.4.0]undec-7-ene (Sigma-Aldrich, 98%, distilled and dried over sieves), phosphazene base P_1-tBu-tris(tetramethylene) (Sigma-Aldrich, dried under vacuum), phosphazene base P_4-tBu (Sigma-Aldrich, dried under vacuum), and tetrabutylammonium hexafluorophosphate (Sigma-Aldrich, 99%, recrystallized x3) were purchased and used without further purification unless otherwise noted. $^{t}Bu_3PhO^{\bullet}$,[80] 1,8-dichloro-9,10-anthracenediol,[62] and (PNP)$ReCl_2$[56] were synthesized and purified according to literature procedures.

5.5.2. Instrumentation and methods

NMR spectra were acquired on an Agilent 400 MHz or 500 MHz spectrometer. ^{1}H spectra were referenced to residual ^{1}H signals from the deuterated solvent with which the sample was prepared,[81] and $^{13}C\{^{1}H\}$, $^{31}P\{^{1}H\}$, and ^{15}N spectra were absolute referenced to the corresponding ^{1}H spectra. IR spectra were obtained using a Bruker Alpha spectrometer containing a diamond ATR unit with 2 cm^{-1} resolution.

Electrochemical measurements were collected using a CH Instruments 600D potentiostat in an Ar glovebox. Cyclic voltammetry (CV) experiments were conducted in 0.2 M tetrabutylammonium hexafluorophosphate (TBA-PF_6) solutions in dry solvent using a glassy carbon disc working electrode (3.0 mm diameter), a platinum wire auxiliary electrode, and a silver wire psuedoreference. Wire electrodes were sanded and rinsed with dry solvent prior to use, and glassy carbon disc electrodes were polished using 0.05 μm alumina powder and rinsed with dry solvent prior to use. Measurements conducted in THF were compensated for internal resistance prior to collecting data. CV experiments were referenced to ferrocene (Cp_2Fe) as an internal standard after completion.

Elemental analyses were obtained from the CENTC Elemental Analysis Facility at the University of Rochester. Microanalysis samples were weighed on a PerkinElmer Model AD-6 Autobalance, analyzed on a PerkinElmer 2400 Series II Analyzer, and handled in a VAC Atmospheres glovebox under argon.

Gas chromatography was performed on a ThermoFisher Trace 1300 GC apparatus equipped with a thermal conductivity detector and a Supelco fused silica capillary column (5 Å molecular sieves, 30 m x 0.53 mm). The system uses N_2 as a carrier gas and allows for determination of H_2 at concentrations greater than 1 ppm.

The mean bond dissociation energy (BDE) of the (PNP)Re(NH_2)(Cl)/(PNP)Re(N)(Cl) complex couple was determined by Isothermal Titration Calorimetry performed in a NanoITC device by TA Instruments with a 24K gold cell and a sample volume of 1 mL operated in overfill mode. 2,4,6-tri-*tert*-butylphenoxyradical ($^tBu_3PhO^\bullet$) was used as the titrant. Measurement by ITCRun Version 3.4.6.0, TA Instruments, 2017 and Evaluation by NanoAnalyze Version 3.7.5 TA Instruments, 2015.

5.5.3. Experimental details

Preparation of (PNP)Re(NH_2)(Cl) (3): A sample of **1** (283.2 mg, 0.459 mmol) was dissolved in benzene (20 mL) under Ar in a resealable Schlenk tube. The solution was degassed and warmed to ambient temperature, and the atmosphere was replaced with NH_3 gas (1 atm) while stirring. There was an immediate color change of the solution from purple to brown. The mixture was stirred for 1 min, then frozen using a liquid nitrogen bath. The flask was placed in an ice water bath, and the benzene was lyophilized at 0 °C to give a light brown powder. The powder was extracted with pentane (3 x 10 mL), and the mixture was filtered through Celite to remove a pale blue solid (109.3 mg). Drying the filtrate under vacuum gave **3** as a brown microcrystalline solid (167.6 mg, 0.280 mmol, 61% yield). Crystals of **3** suitable for XRD grew from a concentrated pentane solution at –40 °C. ^{1}H NMR (400 MHz, C_6D_6): δ 12.70 (br s, 2H, NH_2), 3.59 (m, 2H, N(CH_2CH$_2$)$_2$), 3.34 (m, 2H, N(CH_2CH$_2$)$_2$), 1.89 (m, 2H, N(CH$_2$CH_2)$_2$), 1.60 (m, 2H, N(CH$_2$CH_2)$_2$), 1.36 (vt, 18H, P(*^{t}Bu*)(^{t}Bu')), 1.20 (vt, 18H, P(^{t}Bu)(*^{t}Bu'*)) ppm. ^{31}P{^{1}H} NMR (162 MHz, C_6D_6) δ 40.08 (s) ppm. ^{15}N NMR (51 MHz, C_6D_6): δ –260 (s, *N*H$_2$) ppm. UV-vis (THF solution): 308 nm (ε = 5600 M^{-1} cm^{-1}), 420 nm (ε = 1100 M^{-1} cm^{-1}), 562 nm (ε = 340 M^{-1} cm^{-1}). FTIR (solid,

N–H): 3397, 3338 cm^{-1}. Anal. Calcd.(found) for $C_{20}H_{46}ClN_2P_2Re$ (%): C, 40.16(40.45); H, 7.75(7.74); N, 4.68(4.52).

Preparation of [*trans*-(PNP)Re(NH$_3$)$_2$(Cl)][BAr$^F_4$] (4): A sample of **1** (50.0 mg, 0.081 mmol, 1.0 equiv) and 71.7 mg $NaBAr^F_4$ (71.7 mg, 0.081 mmol, 1.0 equiv) was dissolved in THF (10 mL) in a resealable Schlenk tube under N_2. The N_2 atmosphere was removed with 3 freeze-pump-thaw cycles. The flask was then filled with anhydrous NH_3 (1 atm) while stirring at ambient temperature. There was an immediate color change of the solution from purple to light brown (almost colorless). The mixture was stirred for 1 min. The solvent and excess NH_3 were removed under vacuum to give a green residue. The residue was washed with pentane (3 x 5 mL), and the residue was extracted with THF (2 x 5 mL). Crystallization from a layered THF:pentane solution (12:4 mL) at –40 °C gave a pale green crystalline solid. The solid was collected and washed with benzene (3 x 3 mL), then dried under vacuum to give 54.5 mg of **4** as pale green crystals (0.368 mmol, 45.5% yield). ^{1}H NMR (400 MHz, THF-d_8): δ 7.77 (s, 8H, *o*-BAr^F_4), 7.56 (s, 4H, *p*-BAr^F_4), 5.47 (br s, 6H, NH_3), 4.49 (m, 4H, N(CH_2CH$_2$)$_2$), 2.04 (m, 4H, N(CH$_2$CH_2)$_2$), 1.29 (vt, 36H, P(^{t}*Bu*)$_2$) ppm. ^{31}P{^{1}H} NMR (162 MHz, THF-d_8): δ –9.98 (s) ppm. UV-Vis (THF solution): 328 nm (shoulder, ε = 3700 M^{-1} cm^{-1}). FTIR (solid, N–H): 3392, 3353, 3245, 3174 cm^{-1}. Anal. Calcd.(found) for $C52H_{62}BF_{24}ClN_2P_2Re$ (%): C, 42.22(42.54); H, 4.22(4.16); N, 2.84(2.59).

H$_2$ quantification from 1e^- oxidation of (PNP)Re(NH$_2$)(Cl) (3): Under N_2, 54 mg $FcPF_6$ (0.16 mmol, 1.1 equiv) was slurried in 2 mL THF in a 7 mL scintillation vial. The vial was sealed with a septum cap, and a solution of 89 mg (PNP)Re(NH_2)(Cl) (**2**, 0.15 mmol, 1.0 equiv) in 2 mL THF was injected into the vial via syringe. An immediate color

change from deep blue to orange occurred, as well as formation of a brown precipitate. The reaction was stirred for 10 min at ambient temperature, then chilled for 5 min in a dry ice/isopropanol bath to remove THF vapor from the headspace. 50 μL CH_4 gas was added via airtight syringe into the headspace of the vial as an internal standard, and 50 μL of the headspace of the vial was removed via airtight syringe for H_2 quantification on the GC. No H_2 peak was observed in the resulting chromatograph, indicating less than 1% yield of H_2. The reaction was repeated, with identical results.

Removal of the volatiles under vacuum gave a sticky, dark red-orange residue. The residue was extracted with 2 x 5 mL THF and filtered through Celite. Removal of THF from the orange-brown filtrate under vacuum yielded a dirty orange solid. The solid was redissolved in ~10 mL THF, from which a ~2 mL aliquot was taken. The aliquot was dried under vacuum, dissolved in 0.7 mL THF-d_8, and analyzed using NMR spectroscopy vs. a 1,3,5-trismethoxybenzene (TMB) internal standard to quantify the Re products. Analysis of the ^{1}H NMR spectra showed 52% yield of nitride **5** and 17% yield of dichloride **1** for the first run, and 47% yield of nitride **5** and 20% yield of dichloride **1** for the second run.

H_2 quantification from the 1e^- reduction of [(PNP)Re(NH$_3$)$_2$(Cl)][BAr$^F_4$] (4): Under N_2, 174 mg of [(PNP)Re(NH$_3$)$_2$(Cl)][BAr$^F_4$] (0.12 mmol) was dissolved in 2 mL THF in a 7 mL scintillation vial. The vial was sealed with a septum cap, and a solution of 46 mg Cp*$_2$Co (0.14 mmol, 1.1 equiv) dissolved in 2 mL THF was injected into the vial via syringe. An immediate color change from light tan to dark brown-gold occurred, as well as formation of a yellow precipitate. The reaction was stirred for 10 min at ambient temperature, then chilled for 5 min in a dry ice/isopropanol bath to remove THF vapor from the headspace. 50 μL CH_4 gas was added via airtight syringe into the headspace of

the vial as an internal standard, and 50 μL of the headspace of the vial was removed via airtight syringe for H_2 quantification on the GC. No H_2 peak was observed in the resulting chromatograph, indicating less than 1% yield of H_2. The reaction was repeated, with identical results.

Removal of the volatiles under vacuum gave a sticky, dark brown residue. The residue was extracted with 2 x 5 mL THF and filtered through Celite. Removal of THF from the brown filtrate under vacuum yielded a sticky brown solid. The solid was redissolved in ~10 mL THF, from which a ~2 mL aliquot was taken. The aliquot was dried under vacuum, dissolved in 0.7 mL THF-d_8, and analyzed using NMR spectroscopy vs. a 1,3,5-trismethoxybenzene (TMB) internal standard to quantify the Re products. Analysis of the ^{1}H NMR spectra showed formation of **3** in 73% for the first run and 61% for the second run.

Electrolysis of (PNP)Re(NH$_2$)(Cl) (3): In an Ar glovebox, an H-cell was prepared with the analyte chamber containing a 20 mL solution of 20 mg **3** (3.3 x 10^{-5} mol, 1.7 mM) and 77 μL 2,6-lutidine (6.6 x 10^{-4} mol, 34 mM) in 0.2 M tetrabutylammonium-hexafluorophosphate in THF, and the counter chamber containing a 20 mL solution of 24.4 mg [Cp_2Fe][PF_6] (7.4 x 10^{-5} mol, 3.7 mM, 2.2 equiv) in 0.2 M tetrabutylammonium-hexafluorophosphate in THF. A stir bar was added to each chamber. The analyte chamber was fitted with a glassy carbon working electrode and Ag wire pseudoreference electrode, and the counter chamber was fitted with a Pt mesh auxiliary electrode. The open circuit potential (OCP) of the cell was measured, and a cyclic voltammogram (CV) was taken of the analyte solution (**Figure 5.19**). The potential of the first oxidation event (E_{pa} = +0.56 V vs. Ag) was measured vs. the OCP (–0.07 V vs. Ag), demonstrating that this event occurs

at a potential of OCP +0.63 V. The glassy carbon electrode was removed and replaced with a carbon paper electrode. The OCP was remeasured (+0.05 V vs. Ag), and a CV of the analyte solution was taken to reference the first oxidation peak (E_{pa} = +0.68 V vs. Ag). With the carbon paper electrode, the first oxidation event again occurred at a potential of OCP +0.63 V vs. Ag.

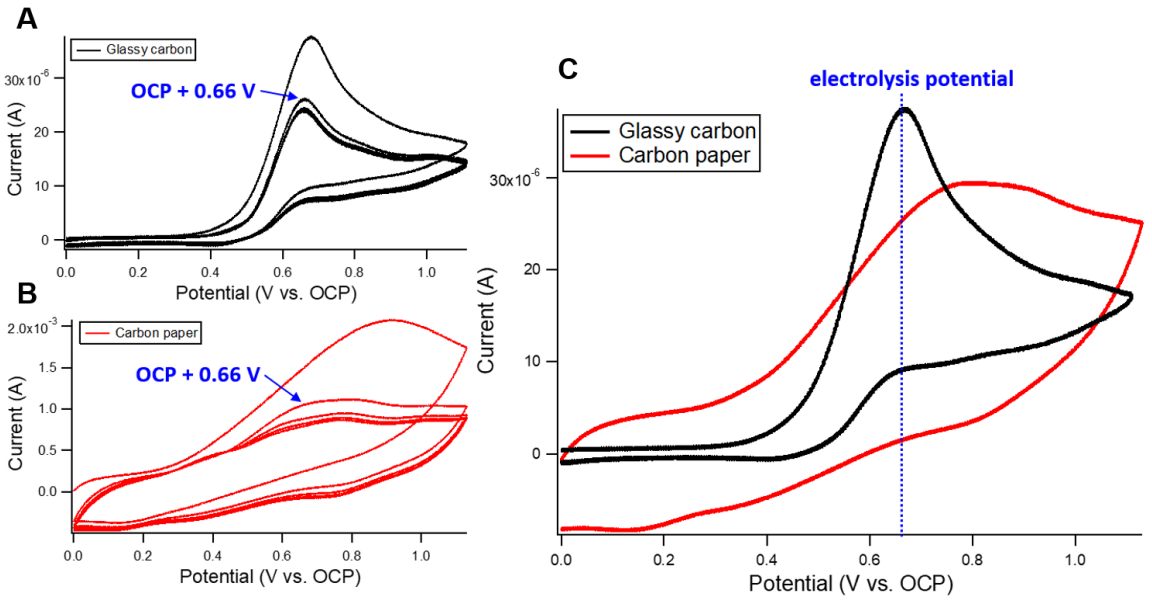

Figure 5.19. A: Cyclic voltammograms of **3** (1.7 mm) and 2,6-lutidine (34 mM) in a 0.2 M tetrabutylammonium-hexafluorophosphate THF solution, using a glassy carbon electrode, Pt mesh auxiliary electrode, and Ag wire pseudoreference. **B:** Cyclic voltammograms of the same solution using a carbon paper electrode. **C:** Comparison of cyclic voltammograms of the analyte solution using different electrodes, with the electrolysis potential labeled in blue. The carbon paper voltammograms are reduced by a factor of 50 for the sake of comparison. All potentials are given vs. the OCP of the solution.

The potential of the analyte cell was then held at +0.68 V vs. Ag, with both chambers gently stirring. Over the course of the electrolysis, the solution in the analyte chamber changed color from brown to orange, and the solution in the counter chamber changed color from blue to yellow. The electrolysis was stopped after 7.09 C of charge had passed (2.2e^- per Re). The charge vs. time plot showed relatively constant passing of charge over the course of the electrolysis (**Figure 5.20**).

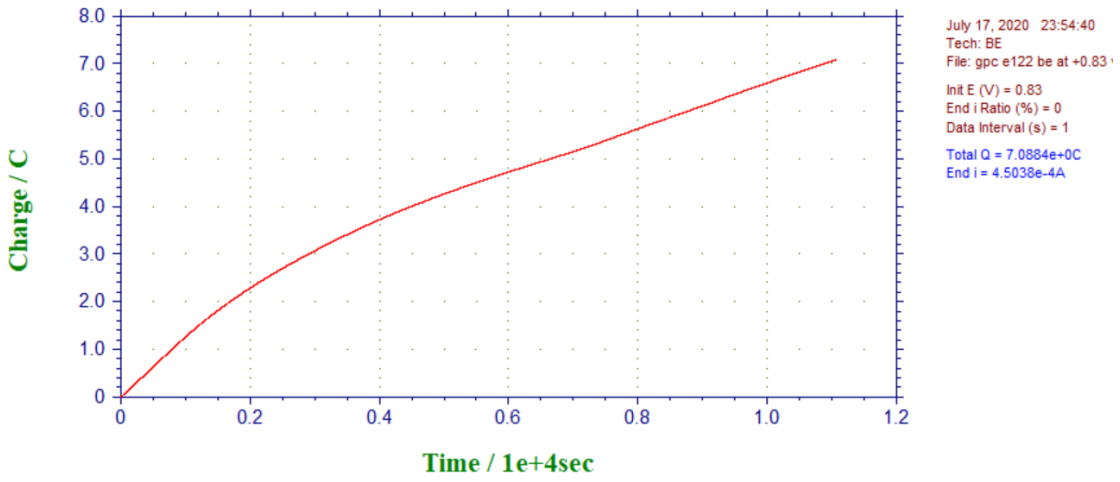

Figure 5.20. Charge vs. time plot of the electrolysis of **3** at OCP +0.63 V.

The contents of the analyte chamber were transferred to a 20 mL scintillation vial and dried under vacuum to give a light orange/white solid. The Re products were extracted with toluene (3 x 3 mL) and benzene (2 x 3 mL), and the extracts were filtered through Celite. The light orange filtrate was dried under vacuum to give 29.7 mg of an orange solid. The solid was dissolved in ~7 mL THF, from which a ~2 mL aliquot was removed. The aliquot was dried under vacuum to give 8.4 mg of solid, which was redissolved in 0.5 mL THF-d_8, along with a known amount of TMB as an internal standard (34.5 mM). The concentration of **5** in the sample (13.0 mM) was calculated by comparing the ^{1}H resonances of **5** vs. TMB in the resulting ^{1}H NMR spectrum (see **Figure 5.17**). This corresponds to a 69% yield of **5** from the electrolysis.

Calorimetric titration of (PNP)Re(NH$_2$)(Cl) (3) with ^{t}Bu$_3$PhO$^\bullet$: The experimental conditions for the titration of (PNP)Re(NH$_2$)(Cl) (**3**) with ^{t}Bu$_3$PhO$^\bullet$ (4.0 equiv) in THF (see **Figure 5.18**) are summarized in **Table 5.3**. Three separate runs were performed, and all measurements were taken at ambient temperature (298 K).

Table 5.3. Reaction details for isothermal titration calorimetry experiments.

	First Run	Second/Third Run
Concentration and volume of **3** (mM / µL)	0.341 / 950	0.341 / 950
Concentration and volume of TBP (mM/µL)	5.28 / 250	5.05 / 180
Injection Steps x Injected Volume (µL)	33 x 7.5	24 x 7.5
Waiting time between two additions (s)	250	250
Stirring rate (rpm)	350	350
Equilibration time before start of experiment (s)	1885	1453 and 1525

Figures 5.21–5.22 show a representative thermogram and integrated titration curve for the titration of **3** with $^{t}Bu_3PhO^{\bullet}$ in THF. Greyed out points are not taken into account in the fitting process. The first point is generally neglected due to the dilution effect within the pre-experiment equilibration time. The mean heat value was determined for the titration steps before the equivalence point.

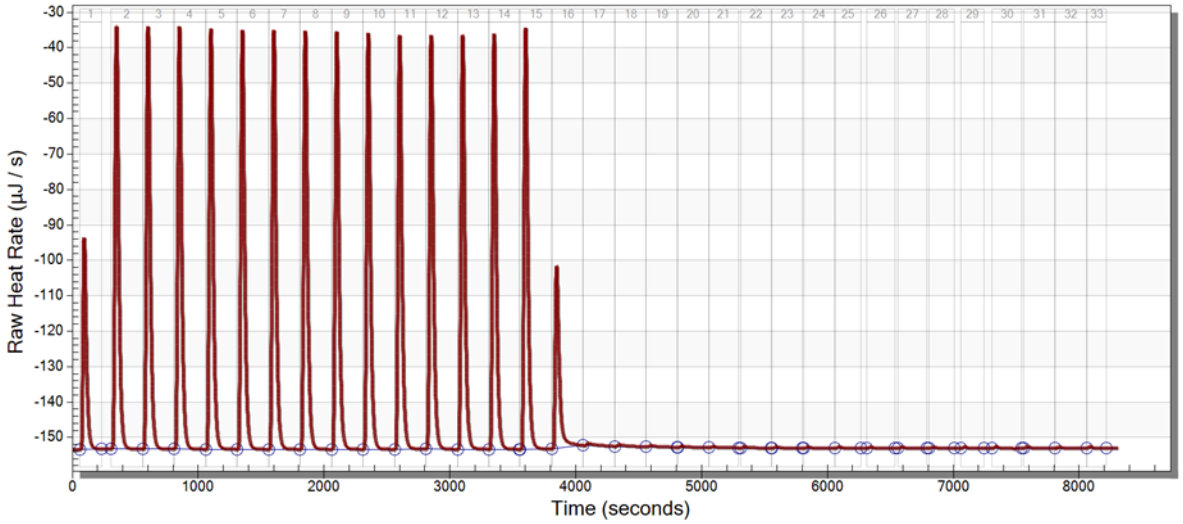

Figure 5.21. Thermogram for the titration of **3** with $^{t}Bu_3PhO^{\bullet}$ (first run).

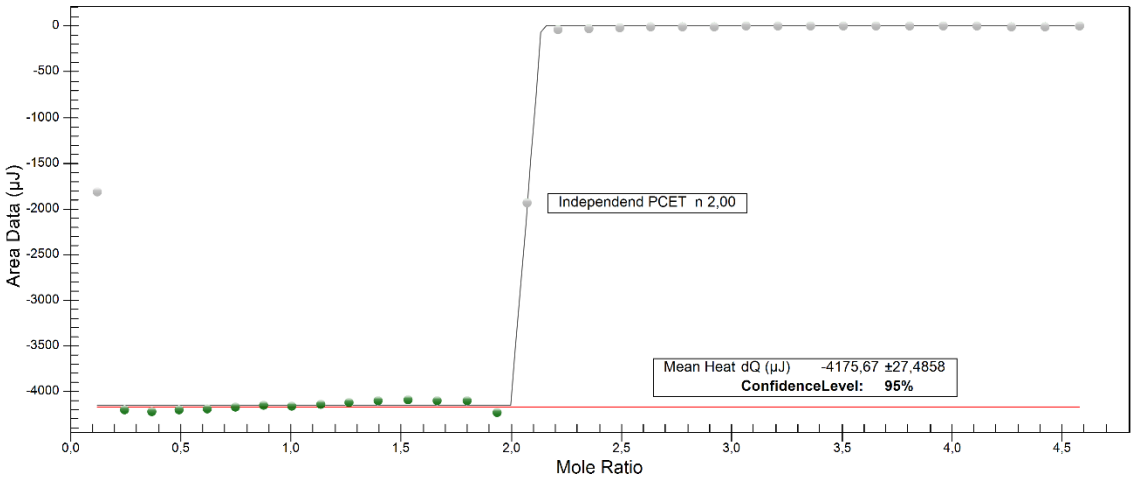

Figure 5.22. Integrated heat curve for the titration of **3** with $^{t}Bu_3PhO^{\bullet}$ (first run).

Table 5.4. Summarized results from isothermal calorimetry titrations.

Run	Mean Heat [µJ]	Consumed moles per injection [nmol]	Enthalpy [kJ/mol]
1	-4176 ± 27	19.62	-213 ± 1
2	-3957 ± 40	18.76	-211 ± 2
3	-4017 ± 39	18.76	-214 ± 2
Mean Enthalpy = $\mathbf{-213 \pm 2\ \frac{kJ}{mol} = -50.9 \pm 0.5\ \frac{kcal}{mol}}$			

The measured enthalpy of the reaction of **3** with 2 equiv of TBP to give **2** (THF, 298 K) is –50.9 ± 0.5 kcal/mol. The average $BDE_{N–H}$ of **3** was therefore calculated to be 59.2 ± 0.2 kcal/mol from the following equations, based on the known $BDE_{O–H}$ of $^{t}Bu_3PhO^{\bullet}$ in THF (84.6 kcal/mol):[92]

$$\mathrm{BDE}^{\mathrm{THF}}_{[\mathrm{Re}]\mathrm{N(H)-H}} = \mathrm{BDE}^{\mathrm{THF}}_{\mathrm{TBP}} - \frac{\Delta H}{2}$$

$$\mathrm{BDE}^{\mathrm{THF}}_{[\mathrm{Re}]\mathrm{N(H)-H}} = \left(84.6 - \frac{50.9}{2}\right)\frac{\mathrm{kcal}}{\mathrm{mol}} = \mathbf{59.2 \pm 0.2\ \frac{kcal}{mol}}$$

5.5.4. Computational details

Density Functional Theory (DFT) calculations were performed using GAUSSIAN09 (revision D.01).[82] All calculations were performed by the clusters at the Yale University Faculty of Arts and Sciences High Performance Computing Center. Structures were optimized using the hybrid functional B3LYP,[83] with basis sets def2-TZVP used for all atoms.[84, 85] Unless otherwise noted, all calculations include the D3 version of Grimme's dispersion correction[86] and a conductor-like polarizable continuum model (CPCM) for THF solvent. Frequency calculations were performed to confirm that the optimized structures were minima; the optimized structures for the complexes reported showed no negative frequencies. Natural Bond Order (NBO) calculations were performed using the NBO6.0 package[87, 88] in GAUSSIAN09. NBO calculations were modified to include Wiberg[89] and Mayer-Mulliken[90, 91] partial bond orders.

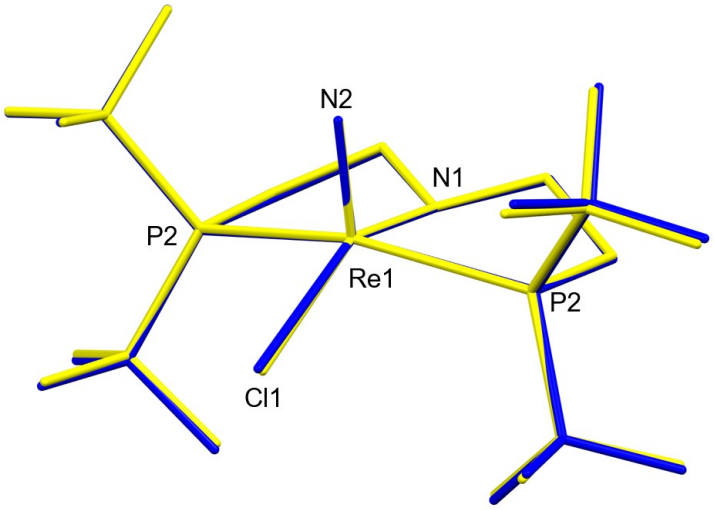

Figure 5.23. Overlay of crystal structure (yellow) and calculated structure (blue) of **2**. Hydrogen atoms are omitted for clarity.

Table 5.5. Calculated structural parameters of **2**.

Bond (Å) / Angle (°)	Experimental	Calculated
Re – N1	2.033(6)	2.036
Re – N2	1.643(6)	1.664
Re – Cl1	2.441(2)	2.521
Re – P (avg)	2.439	2.437
N1 – Re - N2	105.8(3)	106.2
N1 – Re – Cl1	147.7(2)	150.4
N2 – Re – Cl1	106.5(2)	103.4

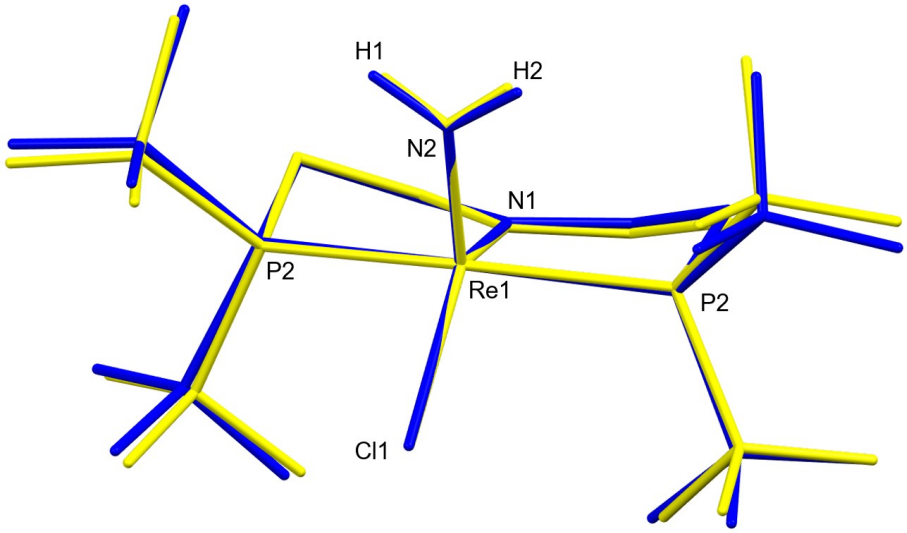

Figure 5.24. Overlay of crystal structure (yellow) and calculated structure (blue) of **3**. Hydrogen atoms (other than amide hydrogens) are omitted for clarity.

Table 5.6. Calculated structural parameters of **3**.

Bond (Å) / Angle (°)	Experimental	Calculated
Re – N1	1.936(3)	1.957
Re – N2	1.959(3)	1.935
Re – Cl1	2.384(1)	2.446
Re – P (avg)	2.390	2.416
N1 – Re - N2	115.5(1)	114.8
N1 – Re – Cl1	135.6(1)	138.3
N2 – Re – Cl1	108.8(1)	106.9

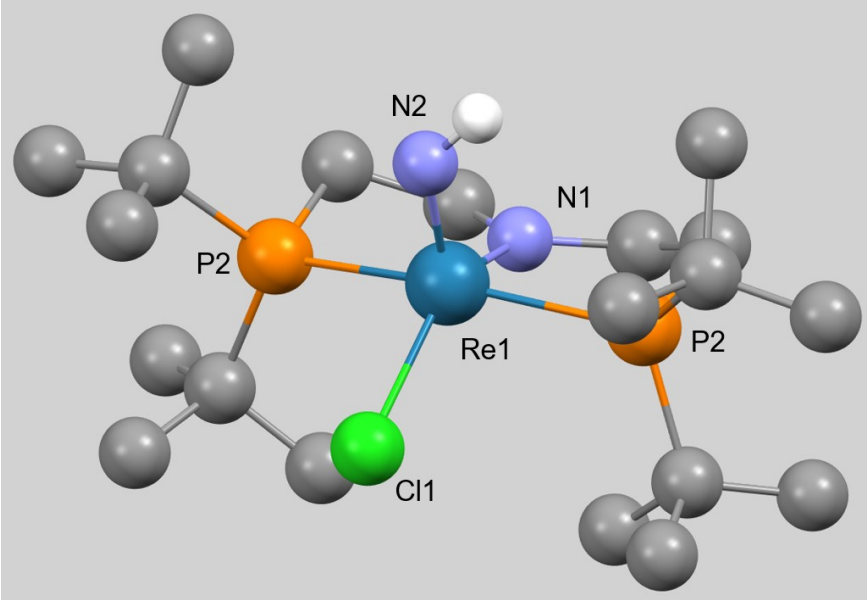

Figure 5.25. Calculated structure of **LRe–NH**. Hydrogen atoms (other than imide hydrogen) are omitted for clarity.

Table 5.7. Calculated structural parameters of **LRe–NH**.

Bond (Å) / Angle (°)	**Calculated**
Re – N1	1.993
Re – N2	1.798
Re – Cl1	2.476
Re – P (avg)	2.448
N1 – Re – N2	112.4
N1 – Re – Cl1	142.1
N2 – Re – Cl1	105.5

Table 5.8. Calculated Wiberg partial bond orders for **2**, **LRe–NH**, and **3**.

Bond	**3**	**LRe–NH**	**2**
Re – NH_x	0.91	1.74	2.46
Re – P*N*P	1.01	0.78	0.64
Re – P1	0.56	0.54	0.53
Re – P2	0.56	0.55	0.53
Re – Cl	0.57	0.51	0.43

Table 5.9. Calculated Mayer-Mulliken partial bond orders for **2**, **LRe–NH**, and **3**.

Bond	**3**	**LRe–NH**	**2**
Re – NH_x	1.22	1.77	2.68
Re – P*N*P	1.19	1.10	0.98
Re – P1	0.94	0.80	0.81

Re – P2	0.94	0.86	0.81
Re – Cl	0.67	0.62	0.57

Table 5.10. Computed enthalpies and energies for **2**, **LRe–NH**, and **3** in THF.

	*(PNP)Re(NH2)(Cl) (**3**)*		*(PNP)Re(NH)(Cl) (**LRe-NH**)*		*(PNP)Re(N)(Cl) (**2**)*	
Experimental Data	**Hartrees**	**kcal/mol**	**Hartrees**	**kcal/mol**	**Hartrees**	**kcal/mol**
Zero-point corr.	0.643644	403.89	0.629436	394.98	0.620653	389.47
Thermal corr. to Energy	0.678238	425.60	0.664242	416.82	0.654646	410.80
Thermal corr. to Enthalpy	0.679182	426.19	0.665186	417.41	0.65559	411.39
Thermal corr. To Gibbs Free Energy	0.584066	366.51	0.568591	356.80	0.561581	352.40
Sum electronic and zero-point energies	-2120.609869	-1330701.78	-2119.999019	-1330318.46	-2119.44947	-1329973.62
Sum electronic and thermal energies	-2120.575275	-1330680.07	-2119.964213	-1330296.62	-2119.415478	-1329952.29
Sum electronic and thermal enthalpies	-2120.574331	-1330679.48	-2119.963269	-1330296.03	-2119.414534	-1329951.69
Sum electronic and thermal free energies	-2120.669447	-1330739.16	-2120.059864	-1330356.65	-2119.508542	-1330010.69

Table 5.11. Computed enthalpies and energies for TEMPO• and TEMPOH in THF.

	TEMPO Radical		*TEMPOH*	
Experimental Data	**Hartrees**	**kcal/mol**	**Hartrees**	**kcal/mol**
Zero-point corr.	0.260874	163.70	0.272316	170.88
Thermal corr. to Energy	0.272897	171.25	0.284559	178.56
Thermal corr. to Enthalpy	0.273841	171.84	0.285503	179.16
Thermal corr. To Gibbs Free Energy	0.224223	140.70	0.236225	148.23
Sum electronic and zero-point energies	-483.64692	-303492.80	-484.234677	-303861.62
Sum electronic and thermal energies	-483.634897	-303485.25	-484.222435	-303853.94
Sum electronic and thermal enthalpies	-483.633953	-303484.66	-484.22149	-303853.34
Sum electronic and thermal free energies	-483.683571	-303515.79	-484.270769	-303884.27

Table 5.12. Computed enthalpies and energies for $^{t}Bu_3PhO$• and $^{t}Bu_3PhOH$ in THF.

	tBu3PhO radical		*tBu3PhOH*	
Experimental Data	**Hartrees**	**kcal/mol**	**Hartrees**	**kcal/mol**
Zero-point corr.	0.427123	268.02	0.439942	276.07
Thermal corr. to Energy	0.448995	281.75	0.462082	289.96
Thermal corr. to Enthalpy	0.44994	282.34	0.463026	290.55
Thermal corr. To Gibbs Free Energy	0.378246	237.35	0.391728	245.81
Sum electronic and zero-point energies	-778.458322	-488489.60	-779.07521	-488876.71
Sum electronic and thermal energies	-778.43645	-488475.88	-779.053069	-488862.81
Sum electronic and thermal enthalpies	-778.435506	-488475.29	-779.052125	-488862.22
Sum electronic and thermal free energies	-778.507199	-488520.27	-779.123423	-488906.96

Table 5.13. Calculated reaction enthalpies of H-atom abstraction from **3** and **LRe–NH** with $^{t}Bu_3PhO$• and resulting $BDE_{N–H}$ values. Referenced vs. $^{t}Bu_3PhOH$ ($BDE_{O–H}$ = 84.6 kcal/mol in THF).[92]

Reaction	**Enthalpy (kcal/mol)**	**BDE (vs. tBu3PhOH)**
(PNP)Re(NH2)(Cl) + 2 tBu3PhO to (PNP)Re(N)(Cl) + 2 tBu3PhOH	-46.08	(average) 61.6
(PNP)Re(NH2)(Cl) + tBu3PhO to (PNP)Re(NH)(Cl) + tBu3PhOH	-3.49	81.1
(PNP)Re(NH)(Cl) + tBu3PhO to (PNP)Re(N)(Cl) + tBu3PhOH	-42.60	42.0

Table 5.14. Calculated reaction free energies of H-atom abstraction from **3** and **LRe–NH** with TEMPO• and resulting $BDFE_{N–H}$ values. Referenced vs. TEMPOH ($BDFE_{O–H}$ = 65.5 kcal/mol in THF).[62]

Reaction	Free Energy (kcal/mol)	BDFE (vs. TEMPOH)
(PNP)Re(NH2)(Cl) + 2 TEMPO to (PNP)Re(N)(Cl) + 2 TEMPOH	-8.89	(average) 61.1
(PNP)Re(NH2)(Cl) + TEMPO to (PNP)Re(NH)(Cl) + TEMPOH	14.05	79.5
(PNP)Re(NH)(Cl) + TEMPO to (PNP)Re(N)(Cl) + TEMPOH	-22.51	43.0

5.5.5. Crystallographic details

Crystals were isolated in an Ar glovebox by decanting the mother liquor from the crystals before transferring and submerging them in high-viscosity petroleum oil on a microscope slide. Single crystals suitable for X-ray diffraction were identified under a polarizing microscope and mounted on 200 μm MiTeGen Dual-Thickness MicroLoops in a mixture of high-viscosity petroleum, then mounted on the diffractometer instrument. Low-temperature diffraction data (ω-scans) were collected on a Rigaku MicroMax-007HF diffractometer coupled to a Dectris Pilatus3R detector with Mo Kα (λ = 0.71073 Å) for the structure of 007c-17049 (**3**). Low-temperature diffraction data (ω-scans) were collected on a Rigaku MicroMax-007HF diffractometer coupled to a Saturn994+ CCD detector with Cu Kα (λ = 1.54178 Å) for the structure of 007b-17124 (**4**). The diffraction images were processed and scaled using either Rigaku CrystalClear software (CrystalClear and CrystalStructure; Rigaku/MSC: The Woodlands, TX, 2005) or Rigaku Oxford Diffraction software (CrysAlisPro; Rigaku OD: The Woodlands, TX, 2015). The structure was solved with SHELXT and was refined against F^2 on all data by full-matrix least squares with SHELXL (Sheldrick, G. M. Acta Cryst. 2008, A64, 112–122).

(PNP)Re(NH$_2$)(Cl) (3, 007c-17049). All non-hydrogen atoms were refined anisotropically. Hydrogen atoms were included in the model at geometrically calculated

positions and refined using a riding model. The isotropic displacement parameters of all hydrogen atoms were fixed to 1.2 times the U value of the atoms to which they are linked (1.5 times for methyl groups). The N-H positions are semi-freely refined with N-H distance restrains of 0.860(2) Å. The H-Re distances of H2a and H2b were restrained to be similar. The N-H hydrogen atoms are also riding on N2.

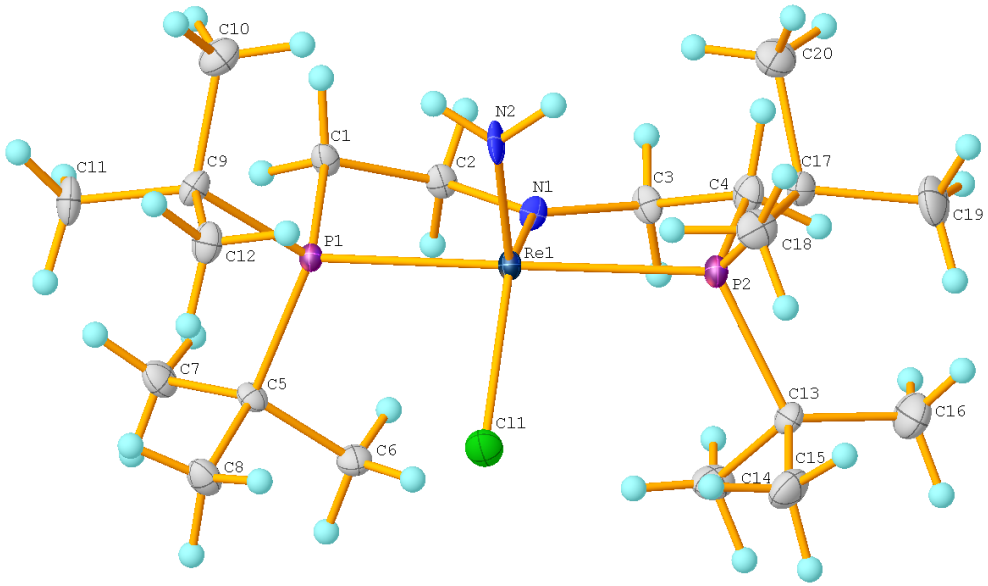

Figure 5.26. The complete numbering scheme of 007c-17049 (**3**) with 50% thermal ellipsoid probability levels. The hydrogen atoms are shown as circles for clarity.

Table 5.14. Crystal data and structure refinement for 007c-17049 (**3**).

Identification code	007c-17049	
Empirical formula	C20 H46 Cl N2 P2 Re	
Formula weight	598.18	
Temperature	93(2) K	
Wavelength	0.71073 Å	
Crystal system	Monoclinic	
Space group	$P2_1/n$	
Unit cell dimensions	a = 8.5852(3) Å	□= 90°.
	b = 23.5810(7) Å	□= 92.515(3)°.

	c = 12.2292(4) Å □ = 90°.
Volume	2473.39(14) Å^3
Z	4
Density (calculated)	1.606 Mg/m^3
Absorption coefficient	5.158 mm^{-1}
F(000)	1208
Crystal size	0.200 x 0.200 x 0.050 mm^3
Crystal color and habit	Green Plate
Diffractometer	Dectris Pilatus 3R
Theta range for data collection	2.937 to 27.483°.
Index ranges	-9<=h<=11, -30<=k<=30, -15<=l<=15
Reflections collected	35252
Independent reflections	5656 [R(int) = 0.0853]
Observed reflections (I > 2sigma(I))	4806
Completeness to theta = 25.242°	99.9 %
Absorption correction	Semi-empirical from equivalents
Max. and min. transmission	1.00000 and 0.53287
Solution method	SHELXT-2014/5 (Sheldrick, 2014)
Refinement method	SHELXL-2014/7 (Sheldrick, 2014)
Data / restraints / parameters	5656 / 4 / 253
Goodness-of-fit on F^2	1.008
Final R indices [I>2sigma(I)]	R1 = 0.0290, wR2 = 0.0621
R indices (all data)	R1 = 0.0383, wR2 = 0.0647
Largest diff. peak and hole	1.871 and -1.100 e.Å^{-3}

[(PNP)Re(NH$_3$)$_2$(Cl)][BAr$^F_4$] (4, 007b-17124). All non-hydrogen atoms were refined anisotropically. Hydrogen atoms were included in the model at geometrically calculated positions and refined using a riding model. The isotropic displacement parameters of all hydrogen atoms were fixed to 1.2 times the U value of the atoms to which they are linked (1.5 times for methyl groups; 1.2 for NH_3 groups). The pentane and BAr^F sites are disordered. Four of the CF_3 groups of the BAr^F are disordered; the atoms involved are {F1, F2, F3}, {F7, F8, F9}, {F13, F14, F15} {C19, C20, C21}. Each group was

modeled over two positions with their site occupancies freely refined. The two sites are distinguished with the suffixes "A" and "B". The converged values of the groups are 0.62(3):0.38(3), 0.60(3):0.40(3), 0.51(2):0.49(2), 0.613(12):0.378(12), respectively. The CF3 groups were restrained to have similar 1,2 C-C and C-F distances for chemically identical bonds. The 1,3 F-F distance were also restrained to be similar. The thermal parameters of the CF_3 groups were retained to behave as a rigid group. The pentane was disordered across the crystallographic inversion center. The special position constraints were suppressed and the site occupancies were fixed at 0.5. The pentane was retained to behave as a rigid group. Atom C3A's thermal parameter was restrained to be identical to that of its neighbor due to C3A's proximity to the crystallographic inversion center.

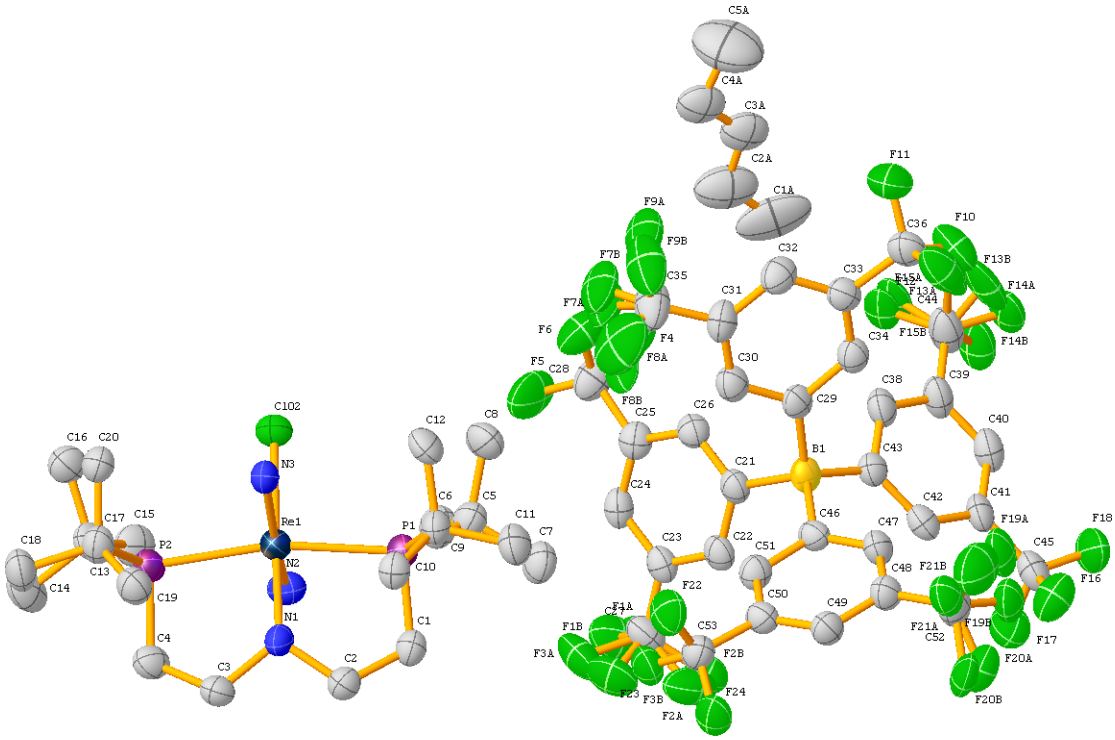

Figure 5.27. The complete numbering scheme of 007b-17124 (**4**) with 50% thermal ellipsoid probability levels. The hydrogen atoms are omitted for clarity.

Table 1. Crystal data and structure refinement for 007b-17124 (**4**).

Identification code	007b-17124
Empirical formula	C54.50 H68 B Cl F24 N3 P2 Re
Formula weight	1515.51
Temperature	93(2) K
Wavelength	1.54184 Å
Crystal system	Triclinic
Space group	P-1
Unit cell dimensions	a = 12.2681(5) Å □= 92.777(3)°.
	b = 15.3208(6) Å □= 109.357(4)°.
	c = 17.9247(8) Å □ = 97.022(3)°.
Volume	3140.5(2) $Å^3$
Z	2
Density (calculated)	1.603 Mg/m^3
Absorption coefficient	5.646 mm^{-1}
F(000)	1518
Crystal size	0.050 x 0.050 x 0.010 mm^3
Crystal color and habit	Green Plate
Diffractometer	Rigaku Saturn 944+ CCD
Theta range for data collection	2.625 to 66.597°.
Index ranges	-14<=h<=14, -18<=k<=18, -21<=l<=21
Reflections collected	109426
Independent reflections	10946 [R(int) = 0.1340]
Observed reflections (I > 2sigma(I))	8233
Completeness to theta = 66.597°	98.4 %
Absorption correction	Semi-empirical from equivalents
Max. and min. transmission	1.00000 and 0.88256
Solution method	SHELXT-2014/5 (Sheldrick, 2014)
Refinement method	SHELXL-2014/7 (Sheldrick, 2014)
Data / restraints / parameters	10946 / 295 / 922
Goodness-of-fit on F^2	1.038
Final R indices [I>2sigma(I)]	R1 = 0.0557, wR2 = 0.1212
R indices (all data)	R1 = 0.0833, wR2 = 0.1364
Largest diff. peak and hole	0.885 and -1.957 $e.Å^{-3}$

5.6 References

1. Smil, V., *Enriching the Earth: Fritz Haber, Carl Bosch, and the Transformation of World Food Production.* MIT Press: Cambridge, MA, 2004.

2. Erisman, J. W.; Sutton, M. A.; Galloway, J.; Klimont, Z.; Winiwarter, W., *Nat. Geosci.* **2008,** 1, 636-639.

3. Renner, J. N.; Greenlee, L. F.; Ayres, K. E.; Herring, A. M., *Interface magazine* **2015,** 24, 51-57.

4. Service, R. F., Ammonia—a renewable fuel made from sun, air, and water—could power the globe without carbon. *Science* July 2, 2018, 2018.

5. Valera-Medina, A.; Xiao, H.; Owen-Jones, M.; David, W. I. F.; Bowen, P. J., *Prog. Ener. Comb. Sci.* **2018,** 69, 63-102.

6. Martin, A. J.; Shinagawa, T.; Perez-Ramirez, J., *Chem* **2019,** 5, 263-283.

7. Adli, N. M.; Zhang, H.; Mukherjee, S.; Wu, G., *J. Electrochem. Soc.* **2018,** 165, J3130-J3147.

8. Warren, J. J.; Tronic, T. A.; Mayer, J. M., *Chem. Rev.* **2010,** 110, 6961-7001.

9. Hochman, G.; Goldman, A. S.; Felder, F. A.; Mayer, J. M.; Miller, A. J. M.; Holland, P. L.; Goldman, L. A.; Manocha, P.; Song, Z.; Aleti, S., *ACS Sustainable Chem. Eng.* **2020,** 8, 8938-8948.

10. Rebreyend, C.; de Bruin, B., *Angew. Chem., Int. Ed.* **2015,** 54, 42-44.

11. van der Ham, C. J. M.; Koper, M. T. M.; Hetterscheid, D. G. H., *Chem. Soc. Rev.* **2014,** 43, 5183-5191.

12. Rosca, V.; Duca, M.; de Groot, M. T.; Koper, M. T. M., *Chem. Rev.* **2009,** 109, 2209-2244.

13. Kyriakou, V.; Garagounis, I.; Vasileiou, E.; Vourros, A.; Stoukides, M., *Catal. Today* **2017,** 286, 2-13.

14. Liu, H.; Wei, L.; Liu, F.; Pei, Z.; Shi, J.; Wang, Z.-j.; He, D.; Chen, Y., *ACS Catal.* **2019,** 9, 5245-5267.

15. Wan, Y.; Xu, J.; Lv, R., *Mater. Today* **2019,** 27, 69-90.

16. Yandulov, D. V.; Schrock, R. R., *Science* **2003,** 301, 76-78.

17. Kuriyama, S.; Arashiba, K.; Nakajima, K.; Tanaka, H.; Kamaru, N.; Yoshizawa, K.; Nishibayashi, Y., J. *Am. Chem. Soc.* **2014,** 136, 9719-9731.

18. Arashiba, K.; Kinoshita, E.; Kuriyama, S.; Eizawa, A.; Nakajima, K.; Tanaka, H.; Yoshizawa, K.; Nishibayashi, Y., *J. Am. Chem. Soc.* **2015,** 137, 5666-5669.

19. Arashiba, K.; Eizawa, A.; Tanaka, H.; Nakajima, K.; Yoshizawa, K.; Nishibayashi, Y., *Bull.Chem. Soc. Jpn.* **2017,** 90, 1111-1118.

20. Ashida, Y.; Arashiba, K.; Nakajima, K.; Nishibayashi, Y., *Nature* **2019,** 568, 536-540.

21. Arashiba, K.; Miyake, Y.; Nishibayashi, Y., *Nat. Chem.* **2011,** 3, 120-125.

22. Wickramasinghe, L. A.; Ogawa, T.; Schrock, R. R.; Muller, P., *J. Am. Chem. Soc.* **2017,** 139, 9132-9135.

23. Itabashi, T.; Mori, I.; Arashiba, K.; Eizawa, A.; Nakajima, K.; Nishibayashi, Y., *Dalton Trans.* **2019,** 48, 3182-3186.

24. Eizawa, A.; Arashiba, K.; Egi, A.; Tanaka, H.; Nakajima, K.; Yoshizawa, K.; Nishibayashi, Y., *Chem. - Asian J.* **2019,** 14, 2091-2096.

25. Anderson, J. S.; Rittle, J.; Peters, J. C., Nature (London, U. K.) **2013,** 501, 84-87.

26. Creutz, S. E.; Peters, J. C., *J. Am. Chem. Soc.* **2013,** 136, 1105-1115.

27. Del Castillo, T. J.; Thompson, N. B.; Peters, J. C., *J. Am. Chem. Soc.* **2016,** 138, 5341-5350.

28. Chalkley, M. J.; Del Castillo, T. J.; Matson, B. D.; Roddy, J. P.; Peters, J. C., *ACS Cent. Sci.* **2017,** 3, 217-223.

29. Chalkley, M. J.; Del Castillo, T. J.; Matson, B. D.; Peters, J. C., *J. Am. Chem. Soc.* **2018,** 140, 6122-6129.

30. Chalkley, M. J.; Drover, M. W.; Peters, J. C., *Chem. Rev.* **2020,** 120, 5582-5636.

31. Du Bois, J.; Hong, J.; Carreira, E. M.; Day, M. W., *J. Am. Chem. Soc.* **1996,** 118, 915-16.

32. Clarke, R. M.; Storr, T., *J. Am. Chem. Soc.* **2016,** 138, 15299-15302.

33. Keener, M.; Peterson, M.; Hernandez Sanchez, R.; Oswald, V. F.; Wu, G.; Menard, G., *Chem. - Eur. J.* **2017,** 23, 11479-11484.

34. Cook, B. J.; Johnson, S. I.; Chambers, G. M.; Kaminsky, W.; Bullock, R. M., *Chem. Commun.* **2019,** 55, 14058-14061.

35. Bhattacharya, P.; Heiden, Z. M.; Wiedner, E. S.; Raugei, S.; Piro, N. A.; Kassel, W. S.; Bullock, R. M.; Mock, M. T., *J. Am. Chem. Soc.* **2017,** 139, 2916-2919.

36. Margulieux, G. W.; Bezdek, M. J.; Turner, Z. R.; Chirik, P. J., *J. Am. Chem. Soc.* **2017,** 139, 6110-6113.

37. Johnson, S. I.; Heins, S. P.; Klug, C. M.; Wiedner, E. S.; Bullock, R. M.; Raugei, S., *Chem. Commun.* **2019,** 55, 5083-5086.

38. Pipes, D. W.; Bakir, M.; Vitols, S. E.; Hodgson, D. J.; Meyer, T. J., J. Am. Chem. Soc. **1990,** 112, 5507-14.

39. Coia, G. M.; Demadis, K. D.; Meyer, T. J., *Inorg. Chem.* **2000,** 39, 2212-2223.

40. Bhattacharya, P.; Heiden, Z. M.; Chambers, G. M.; Johnson, S. I.; Bullock, R. M.; Mock, M. T., *Angew. Chem., Int. Ed.* **2019,** 58, 11618-11624.

41. Nakajima, K.; Toda, H.; Sakata, K.; Nishibayashi, Y., *Nat. Chem.* **2019,** 11, 702-709.

42. Dunn, P. L.; Johnson, S. I.; Kaminsky, W.; Bullock, R. M., *J. Am. Chem. Soc.* **2020,** 142, 3361-3365.

43. Scheibel, M. G.; Abbenseth, J.; Kinauer, M.; Heinemann, F. W.; Wuertele, C.; de Bruin, B.; Schneider, S., *Inorg. Chem.* **2015,** 54, 9290-9302.

44. Thusius, D. D.; Taube, H., *J. Phys. Chem.* **1967,** 71, 3845-57.

45. Taube, H.; White, J. D., *J. Phys. Chem.* **1970,** 74, 4142-9.

46. Buhr, J. D.; Taube, H., *Inorg. Chem.* **1979,** 18, 2208-12.

47. Collman, J. P.; Hutchison, J. E.; Ennis, M. S.; Lopez, M. A.; Guilard, R., *J. Am. Chem. Soc.* **1992,** 114, 8074-80.

48. Ishitani, O.; White, P. S.; Meyer, T. J., *Inorg. Chem.* **1996,** 35, 2167-8.

49. Ishitani, O.; Ando, E.; Meyer, T. J., *Inorg. Chem.* **2003,** 42, 1707-1710.

50. Zott, M. D.; Garrido-Barros, P.; Peters, J. C., *ACS Catal.* **2019,** 9, 10101-10108.

51. Habibzadeh, F.; Miller, S. L.; Hamann, T. W.; Smith, M. R., III, *Proc. Natl. Acad. Sci. U. S. A.* **2019,** 116, 2849-2853.

52. Najafian, A.; Cundari, T. R., *J. Phys. Chem. A* **2019,** 123, 7973-7982.

53. Klopsch, I.; Finger, M.; Würtele, C.; Milde, B.; Werz, D. B.; Schneider, S., *J. Am. Chem. Soc.* **2014,** 136, 6881-6883.

54. Lindley, B. M.; van Alten, R. S.; Finger, M.; Schendzielorz, F.; Würtele, C.; Miller, A. J. M.; Siewert, I.; Schneider, S., *J. Am. Chem. Soc.* **2018,** 140, 7922-7935.

55. Klopsch, I.; Kinauer, M.; Finger, M.; Würtele, C.; Schneider, S., *Angew. Chem., Int. Ed.* **2016,** 55, 4786-4789.

56. Connor, G. P.; Mercado, B. Q.; Lant, H. M. C.; Mayer, J. M.; Holland, P. L., *Inorg. Chem.* **2019,** 58, 10791-10801.

57. Klopsch, I.; Finger, M.; Wuertele, C.; Milde, B.; Werz, D. B.; Schneider, S., *J. Am. Chem. Soc.* **2014,** 136, 6881-6883.

58. Hillhouse, G. L.; Bercaw, J. E., *J. Am. Chem. Soc.* **1984,** 106, 5472-8.

59. Lindley, B. M.; Bruch, Q. J.; White, P. S.; Hasanayn, F.; Miller, A. J. M., *J. Am. Chem. Soc.* **2017,** 139, 5305-5308.

60. Bezdek, M. J.; Guo, S.; Chirik, P. J., *Science* **2016,** 354, 730-733.

61. Matson, B. D.; Peters, J. C., *ACS Catal.* **2018,** 8, 1448-1455.

62. Wise, C. F.; Agarwal, R. G.; Mayer, J. M., *J. Am. Chem. Soc.* **2020,** 142, 10681-10691.

63. Tshepelevitsh, S.; Kütt, A.; Lõkov, M.; Kaljurand, I.; Saame, J.; Heering, A.; Plieger, P. G.; Vianello, R.; Leito, I., *Eur. J. Org. Chem.* **2019,** 2019, 6735-6748.

64. Schwesinger, R.; Willaredt, J.; Schlemper, H.; Keller, M.; Schmitt, D.; Fritz, H., *Chemische Berichte* **1994,** 127, 2435-2454.

65. Schwesinger, R.; Schlemper, H.; Hasenfratz, C.; Willaredt, J.; Dambacher, T.; Breuer, T.; Ottaway, C.; Fletschinger, M.; Boele, J.; Fritz, H.; Putzas, D.; Rotter, H. W.; Bordwell, F. G.; Satish, A. V.; Ji, G.-Z.; Peters, E.-M.; Peters, K.; von Schnering, H. G.; Walz, L., *Liebigs Annalen* **1996,** 1996, 1055-1081.

66. Cappellani, E. P.; Drouin, S. D.; Jia, G.; Maltby, P. A.; Morris, R. H.; Schweitzer, C. T., *J. Am. Chem. Soc.* **1994,** 116, 3375-88.

67. Bruch, Q. J.; Connor, G. P.; Chen, C.-H.; Holland, P. L.; Mayer, J. M.; Hasanayn, F.; Miller, A. J. M., *J. Am. Chem. Soc.* **2019,** 141, 20198-20208.

68. Man, W.-L.; Tang, T.-M.; Wong, T.-W.; Lau, T.-C.; Peng, S.-M.; Wong, W.-T., *J. Am. Chem. Soc.* **2004,** 126, 478-479.

69. Scheibel, M. G.; Wu, Y.; Stückl, A. C.; Krause, L.; Carl, E.; Stalke, D.; de Bruin, B.; Schneider, S., *J. Am. Chem. Soc.* **2013,** 135, 17719-17722.

70. Abbenseth, J.; Finger, M.; Wuertele, C.; Kasanmascheff, M.; Schneider, S., *Inorg. Chem. Front.* **2016,** 3, 469-477.

71. Stephan, G. C.; Sivasankar, C.; Studt, F.; Tuczek, F., *Chem. - Eur. J.* **2008,** 14, 644-652.

72. Bezdek, M. J.; Pappas, I.; Chirik, P. J., Determining and Understanding N-H Bond Strengths in Synthetic Nitrogen Fixation Cycles. In *Nitrogen Fixation*, Nishibayashi, Y., Ed. Springer International Publishing: Cham, 2017; pp 1-21.

73. Wang, D.; Loose, F.; Chirik, P. J.; Knowles, R. R., *J. Am. Chem. Soc.* **2019,** 141, 4795-4799.

74. Bezdek, M. J.; Chirik, P. J., *Angew. Chem., Int. Ed.* **2018,** 57, 2224-2228.

75. Pappas, I.; Chirik, P. J., *J. Am. Chem. Soc.* **2016,** 138, 13379-13389.

76. Ashida, Y.; Arashiba, K.; Tanaka, H.; Egi, A.; Nakajima, K.; Yoshizawa, K.; Nishibayashi, Y., *Inorg. Chem.* **2019,** 58, 8927-8932.

77. Chalkley, M. J.; Oyala, P. H.; Peters, J. C., *J. Am. Chem. Soc.* **2019,** 141, 4721-4729.

78. Schluschass, B.; Abbenseth, J.; Demeshko, S.; Finger, M.; Franke, A.; Herwig, C.; Wuertele, C.; Ivanovic-Burmazovic, I.; Limberg, C.; Telser, J.; Schneider, S., *Chem. Sci.* **2019,** 10, 10275-10282.

79. Hebden, T. J.; Schrock, R. R.; Takase, M. K.; Mueller, P., *Chem. Commun.* **2012,** 48, 1851-1853.

80. Manner, V. W.; Markle, T. F.; Freudenthal, J. H.; Roth, J. P.; Mayer, J. M., *Chem. Commun.* **2008**, 256-258.

81. Fulmer, G. R.; Miller, A. J. M.; Sherden, N. H.; Gottlieb, H. E.; Nudelman, A.; Stoltz, B. M.; Bercaw, J. E.; Goldberg, K. I., *Organometallics* **2010,** 29, 2176-2179.

82. Frisch, M. J.; Trucks, G. W.; Schlegel, H. B.; Scuseria, G. E.; Robb, M. A.; Cheeseman, J. R.; Scalmani, G.; Barone, V.; Mennucci, B.; Petersson, G. A.; Nakatsuji, H.; Caricato, M.; Li, X.; Hratchian, H. P.; Izmaylov, A. F.; Bloino, J.; Zheng, G.; Sonnenberg, J. L.; Hada, M.; Ehara, M.; Toyota, K.; Fukuda, R.; Hasegawa, J.; Ishida, M.; Nakajima, T.; Honda, Y.; Kitao, O.; Nakai, H.; Vreven, T.; Montgomery, J. A.; Peralta, J. E.; Ogliaro, F.; Bearpark, M.; Heyd, J. J.; Brothers, E.; Kudin, K. N.; Staroverov, V. N.; Kobayashi, R.; Normand, J.; Raghavachari, K.; Rendell, A.; Burant, J. C.; Iyengar, S. S.; Tomasi, J.; Cossi, M.; Rega, N.; Millam, J. M.; Klene, M.; Knox, J. E.; Cross, J. B.; Bakken, V.; Adamo, C.; Jaramillo, J.; Gomperts, R.; Stratmann, R. E.; Yazyev, O.; Austin, A. J.; Cammi, R.; Pomelli, C.; Ochterski, J. W.; Martin, R. L.; Morokuma, K.; Zakrzewski, V. G.; Voth, G. A.; Salvador, P.; Dannenberg, J. J.; Dapprich, S.; Daniels, A. D.; Farkas; Foresman, J. B.; Ortiz, J. V.; Cioslowski, J.; Fox, D. J., Gaussian 09, Revision B.01. In Wallingford CT, 2009.

83. Stephens, P. J.; Devlin, F. J.; Chabalowski, C. F.; Frisch, M. J., J. *Phys. Chem.* **1994,** 98, 11623-7.

84. Andrae, D.; Haeussermann, U.; Dolg, M.; Stoll, H.; Preuss, H., *Theor. Chim. Acta* **1990,** 77, 123-41.

85. Weigend, F.; Ahlrichs, R., *Phys. Chem. Chem. Phys.* **2005,** 7, 3297-3305.

86. Grimme, S.; Antony, J.; Ehrlich, S.; Krieg, H., *J. Chem. Phys.* **2010,** 132, 154104/1-154104/19.

87. Glendening, E. D.; Landis, C. R.; Weinhold, F., *J. Comput. Chem.* **2013,** 34, 1429-1437.

88. Glendening, E. D.; Badenhoop, J. K.; Reed, A. E.; Carpenter, J. E.; Bohmann, J. A.; Morales, C. M.; Landis, C. R.; Weinhold, F., *NBO 6.0*, Theoretical Chemistry Institute, University of Wisconsin, Madison: Madison, WI, USA, **2013**.

89. Wiberg, K. B., *Tetrahedron* **1968,** 24, 1083-1096.

90. Mayer, I., *Chem. Phys. Lett.* **1983,** 97, 270-4.

91. Mayer, I., *Int. J. Quantum Chem.* **1984,** 26, 151-4.

92. Abbenseth, J.; Delony, D.; Neben, M. C.; Würtele, C.; de Bruin, B.; Schneider, S., *Angew. Chem., Int. Ed.* **2019,** 58, 6338-6341.